# Spatial and Spectral Brightness Improvement of Single-Mode Laser Diode Arrays

Natalia Trela

Submitted for the degree of Doctor of Philosophy

Heriot-Watt University

School of Engineering and Physical Sciences

Physics Department

May 2012

# ABSTRACT

This thesis addresses the strong need for efficient and compact techniques for brightness enhancement of laser diode arrays and responds to the challenges created for high performance optics and techniques for laser characterisation.

A novel optical inter-leaving method for a 7-bar stack of single-mode emitters, providing a nearly 2-fold improvement in the slow axis beam parameter product, enabling fibre-coupling, is demonstrated.

A laser-written dual-axis optics approach is used to perform challenging slow axis collimation combined with fast axis correction for closely-packed 49-single-mode emitter bars, to provide low-loss collimation with high pointing accuracy of less than 3% and 10% of a beam divergence in the fast and slow axis direction, respectively. This produces excellent source for application beam-combined laser diode systems.

An emitter-by-emitter simultaneous analysis is used to provide spectra and far field pointing for all emitters and evaluate the performance of various external cavity configurations with Volume Holographic Gratings (VHGs). For the ultra-collimated bars, high efficiency VHG-locking is shown to be maintained over enhanced range of temperatures (>17˚C) and large laser-VHG distances (>110 mm). Highly effective feedback enables the use of a folded cavity configuration for wavelength selection over a range of 8 nm for the full 49-emitter bar, giving a prospect for multi-wavelength single-VHG-locking of bars for cost-effective spectral combining. An innovative technique of wavelength stepping by individually-formed folded cavities for 5 and 7 sections along the bar demonstrates a potential to produce a source for high performance dense spectral beam combining.

In a VHG-based Talbot cavity, eight emitters are coherently locked with a high-visibility interference pattern at 1W of output power. The results of phase-locking for full 49-emitter bar show that the slow axis pointing variation of ± 2mrad produces different supermodes, for a fixed alignment of the cavity, thus it must be additionally corrected for further improvement.

*To my parents*

*Moim rodzicom*

The research has been carried out at the *Laser and Photonics Application (LPA)* group at the *School of Engineering and Physical Sciences* at *Heriot-Watt University* (Edinburgh, UK).

The author gratefully acknowledges the support of Heriot-Watt *Innovative Manufacturing Research Centre*, UK Engineering and Physical Sciences Research Council and Selex Sensors and Airborne Systems, Edinburgh.

# ACKNOWLEDGEMENTS

I would like to thank my supervisors Prof. Denis R. Hall and Prof. Howard J. Baker for giving me the opportunity to work in *Laser and Photonics Application Group*. I would like express my sincere gratitude to Howard for his invaluable guidance, encouragement and support during the course of my study. I am also very grateful for the trust and support I was given by Denis.

I am also very grateful to Prof. Krzysztof M. Abramski, who mentored me in the beginning of my studies back in Poland and helped me to establish the link with the research group at *Heriot-Watt University*. Without his help I would not have had the chance to work on this project.

I would also like to thank my colleagues Dr Ian J. Thomson, Dr Aaron M. McKay (who I am still to beat in squash), Alberto Campos Zatarain and Dr. Krystian L. Wlodarczyk for their assistance, advice and for sharing the enjoyable times during my time at *Heriot-Watt*. It was a pleasure to work with you guys! I would also like to thank Dr Jesus Fernando Monjardin for his guidance in the first couple of months of my study that I kept finding useful throughout the duration of my work.

I would also like to thank Dr Roy McBride and Dr Józef J. Wendland for the collaboration that added a significant value to the project by giving me access to such tools as and laser-written refractive optics technique. I also appreciate their encouraging interest in my work and providing very valuable comments.

I cannot express my endless gratitude to parents and my little brother for their never ending trust and love.

I thank my Polish friends Anka, Wower, Mira, Bartek and Sucha who made me feel back at home each time I went to Poland.

I also thank my friends in Edinburgh (you know who are!) who made my stay here very enjoyable and unforgettable.

Last but not least, I unspeakably grateful to Peter for standing by me at all times, for his love and affection, delicious cooking and making me smile every single day!

# DECLARATION STATEMENT

(Research Thesis Submission Form should be placed here)

# LIST OF CONTENTS

# List of publications

**JOURNAL PUBLICATIONS:**

1. N. Trela, H. J. Baker, J. J. Wendland, D. R. Hall; *Dual-axis beam correction for an array of single-mode diode laser emitters using a laser written custom phase plate*; Optics Express, Vol. 17, Issue 26, pp. 23576-23581, 2009.
2. N. Trela, H. J. Baker, D. R. Hall, *VHG-locking and wavelength selection of an Ultra-collimated 49 Element Single-mode Diode Laser*, Optics Express, in preparation.
3. A. M. McKay, N. Trela, H. J. Baker, D. R. Hall, *Reformatting of diode bars to hexagonal arrays of circular beams using laser-cut micro-optics*, Optics Express, in preparation.

**PATENT APPLICATIONS:**

1. N. Trela, H. J. Baker, R. McBride, *Multi-wavelength diode laser array*, British Patent Application #1107948.0, filed on May 12, 2011.

**CONFERENCE PRESENTATION:**

1. N. Trela, H. J. Baker, D.R. Hall, *High-brightness, ultra-collimated single-mode emitter arrays in a VHG-based external cavity configuration*, Invited paper on High Power Diode Lasers & Systems, Coventry, 2011
2. R. McBride, N. Trela, J.J. Wendland, H. J. Baker, *Compensating the effects of smile in VHG stabilized diode laser bar*, High Power Diode Lasers & Systems, Coventry, 2011
3. R. McBride, N. Trela, J.J. Wendland, H. J. Baker, *Extending the locking range of VHG-stabilized diode laser bars using wavefront compensator phaseplates*, SPIE-DSS, SPIE Proceedings, 2011.
4. N. Trela, H. J. Baker, D. R. Hall, *Wavelength-locking of an Ultra-collimated 49 Element Single-mode Diode Laser Array by a Distant VHG*, CLEO-QELS, San Jose, 2010.
5. H. J. Baker, N. Trela, D. R. Hall, R. McBride, and J. J. Wendland, *Beam Reformatting and Combining of High-Power Laser Diode Stacks*, Conference on Lasers and Electro-Optics, OSA Technical Digest (CD) (Optical Society of America, 2010), paper CThX2.
6. N. Trela, H. J. Baker, J. J. Wendland, D. R. Hall; *Demonstration of high pointing accuracy, dual-axis collimation of 49 emitter diode bar using a laser written custom phase plate*, SPIE Photonics West, San Francisco, 2010.
7. I. J. Thomson, H. J. Baker, K. L. Wlodarczyk, N. Trela, D. R. Hall; *400W Yb:YAG planar waveguide laser using novel unstable resonators*, SPIE Photonics West, San Francisco, 2010.

8. S. Alam, K. Chen, J. R. Hayes, D. Lin, A. Malinowski, H. J. Baker, N. Trela, R. McBride, D. J. Richardson, *Over 55W of frequency doubled light at 530nm pumped by an all-fiber, diffraction limited, picosecond fibre MOPA*, SPIE Photonics West, San Francisco, 2010.
9. N. Trela, H. J. Baker, R. McBride, D. R. Hall; *Low-Loss Wavelength Locking of a 49-Element Single Mode Diode Laser Bar with Phase plate Beam Correction*; CLEO Europe , Munich, 2009.
10. N. Trela, H. J. Baker, R. McBride, D. R. Hall; *New optical techniques for diode lasers in manufacturing applications*, James Watt Institute for High Value Manufacturing Conference, Edinburgh, 2009.
11. I. J. Thomson, H. J. Baker, N. Trela, J. F. Monjardin, J. D. R. Valera, D. R. Hall; *Double sided diode edge-pumped Yb:YAG laser with 230W output power*; CLEO Conference, Baltimore, 2009.
12. I. J. Thomson, J. F. Monjardin, N. Trela, J. D. R. Valera, H. J. Baker, D. R. Hall; *Width scaling of diode pumped Yb:YAG planar waveguide lasers*; Europhoton ’08 , Paris 2008.
13. I J Thomson, J F Monjardin, N Trela, J D R Valera, H J Baker, D R Hall; “Development of width-scaled edge pumped planar waveguide lasers”; IoP Photon ’08 Conference, Edinburgh, 2008.
14. H J Baker, J F Monjardin, I J Thomson, N Trela, J D R Valera, D R Hall; “Development of edge pumped planar waveguide lasers”; SPIE Photonics West Conference, San Jose 2008.

# LIST OF ACRONYMS

| | | |
|---|---|---|
| AlGaAs | - | *aluminium gallium arsenide* |
| BSM | - | *Bookham, single-mode emitter bar* |
| BBA | - | *Bookham, broad-area emitter bar* |
| EFL | - | *effective focal length* |
| FAC | - | *fast axis collimator* |
| FL | - | *focal length* |
| FWHM | - | *full width half maximum* |
| HPLDA | - | *high-power laser diode array* |
| HR | - | *highly reflecting* |
| CBC | - | *coherent beam combining* |
| CL | - | *cylindrical lens* |
| LD | - | *laser diode* |
| LDA | - | *laser diode array* |
| SAC | - | *slow axis collimation* |
| SBC | - | *spectral beam combining* |
| SDG | - | *surface diffraction grating* |
| SL | - | *spherical lens* |
| VHG | - | *volume holographic grating* |

# Chapter 1.
# Introduction

## 1.1 Background and motivation

Over the last decade, the extensive developments in laser diode technology have resulted in excellent values for power conversion efficiency, with current laser diodes now reaching efficiencies of nearly 75% [1, 2] and high output powers up to multi-kW-levels from laser diode stacks. This, together with extreme compactness and high reliability, led to a rapid growth in the laser diode industry [3]. Although state-of-the-art surface-emitting laser diode sources can now provide up to over 200 W from a large two-dimensional array [4, 5], edge-emitting GaAs-based diode lasers remain dominant in terms of power, efficiency and range of available wavelengths. Current high-power diode laser systems have the potential to compete with gas, solid-state and fibre lasers widely used in direct material processing applications. However, there are still issues with power scaling and especially the preservation of beam quality that require further improvements.

For edge-emitting laser diodes with a typical emission area of 1 μm by 100 to 150 μm for broad-area emitters or 1 μm by 3 to 6 μm for single-mode emitters, the power density at the facets may reach multi-MW/cm$^2$ levels and the possibility of catastrophic optical damage (COD) [6, 7] imposes stringent limitations on the power that can be achieved from a single emitter. Nevertheless, developments in special facet coatings [8, 9], together with increasing the width of the emission area and improvements in purity of semiconductor materials have allowed the power achievable from a single emitter to be significantly increased. Currently, powers up to 20 W per emitter can be obtained [10]. Other effects including thermal rollover, spatial hole burning and spectral hole burning are increasingly recognized as key limitations for further power scaling of laser diodes [11].

Higher output power levels are produced by combining a large number of mutually incoherent laser diodes into arrays. One-dimensional laser diode arrays can now provide up to 1 kW [12]. Typical diode laser bars are 10 mm long and contain from 19 to 49 emitters with fill factors (commonly defined as emitters width divided by emitter pitch) from 8% to 80%.

The high power from laser diode bars is achieved at the expense of highly asymmetric output beam. In the direction perpendicular to the junction (i.e. fast axis), nearly diffraction limited beams are emitted from an approximately 1-μm-wide area producing a large divergence angle (FWHM) of ≈ 30˚, resulting in a beam parameter product (half angle x beam radius) of about 0.3 mm.mrad. Poor beam quality and large emitting area in the so called slow axis (with typical divergence angle of 7-8˚ FWHM) result in a beam parameter product the order of 500 mm.mrad.

Further power scaling is often obtained by using laser diode stacks composed of multiple laser bars. In such systems, bars with highly asymmetric beam parameter product are separated by micro-channel heat sink coolers, and are therefore spaced by 1.5 - 2 mm for CW operation. As a consequence, high-power laser diode stacks containing large numbers of incoherent emitters suffer from poor beam quality and a broad spectrum. Thus, to answer the requirements of high brightness applications, external beam modifications are necessary.

In addition to the systematic design limitations discussed above, the beam quality of commercial diode laser arrays is affected by manufacturing tolerances and environmental influences. The main causes of beam quality degradation are bonding-induced smile error and fast axis lens aberrations and misalignment errors, as discussed in Chapter 6. The beam pointing is also determined by the intrinsic properties of the laser waveguides, fabrication induced distortions such as facet bending and twisting and external feedback, however these aspects are not addressed in this thesis. Strain and thermal gradient in the laser chip produce nonuniformity in wavelength distribution across a laser array. As a result, although all emitters in a laser diode array are designed to have identical spatial and spectral properties, each individual emitter produces a slightly different spectrum, pointing angle and far field divergence.

As a consequence of the combination of the factors discussed above, high-power diode lasers provide brightness that is two orders of magnitude lower than other types of industrial lasers such as Yb:YAG (250W) providing up to 10 GW $cm^{-2}$ $ster^{-1}$ and $CO_2$ (5kW): 5000 MW $cm^{-2}$ $ster^{-1}$ (calculated based on state-of-art industrial systems using the formula given later in Eq. 2.11). In order to enable direct diode laser systems to replace other type of lasers in material processing applications, their brightness must be improved to deliver sufficient power at a specified spot size at the workpiece or via coupling into an optical fibre.

There have been many different approaches of brightness improvement for high-power laser diodes. As shown in Chapter 3, spatial [13-15], and spectral [13, 14] beam

combining approaches have proven their scalability to provide kW-laser output power levels. However, the performance and scalability of most of the brightness improvement techniques strongly depends on geometry and the intrinsic properties of the laser diode arrays. In particular, one of the challenges of efficient beam combination of large laser diode arrays is to control both the divergence of the emitters, and their propagation direction at the same time. Based on the literature reviewed in Chapter 3, as well as experimental evidence shown later throughout this thesis, it is evident that excellent spatial properties of the beams are essential in order to achieve high performance in any potential beam formatting methods for large laser arrays as well as feedback-based external cavity configurations. This factor has largely motivated the work presented in this thesis, where the improvement of initial properties of the beams is achieved and acts as the foundation for further brightness enhancement techniques.

Prior to this study, the former members *of Laser and Photonics Application Group* have developed a technique for effective correction of fast axis errors of laser diode arrays using laser-written optics [15-17]. Such optical elements can be produced using a highly specialised $CO_2$ laser machining/polishing workstation in an ablation process involving a scanned-pulsed $CO_2$ laser [15, 16].

The corrective surfaces for compensating fast axis errors induced by smile deformation, lens misalignment and aberrations are designed based on accurate beam characterisation with a wavefront sensing device specially developed in the group [17]. The accurate beam characterisation technique and the laser machining system for corrective micro-optics production are currently commercialized by PowerPhotonic Ltd.

In this thesis, the flexible laser-written optics technique is utilized in several different schemes for brightness improvement of single-mode emitter arrays. The approaches used in this work are introduced in the following section.

## 1.2 Approaches taken in this thesis

Most of the work presented in this project was performed with full size single-mode emitter bars as they were the brightest sources commercially available in bar at the time when the project was started. However, the approaches used in this project are transferable to other high brightness sources such as tapered emitter bars, or small fill factor bars mentioned later in Chapter 2.

**Ultra-collimation for laser diode bars**

One of the objectives of this work was to identify and address collimation issues in both the fast and slow axis directions, and to provide an ultra-collimated array of single-

mode emitters. As a result, an excellentsource for further experiments on beam combining was obtained. Good slow axis collimation is particularly important for densely packed single mode emitter bars where power loss needs to minimized and good beam quality in the slow axis direction should be preserved. The laser-written collimation optics integrated with correction for smile and lensing errors is also highly beneficial for broad-area emitter bars, where compact methods for collimation and control of pointing may enhance the performance of beam formatting and combining systems.

**Brightness enhancement techniques for single mode emitter bar**

The main focus of this work is spatial and spectral brightness improvement of single mode emitter bars. The methods explored in this work include spatial beam formatting, wavelength locking, wavelength stepping for spectral beam combining and phase-locking.

The underlying approach so as to obtain high accuracy collimation to reduce divergence, minimize power loss and maintain uniform pointing across the laser bar is essential for the performance of the techniques presented in this thesis. This is achieved by dual-axis ultra-collimation with laser-written optics designed by the author and manufactured in collaboration with PowerPhotonic Ltd.

## 1.3 Thesis layout

Chapter 2 presents an overview of the recent developments and limitations in laser diode technology in terms of power scaling and brightness improvement. This chapter also contains essential definitions and identifies current efforts of laser diode developers. Chapter 3 reviews some of the brightness improvement techniques for laser diode arrays presented in the literature to date. The emphasis in this review is placed on approaches that inspired the work presented later in this thesis, such as high efficiency wavelength locking, spatial beam combining and passive phase-locking.

The experimental methods and tools used in this work are introduced in Chapter 4. Later, Chapter 5 describes the work on spatial beam formatting for a stack of single-mode emitter bars achieved by optical beam interleaving. Chapter 6 presents a new approach for beam quality conservation employing a laser-written corrective optics technique to provide a single optical component for fast axis error correction and accurate slow axis collimation. The technique is further utilized in work on spectral brightness improvement by wavelength locking using Volume Holographic Gratings (VHGs), presented in Chapter 7. Chapter 8 presents results on wavelength selection in a

folded cavity configuration and introduces an innovative way for wavelength variation within a laser array. Chapter 9 discusses preliminary results on phase-locking of a single-mode diode laser array.

# Chapter 2.
# Developments in high brightness laser diodes

## 2.1 Introduction

The first report on coherent infrared radiation from a semiconductor material was published by Hall *et al.* in 1962 [18]. Over the years, great progress in the semiconductor lasers has been made in terms of power scaling and beam quality improvement. The maximum power obtained from a laser diode has now reached 20 W [10] from a broad-area emitter and 12 W from a nearly diffraction limited tapered emitter [19].

To understand the directions and challenges in developments of diode lasers, it is necessary to review the methods for quantifying the beam quality for such lasers and localize the main limits in fundamentals of the technology. Section 2.2 presents a brief overview of laser diode fundamentals that are useful in understanding what aspects need further improvement, and why. Section 2.3 presents the terms typically used to describe the beam quality of laser diodes and target parameters in laser development. Sections 2.4 and 2.5 discuss the recent developments in laser diode technology at the emitter level and in packaging methods that aim for improvement in output beam quality.

## 2.2 Fundamentals of laser diode technology

Fig. 2.1 shows a schematic of the bands formed by energy states in a semiconductor material. These comprise the conduction band, valence band and regions of forbidden energy forming the so called bandgap. In equilibrium, the valence band is full and the conduction band is empty. As opposed to other, optically pumped lasers, in diode lasers the population inversion required to reach lasing threshold is obtained by the injection of electrical carriers into a pn structure. The electrons raised to the conduction band by electrical pumping redistribute themselves at the lowest energy states in this band. As a consequence, the holes occupy the highest energy states in the valence band. This process is commonly quantified by using quasi-Fermi levels $E_{fc}$ and $E_{fv}$ to separately describe filled states in the valence and conduction band, as illustrated in Fig. 2.1. the states in the valence band above $E_{fv}$ are filled with holes and all conduction band states below $E_{fc}$ are filled with electrons.

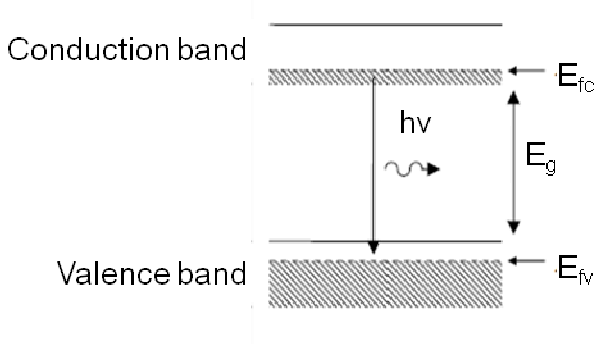


Fig. 2.1. Schematic diagram of illustrating emission in semiconductor material.

The photon emission is achieved by radiative recombination of electron and holes as spontaneous or stimulated emission. The necessary condition for the stimulated emission to occur is defined by the so called *transparency condition* derived by Bernard and Duraffourg in 1961 in [20] and can be written as:

$$E_g \leq E_{fc} - E_{fv}. \tag{2.1}$$

This condition can be used to determine the threshold current density for simple diode lasers where absorption becomes net gain.

For the laser operation to occur, the stimulated emission needs to be produced and amplified. This is achieved by feedback to the active region by mirrors, which in the case of semiconductor lasers is often provided by the cleaved facets of the semiconductor or by Bragg gratings (as in DFB lasers).

The earliest semiconductor lasers were realized as pn homojunctions. As shown in Fig. 2.2 (a), in equilibrium, the Fermi level in the p-doped region and the Fermi level in the n-doped region become equal.

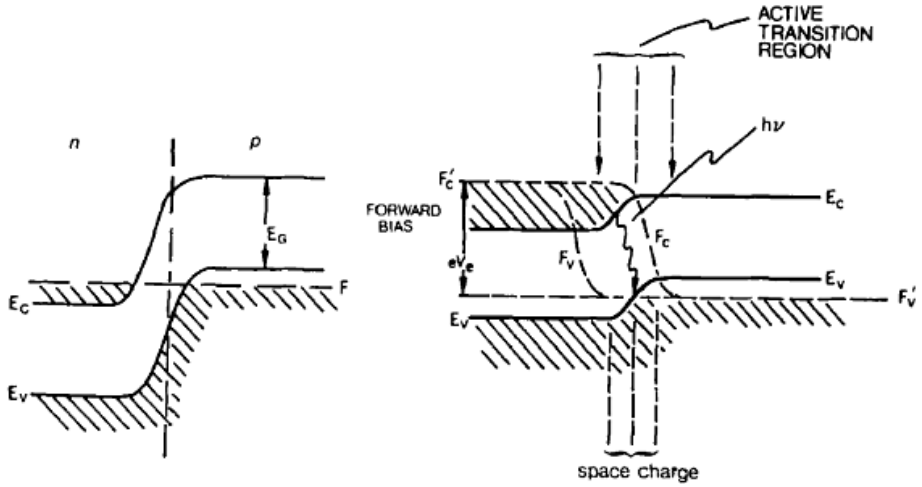


Fig. 2.2. Energy diagram of a pn junction (a) no bias, (b) forward bias [21].

When forward bias is applied the two Fermi levels are separated and the active region is formed between the p-doped and n-doped regions (as illustrated in Fig. 2.2). In such a structure, the population inversion in the junction pumped by injection current, together with the feedback provided by the mirrors formed by cleaved facets of the crystal produce a laser operation.

### 2.2.1 Gain structures in semiconductor lasers

The structure of the active region of diode lasers evolved over the years. The first laser diodes were simple pn homojunction devices based on GaAs with an active region thickness of about 2 micron produced by diffusion [18]. The following generations of lasers were realized with heterojunctions and quantum well structures. These brought the potential for lower current threshold, higher efficiency, better thermal stability as well as a wider range of available wavelengths for diode laser technology. In a heterojunction, the active region is composed of layers of semiconductor materials with different composition, band gap energy and refractive index, as opposed to just p and n doped uniform GaAs composition of homojunctions. Liquid phase epitaxy (LPE) was the enabling technology for the production of single heterojunction structures [22, 23] that gradually evolved into the double heterojunction [24-26] technology.

Currently, the active region in most of the current diode lasers is formed by a quantum well (QW) with thickness of several nanometers obtained by modern epitaxial growth methods. QWs require lower injection current and exhibit high efficiency of radiative recombination allowing low doping and thus low loss. Additionally, QWs may be in the form of a strained layer, bringing more flexible choice of wavelength.

#### *2.2.1.1 Optical and electrical confinement*

For high efficiency laser performance, both optical guiding and carrier confinement must be optimized. Good optical confinement ensures high modal gain, while efficient electrical confinement decreases the threshold current and internal losses. There are two methods for optical confinement that can be distinguished in laser diode technology: gain guiding and index guiding.

Gain guiding is performed by applying narrow contact stripes that locally inject high density carriers. In most structures, the profile of carrier density leads to a decrease in the refractive index which leads to anti-guiding. As a consequence, although gain guiding structures are easier to manufacture, they are less attractive due to weak lateral confinement and difficulty with maintaining single-mode operation [24].

The drawback of gain guiding can be overcome by creating an index guiding structure in which the light is confined in a waveguide formed by material with higher refractive index sandwiched between the layers of material with lower refractive index.

In real devices, the two confinement methods may be co-operating and one of them may dominate over the other one depending on the laser structure.

The electrical confinement in diode lasers is typically obtained by potential barriers of materials with larger band gaps or insulating layers added to the wafer under the metalized contact.

Fig. 2.3 shows a schematic view of some of the epitaxial laser structures designed for good optical and electrical confinement. As a single quantum well is too small to form a good waveguide, it is typically embedded in a different refractive index material that is a core region and surrounded by a lower refractive index material that forms claddings. Such a structure is referred to as separate confinement heterostructure (SCH), as shown in Fig. 2.3 (a) [25, 26]. In SCHs, properly designed layers and index profiles allow lower threshold currents to be obtained compared with equivalent double heterostructures. Further improvement of laser performance is obtained in so called graded-index separate confinement heterostructures (GRINSCH) (see Fig. 2.3 (b)) proposed by Tsang [27, 28]. In a GRINSCH structure, the band gap energies of the semiconductor barriers decrease gradually until they reach the band gap of the active region. Compared to SCHs, such a structure provides better mode discrimination and allows even lower threshold currents to be achieved.

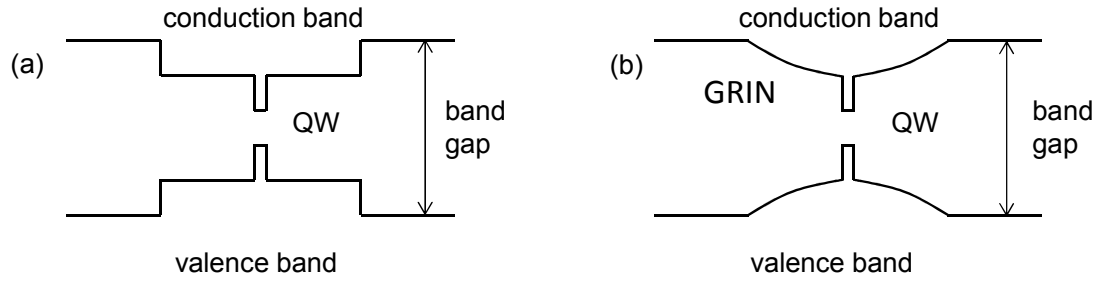


Fig.2.3. Separate confinement heterostructure (SCH) and graded-index separate confinement heterostructure (GRINSCH).

Another way of improving optical confinement in the laser structure is to introduce multiple quantum wells [29]. The effective refractive index of a structure with multiple QWs is increased allowing index guiding to occur. The first demonstration of multi-quantum-well heterostructure lasers prepared by molecular beam epitaxy was reported in 1979 by Tsang *et al.* [30].

### 2.2.2 Laser diode resonator

A typical geometry of a diode laser is based on a Fabry-Perot resonator formed by the cleaved facets of the semiconductor chip. The high gain of the active area allows the use of low reflectivity reflectors. The front facet is typically coated to reduce the reflectivity of the facet to less than a few percent. Low reflectivity enables high power conversion efficiency to be obtained, but also increases sensitivity to external optical feedback. Although emitters are easy to manufacture in high volume with a high precision, their performance suffers from low mode selectivity of the F-P resonator leading to multimode operation in both the longitudinal and transverse directions.

#### *2.2.2.1 Spatial beam quality of laser diodes*

In the vertical direction, the design of hererostructure lasers has to be optimized to satisfy many demands for high power, high efficiency and good modal discrimination. In SCH lasers, the thicknesses of the core and cladding, and the composition of the semiconductor materials can be chosen to support only a single vertical mode by ensuring the correct degree of optical confinement. However, the consequence of such geometries is a high facet load that limits the output power and affects lifetime of the devices. Moreover, the strong confinement in a narrow active layer (~1μm) results in a large divergence angle that increases cost of efficient beam shaping. To manage the high divergence in the so called fast axis (typically about 40˚), aspherical microlenses must be used for beam collimation [31, 32]. The divergence and facet load can be reduced by enlarging the core thickness at the cost of lower modal gain and thus higher threshold current and reduced power conversion efficiency.

The lateral dimension of a typical broad-area emitter varies from 90 to 150 μm. The divergence of the so called slow axis is 8-9˚. In this dimension of the resonator, many spatial modes can be supported. This leads to chaotic behaviour under even a slight change in current, external feedback or change in temperature. Poor beam quality in the slow axis and increase of the divergence with current make efficient collimation of the beam very difficult.

#### *2.2.2.2 Spectral properties of laser diodes*

The width of diode laser gain spectra is typically around 50 nm, as shown in [33]. The multimode beams from broad-area emitters tend to produce spectra a few nanometers in the region of maximum gain. The threshold gain of the adjacent modes are very close to

each other and even weak current changes, temperature gradient or external feedback can cause mode hopping and degradation of the beam characteristics.

In multi-element laser arrays, the overall spectrum is also determined by the strain gradient, the temperature gradient and nonuniformity of epitaxial layers across the array. As a consequence, the wavelength is slightly detuned from emitter-to-emitter resulting in broadening of the total emission spectrum.

The spectral properties of single-mode emitters and broad-area emitters are experimentally investigated later in Chapter 7.

### 2.2.3 Power limitations

The main factors limiting power that can be obtained from a single laser diode emitter include catastrophic optical degradation, multimode operation and thermal rollover. The last point is a consequence of temperature rise which leads to the loss of electrical confinement, as discussed in [34].

#### *2.2.3.1 Catastrophic optical damage*

Catastrophic optical damage (COD) refers to thermally induced damage of the laser facet due to high optical power density. The rapid temperature rise at the facet has been attributed to a combination of co-acting effects such as non-radiative recombination increasing with current density, photon absorption and band gap energy reduction. In 1991, Tang *et al.* [35] reported on experimental investigations of heat generation mechanisms for quantum well lasers. Their results, analytically confirmed by Chen *et al.* in 1993 [6], showed that non-radiative recombination at high current density plays the main role in the initial temperature increase. The temperature rise in the initial heating stage increases the absorption coefficient at the lasing wavelength, leading to photon absorption and a further temperature rise. The band gap shrinkage due to the heating increases the photon absorption even further. Eventually, the positive feedback in the temperature rise leads to a thermal runaway effect and damage of the laser facet.

According to Botez [36], the maximum CW power that can be obtained from a laser with a lateral near field width $W$ and reflectivity of the front facet $R$, can be calculated as:

$$P_{max} = W \cdot \left(\frac{d}{\Gamma}\right) \cdot \left(\frac{1-R}{1+R}\right) \cdot p_{COD}, \tag{2.1}$$

where $p_{COD}$ is the internal power density and $d/\Gamma$ is the so called *equivalent vertical spotsize* that is a measure of vertical near field width, where $d$ is the width of the thickness of active layer and $\Gamma$ is the vertical optical confinement. An uncoated facet of an AlGaAs laser can typically stand a power density at of 1-5 MW/cm$^2$. This imposes a strong limit for the power level, considering that for a single-mode emitter with dimensions of 1 μm in the perpendicular direction and 3 μm in the parallel direction a power level less than 1 Watt results in 3-10 MW/cm$^2$ power density at the facet.

Currently, however, COD may be considered less critical due to developments in facet coatings and passivation techniques [8, 9, 37, 38], which significantly increased the damage threshold for laser facets.

#### *2.2.3.2 Filamentation*

Increasing the size of the emitting area allows for a reduction in the power density at the laser facet and an increase in the output power. However, as a consequence, multimode operation may lead to significant beam quality degradation [37]. The multimode operation results from the perturbation of the refractive index or gain profile in the waveguide caused by inhomogeneities in local carrier population and temperature. Such behaviour can result in beam filamentation [38, 39]. The filaments are spatially localised regions of high current flow within the active area of the semiconductor that result from spatial hole burning. This is caused by a nonlinear interaction between the amplified optical field and the carrier density in the medium, which produces an inhomogeneous effective refractive index. As a consequence, self-focusing inside the medium creates filaments that significantly degrade the beam quality and decreases the COD power.

The record power obtained for a single conventional broad-area emitter is 20W [10]. Further power scaling can presently only be achieved by combining multiple mutually incoherent laser emitters into arrays.

The brightness available from a single emitter can be increased in two ways: increasing the power or improving the beam quality at the emitter level. As shown earlier, power scaling can lead to beam quality degradation and is strongly limited by the COD of the semiconductor materials and filamentation. The next section reviews the developments in high brightness diode laser technology with the main focus on improving beam quality of single emitters.

## 2.3 Terms for quantifying brightness of laser diodes

As the main focus of this work is to provide competitive techniques for the improvement of beam quality of laser diode arrays, it is necessary to review some of the essential definitions related to quantification of this property. The most general definition of beam quality provides a measure of how well the beam can be focused. There are a few terms that are commonly used to quantify beam quality. The following section reviews the key terms used for characterisation of laser diodes.

### 2.3.1 Beam propagation factor and beam parameter product

A Gaussian beam represents an ideal laser beam profile. The irradiance profile for a perfect Gaussian beam is pictured in Fig. 2.4.

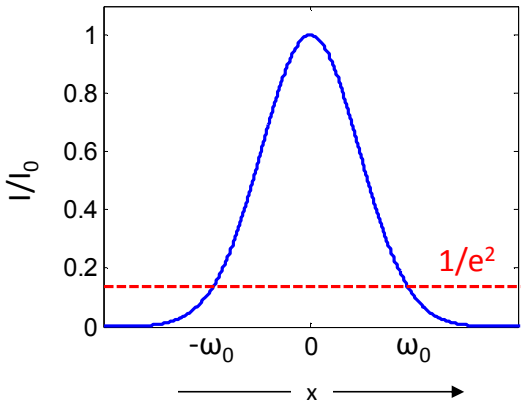


Fig. 2.4. Irradiance profile for a perfect Gaussian beam.

It is characterised by the beam waist radius $\omega_0$, half-angle far field divergence $\theta_0$ and wavelength $\lambda$. The beam waist radius is defined as the half-width at the $1/e^2$ value of the peak intensity $I_0$. When the beam propagates along the z-axis, the beam radius changes according to:

$$\omega(z) = \omega_0 \cdot \sqrt{\left(1 + \frac{z}{z_R}\right)^2}, \tag{2.2}$$

here $z_R = \frac{\omega_0^2 \cdot \pi}{\lambda}$ is the Rayleigh range and defines the distance at which the beam radius is equal to $\sqrt{2} \cdot \omega_0$.

The far field divergence for a perfect Gaussian beam is calculated for $z >> z_R$ as:

$$\theta_0 = \frac{\lambda}{\pi \cdot \omega_0}. \tag{2.3}$$

The product of the half-angle far field divergence and the beam waist radius is referred to as the *beam parameter product (BPP):*

$$\mathrm{BPP} = \theta_0 \cdot \omega_0. \tag{2.4}$$

The minimum value of beam parameter product is equal to $\lambda/\pi$ and defines the so called *diffraction limit* for the beam with a given wavelength $\lambda$.

For the *non-diffraction limited beams*, the divergence for a given beam waist radius $\omega_0$ is expressed as:

$$\theta_0 = \frac{M^2 \cdot \lambda}{\pi \cdot \omega_0}, \tag{2.5}$$

where $M^2$ is the *beam propagation factor*. $M^2$ defines how much the beam deviates from the diffraction limit. The beam parameter product for such a beam is given by:

$$\mathrm{BPP} = M^2 \cdot \theta_0 \cdot \omega_0 = M^2 \cdot \frac{\lambda}{\pi}. \tag{2.6}$$

Neither the *beam propagation factor* nor the *beam parameter product* contain information on laser power, but both quantify the spatial properties of the beam.

In laser diode technology, it is most common to describe the typically multimode, non-diffraction limited beams using the term *radiance* or *brightness*, or providing the BPP and the output power of the beam.

#### *2.3.1.1 Inconsistency of beam width definition*

The beam parameter product is often quantified in an inconsistent manner throughout the literature and commercial data sheets. This is mainly due to the difficulty in providing a definition for beam width and far field divergence of a beam that is equally meaningful for all types of beam. Both values can be measured based on the intensity profile of a beam at a given plane. Commonly used definitions for beam width include full- or half-width at half maximum, width at $1/e^2$ and diameter containing 86% of total energy. These terms can provide a meaningful description for a Gaussian beam. However, for beams with an irregular structure in the intensity profile, the 4-sigma (ISO Standard 11146) and knife-edge widths at 10-90% or 5-95% of integrated intensities are more suitable [40]. Throughout this thesis, beam widths are defined as knife-edge widths calculated based on integrated intensity profiles.

### 2.3.2 Spatial and spectral brightness

The term *radiance* combines information on power and beam quality and is defined as:

$$B = \frac{P}{A \cdot \Omega} = \frac{P}{\pi^2 \cdot BPP^2}, \tag{2.7}$$

where $P$ is the output power, $A$ is the emission area and $\Omega$ is the solid angle of the beam (far field divergence). The SI unit of radiance is watts per steradian per square metre ($W \cdot sr^{-1} \cdot m^{-2}$).

In laser technology, the term *brightness* is often used as an equivalent of *radiance* [41], and expressed in non-SI units *($W \cdot sr^{-1} \cdot cm^{-2}$)*. In this thesis, the term *brightness* is used mainly in a qualitative way and when it is quantified, it actually refers to the measure of *radiance* defined by Eq. (2.7) and denoted as B.

The *spectral radiance* of a laser is defined as radiance per unit wavelength, which can be written as follows:

$$B_\lambda = \frac{P}{\pi^2 \cdot BPP^2 \cdot \Delta\lambda}, \tag{2.8}$$

The SI unit for *spectral radiance* is *($W \cdot sr^{-1} \cdot m^{-3}$),* but in the literature it is often expressed in *($W \cdot sr^{-1} \cdot cm^{-2} \cdot nm^{-1}$)*.

### 2.3.3 Brightness of highly asymmetric beams

Highly asymmetric beams from edge-emitting laser diodes need to be described by a set of two beam parameter products $BPP_{fast}$ and $BPP_{slow}$ for the quickly diverging and slowly diverging axes of the laser, respectively.

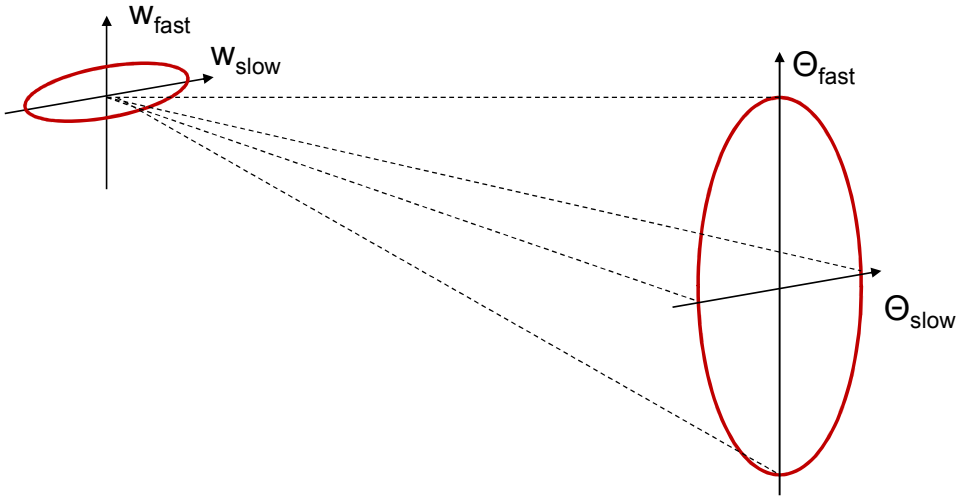


Fig. 2.5. Typical emission characteristics for a edge-emitting emitters

The brightness for an asymmetric beam can be written as:

$$\mathrm{B} = \frac{\mathrm{P}}{\pi^2 \cdot \mathrm{BPP}_{\mathrm{total}}^2}, \tag{2.9}$$

where $BPP_{total}$ is the overall beam parameter product of the beam. One way of calculating the $BPP_{total}$ is to use a geometrical mean of the beam parameter products for the two axes [41]:

$$BPP_{total} = \sqrt{BPP_{fast} \cdot BPP_{slow}}. \tag{2.10}$$

Following this definition, the brightness can be calculated as:

$$B = \frac{P}{\pi^2 \cdot BPP_{slow}^2 \cdot BPP_{fast}^2} = \frac{P}{\lambda^2 \cdot M_{slow}^2 \cdot M_{fast}^2}. \tag{2.11}$$

According to Eq. (2.11), the value of brightness for a 1W diffraction-limited beam at 1 micron is 100 $MWcm^{-2}ster^{-1}$.

The alternative way to calculate the $BPP_{total}$ is to use a RMS-value of the two beam parameter products [41]:

$$\mathrm{BPP}_{\mathrm{total}} = \sqrt{\mathrm{BPP}_{\mathrm{fast}}{}^2 + \mathrm{BPP}_{\mathrm{slow}}{}^2}. \tag{2.12}$$

For an asymmetric beam, the RMS-value carries information on the asymmetry, while the geometrical mean does not depend on the ratio between the beam parameter products in the separate directions.

### 2.3.4 Brightness of laser diode arrays

Typical diode laser systems are based on one or two-dimensional laser arrays. The beam parameter product must be calculated using a total beam divergence and the dimensions of the emitting area determined by the size of the array. For a one dimensional case, the total beam parameter product of a $N$ element array with fill factor of $F$ can be defined by:

$$\mathrm{BPP}_{1\mathrm{D}} = \omega_{\mathrm{total}} \cdot \theta_{\mathrm{total}}, \tag{2.13}$$

where $\theta_{total}$ is the overall half-width divergence angle of the beam and $\omega_{total}$ is the radius of the beam consisting of $N$ individual beams that can be defined as:

$$\omega_{total} = \omega_0 \cdot \mathrm{N} \cdot \mathrm{FF}. \tag{2.14}$$

In order to calculate beam parameter product of a two-dimensional, typically highly asymmetric, diode laser beam, the beam quality of the beam for both directions separately must be determined. A low fill factor of the array can seriously reduce the overall beam quality, unless the beam combining methods are applied. Similarly, in two dimensional laser arrays, the bar-to-bar spacing determined by the thickness of heatsinks is typically in the range from 350 μm to 2 mm and significantly decreases the power density of the devices.

### *2.3.4.1 Beam symmetrisation*

The typical 1μm x 10 mm dimensions of the emitting area of a laser bar lead to a strong disproportion between the BPP in the fast- and slow axis directions. Many applications, including material processing and fibre laser pumping, require a symmetrical laser beam. It is impossible to obtain a symmetrical focus spot by use of a common optical focusing system for a highly asymmetric laser beam. Thus, for typically asymmetric diode laser arrays, the beam parameter product equalisation must be performed before the laser can be employed in material processing or fibre laser pumping systems. The basic principle of beam symmetrisation is presented in Fig. 2.6.

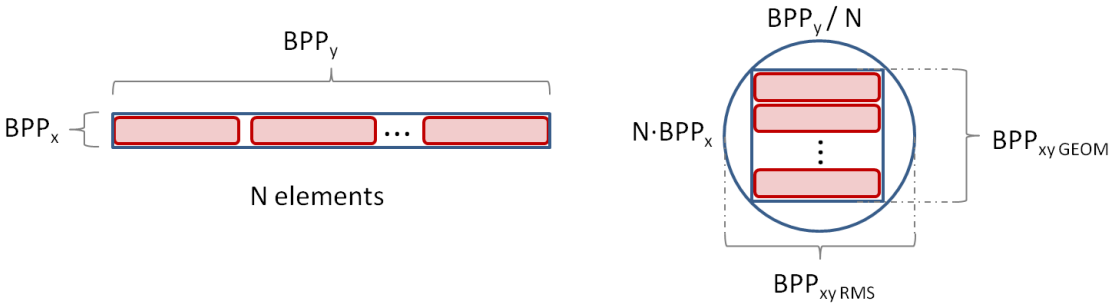


Fig. 2.6. Principle of symmetrisation of a laser array.

Full BPP-equalisation can be obtained when either the far field divergences and sizes of emitting area are equal in both directions or when the beam divergence ratio is equal to reciprocal of the beam dimension ratio. Beam symmetrisation can be obtained to a certain extent with a set of cylindrical lenses. However, for highly asymmetric arrays, beam reconfiguration is required to perform the equalisation with respect to the dimension of the emitting area. Several different approaches for beam symmetrisation are discussed in Chapter 3.

The BBP of a laser array after beam symmetrisation can be defined in two ways [41] – either as a RMS-value of the beam parameter products in both directions:

$$\mathrm{BPP_{xy\,RMS}} = \sqrt{\mathrm{BPP_x^2} + \mathrm{BPP_y^2}},$$

or as a geometrical mean:

$$\mathrm{BPP_{xy\ GEOM}} = \sqrt{\mathrm{BPP_x} \cdot \mathrm{BPP_y}}.$$

Note, that for an exactly symmetric beam

$$\mathrm{BPP_{xy\ GEOM}} = \mathrm{BPP_x} = \mathrm{BPP_y},$$

and

$$BPP_{xy\ RMS} = \sqrt{2} \cdot BPP_{xy\ GEOM}.$$

#### *2.3.4.2 Fiber coupling*

Knowing the beam parameter product of a symmetric beam, one can calculate the upper and lower limits for the diameter *(D)* and numerical aperture *(NA)* of a fibre for efficient fibre coupling. Alternatively, knowing a diameter and *NA* of a fibre, one can calculate the maximum BBP of the beam that ensures efficient fibre coupling. This condition can be written as:

$$BPP_{xy\ RMS} \leq NA \cdot \frac{d}{2}. \tag{2.15}$$

## 2.4 Brightness enhancement at the emitter level

Brightness enhancement of laser diode emitters is typically performed by modification of the lateral structure the chip. The state-of-art high brightness diode laser sources include power-scaled broad-area emitters and single-mode emitters that offer good beam quality in the slow axis direction.

### 2.4.1 Power-scaled broad-area emitters

State-of-art broad-area emitters can deliver powers up to 20W [10] at ~980 nm and up to 3W at 650 nm [42]. However, theirhighly asymmetric waveguides produce elliptical and astigmatic beams. Moreover, multiple transverse modes in the slow axis direction lead to severe degradation in beam quality, producing $M^2_{slow}$ of the order of 10-30. The brightness of broad-area emitters is limited due to their modal instabilities, filamentation and catastrophic optical damage (COD) of the front facet.

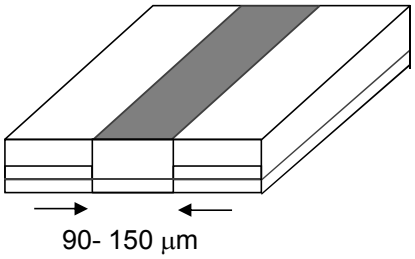


Fig. 2.7. Broad-area emitter.

### 2.4.2 Single-mode narrow stripe emitters

Single transverse mode emission can be achieved from narrow stripe laser diodes. A schematic drawing of such an emitter is illustrated in Fig. 2.8.

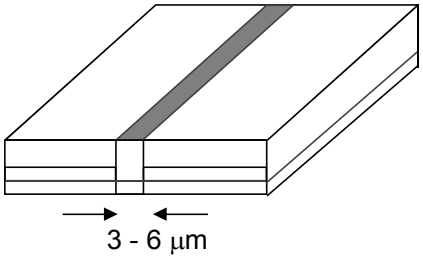


Fig.2.8. Narrow stripe diode laser.

The typical dimensions are 1 x 3-6 μm allowing a nearly diffraction-limited beam to be produced in both directions. Narrow stripe laser diodes can currently provide nearly 1.5 W at 980 nm in a circular, astigmatism free beam with $M^2$ of 1.3 in both axes [43]. In 2004, Lichtenstein *et al.* [44] reported on 1.75 W of single-mode emission at 980 nm from a narrow stripe emitter. Far field divergences of 8˚ and 24˚ along the fast and slow axes were obtained, resulting in $M^2$ of 1.3 for both directions. Such a device was realized with molecular beam epitaxy as a ridge waveguide based on a graded index carrier confinement single quantum well (GRICC-SQW) structure. The authors also demonstrated the capacity to provide high brightness laser arrays consisting of 50 single-mode emitters, producing an output power of 50W. In this thesis, a commercial version of such an array with 49 emitters producing 30 W of output power was used in experiments on spatial and spectral brightness improvement methods.

### 2.4.3 Tapered emitter with large aperture for high power and good beam quality

There have been a few different approaches proposed for obtaining power-scaled broad-area structures that can support only a single transverse mode. These include tapered lasers [45, 46], distributed feedback lasers DFB [47, 48] and monolithic master oscillator power amplifiers (MOPAs) [49] that can be realized as a distributed Bragg reflector (DBR) [50]. However, the last two structures require an expensive epitaxial

re-growth step or the fabrication of a holographic grating, making makes them less attractive for high volume, cost-effective production. The tapered lasers are increasingly popular solutions that overcome the poor beam quality of broad-area emitters and COD of the laser facet and have a relatively simple structure. The first reports on tapered amplifiers and tapered laser diodes were published in the 1990s [51, 52]. The basic idea was to form a waveguide structure that comprises a narrow ridge section for mode filtering and a wide tapered section that supports power scaling. A schematic drawing of such a device is presented in Fig. 2.9.

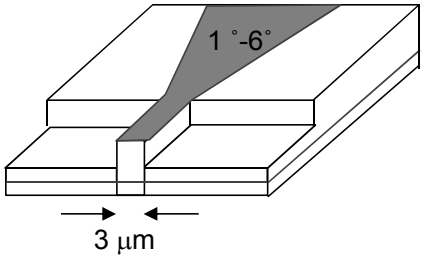


Fig.2.9. Schematic drawing of a tapered laser.

In tapered lasers, the whole chip acts as a resonator with the narrow ridge section designed to suppress the higher order modes generated in the tapered section. The tapered part can be realized as a gain-guiding or index-guiding structure. The typical taper angles are between 4 and 6 degrees. Mode filtering is often supported by cavity spoiling elements or additional absorbers.

Tapered lasers were reported in several publications [46, 53-55]. The common issue with the devices is the difference in the position of the focal points for the vertical and lateral directions resulting in astigmatism of the beams. In the lateral direction (slow axis), the focal point is located close to the transition from the ridge to the tapered part and in the vertical direction, it is located at the front facet of the emitter.

Recently, a single-mode tapered emitter reached the output power of 11.4W at 976 nm with the slow axis beam propagation factor of 1.1 and 72% of power in the main lobe in the far field was demonstrated by Fiebig *et al.* [19].

### 2.4.4 Large optical mode Slab-Coupled Optical Waveguide Lasers (SCOWLs)

The slab-coupled optical waveguide lasers (SCOWLs), invented in MIT's Lincoln Laboratory in Lexington, offer a solution that eliminates the issue of large divergence in the fast axis and high asymmetry of the ridge waveguides modes. The principle of operation of the slab-coupled optical waveguide lasers is based on slab-coupled mode theory presented by Gloge and Marcatili in 1973 [56]. When a large passive rib waveguide is brought close to a slab, some of the waveguide modes will couple with the

slab. When the dimensions of the waveguide and the slab and their relative position are appropriately chosen, only the fundamental mode of the waveguide will couple to the slab, allowing the higher order modes to be separated. The gain structure of such a device is designed to prevent the oscillation of the slab-coupled modes.

The first proof-of-concept SCOWL device was demonstrated by Walpole *et al.* in 2002 [57].The device provided 0.3 W with dimensions of the near-field intensity pattern of about 4.0 x 2.2 μm full-width at half-maximum (FWHM), and the far-field divergence of 8˚ x 18 ˚FWHM. Over the last ten years, the technology improved allowing increased power and mode size of the lasers. A schematic view of a current structure for slab-coupled optical waveguide laser with three strained InGaAs quantum wells is shown in Fig. 2.10.

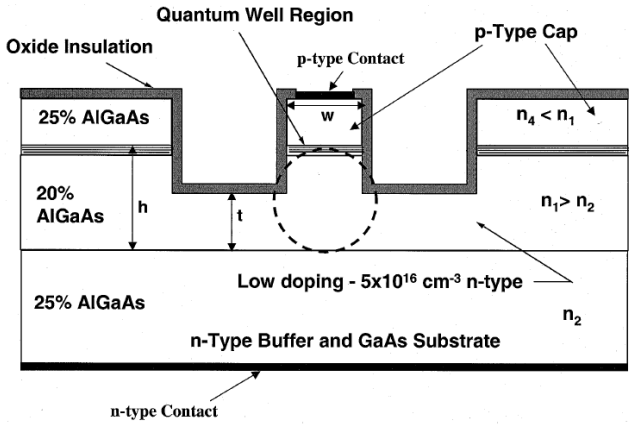


Fig. 2.10. Cross-sectional diagram of 980-nm SCOWL structure [58].

State-of-art SCOWLs can now produce up nearly 1.5 W per emitter in a single-mode with near field dimensions of 5.7 x 5 μm and $M^2$ of 1.1 [14]. The lasers were successfully combined into large arrays, with up to 100 elements and could produce up to 90 W of output power [14].

### 2.4.5 Summary on brightness scaled laser diodes

Table 2.1 presents a summary of the state-of-art brightness-enhanced laser diode emitting at ~980 nm. The included beam propagation parameters and output powers are based on the best values published to date for single emitters.

Table 2.1 Summary on high brightness diode lasers with regards to single emitters

| Emitter type | Power per emitter* [W] | $M_{fast}^2$ ($1/e^2$) | $M_{slow}^2$ ($1/e^2$) | Brightness per emitter** [MW $cm^{-2}ster^{-1}$] |
|---|---|---|---|---|
| Broad-area emitter ( 96μm) [10] | 20 | 1.3 | 22 | 72 |
| Narrow stripe single-mode emitter [44] | 1.5 | 1.3 | 1.3 | 92 |
| Tapered emitter [19] | 8.2*** | 1.1 | 1.1 | 705 |
| SCOWL [14] | 1.5 | 1.1 | 1.1 | 129 |

* Maximum reported in literature

** Calculated from Eq. (2.11)

*** 11.4W but only 72% in the main lobe, and M2 = 1.1 for the main lobe

It is worth noting that the power level that can be achieved for a single emitter cannot be reproduced in a laser bar as efficient cooling of densely packed emitters becomes very challenging. Typically, the maximum power per emitter is now about half of the power obtained for a single emitter with similar technology.

At the start of the project, narrow stripe single-mode emitters were the brightest sources available in a full size bar. A bar with a conversion efficiency of 55% and 30 W of output power, 0.72 W per emitter, was a commercial product provided by Bookham (now Oclaro). Such a bar is excellent for beam combining experiments. Therefore, it was chosen for this project. Since then, developments in power-scaled broad-area emitter in low fill factor bars (see later Section 2.5.1) and mini-bars of tapered emitters provided a range of new sources that would be equally interesting to work with. Most of the techniques developed in this project can be transferred to new types of laser arrays.

## 2.5 Tailored geometries of laser diode arrays

The evolution of diode laser technology towards brightness enhancement can also be observed at the array level. There have been new geometries for diode laser bars and stacks proposed to obtained a better beam parameter product and increase power density.

### 2.5.1 Mini-bars and low fill-factor bars

As mention earlier, a typical 1 cm bar produces a highly asymmetric beam with a beam parameter product ratio of 1:500 for the two orthogonal axes. Recently, many diode laser manufacturers have shifted their attention towards tailored geometries of so called mini bars that aim at maximising fibre-coupling efficiency [59]. Shorter bars provide a better beam parameter ratio and enable a much smaller smile deformation to be

obtained. In 2010, the Ferdinand Braun Institute reported on a design for a new 1.6 mm wide mini bar densely packed with 13 emitters producing more than 200 W of peak power. The bars were built into a quasi-CW stack providing 1kW of peak power design for fibre coupling. [60]. CEO (Northrop Grumman) offers high power 3 mm, 4 mm, and 5 mm wide mini bars in stacks with up to 30 diode bars per stack. In parallel, the developments led towards a decreasing number of emitters per bar and an increasing pitch between the emitters. Low fill-factor bars can be cooled more efficiently, so the power per emitter in a bar can be increased. Some products ombine the two approaches forming low-fill factor mini-bars. For instance, Oclaro now offers a range of low-fill factor 5 mm wide bars with 18% fill factor, giving 50W of CW output power at 980 nm [61]. At the end of 2010, OSRAM released a range of products based on mini-bar technology. Highly efficient mini-bars were presented with a fill factor of 10% and 8 W of output power per emitter. Bars with a fill factor less than or equal to 20% and over 4 W power per emitter are now available from most of the leading laser diode manufacturers.

### 2.5.2 High density stacks

The development in technology for laser diode stacks provided new solutions for densely packed stacks that greatly improve the power density in the stacking direction. CEO reported on a high density stack technology for a quasi-CW laser that allows 2kW of peak power to be obtained from an emission area of 3 x 3 mm [62]. Close packing of the bars with approximately 150 μm spacing between the bars was feasible for the short pulse width quasi-CW operation, as the junction temperature rise in such sources is relatively small.

## 2.6 Summary

A brief summary in this chapter showed that the directions in laser diode technology are converging towards beam quality improvement at the emitter and array levels. A variety of types of sources and bars are now available for experiments on beam combining. When choosing a type of source for high-power beam combined system, one should consider brightness at the emitter level, geometry of the array (accounting for suitability for using available micro-optics), reliability and manufacturability that determines cost of the system. Brightness-enhanced sources can be combined into high-power systems and provide platforms for direct diode processing that are competitive with the expensive and less efficient solid-state and gas lasers.

# Chapter 3.
# Techniques for brightness improvement for LDAs

## 3.1 Introduction

This chapter presents a brief overview of the most common beam combining methods used for laser diodes. As the focus of this project was brightness enhancement of existing sources rather than the technology of their production, the overview presented here focuses mainly on approaches that can be applied to off-the-shelf laser diode arrays, including techniques employing external extensions such as beam formatting optics, optical combiners and external cavities.

In general, the techniques can be classified into two major groups: incoherent beam combining and coherent beam combining. The techniques for combining of mutually incoherent beams include optical stacking, polarisation combining and spectral beam combining.

Spatial beam combining methods consist of using refractive, reflecting and diffractive optics to optically inter-leave and/or rotate the beams in order to achieve aperture filling and symmetrisation of the beam parameter product. A review of spatial beam formatting methods is presented in Section 3.2.

In spectral combining methods, lasers operating at different wavelengths are spatially inter-leaved by spectrally selective or dispersive components. Spectral beam combining is an attractive solution for direct material processing systems, where the high-power beam must be focused into a small spot and the spectral properties of the beam are not critical.

For coarse spectral beam combining, the individual lasers can be chosen to have different nominal wavelengths as in [63]. Dense spectral beam combining typically requires the lasers to be locked into a narrow, well defined bandwidth as in [64, 65]. Wavelength locking and line narrowing for laser diode bars and stacks is typically performed using external cavity configurations employing Volume Holographic Gratings (VHGs) [66-68] or Surface Diffraction Gratings (SDGs) [69, 70]. The spectrum of the laser can be controlled by the internal structure of the emitter, as in a distributed feedback laser diode [71]. The spectrum can be also controlled by using a MOPA configuration with external injection from a master oscillator [72, 73] as well as monolithic structures with the master oscillator integrated with gain regions [74].

However, the complex internal structure and active methods for spectral control are relatively difficult to obtain for large, power-scaled laser arrays. Apart from dense spectral beam combining systems, the potential applications for narrow band laser diode arrays include the pumping of rare-earth doped solid-state lasers and gas lasers, medicine and spectroscopy.

Incoherent combining methods offer the most straightforward solution for increasing power density, however their potential is limited. In theory, coherent combining of laser beams offers the best brightness improvement potential. The most commonly used methods include injection locking and self-organising systems such as Talbot cavities. Coherently combined lasers are highly desirable for such applications as space and underwater communication and high-energy non-linear optical processes, which require the excellent spatial beam properties and narrow linewidth to be delivered simultaneously. However, despite a large number of reports on different attempts to phase lock laser diode arrays, a successful demonstration of a phase-locked high-power diode laser array has not yet been delivered.

The choice of brightness improvement technique is mostly driven by the requirements of the target application. The common challenge for all beam combining methods is to obtain a highly reliable bright source at low cost and low power loss. In practice, the methods are developed towards a good trade-off between the cost of the system, the heat removal requirements and brightness to meet the requirements of industrial applications such as high efficiency, small footprint, low sensitivity to environmental conditions and manufacturability.

This chapter is organised as follows. Spatial combining methods are discussed in Section 3.2. Polarisation combining is briefly introduced in Section 3.3. Section 3.4 presents the techniques for wavelength locking and tuning. The methods of spectral beam combining are reviewed in Section 3.5. Coherent beam combining is discussed in Section 3.6.

## 3.2 Spatial beam formatting techniques

Spatial beam shaping methods can in principle rearrange the beams to ensure that there are nearly no dead spaces between them. For an aperture-filled array of $N$ lasers, provided that the overall power and far field divergence are conserved, the emitting area of the laser array is $N$ times bigger than the emitting area of a single emitter and the power delivered by the system is $N$ times bigger than from a single emitter. Thus, the

maximum brightness that can be obtained from a spatially combined laser array is equal to the brightness of a single element in the array.

Despite this limit, beam shaping and optical interleaving that aim for aperture filling and beam parameter equalisation for laser diode arrays are very common approach in commercial diode laser systems. Several different techniques suitable for laser bars and stacks have been developed. A brief overview of the most effective solutions is presented in the following section.

### 3.2.1 Fast and slow axis collimation

#### *3.2.1.1 Fast axis collimation*

Due to the high divergence angle in the fast axis direction of the laser diode emission, the majority of applications require the fast axis to be collimated. The key requirements for fast axis collimation lenses are low aberration and high numerical aperture to preserve intrinsically good beam quality in the fast axis direction. It has been shown in [31, 75, 76], that plano-aspheric lenses with high refractive indices offer the best performance for fast axis collimation. Alternatively, Doric™ graded index cylindrical lenses with their Luneberg-lens properties offer low aberrations and less sensitivity to misalignment compared to the plano-aspheric lenses. The effective brightness preservation by Doric™ lenses were experimentally assessed by Holdsworth and Baker in [32].

Even for the best available optics, however, the impact of the intrinsic laser beam properties as well as aberrations and attachment errors of the collimating optics often lead to a degradation of the beam quality of laser beams. The aberrations of the lenses can produce side lobes and residual divergence that can be additionally increased by attachment errors of the collimating lens and contribute to the overall reduction of beam quality in fast axis direction. In a typical laser diode bar, a bonding-induced ‘smile’ deformation results in pointing errors due to a slight displacement between the individual emitters and the fast axis collimating (FAC) lens, as illustrated in Fig. 3.1. In a lensing procedure, the fast axis collimating lens is usually aligned to be in axis with the average x-position of emitters in a bar in order to obtain the minimum average pointing error for that bar. The smile-induced offset of individual emitters, typically varying from 0.5 to 2 microns peak-to-valley across a bar, is translated into an angular spread of pointing direction across the bar. The pointing error for an emitter displaced by a distance ρ from the centre of the lens with focal length $f_{FAC}$ can be calculated as:

$$\phi_{error} = \frac{\rho}{f_{FAC}}. \quad (3.1)$$

Equivalent pointing error can be produced by displacement of the lens in the fast axis direction. The effect of the smile (or lens position error) is stronger for a shorter focal length of the FAC lens.

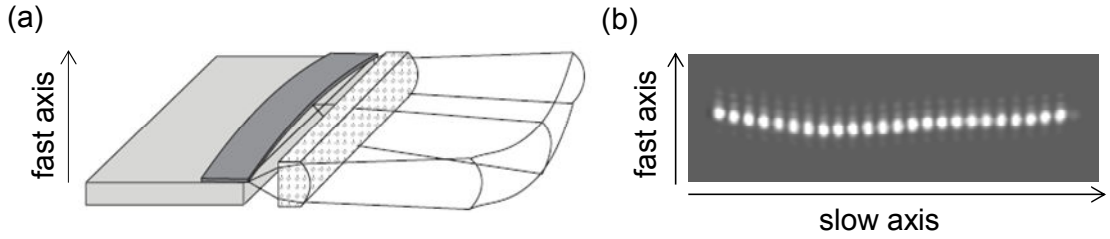


Fig. 3.1. (a) Bonding-induce smile deformation of a laser bar (adapted from [41] and an example of an emitter resolved far field pattern (see Section 4.2.2.2) affected by a smile deformation.

The main difficulty of fast axis collimation arises from high numerical apertures of the laser diode beams, and thus the current developments towards reduction of the fast axis divergence angle of diode lasers are likely to relax the stringent requirements imposed on the collimating optics. The current types of fast axis collimation optics were designed to handle beams from previous generations of laser diodes, with divergence reaching 60º. Currently, the state-of-the-art commercial laser diodes offer fast axis divergence on the order of 40º (95% power). The trend of new developments is to increase the internal guiding mode height and minimize the far field angle even further [77, 78]. These new technologies provide GaAs-based sources with divergence at a level of 30º (95% power) in reliable continuous wave power [78]. Low divergence significantly reduces the impact of lens aberrations. Reduced beam size at the lens aperture prevents the beam hitting the distorting parts of the lenses. Low numerical aperture of the beams also enables using fast axis collimation optics with longer focal length, reducing sensitivity of alignment as well as the impact of smile deformation.

### *3.2.1.2 Slow axis collimation*

The smaller, typically 8-9˚ divergence angle in the slow axis direction allows more conventional optical components to be used for collimation. For a broad-area emitter bar, the use of an array of slow axis collimating lenses can improve beam parameter product of a laser diode bar by aperture filling, by decreasing the far field divergence by a factor of approximately two [41].

The main challenge arises from the close-packing of the emitters in a laser bar. Bars with a 130-200 μm pitch are difficult to collimate and require more sophisticated

optics, such as slow axis collimation telescopes [79]. In general, for the best performance of slow axis collimation, the beam overlap and scatter on the edges of adjacent lenses should be minimised. The issues of slow axis collimation for closely-packed laser arrays are discussed in more detail in Chapter 6.

Good collimation in both directions can be critical for the performance of high-power diode laser arrays. In a spatially combined system, good collimation is necessary to allow the beams to be rearranged with more accuracy and the power loss to be minimized (see later Chapter 5). As discussed in Chapter 7, pointing errors and beam truncation on collimation optics can also significantly constrain the techniques for wavelength locking and phase-locking in external cavity diode laser configurations, where uniform feedback is necessary. This was the motivation for the work presented in Chapter 6, where the challenge of accurate dual-axis collimation for laser diode laser bars is addressed by using laser-written micro-optics.

### 3.2.2 Beam twisting micro-optics

Beyond beam collimation, sophisticated micro-optics can also provide solutions for the equalisation of the beam parameter product for highly asymmetric laser diode bars. This can be performed by rotating the divergence of each element by using components such as micro-prisms or micro-lenses.

#### *3.2.2.1 Twisting telescope*

The principle of beam twisting using a tilted cylindrical lens telescope to rotate the beams by 90˚ as illustrated in Fig. 3.2 (a) to transform a highly asymmetric beam from a bar into a nearly quadratic shape. Such components are now offered by Limo Lissotschenko Mikrooptik GmbH as commercial products called Beam Transformation Systems (BTSs) which contain a fast axis collimation lens and a beam rotating cylindrical lens telescope, as shown in Fig. 3.2 (b).

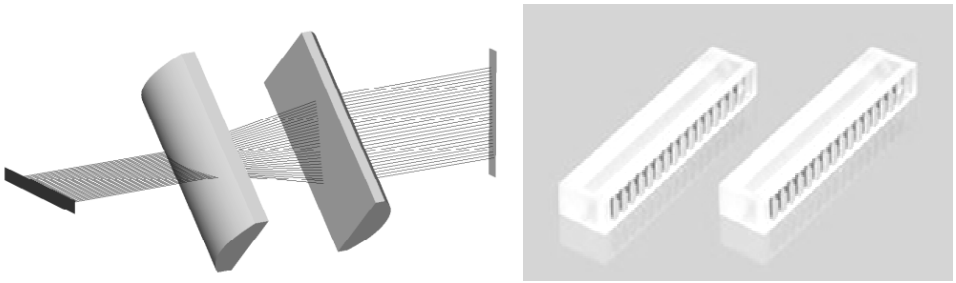

Fig. 3.2. (a) Principle of beam twisting by cylindrical lens telescope, (b) commercial beam twisters for an array of laser diodes (BST [80]).

The approach is widely used in fibre-coupling schemes[81]. An interesting application of the beam twisting telescopes was presented in [82], where such a component was used to avoid beam overlapping in an off-axis external cavity employing two volume holographic gratings for spectral bandwidth narrowing of a laser diode bar.

### *3.2.2.2 Twisting prisms*

The beams from a laser bar can also be rotated by an array of micro-prisms. In Ref. [83], Yamaguchi *et al*. proposed using a multi-prism array consisting of isosceles trapezoids designed to twist the beams by means of multiple total internal reflections. The schematic drawing of such a multi-prism array is presented in Fig. 3.3 (top).

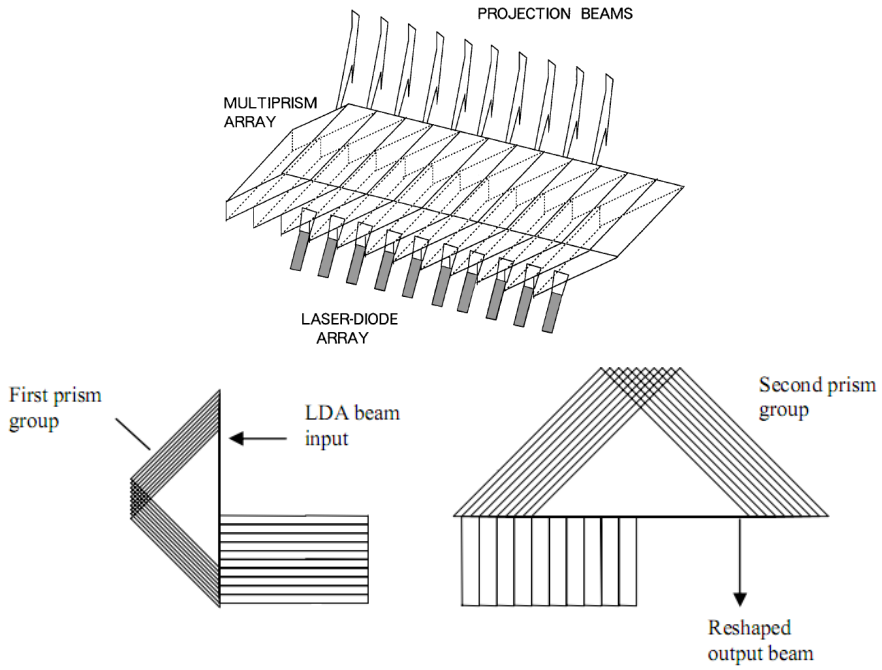


Fig. 3.3. (top) Multiprism array [83]. (bottom) beam shaper with isosceles triangular prisms [84].

Another approach, proposed by Wang *et al*., is to use a group of isosceles triangular prisms to divide and rearrange the beams from a laser bar, as shown in Fig. 3.3 (bottom) [84]. In the experimental demonstration performed with a 40 W bar, 33 W of output power from a fibre with 600 μm diameter and 0.22 NA was obtained [84]. Recently, the rotating prisms were also used by DILAS in their 1.2 kW 400 μm / 0.2 NA fibre-coupled laser system reported in [85].

The beam twisting micro-optics finds its application in many fibre-coupling schemes. However, the applicability of this technique is constrained by manufacturing limits, as it is very difficult to realise for high fill factor arrays. Using such components can also significantly increase the cost of the laser system due to the price of the

sophisticated optics and the requirement for high accuracy mounting. Thus, for large laser diode arrays, use of a macro-optical beam shaper is often more effective.

### 3.2.3 Optical stacking techniques

The methods discussed in this section can be classified as non-imaging. The beam parameter equalisation is performed by subdividing a beam from a laser array and rearranging it in order to decrease beam parameter product in the 'wider' dimension of the array.

The optical stacking methods discussed in this section include approaches applicable to both 1- and 2-dimensional arrays. For laser bars, the slow axis beam parameter product is very high due to the dead spaces between the emitters. In the case of a diode laser stack, the typical 1.7-2 mm spacing between the bars, which are actively cooled by microchannel heat sinks, results in beam quality reduction in the stacking direction. Thus, it is very common to improve the overall beam parameter product of commercial diode laser systems by aperture filling techniques consisting of the subdividing and optical stacking of the beams.

#### *3.2.3.1 Micrograting-array*

The technique proposed by Zheng *et al.* consists of splitting the beams of a laser bar in the slow axis direction and rearranging it in order to equalize the beam parameter product of both axes by means of an array of microgratings [86]. The principle of operation of such a shaper is illustrated in Fig. 3.4 (a).

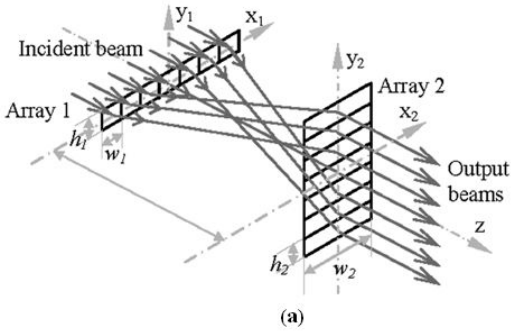


Fig.3.4. Micrograting-array beam shaper [86].

The individual microgratings in the arrays are designed to diffract the collimated beam by a blazed angle. The first array redirects the incident beam into segments in the slow axis and directs each segment separately to the appointed position on the second array. The second grating compensates for the angles produced by the first grating, so that the beams propagate in parallel to each other.

In the experiment carried out for a 19 emitter bar with power of 40 W, the beam parameter product was reduced to 7.5 and 7.6 mm.mrad in the slow- and fast axis directions, respectively.

According to the simulations presented in [86], the technique can provide satisfactory results with a smile up to 3 μm. However, the performance of the technique will also depend on the wavelength stability of the laser. In principle, such an approach can also be used to produce different beam distributions.

### *3.2.3.2 Rhomboid prism arrays*

In Ref. [87], Zheng *et al.* proposed realising a similar beam transformation with a pair of integrated rhomboid prism arrays. As shown in Fig. 3.5, the beams are separated in the slow axis direction and stacked in the fast direction by TIR-guided propagation in plane-parallel glass blocks.

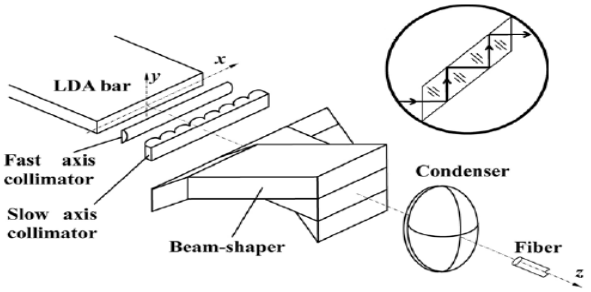


Fig.3.5. Beam combiner based on rhomboid prism arrays. Adapted from [87].

### *3.2.3.3 Stepped mirrors*

Another method for beam parameter product equalisation for laser diode bars is based on a pair of stepped mirrors [88, 89]. The fast axis collimated beams from a laser bar are deflected and displaced by the first stepped mirror. The second stepped mirror shifts the beams in the slow axis direction and deflects them so that they propagate parallel to each other (see Fig. 3.6.).

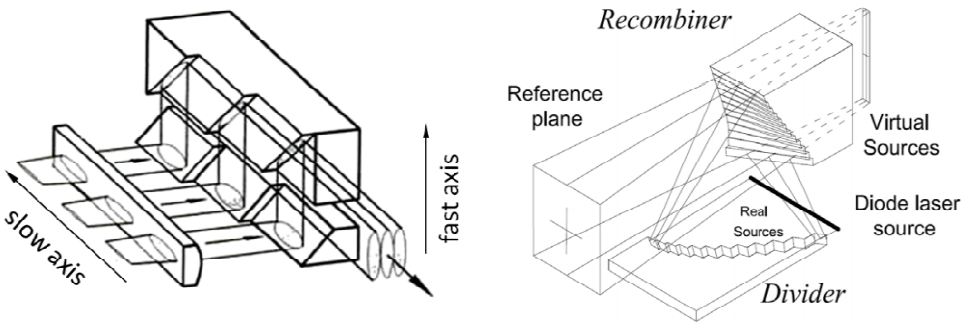


Fig. 3.6 (a) Beam shaper based on stepped mirrors. (b) Stepped-mirror beam shaper with optical path equalisation [90].

Similarly to many of the other techniques discussed above, the stepped-mirror approach presented in [88] has the disadvantage of producing an optical path length difference along the subdivided beams at the plane of focusing optics. Bonora *et al.* proposed an alternative solution consisting of using a stepped mirror with optical path length compensation [90]. The 'divider' and 'recombiner' illustrated in Fig. 3.6 (b) are designed to keep the total optical path length for each emitter the same. The experimental demonstration was realised with a 100 W QCW laser diode bar. A spot size of 250 x 320 μm obtained for the combined beam was obtained and coupled into a 400 μm diameter fibre with 62 % efficiency.

### *3.2.3.4 Two-mirror beam shaping*

A simple and effective method for optical beam shaping for laser diode bars was proposed by Clarkson and Hanna [91] who used two-mirror setup for beam parameter equalisation as shown in Fig 3.7.

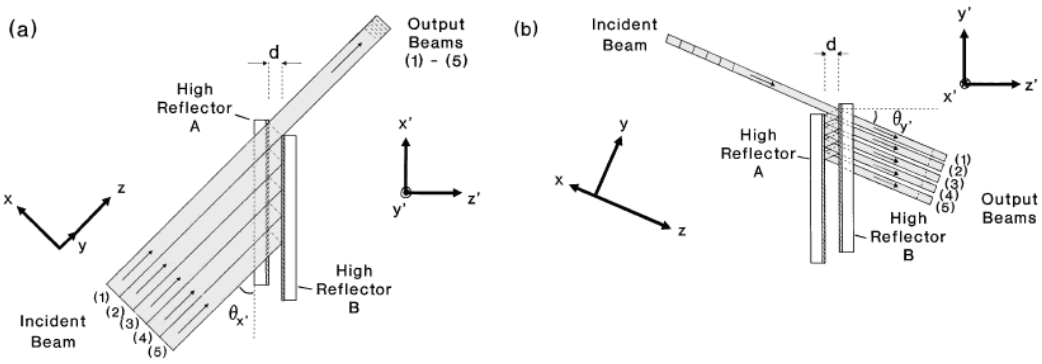


Fig. 3.7. Two-mirror beam shaper: (a) plan view, (b) side view [91, 92]

As a result of multiple reflections between the two parallel high-reflectivity mirrors, beams are stacked in the fast axis dimension providing efficient beam parameter equalisation. The idea was patented in 1998 [29].

Hanna and Clarkson performed the first experimental demonstration of the method with a bar of 24 broad-area emitters with an output power of 20W and $M^2$ of 1300 in the slow axis direction. The reshaped beam was focused to a very intense, nearly circular ($M_x^2$ ~ 37 and $M_y^2$ ~42,) spot with a $1/e^2$ beam diameter of ~100 μm and a far field beam divergence (half-angle) of ~200 mrad.

The same approach was applied by Jeffries and Coutts in [93], where the beams from a 60-emitter bar with 94% fill factor were reformatted into a 15 × 4 two-dimensional array of beams. Eventually, the reshaped output beam of the array was successfully used to end pump a Yb:S-FAP laser.

### *3.2.3.5 Striped mirrors*

A method for the beam formatting of laser diode stacks by means of stripe mirror plates was presented in [94]. In the setup shown in Fig. 3.8, a collimated beam of each bar in a diode stack is offset into three parts and vertically shifted in order to be eventually interlaced. In this way, the slow axis width of the beam from the stack is decreased three times, which corresponds to a 3-fold improvement in the beam quality.

For the 314W output power laser stack used in the experimental demonstration presented in [94], the power density was effectively enhanced to 506 W/cm$^2$ from the initial value of 192 W/cm$^2$ for the raw collimated beam. The reshaped beam was launched into a double-clad fibre (core: 20 μm diameter; NA, 0.06; single-mode, an octagonal first cladding: 400 μm diameter; NA, 0.46) with 66 % optical to optical coupling efficiency.

The system was relatively robust and provided significant improvement in the beam quality, but due to the geometry of the beam shaper, the performance was sensitive to fast axis imperfections, including packaging- induced bending and defocusing of the fast axis collimating lens.

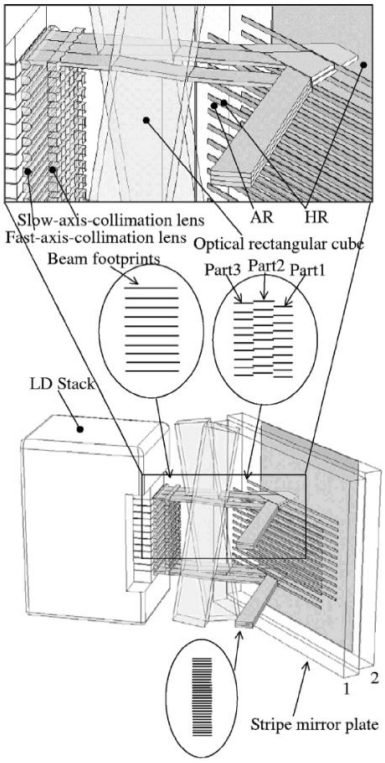


Fig. 3.8. Stripe-mirror beam combiner [94].

Another approach employing a stripe mirror was presented in [95, 96]. Here, a set of two parallel mirrors, including one striped mirror, is used to perform aperture filling in the stacking direction. As shown in Fig. 3.9, the top bar in a laser stack is reflected by

the top mirror and sent to the HR-coated stripes in the bottom mirror that redirects the beam to propagate in parallel with the beam from the bottom bars. In this way, the top beams fill the dead spaces between the bottom beams.

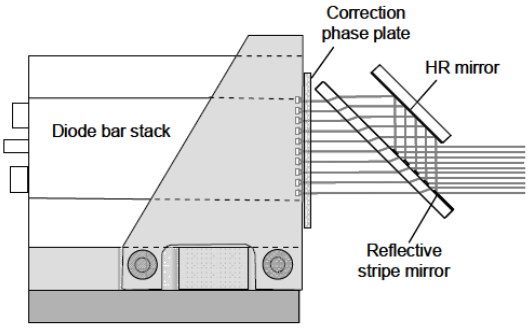


Fig. 3.9. A 2-mirror interleaving system for a 10-bar laser diode stack [97].

In Ref. [97], the technique was applied to aperture-fill two 1 kW diode laser stacks, each containing 10 bars. Both stacks were corrected for smile and lensing errors were corrected with the laser-written correction technique [98]. The beam-formatted stacks were polarisation-combined to deliver 1.6 kW output power and a BPP of 102 × 110 mm.mrad.

Recently, an approach similar to that presented in [97] was applied in a beam formatting system for a 10-bar stack coupled into a 550 μm / 0.22 NA fibre with 1kW of output power with unreported efficiency [99].

## 3.3 Polarisation combining

Two laser beams can be polarisation combined if both are linearly polarised and orthogonal to each other. Polarisation combining can be performed by a polarisation beam splitter cube, thin film polariser or birefringent crystals. The key parameters for such components are damage threshold and efficiency.

In theory, the polarisation combining can provide a 2-fold improvement in brightness. However, the typical degree of polarisation for laser diodes is only 90-95% [100] and the polarisation-sensitive beam combiner will also introduce some losses, the brightness enhancement is usually of the order of 1.7-1.8. This approach is typically used in combination with other techniques, such as spectral or spatial beam combining.

## 3.4 Wavelength locking and spectral line narrowing

For applications such as gas laser pumping [101, 102] or spin-exchange optical pumping [103], excellent spectral beam properties of the laser source are required. Line width narrowing and wavelength stabilisation for laser diode arrays have been

approached in a number of ways. In the field of laser diodes, methods based on surface diffraction gratings [69, 70] and, more recently, volume holographic gratings [67, 104, 105] are most popular due to their scalability to large laser arrays and relatively straightforward configurations. In both approaches, a tunable configuration can be obtained, so that wavelength selection for accurate wavelength matching with absorption spectra or continuous tuning for spectroscopic applications can be achieved.

### 3.4.1 Techniques based on dispersive surface diffraction gratings

The most popular techniques for wavelength locking based on surface diffraction gratings (SDGs) include the Littrow and Littman-Metcalf [106] configurations. A basic Littrow configuration contains a collimating lens and a diffraction grating (see Fig. 3.10 (a)). The first order diffraction beam provides spectrally selective feedback to the laser. The wavelength of the laser can be tuned by rotation of the grating. The Littman-Metcalf configuration contains an additional mirror reflecting the first order back to the grating, as illustrated in Fig. 3.10. The feedback beam passes the diffraction grating twice providing stronger filtering and thus a narrower output spectrum. Rotation of the mirror can be used to tune the wavelength of the laser. The zeroth order of the grating is lost in such a configuration, contributing to the loss of the system.

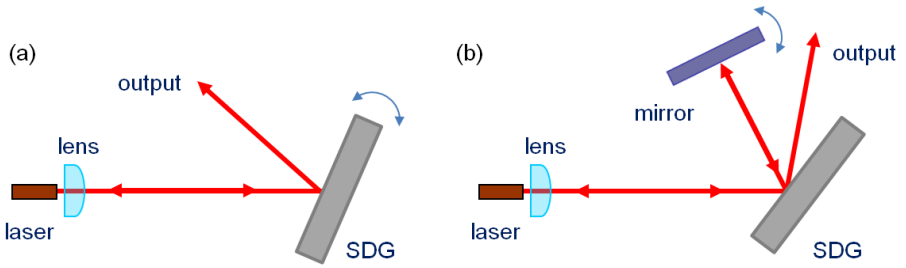


Fig. 3.10. SDG-based external cavity configurations: (a) Litttrow and (b) Littman-Metcalf.

In practical implementations for power-scaled diode laser systems, both Littrow [70, 107] and Littman-Metcalf [108, 109] configurations contain additional optical components for beam expansion and compensation for smile-induced pointing errors.

There have been a number of reports on the wavelength locking of laser diode arrays in a Littrow cavity. Babcock *et al.* [70] narrowed the linewidth of a 49 emitter bar to 140 pm with 33 % power loss and tuned over 9 nm. Talbot *et al.*[69] reported a 150 pm linewidth obtained for a 19-emitter bar with a large 7.6 μm smile. In both experiments, an optical telescope was added to the configuration to compensate for smile-induced pointing error. A linewidth as narrow as 60 pm for an array of 3-broad-area emitters was obtained in [110] by extending the grating-based configuration by inserting a narrow Fabry-Perot etalon into the cavity. Single broad-area emitters with

6.8 W output power were locked to 100 pm linewidth and tuned over 40 nm using the Littrow configuration [111].

### 3.4.2 Techniques based on spectrally-selective volume holographic gratings

Alternatively to surface diffraction gratings, volume holographic gratings (VHGs) can be used to provide spectrally selective feedback for wavelength stabilisation and line narrowing. The efficiency of such gratings can range from very low values up to 100%, enabling the optimization of optical systems depending on the configuration. A wide range of bandwidths down to below 100 pm are available from commercial providers.

A volume holographic grating is formed by periodically spaced perturbations produced by weak modulation of the refractive index in a block of photo-thermo-refractive PTR glass. The refractive index modulation can be represented as [112]:

$$n(\mathbf{r}) = n_0 + n_1 \sin(\mathbf{K} \cdot \mathbf{r}), \tag{3.2}$$

where $n_0$ is the average refractive index, $n_1$ is the modulation depth and **K** is the grating vector. The scattering planes, formed by the perturbations, partially reflect the light at an angle equal to the angle of incidence. A significant diffraction occurs in the holographic grating when the beams reflected from the scattering planes interfere constructively. The period of the grating determines the wavelength for which a maximum coupling strength is achieved. For a given period of the grating, the diffracted wavelength is determined by the angle between the incident beam and the grating vector. The relationship between the diffracted angle and wavelength is defined by the Bragg condition [113]:

$$\lambda_B = 2n_0 \Lambda cos\theta, \tag{3.3}$$

where $\lambda_B$ is the diffracted wavelength, $\theta$ is the incident angle (in the medium), $n_0$ is the mean refractive index of the medium and $\Lambda$ is the period of the grating. However, the Bragg condition is fully obeyed only for an infinitely thick grating. A finite thickness of a grating leads to the relaxation of the condition, so that it can be satisfied by the light with a spectral emission that lies in close proximity to the Bragg wavelength. The range of the accepted spectrum is referred to as the spectral selectivity of the grating. The same effect takes place in the angular domain. The range of angles that satisfy the Bragg condition is referred to as the angular selectivity of the grating. For a given incident angle, the diffraction efficiency of the grating has its maximum at a certain wavelength that satisfies the above relationship. The angular and spectral selectivity both strongly depend on the thickness of the grating.

### 3.4.2.1 Effective reflectivity of a reflecting VHG

The diffraction properties of VHGs are most commonly analysed using the coupled wave theory derived by Kogelnik [114]. The theory assumes that only two waves propagate through the holographic material: the undiffracted beam propagating at its initial angle and the Bragg condition matching beam diffracted at angle equal to incident angle with respect to the grating vector. This approximation is perfectly suitable for the analysis of weakly modulated holographic gratings. The higher diffraction orders, if they exist, contain a negligibly small fraction of the power. The well established Kogelnik's theory can be used to provide a quantitative description of the spectral and angular response of a finite thickness VHG.

Following the model published by Glebov *et al.* [68], who applied Kogelnik's theory to describe behaviour of volume holographic gratings, the diffraction efficiency η for a reflecting grating is given by:

$$\eta = \left(1 + \frac{1 - \frac{\xi^2}{\Phi^2}}{\sinh^2\sqrt{\Phi^2 - \xi^2}}\right)^{-1}, \tag{3.4}$$

where Φ is the parameter which determines the maximum diffraction efficiency of the VHG when the Bragg condition is obeyed. ξ is the dephasing parameter, which describes deviation from the Bragg condition by detuning from either θ or $\lambda_B$. For an unslanted grating, Φ is defined as:

$$\Phi_0 = \frac{\pi t n_1}{\lambda_0 |\cos\theta^*|} = \frac{2\pi n_0 t n_1}{f\lambda_0^2}, \tag{3.5}$$

and the dephasing parameter is defined as:

$$\xi = \frac{\pi f t}{\cos(\varphi - \theta^*) - \frac{f\lambda_0}{n_0}\cos\varphi}\left(-\Delta\theta_m \sin\theta^* + \frac{f}{2n_0}\Delta\lambda\right). \tag{3.6}$$

where *t* is the thickness and *f* is the frequency of the grating, $\lambda_0$ is the Bragg wavelength and θ* is the Bragg angle inside the medium. For a given frequency of the grating, the maximum diffraction efficiency of the grating is determined by the strength of the modulation of the refractive index and the grating thickness.

Fig. 3.11 (a) shows a spectral selectivity curve obtained for the 15%-reflective 1.5 mm thick grating that was used in the experiments presented in Chapters 7 and 8. For this grating, the nominal Bragg wavelength at normal incidence is 974.4 nm. Using Eq. 3.3 and the value for average refractive index provided by the manufacturer of 1.492,

the spatial frequency of the grating was calculated to be approximately 3062.4 $mm^{-1}$. For the nominal diffraction efficiency of the grating at normal incidence of 15% and the thickness of the grating of 1.5 mm, a modulation strength of $n_1 = 84$ ppm could be calculated using Eq.3.5. The FWHM bandwidth of the grating was 200 pm.

For comparison, Fig. 3.11 (b) shows a similar plot calculated for a 5 mm thick grating with nearly 10% of nominal reflectivity and 70 pm of full-width half-maximum bandwidth. This time, the spatial frequency of 3057 $mm^{-1}$ resulted in the nominal Bragg wavelength of 976 nm. The modulation strength of the grating was 20 ppm.

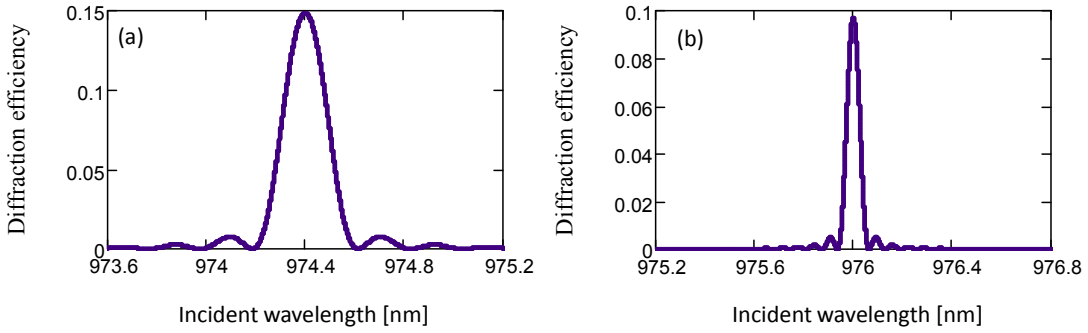


Fig. 3.11. Spectral selectivity for (a) 15% DE 1.5 mm thick VHG with n1= 84 ppm, $\lambda_B = 974.4$ nm and (b) 10% DE 5 mm thick VHG with n1 = 20 ppm, $\lambda_B = 976$ nm.

The angular selectivity curves for the same VHGs are presented in Fig. 3.12. As mentioned before, the widened angular acceptance is a result of the relaxed Bragg condition. The constructive interference in the grating will produce a significant diffracted beam at the Bragg angle as long as the incident angle lies within the angular selectivity of the grating, which strongly depends on the thickness of the grating. The full-width half-maximum angular acceptance for the 1.5 mm thick grating is about 2.4˚, while for the 5 mm thick grating it is reduced to about 1.3˚. The narrower the bandwidth of the VHG, the smaller the angular acceptance is. Thus, in applications where the VHGs are used for extreme line narrowing [104, 115], the amount of light effectively diffracted by the VHG will strongly depend on the beam divergence and pointing errors.

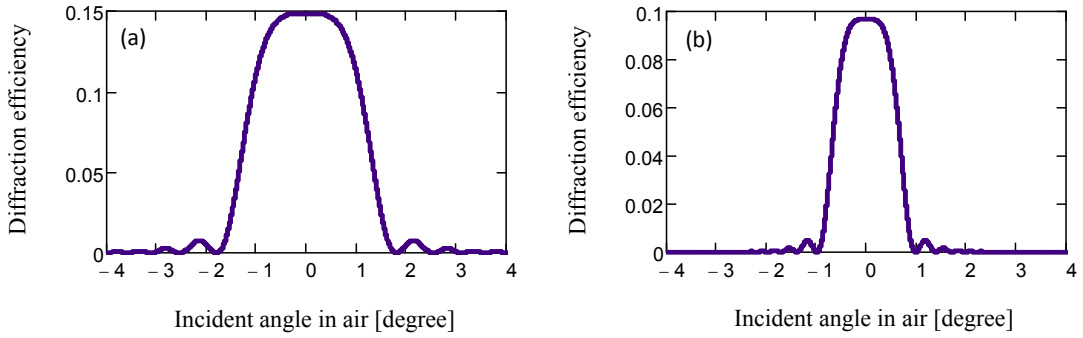


Fig. 3.12. Angular selectivity of for (a) 15% DE 1.5 mm thick VHG with n1= 84 ppm, $\lambda_B = 974.4$ nm and (b) 10% DE 5 mm thick VHG with n1 = 20 ppm, $\lambda_B = 976$ nm.

For the high performance of VHG-based external cavity configurations with laser diode arrays, it is necessary to provide a sufficient amount of feedback to each emitter in a laser array to ensure uniform locking with a good locking range. For practical implementations with laser diode arrays, the impact of beam divergence, spectral width and, in some cases, oblique incidence on the VHG must be also accounted for.

*Diverging polychromatic beams*

For a diverging polychromatic beam one must account for a loss of diffraction efficiency caused by the spectral and angular selectivity of VHGs. When the divergence of the beam is comparable with or larger than the angular acceptance of the grating only the central part of the beam will match the Bragg condition of the grating. Ref. [116] showed that both divergence equal to angular acceptance and spectral width equal to spectral selectivity of the grating, respectively, will result in a 10% drop of efficiency for a reflecting VHG and 40 % drop for a transmitting VHG. A similar analysis was performed for a laser beam that was highly focused inside the grating [117]. The authors calculated the reduction of the diffraction efficiency as a function of the divergence of the beam in both directions. Their results show that a divergence equal to the nominal angular acceptance of the grating leads to a reduction of maximum diffraction efficiency by a factor of two.

*Finite beams and oblique incidence*

The coupled wave theory derived by Kogelnik is widely used to describe VHGs because, despite its simplicity, it provides a reliable modelling tool for most of the implementations. However, the accuracy of the plane wave approximation becomes insufficient when a sharply focused beam or a small size beam incident at a large angle is to be considered. To address this issue, Hsieh *et al.* [112] conducted some theoretical analysis and experimental study on the impact of oblique incidence on the spectral filtering of narrow laser beams. The authors used the Fourier-transform relationships combined with the coupled wave theory to demonstrate that the angular acceptance is not only dictated by the spectral selectivity of the VHG, but that it also decreases with increasing incidence angle. When the angle of incidence is varied, the VHG diffracts light at the wavelength corresponding to the Bragg condition for the given angle. However, the angular acceptance decreases when the incidence angle increases. A narrower angular acceptance implies that only a small portion of the spatial harmonics of the beam is diffracted, resulting in a decrease in diffraction efficiency. Such

behaviour can be critical in configurations where small laser beams are locked by angularly tuned VHGs (see for example Chapter 8).

### *3.4.2.2 Implementations of wavelength locking with a VHG*

VHGs are commonly used in laser diode external cavity configurations where they provide spectrally selective feedback to lock single emitters [115, 117] and full bars or stacks [66, 82, 104, 118]. A typical VHG-based external cavity diode laser array contains only a fast axis collimation lens and a reflecting VHG. Fig. 3.13 shows a typical arrangement for a wavelength locked diode laser with a reflecting VHG.

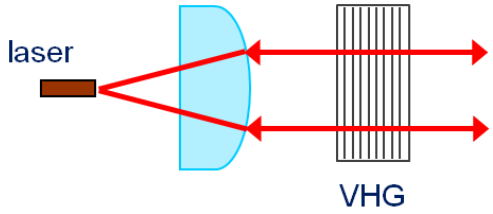


Fig. 3.13.Typical configuration for wavelength locking using a VHG.

The compactness of VHG-based wavelength locked lasers can be improved even further by integrating the VHG with the fast axis lens into a so called VHG-FAC [67].

VHG-based external cavities can perform extreme line narrowing, when diode lasers are locked to a spectral bandwidth below 100 pm. Such narrow-band lasers are desirable for the pumping of alkali lasers and for gas detection. Gourevitch *et al.* [119] reported a 14 pm spectral width at 780 nm obtained for a 2 W output power VHG-locked broad-area emitter with 10% power loss. In Ref. [115], the same research group reported obtaining a 30 pm bandwidth for a 24-broad-area emitter bar locked with a 70%-reflective VHG. The power loss compared to an identical free running laser with optimised facet coating was reported to be 10 %. An even narrower bandwidth was obtained in [104], where a 19-broad-area emitter bar was locked into a 13 pm bandwidth at 759 nm using a 14 mm thick VHG. An output power of 13.5 W was obtained with a 25%-reflective VHG as the output coupler for the AR-coated front facet of the bar. However, in this experiment, the authors observed that smile-induce pointing error constrained locking performance with such a thick grating, resulting in only 86% of total power being included in the narrow band emission.

A VHG has also been used as a highly reflective end mirror of a laser cavity. In Ref. [120], such an approach was demonstrated with a tapered amplifier. The laser was locked into a 20 pm bandwidth and locking could be maintained even when the ASE wavelength was detuned by ±8 nm from the Bragg wavelength of the VHG.

### 3.4.2.3 *Wavelength tuning with a VHG*

There have been a few different approaches to the wavelength tuning of VHG-locked lasers demonstrated in the literature. In general, the wavelength of the VHG-based external cavities can be tuned thermally or angularly.

In Ref. [119], a VHG-locked single broad-area emitter was thermally tuned over a 300 pm spectral range to precisely overlap with the Rb absorption band. For a full laser bar locked with a 70%-reflective VHG, a thermal tuning range of 400 pm was reported in [115]. In both papers, it was shown that the thermal shift of the wavelength does not affect the bandwidth of the locked lasers. Although thermal tuning of VHG-locked lasers was shown to be useful in obtaining a small spectral shift to match the absorption bands of pumped materials, the ~8 pm/K of thermally-induced shift in wavelength strongly constrains the tuning range that can be obtained with this method.

Alternatively, the angular tuning of VHGs was demonstrated to be an excellent way to extend the achievable tuning range [121-123]. In such an approach, a VHG is purposely misaligned to change the relative angle of the incident beam and produce diffraction at a different wavelength. When the VHG is rotated, the diffracted beam is no longer parallel to the incident beam, therefore it does not counter-propagate back to the aperture of the laser. It is then necessary to use an additional mirror to send the feedback beam back to the laser.

One possible arrangement is a self-aligned external cavity configuration utilizing the so called *cat's eye effect* [117, 124]. Such a cavity can be formed by a VHG and a mirror placed in the plane between the collimating lens and the laser facet, at the focal plane of the lens as shown in Fig. 3.14.

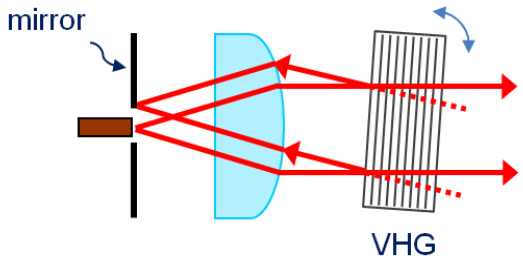


Fig. 3.14. The *'cat's eye'* configuration with a VHG.

The angular tuning of VHG-locked diode lasers in the '*cat's eye*' configuration based on a FAC-lens was reported by Moser *et al.* The technique provided a spectral tuning range of 1 nm [121] and about 0.6 nm [125] for a single laser diode and for a 19-broad-area emitter bar, respectively.

The *cat's eye effect* approach improves the alignment sensitivity of an external cavity. This is certainly advantageous in configurations such as that demonstrated in [117], which use a VHG as an end-mirror in a laser cavity with a tapered amplifier. However, in terms of tunability, the angular tuning range is constrained by the numerical aperture of the collimating lens, so this approach is at a considerable disadvantage.

The angular tuning range can be extended by compensating for the change of angle and feeding the diffracted beam back to the emitters by means of an external mirror arranged in one of the two ways illustrated in Fig. 3.15. As proposed in [123],this can be realized by combining a VHG with a broadband mirror attached with a fixed angle between them, as shown in Fig. 3.15 (a). Such a tunable filtering method was applied by Jacobsson and his co-workers to provide a narrowband and tunable optical parametric oscillator (OPO) [126]. However, in this experiment the tuning range was limited to 0.2 nm due to the drop of diffraction efficiency at oblique incidence. Coarse tuning over a range of 5 nm was demonstrated with simultaneous adjustment of the crystal temperature that brought the natural wavelength of the emission closer to the Bragg wavelength of the angularly-tuned VHG. The same group reported using similar technique for a Yb:KYW laser to obtain a wide tuning from 997 nm to 1050 nm with a bandwidth <0.1 nm [122].

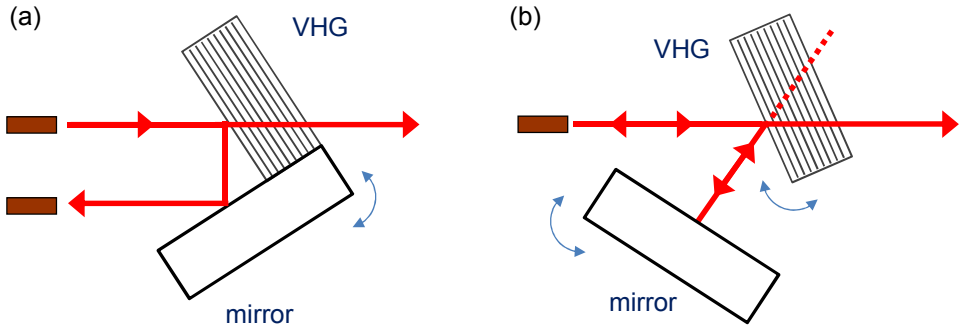


Fig. 3.15. (a) VHG with fixed mirror (b) VHG with independently aligned mirror.

An alternative approach is to arrange the VHG and the mirror independently, so that rotation of the mirror placed at a distance from the VHG corrects for misalignment of the VHG, as shown in Fig. 3.15 (b). Jacobsson *et al.* applied such an approach for an OPO and obtained about 60 nm tuning range [127]. The capability of this technique to provide a wide tuning range for solid-state and fibre lasers was also demonstrated. Kim *et al.*[128] applied this approach for an Er-Yb fibre laser and obtained 22 nm of tuning range. In Ref. [129], Hemmer *et al.* used a similar technique to obtain a 62 nm range tuning for a Ti:Sapphire laser. In the work presented in [129], it was observed that the

drop of effective reflectivity of the VHG at the end of the tuning range results in an increase of the lasing threshold.

### 3.4.3 Comparison between VHG- and SDG-based techniques

The key advantage of volume holographic gratings is their capability to provide a desirable level of diffraction efficiency, including the case where the full beam is entirely diffracted by the grating. An efficiency of 100% cannot be obtained with a surface diffraction grating. In contrast to VHGs, when a typical surface grating is used, a part of the power may be absorbed [130] and sent to other diffraction orders.

Line narrowing with surface diffraction gratings requires a series of additional components, such as focusing lenses and output couplers. The low angular dispersion of SDGs requires long focal length lenses to be used. The large dimensions of the optical system make it highly sensitive to vibrations and mechanical tolerances. An appropriately aligned VHG is fully sufficient to lock a laser array, providing a very compact solution.

VHGs outperform the surface diffraction grating in terms of a better tolerance to high-power laser radiation and low absorption coefficient approaching $2\times10^{-4}$ $cm^{-1}$ for wavelengths around 1 μm. Moreover, as the VHGs are spectrally selective as opposed to spectrally dispersive diffraction gratings, the temperature rise in the grating produced by high-power laser beams leads to a shift of the wavelength, but not to a degradation of the beam quality.

## 3.5 Spectral beam combining (SBC)

In principle, spectral combining can offer up to an *N*-fold improvement in the brightness of a laser system, where *N* is the number of combined wavelengths. The general approach for spectral beam combining is to spatially overlap the near field and far field patterns of incoherent sources differing in wavelength. This can be performed with such components as edge-filters [131], dichroic filters [132], dispersive diffraction gratings [64] or volume holographic gratings [133, 134]. Spectral combining can be performed for laser sources that nominally produce light at different wavelengths [63], but it usually constrains the minimum channel spacing to several nanometres. Alternatively, the individual sources can be spectrally narrowed and locked into different wavelengths spaced by a designed channel spacing to be efficiently combined by high resolution dispersive components [13, 64, 135].

In the most general classification, spectral combining methods can be split into two groups: parallel and serial. Serial combining methods are typically based on spectrally selective components (dichroic mirrors, interference filters, VHGs) that spatially superimpose two beams with each spectral combiner. In parallel combining, a single spectrally-dispersive component (diffraction grating, transmitting VHG, prism) is used to combine many lasers at once.

### 3.5.1 Spectral beam combining based on surface diffraction gratings

One of the most commonly used parallel SBC methods was developed in the MIT Lincoln Laboratory [64]. The principle of operation is presented in Fig. 3.16. In such a configuration, the diffraction grating performs both wavelength locking of individual elements and dispersion-based beam combining.

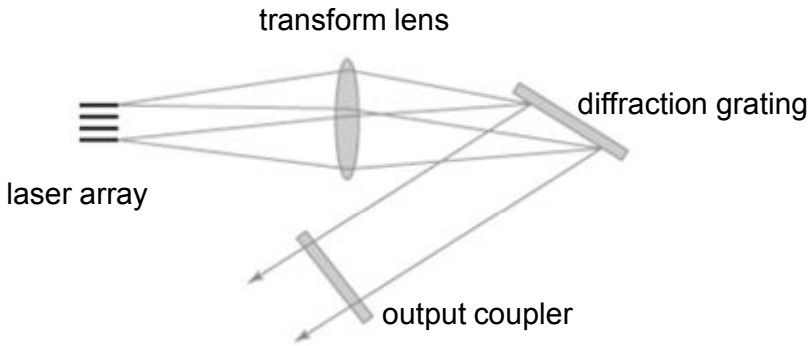


Fig. 3.16. Spectral beam combining configuration with a diffraction grating.

This external cavity configuration consists of a cylindrical transform lens placed at focal length away from the laser, a diffraction grating placed at focal plane of the lens and a partially reflective output coupler. The position of each laser is converted by the transform lens into an angle of incidence and then translated into a wavelength by the diffraction grating. For the feedback beam, the wavelength is converted into an angle and then translated into a position in the near field of the laser by the transform lens. All of the beams are spatially overlapped at the grating, with each beam at different incidence angle. For a given focal length of the lens *f* and size of the emitting area of the laser array *d*, the wavelength spread caused by difference in angle of incidence is given by [13]:

$$\Delta\lambda \approx \frac{\mathrm{d}}{\mathrm{f} \cdot (\mathrm{d}\beta/\mathrm{d}\lambda)}, \tag{3.7}$$

where $d\beta/d\lambda$ is the dispersion of the grating related to groove spacing *g* and diffraction angle $\beta$ by:

$$\frac{d\beta}{d\lambda} = g\cos\beta. \tag{3.8}$$

Due to the dispersion of the grating, the beams are propagating coaxially in the near and the far field. The feedback beam reflected from the output coupler is dispersed by the grating and the transform lens translates the angle of dispersion into a position at the front facet of the laser array to provide the spectrally selective feedback.

In Ref. [14], the approach presented in Fig. 3.16 was implemented for a 100-element array slab-coupled optical waveguide lasers (SCOWLs) with dense ~0.15 nm channel spacing. The output beam with 30 W of cw power and $M_{x,y}^2 = 2$ was achieved. More recently, a similar technique was applied to an array of 12 tapered emitters [136]. The beam was combined with 63% combining efficiency to produce 9.3 W of output power and an $M^2$ in the slow axis of 5.3. The approach was also widely applied in fibre lasers systems. In Ref. [137], three fibre lasers spectrally separated by 6.5 nm were combined into a beam with 100 W of output power and $M^2 = 2.7$.

In the method presented in Fig. 3.16, however, the power scaling can be a subject of trade-off between delivering a sufficient amount of feedback to wavelength-lock all elements and the efficiency of the combined laser system. This issue is overcome in the spectral combining system based on MOPA fibre lasers, where the wavelength of the individual lasers is not dependent on the external feedback. With the approach illustrated in Fig. 3.17, Loftus *et al.* combined three fibre lasers into a nearly diffraction limited beam with 522 W of output power and $M^2 = 1.2$ [65]. Even further power scaling obtained in a similar manner was reported in [138], where four photonic crystal fibre amplifiers were spectrally combined into a 8.2 kW output beam with $M^2 \approx 4$.

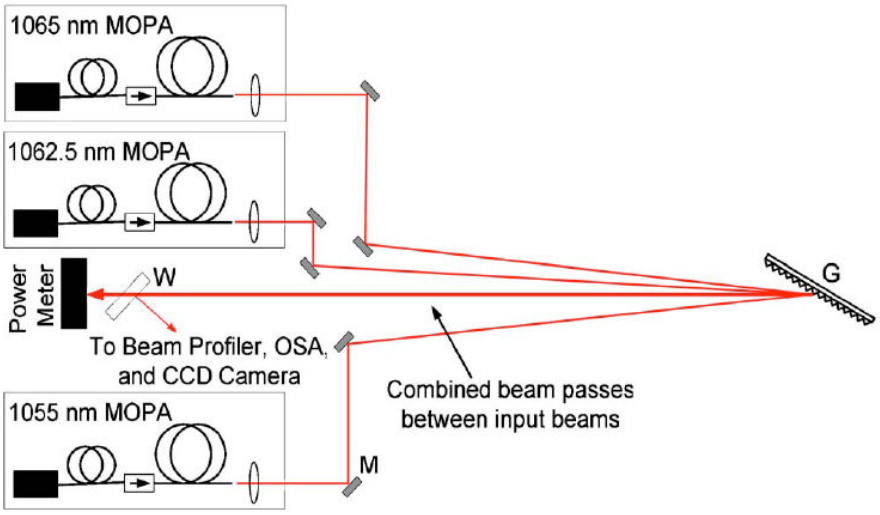


Fig. 3.17. Optical configuration of spectral combining of three fibre MOPA lasers [65].

An alternative way of controlling the wavelength of individual elements in the laser array which is spectrally combined with a surface diffraction grating was demonstrated by researchers from the MIT Lincoln Laboratory in collaboration with PD-LD Inc in [139]. They used a linearly-chirped VHG to vary the wavelength in a laser diode array, as shown in Fig. 3.18. They reported on the robust combining of beams from a 3-bar laser diode stack with an output power of 89.5W with 90% efficiency. The 15%-reflective chirped VHG provided spectrally selective feedback to the emitters, so that the wavelength was varied in the horizontal (slow axis) direction with a 15 nm/cm gradient and remained uniform in the vertical (stacking) direction. Spectral combining was performed for each bar resulting in an output beam quality in the horizontal axis approximately equal to that of a single broad-area emitter, while the beam quality in the stacking direction remained unchanged. The spectrally combined beam was coupled into a 100 μm diameter, 0.22 NA fibre resulting in 77% efficiency and 52.7W of cw output power. The authors pointed out that the performance of the technique was affected by smile and lensing errors.

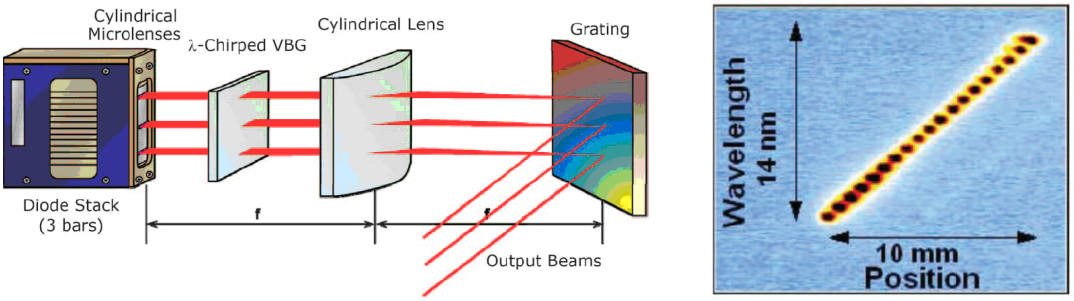


Fig.3.18. (a) Implementation of SBC of 3-bar laser diode stack by using a wavelength-chirped VHG. (b) Spectrally resolved near field image for one bar [139].

The diffraction-based approaches have proven their scalability to high power levels and large numbers of elements. The power achieved from spectrally combined fibre amplifiers exceeded 8 kW [138]. The record number of spectrally combined locked laser diode emitters reached 1400 in [140]. However, in order to maintain good feedback for all elements, the 7-bar stack of single-mode emitters spaced by 50 μm had to be fitted with a special lenslet array for the collimation of both axes and smile reduction.

Further power scalability can be limited due to requirements on optical components and laser sources themselves. Thermal damage of the diffraction grating and change of behaviour under exposure with a high intensity beam need to be considered. The use of diffraction gratings imposes high requirements on the spatial properties of the combined beams. To obtain a high resolution with a diffraction grating,

the beam size on the grating has to be large and the beam divergence of the beams has to be small enough to ensure angular separation between the adjacent channels. As a consequence, the external cavity length has to be increased as long focal length lenses or beam expanders need to be included. Large cavities are not desirable due to their high sensitivity to vibrations and mechanical tolerances. This sets the limit for the minimum channel spacing that can be achieved. Typically, a channel spacing of 1-10 nm can be obtained within reasonable cavity dimensions.

The performance of grating-based SBC techniques is also dependent on the pointing accuracy across the laser array. The pointing errors of the beams are required to be within a small fraction of the far field divergence to prevent feedback loss. In the case of laser diode bars, if the beam combining is performed in the slow axis direction, smile error will affect the beam quality of the output beam in the fast axis direction and reduce the feedback efficiency. Thus, in many systems for wavelength locking and spectral beam combining employing diffraction gratings, the loss in feedback caused by smile error is compensated by the use of optical telescopes in the external cavity [69, 70, 107, 141].

### 3.5.2 VHG-based spectral beam combining techniques

#### *3.5.2.1 Spectral combining with reflecting VHGs*

Recently, spectral beam combining techniques employing VHGs provided a very attractive alternative for dispersion gratings. At the University of Central Florida (CREOL), volume holographic gratings were used as spectrally selective filters in a serial combining configuration as shown in Fig. 3.19.

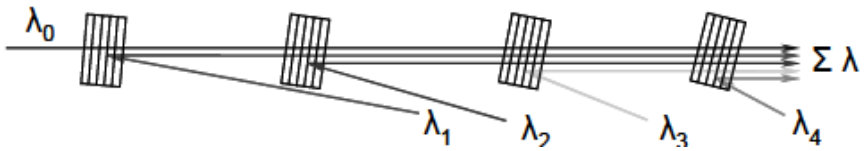


Fig. 3.19. Concept of spectral beam combining with reflecting VHGs.

Each VHG reflects one of the wavelengths while being transparent for all other wavelengths. The VHGs can be angularly tuned to the appointed wavelength or chosen to diffract a different wavelength for the same angles of incident beams.

A five channel implementation of the technique providing a 750 W nearly diffraction-limited beam was presented in [142].

An alternative approach for SBC employing the VHG technology is to use multiplexed VHGs to spatially overlap beams with different wavelengths, as illustrated

in Fig. 3.20. The monolithic multichannel combiner contains multiple gratings written within one block of PTR glass with different Bragg wavelengths and grating vectors. In Ref. [134], a four channel version of such a combiner with 0.7 nm spectral spacing and 90% efficiency was presented.

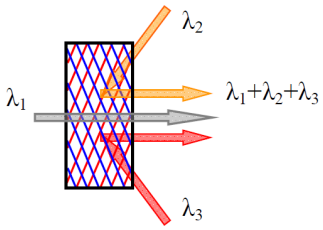


Fig. 3.20. Concept of multi-channel spectral beam combining with a multiplexed VHG [130].

### *3.5.2.2 Spectral combining with transmitting VHGs*

In theory, transmitting VHGs can act as dispersive components when used to combine beams with a spectral separation smaller than the spectral selectivity of the grating [130]. In Ref. [143], Chu *et al.* proposed the use of cascaded transmitting VHGs and increasing the number of channels by combining many beams with closely spaced wavelengths that satisfy the same Bragg condition and thus diffract with the same angle. The principle of operation for this approach is illustrated in Fig. 3.21. To the knowledge of the author, the experimental implementation has not been yet reported.

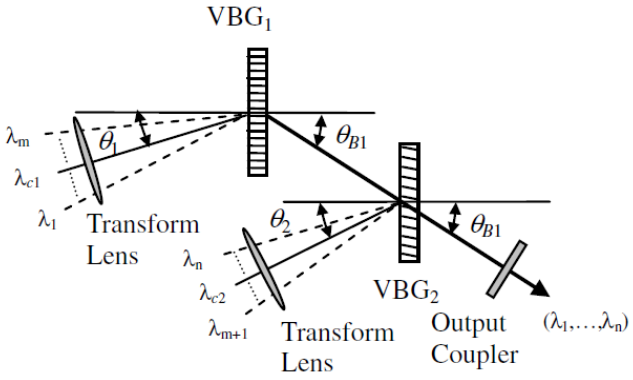


Fig. 3.21. Concept of spectral beam combining system based on cascaded VHGs [143].

### 3.5.3 Dielectric edge filters

As an alternative to SDGs and VHGs, a multi-filter concept can be used to perform spectral beam combining of laser diode arrays. The concept illustrated in Fig. 3.22 can be applied in the system containing multiple bars with emission at different wavelengths.

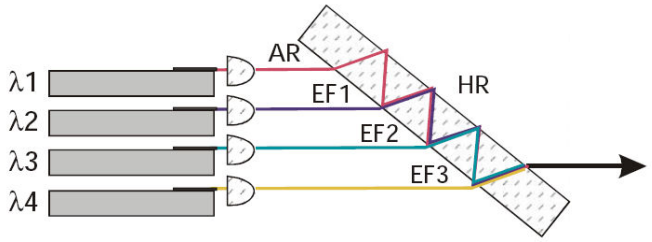


Fig.3.22. Principle of the multi-filter concept for 4 different wavelengths [131].

The method presented in [131] consists of using a spanned coated etalon with edge-filters. Due to appropriately chosen and distributed AR- and HR-coatings, the beam is guided inside the etalon and then is combined with the others. The authors reported on the wavelength and polarisation multiplexing setup of 4 bars with different wavelengths (778, 804, 902 and 970 nm), which provided optical output power of 190 W.

## 3.6 Coherent coupling

Theoretically, coherent coupling of laser arrays can produce an on- axis intensity that is proportional to the square of the number of elements in the array. Phase-locking of small, low power laser diode arrays has been verified experimentally using complex master-slave configurations [144] or diffractive coupling [145, 146]. However, large power-scaled laser diode arrays are highly nonlinear systems that exhibit a variety of complex behaviours, thermal and electrical fluctuations and nonuniformities in the laser chip, which strongly affects the performance of coherent combining methods. As a consequence, despite a number of different approaches being proposed over the last few decades, phase-locking of high power laser arrays remains an unfulfilled goal in the field of high-brightness diode lasers.

The techniques of phase-locking can be based on active or passive mechanisms. Active approaches include various injection locking configurations [147-149]. However, due to the requirement of accurate phase compensation, complex electrical control over the individual elements has to be involved. This is particularly challenging to realise for large laser arrays. Passive phase-locking methods, on the other hand, do not require the use of active components. The most common techniques for passive phase-locking include evanescent wave or leaky-wave coupling [150, 151], *1-to-N* cavities [152, 153], phase-conjugation [154, 155] and Talbot cavities [156-158]. One of the more recent approaches for passive phase-locking is to use an angularly and spectrally selective VHG in a Talbot cavity [159-161].

### 3.6.1 Injection locking

Injection-locking is effective, but very complicated way of synchronizing lasers. Injection-locked lasers can produce a single transverse and longitudinal mode with a spectrum bandwidth close to that of the seed laser. The challenge of this approach stems from the fact that the phase difference between the combined lasers has to be controlled to the level of λ/10 [13]. A typical configuration contains a single-mode seed source and a complex phase-control system.

The first demonstrations of injection locking were performed with low-power single broad-area lasers [162, 163]. In 2002, Lie *et al.* reported on the injection locking of individual broad-area emitters in a 19-emitter bar with a nominal output power of 20 W[164]. Each of the injection locked emitters produced 600 mW in a single-mode. The operational condition for individual emitters had to be individually adjusted to tune the laser mode to be close to that of the longitudinal mode of the seed. The strength of injection determines the limits for frequency detuning acceptable for efficient locking.

Since then, excellent progress in injection-locked laser diode arrays has been made. In the last couple of years, researchers from MIT Lincoln Laboratory reported on a series of successful experiments on the injection locking of individually addressed slab-coupled optical waveguide lasers [157, 165, 166]. The phases of the individual elements in the laser arrays were controlled by the stochastic-parallel-gradient-descent (SPGD) algorithm, which manipulated small changes in drive current for individual elements to determine the phase relations within the laser array. In Ref. [165], 20 W of output power was achieved by the active phase-locking of two 21-element bars packed into a specially developed 2-dimensional modular architecture. Recently, the active coherent combining was scaled up to 218 elements (eleven bars of 21 emitters each) in a similar manner, providing 38.5W of output power [166].

### 3.6.2 Talbot cavity

#### *3.6.2.1 Concept of phase-locking in a Talbot cavity*

The Talbot effect, first observed by Talbot [167], is a consequence of the Fresnel diffraction effect. The Talbot effect results in the formation of images of a periodic array of coherent light sources at so called Talbot distances, defined as:

$$Z_T = \frac{2d^2}{\lambda}, \tag{3.9}$$

where d is the period of the array and λ is the wavelength of light.

At the fractional Talbot distances (1/2, 1/4, 1/8 etc.), the light distribution produces images consisting of multiple copies of original apertures shifted with respect to each other by a certain distance. The phase is constant across a single copy, but changes step-wise from copy to copy within one period [168].

The idea of using the Talbot effect to perform the phase-locking of a periodical array of $CO_2$ lasers was proposed by Antyukov in 1986 [169]. Since then, there have been many different approaches to apply Talbot cavity configurations to various types of lasers. In a Talbot cavity, the round-trip is equal to full or fractional Talbot distances, so that an image of the initial light distribution is superimposed on the exit apertures of the emitters. For an array of mutually coherent emitters, the Talbot cavity feeds the self image of the array back into the apertures of the emitters. The incoherent light from the emitters is spread out across the entire array. Thus, for small fill factor bars most of the light from the incoherent states do not enter the apertures. In this way, the Talbot cavity only supports lasing in a coherent state. However, a Talbot cavity formed for a *N*-emitter array can in principle support *N* different supermodes, including the in-phase mode and higher-order modes (for initial phases differing between 0 and $\pi$) [170]. To obtain good coherence, the coupled laser array has to operate in a single supermode. Therefore, mode selection has to be performed by ensuring low loss for one of the modes and a higher loss for all others. However, due to the closeness of the thresholds for several supermodes, single-mode selection is very difficult. The separation between the modes depends on the number of emitters and the fill factor of the array. For a fixed fill factor, increasing the number of emitters increases the number of modes and decreases the separation between adjacent modes. Although a low fill factor improves the modal selectivity of the Talbot cavity, it also increases the impact of edge effects, as investigated in [171].

In many studies, mode selection was performed based on the spatial distribution of the supermodes at a fractional Talbot distance. One of the approaches is to introduce a selective loss using by using spatial filters matching light distribution of the unwanted higher order modes [172]. Alternatively, phase shifting plates were introduced to convert the modes inside a cavity [173].

The modal analysis of a Talbot cavity, reported in [170], shows the dependence of thresholds for particular supermodes on the round-trip length of the cavity. Fig. 3.23 shows the modal thresholds for an eight-element array with a fill factor of 8%. In Fig. 3.23, $v = 1$ corresponds to the in-phase mode and $v = 8$ corresponds to the out-of-phase mode. For a round-trip cavity length equal to half of the Talbot distance, the cavity has

a minimum loss for the out-of-phase mode and a maximum loss for the in-phase mode. Fig. 3.23 shows as well that when the round-trip cavity length is equal to the full Talbot distance, both the in-phase and out-of-phase modes have low thresholds which proves the advantage of a fractional Talbot cavity length. Clearly, due to the difference in modal threshold between the in-phase and out-of-phase modes, a quarter-Talbot cavity allows better mode discrimination.

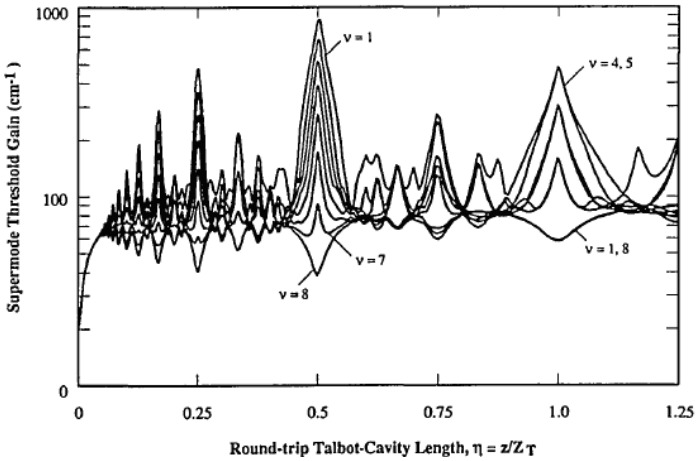


Fig. 3.23. Supermode threshold gain for an 8-emitter array as function of round-trip cavity length [170].

*Quarter-Talbot cavity*

The light distribution at various Talbot distances is schematically illustrated in Fig. 3.24 [146].

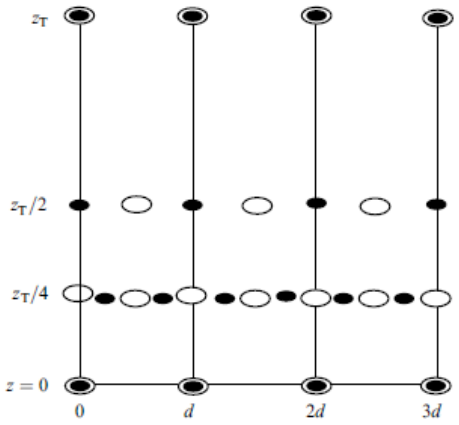


Fig. 3.24. Light distribution at Talbot distances, dashed ovals correspond to the in-phase mode, dark ovals correspond to the out-of-phase mode [146].

At a half-Talbot distance, the distribution for the in-phase mode is a complete reproduction of the initial distribution, but is spatially shifted by $d/2$, where $d$ is the pitch of the laser array. At the same distance, the highest order mode for which the neighbouring emitters have opposite phases (that is shifted by $\pi$), forms a similar distribution at the same lateral position as the initial distribution. In a quarter-Talbot cavity, the round-trip length is equal to $Z_T/2$, so that the out-of-phase mode is

reproduced at the source. In such a configuration, the in-phase mode encounters high losses as it is imaged at the dead spaced between the emitters. When the output coupler is tilted by $\alpha = \lambda/2d$, the field distribution reproduced at the source after the round-trip is shifted by $d/2$. In this way, the in-phase supermode distribution can be superimposed on the laser apertures. Such an approach for in-phase mode selection in a quarter-Talbot cavity was proposed by Glova [173] and widely applied in phase-locking experiments [159, 160].

#### *3.6.2.2 Supermodes in a diffraction coupled laser array*

For an incoherent laser array, the mode of oscillation for each individual element is described by its independent field distribution and propagation constant. The far field pattern of the array is an incoherent summation of the individual fields. For a phase-locked array, the elements share a common field distribution and produce a common mode of oscillation.

There have been many different approaches presented for the modal analysis of the phase-locked lasers arrays. For arrays locked by weak evanescent coupling, the field was calculated as the superposition of the wave functions of the individual elements [174, 175]. For the analysis of strongly coupled gain-guided and antiguided arrays, Botez *et al.* proposed a matrix formulation presented in [176]. Using the latter one, Lu *et al.* [177] presented an analysis of externally phase locked arrays that can be applied to describe the propagation in simple external cavities formed for $N$ elements. Such a cavity can support $N$ different supermodes. When only coupling between the neighbouring emitters is considered, according to the coupled mode theory, the near field distribution for the $v^{th}$ supermode can be calculated based on the coupling matrix following [176, 177] as:

$$u_v(x_0) = \sum_{n=1}^{N} \sin\left(\frac{\pi v n}{N+1}\right) \exp\left(\frac{(x_0 - x_n)^2}{\omega_0}\right). \tag{3.10}$$

For a laser diode array, $x$ defines the slow axis and $x_n$ is the coordinate of the centre of the $n^{th}$ emitter. Knowing the initial field distribution for the particular supermodes, the corresponding far field pattern obtained at the focal point of a lens with focal length $f$ can be obtained by calculating the diffraction integral of the near field distribution. The far field intensity pattern can be then calculated as the amplitude multiplied by its complex conjugate. As an example, the calculated near field and far field distributions for five coupled emitters are plotted in Fig. 3.25.

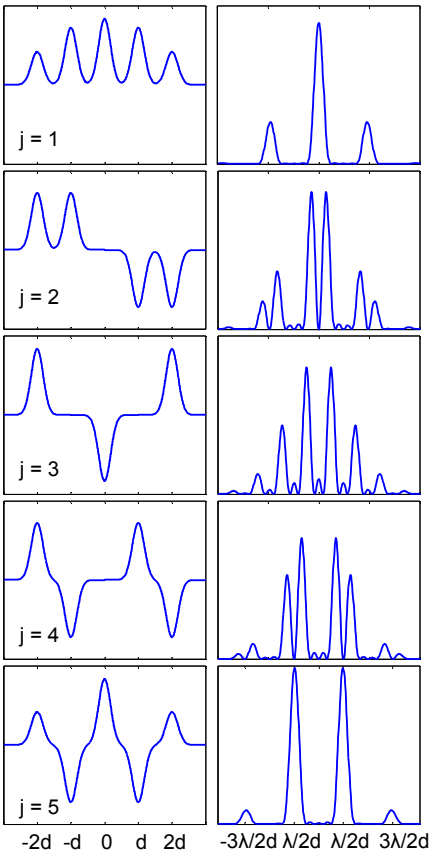


Fig.3.25. Calculated near field distribution (left) and far field patterns (right) for supermodes of a 5-emitter array with d = 200 μm pitch, emitting at 980 nm.

As shown in Fig. 3.25, the far field pattern of a phase-locked laser array consists of narrow peaks spaced by $\lambda/d$. The diffraction limit for the FWHM width of the interference peaks is equal to $\lambda/Nd$, where N is the number of phase-locked emitters. The number of fringes depends on pitch of the array and divergence of a single emitter. The intensity envelope of the peaks is determined by the far field pattern of the free running laser. For a given divergence, the number of observed fringes increases as the pitch of the bar decreases.

Based on the far field pattern, the quality of phase-locking can be evaluated by calculating fringe visibility as:

$$V = \frac{I_{max} - I_{min}}{I_{max} + I_{min}}, \tag{3.11}$$

where $I_{max}$ is the peak intensity of the fringes and $I_{min}$ is peak of the incoherent pedestal in the intensity profile. The visibility of the interference pattern is a measure of coherence and is equal to 1 for fully coherent light, and equal to 0 for fully incoherent light.

### *3.6.2.3 Experimental implementations with laser diode arrays*

The first reports on the phase-locking of laser diode arrays concerned small aperture single-mode emitters in low fill factor arrays. In the experiment reported in [178], an array of 20 small aperture emitters with a total output power of 900 mW was phase-locked in a quarter-Talbot cavity. The array, with very low fill factor of about 8%, ensured strong mode discrimination. This array was coherently combined into a beam with an output divergence of the main lobe corresponding to 1.7 times the diffraction-limit.

Further investigations aimed to obtain efficient phase-locking of wide aperture emitter arrays with high a fill factor. In the late 1990s, Apollonov *et al.* reported on a series of experiments on the phase-locking of 120-μm-wide broad-area emitters in 4-, 8- and 12-element arrays with a fill factor of 0.6 [179]. They used a quarter-Talbot cavity configuration formed by a partially reflective mirror that was tilted by $\alpha=\lambda/2d$ to switch between the in-phase and out-of-phase modes [173]. The same research group performed an experiment with two 8-elements arrays separated by 1600 μm [180]. Again, the quarter-Talbot cavity with the tilted mirror was used. Although Apollonov *et al.* produced some evidence for the phase-locking of wide aperture emitter bars with a reasonable fill factor, high visibility interference patterns were not observed and a single lobe was not obtained in far field.

*Intra-cavity filters for mode discrimination*

In Ref. [156], D'Amato demonstrated that spatial filtering inside a Talbot cavity can help suppress undesired higher order modes, which occur at higher drive currents. Such a filter was applied in a half-Talbot cavity formed for an array of 30 index-guided 10-μm-wide emitters with a fill factor of 0.1. The spatial filter was placed in the cavity, as shown in Fig. 3.26 (a). Fig. 3.26 (b) and (c) show the improvement of coherence of combined beams with spatial filtering.

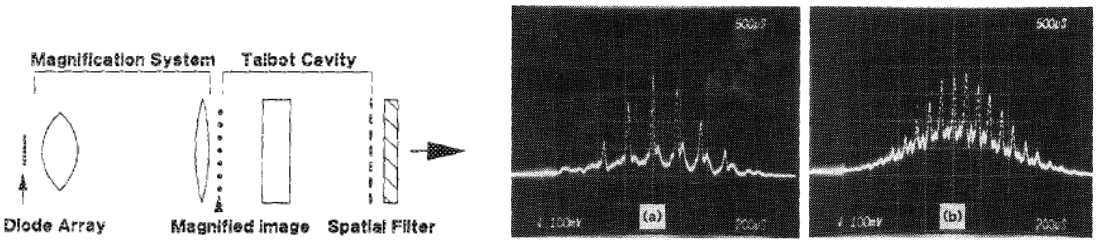


Fig. 3.26. (b) Talbot cavity with a spatial filter and (b) far field of laser array combined in the cavity with (b) and without (c) the spatial filter cavity [156].

More recently, Li *et al.* used an amplitude compensator to increase the losses for the higher order modes and select the in-phase mode that produces a single lobe in the far field pattern [172, 181]. The compensator was designed to match the in-phase mode distribution at quarter-Talbot distance, as plotted in Fig. 3.27 (a) and was placed in the plane of a 90%-reflective output coupler which formed a quarter-Talbot cavity. The experimental implementation was performed with a 50% fill factor array of 49-broad-area diodes spaced by 200 μm. To enhance the performance of the cavity, the laser bar was packed into a patented sandwich structure in order to reduce the "smile" effect.

The use of the amplitude compensator allowed the multimode distribution with power of 1.57 W (Fig. 3.27 (b)) to be transferred into a single lobe with 0.96 W of power (Fig. 3.27 (c)). The far-field divergence of the phase-locked beam was 1.8 mrad. The spectral bandwidth (FWHM) of 1.7 nm was reduced to 0.16 nm. Although the authors claimed the potential of scaling to a level of 10 W in a single supermode (by increasing the power per emitter and decreasing the reflectivity of the cavity mirror), there have been no reports of further improvements.

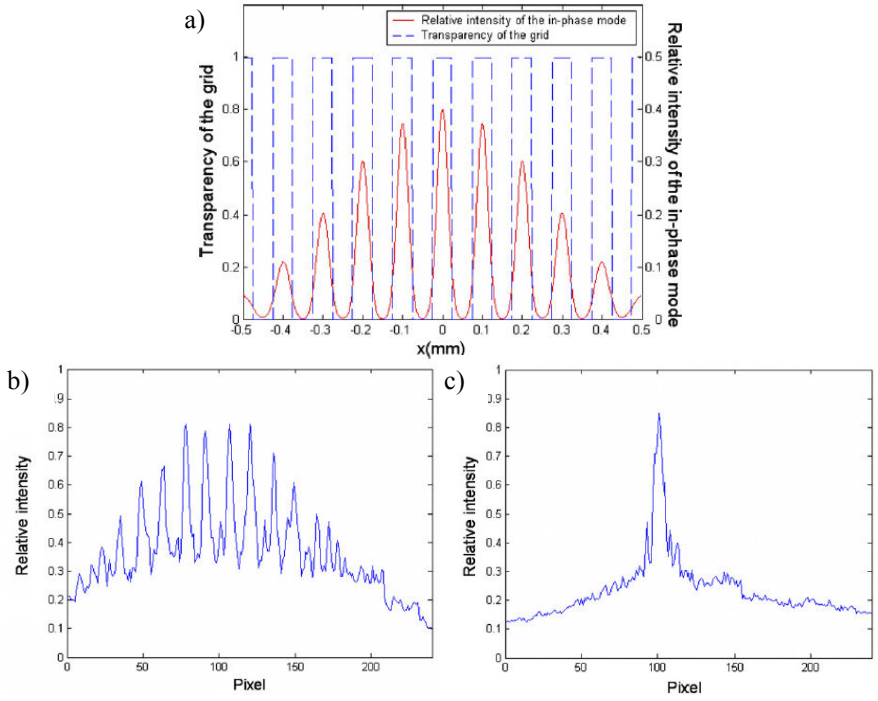


Fig. 3.27. (a) Distribution of the in-phase mode at quarter- Talbot distance. Far-field pattern for the laser array combined in the Talbot cavity (a) without and (c) with amplitude compensator [181].

*Talbot cavity with individually addressed SCOWL arrays*

Due to their good beam quality, SCOWLs (discussed earlier in Section 2.4.4), are excellent sources for phase-locking experiments. Huang *et al.* reported on phase-locking using a quarter-Talbot cavity configuration for a 10-element array of individually addressed SCOWLs [157]. The individual current control allowed the optical path

difference of all the emitters to be controlled to the level of λ/10. A high visibility signature of passive phase-locking in the quarter-Talbot cavity was recorded for the array operated at low current with 2 W of output power. However, the high fill factor of the bar collimated with micro-optics led to the local locking of groups of emitters. The authors reported a similar experiment performed for the same bar with a bulk cylindrical lens instead of the micro-lens array (reduced fill factor), which yielded an output power of an7 W. This time, the interference pattern revealed less visibility and broadened peaks, showing evidence of coherence degradation. The actual visibility and width of the peaks were not reported.

*V-shape Talbot cavity with broad-area emitter bars*

Liu *et al.* proposed using a V-shaped external cavity for phase-locking based on the Talbot effect [158, 182]. They extended the approach for spatial filtering by off-axis feedback reported earlier in [183-187] by forming a diffraction grating-based half-Talbot cavity in the feedback path of the off-axis configuration. In the first experimental demonstration for a 49-broad-area emitter bar with 200 μm emitter pitch and 100 μm emitter width, they obtained 9 W of coherent emission with bandwidth narrowed to 100 pm. However, the visibility of the obtained patterns exposed the need for further improvement. In 2010, the same authors published a slightly modified approached (see Fig. 3.28), in which an additional diffraction grating was introduced in the output path of the configuration, so that a closed feedback loop was formed between the two gratings [158].

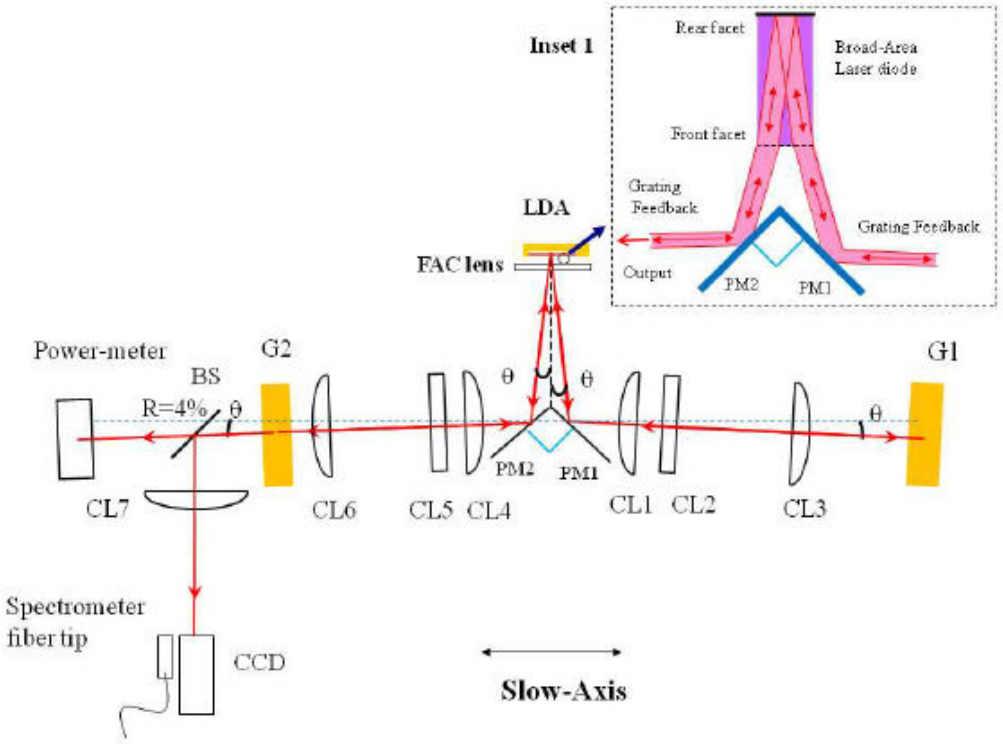


Fig.3.28. Closed-loop V-shaped external Talbot cavity [158].

This time, the demonstration for a 47 element bar with 100 μm emitters spaced by 200 μm provided 12.8 W of output power and a far field interference pattern with 87% visibility. However, the resulting FWHM width of the main lobe of 1.5 mrad was much larger than the diffraction limit of 0.1 mrad defined for 47 coherently locked emitters.

*VHG-based Talbot cavity formed for an array of tapered emitters*

Over the last few years, the researchers involved in the European project BRIGHTER.EU published a series of papers on the phase-locking of tapered emitter bars in a Talbot cavity employing a VHG acting as an output coupler [159, 160, 188]. In the configuration illustrated in Fig. 3.29, the VHG was tilted by $\lambda/2p$ (where $p$ is the emitter pitch) to select the in-phase mode. Fig. 3.29 (b) shows the far field pattern obtained for an array of 10-tapered emitters operated at 3A of drive current with an output power of 1.2 W [159]. The FWHM divergence of the central peak was 1.2 mrad compared to the diffraction limit of 1 mrad. The highest phase-locked power claimed by the authors was 1.7 W with a far field pattern with 70% visibility obtained for the 10-tapered emitter bar.

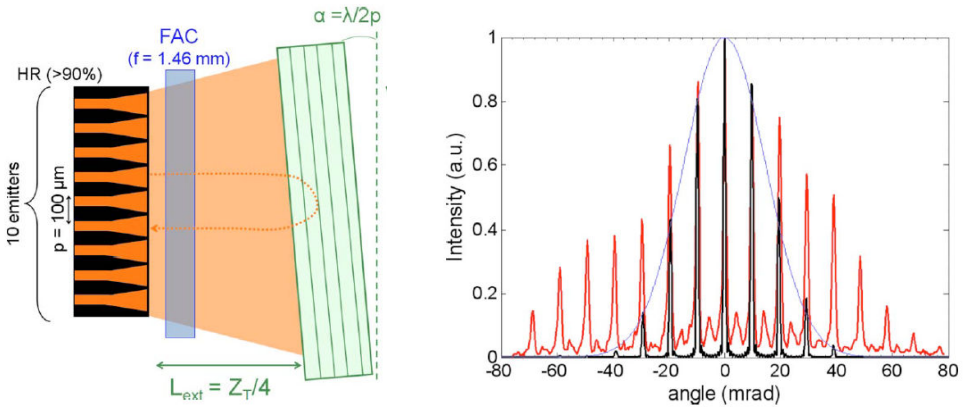


Fig. 3.29. (a) Experimental setup. (b) Far-field profiles: (red line) experimental measurement, (black line) numerical result, and (blue line) theoretical far field of a Gaussian emitter $I$ = 3 A, $P$ = 1.2 W [159].

## 3.7 Summary

This chapter provides an overview of the techniques used for the brightness enhancement of laser diode arrays, mainly focused on methods which are transferable to off-the-shelf devices. The choice of combining method is strongly dependent on the type of source and the target application and must be a trade-off between the brightness improvement and system complexity.

Spatial beam combining methods are relatively straightforward and provide a robust system for the combining of high-power diode lasers stacks at multi-kW power levels. However, their limitations stem from the maximum brightness which is constrained to the brightness of a single element in the array.

Further brightness improvement can be obtained by spectral beam combining methods. The power achieved from spectrally combined fibre amplifiers exceeded 8 kW [189]. Although the spectral combination of a large number of beams is performed at the expense of widened output spectrum, these methods are undoubtedly one of the most effective approaches for applications where the laser wavelength is not critical. The robustness and reliability of spectral combining methods makes them advantageous for many industrial applications. In high-power laser systems, spectral beam combining techniques are often used in conjunction with other beam combining methods, including polarisation multiplexing and spatial beam transformations [131, 190].

Coherent beam combining methods have the potential for increasing brightness while maintaining a narrow spectrum of the beams. However, despite the noticeable progress made in phase-locking laser diode arrays over the last decade, passive coherent locking of large number of emitters has not been achieved yet. The experiments on high beam quality lasers including tapered emitters and large mode SCOWLs packed into mini-bars of 10 emitters, provided coherent beams at the few Watt power level. In large

arrays, the emitters tend to lock locally, resulting in degradation of the coherence of the output beams. Although the developments in coherent combining have not reached commercialisation after many years of research, it continues to attract much attention due to its great potential.

Despite the many successful implementations of spectral and spatial beam combining methods and improvements in phase-locked diode laser arrays demonstrated over recent years, the scaling in both methods is often limited by the intrinsic properties of large laser diode arrays. Many of the reports mentioned in this review, indicated that high performance of multi-element beam combining systems can only be achieved with good spatial properties of the combined beams. This was one of the main motivations for the work conducted in this project, which aims to provide a nearly ideal source where smile, beam divergence and other beam distortion have negligible impact on the performance of brightness improvement techniques.

# Chapter 4.
# Experimental methods and tools for laser diode arrays

## 4.1 Introduction

This chapter introduces the experimental techniques used throughout the project. The first part of the chapter presents the beam diagnostic methods developed by the author for the purpose of evaluating beam quality improvement techniques for diode laser arrays. The methods for the accurate characterisation of the spatial and spectral beam properties were chosen so as to be suitable for high-power laser diode arrays and to provide the information necessary for the evaluation of the investigated techniques. In some experiments, it was necessary to provide a quick and accurate way for the simultaneous viewing of both the spatial and spectral properties of the beams. The characterisation techniques had to be capable of providing information on the full beam of a laser bar, each single emitter in an array and all emitters simultaneously. The use of closely-packed laser arrays with 30-60 W of output power required the capacity to address both the handling of high-power laser beams and the selection of a single beam from an array. The novelty of the experimental methods used by the author consisted of providing an optical system that has the capability to perform all of the required measurements in parallel.

The experimental setup for simultaneous spatial and spectral beam analysis developed by the author is introduced in Section 4.2. The beam profiling branch (of the overall measurement system) described in Section 4.2.1 provides a method for the quick evaluation of collimation errors, smile error and beam divergence based on full beam far field and emitter-resolved far field measurements. The imaging spectrometer and single channel high resolution spectrometer, forming a spectral analysis measurement branch, are presented in Section 4.2.2. The information extracted from the spectral analysis includes the accurate wavelength and the bandwidth of the laser, thermal tuning, wavelength distribution across a bar and the efficiency of wavelength locking with a VHG.

The second part of the chapter introduces the tools and techniques that were available to the author through collaboration with PowerPhotonic Ltd and significantly enriched the results obtained in the project. The access to a unique wavefront sensing device facilitated by the company provided a method for the accurate analysis of the

spatial beam properties for the laser diode arrays, as discussed in Section 4.3. Finally, the technology for laser-written refractive optics, now commercialized by PowerPhotonic Ltd, enabled a set of optical components to be fabricated based on the design provided by the author. These optics improved the quality of the achieved results and extended the range of possible experiments. It will be shown throughout this thesis that the access to such technologies enabled original experiments that would have been otherwise impossible to perform.

## 4.2 Spatial and spectral beam diagnostics

The simultaneous control of the spatial and spectral properties of the laser arrays was a key approach in the experiments on external cavity laser diode arrays. In particular, the dependence between the spatial properties of the beams and the performance of the VHG locking technique is investigated in Chapter 7. In Chapter 8, the controlled array beam pointing (achieved using laser-written optics) was used to select VHG-locked wavelengths for the individual emitters in a bar. Furthermore, in the phase-locking experiments presented in Chapter 9, the far field pattern is used for the detection of coherent combining and provides information on the beam pointing direction for individual emitters, while the emitter-resolved spectrum acts as an indicator of feedback efficiency and the alignment of the VHG.

A functional diagram of the experimental setup for the simultaneous spatial and spectral analysis of laser diode bars is presented in Fig. 4.1.

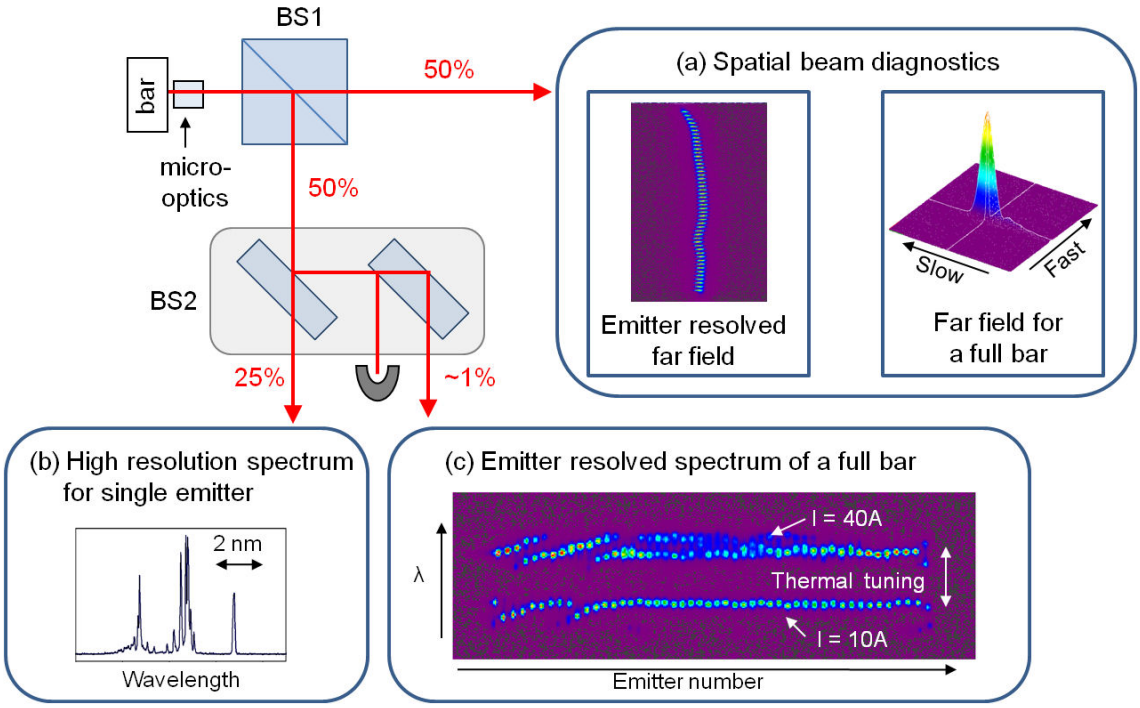


Fig. 4.1 Functional diagram of the experimental setup for spatial and spectral analysis.

In the optical system, the output laser beam is split between the three functional branches: one for the spatial analysis of the beams and two for spectral analysis. The spatial analysis branch (a) of the system allows the recording of the far field divergence of the full bar and the emitter resolved fast axis far field. Switching between the two functions is obtained by introducing a cylindrical lens, as shown in Section 4.2.1. The far field pattern can also be measured for a single emitter selected from a bar, as shown in Section 4.2.3. The spatial analysis branch provides information on beam divergence, pointing errors along the bar and the quality of collimation.

The spectral analysis branches (b) and (c) include a high resolution single channel spectrometer and an imaging spectrometer based on a Czerny-Turner monochromator, respectively. These allow the observation of the wavelength shift for chip temperature measurement, the non-uniform wavelength distribution along the array and longitudinal mode emission from individual emitters.

The individual functions of the configuration are discussed separately in the following sections.

### 4.2.1 Characterisation of the spatial properties of the beams

#### *4.2.1.1 Far field measurement*

The measurement of the far field pattern of a beam is a simple way to evaluate the beam profile and the far field divergence. This approach provides information on the average pointing error, the remaining divergence and the beam deformation caused by a combination of smile error, lens aberrations and misalignment.

The measurement is performed using the setup presented in Fig. 4.2. A spherical lens is used to produce a far field pattern on a black screen placed at the focal point of the lens. The screen is rotating to avoid damage and prevent speckle on the scattered pattern that is then recorded by a Spiricon camera. In such a configuration, only a very small fraction of the light reaches the CCD sensor, preventing any damage. Additional neutral density filters (ND) are attached to the camera when needed. Due to the low intensity of the light, thermal lensing in the ND filters does not impose a problem. Fixed pattern camera noise and background radiation are corrected using the *ultra-cal* function in the Spiricon software. The recorded images are exported to an ASCII file and processed in the Matlab-based software to extract the parameters of interest.

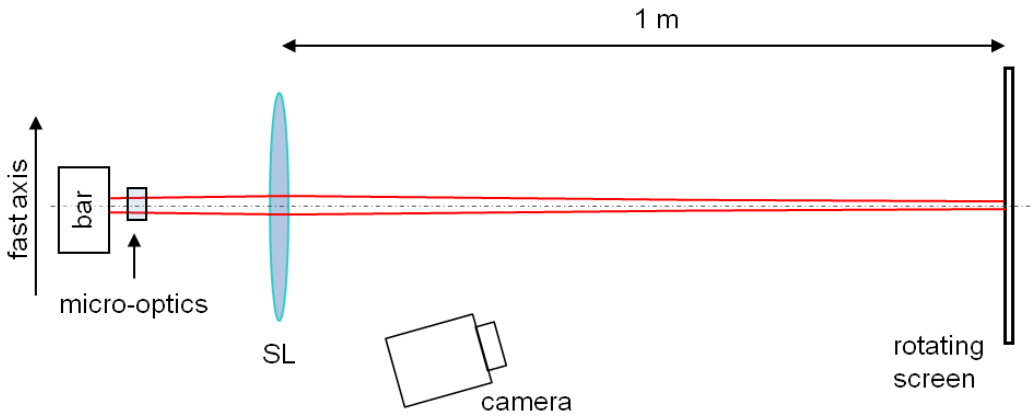


Fig. 4.2. Setup for the measurement of the far field pattern of the full bar. SL is a 1 m focal length spherical lens.

*Edge-knife calculation for the beam width*

Based on its far field pattern, the far field divergence of the beam can be calculated. In this work, the knife-edge beam width technique was used most frequently. Fig. 4.3 illustrates the methods of calculating the 5-95% edge-knife beam width from a far field profile of an ideal Gaussian beam. The knife-edge graph is obtained by integrating the intensity profile.

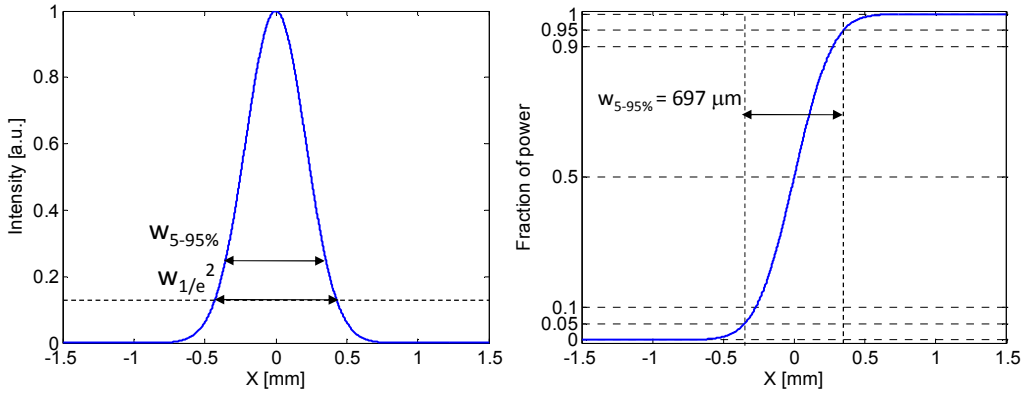


Fig. 4.3 Intensity profile and edge-knife plot for a ideal Gaussian beam.

Both the far field beam profile and the corresponding edge-knife graph carry information about the beam quality of the laser bar. However, some of the lensing errors and smile-induced pointing variations are manifested in an indistinguishable way as side lobes, broadening of the far field pattern and "wings" in the edge-knife plot. Thus, the far field measurement alone does not provide sufficient information to explain the causes of any beam degradation observed.

### *4.2.1.2 Emitter resolved far field pattern*

An emitter-resolved fast axis far field pattern provides a better qualitative description of the causes for any beam quality degradation observed for a laser bar. In such an image,

the smile-induced pointing errors for individual emitters are visualised and the lensing errors become easier to distinguish.

The pattern is obtained by modifying the setup presented in Fig. 4.2 by introducing a 200 mm focal length cylindrical lens that creates a slow axis image of the bar at the screen (see Fig. 4.4). Such an image presents a near field image in the slow axis direction and a far field image in the fast axis direction, as shown in Fig. 4.1 (a). In this way the fast axis errors that stem from smile deformation and lensing errors for each individual emitter can be resolved. A similar approach was applied in Ref. [98] to visualise the smile error for a laser diode bar. However no spherical lens was used in this approach and the beams were propagated over a distance of 2 m to provide the far field beam distribution along the fast axis.

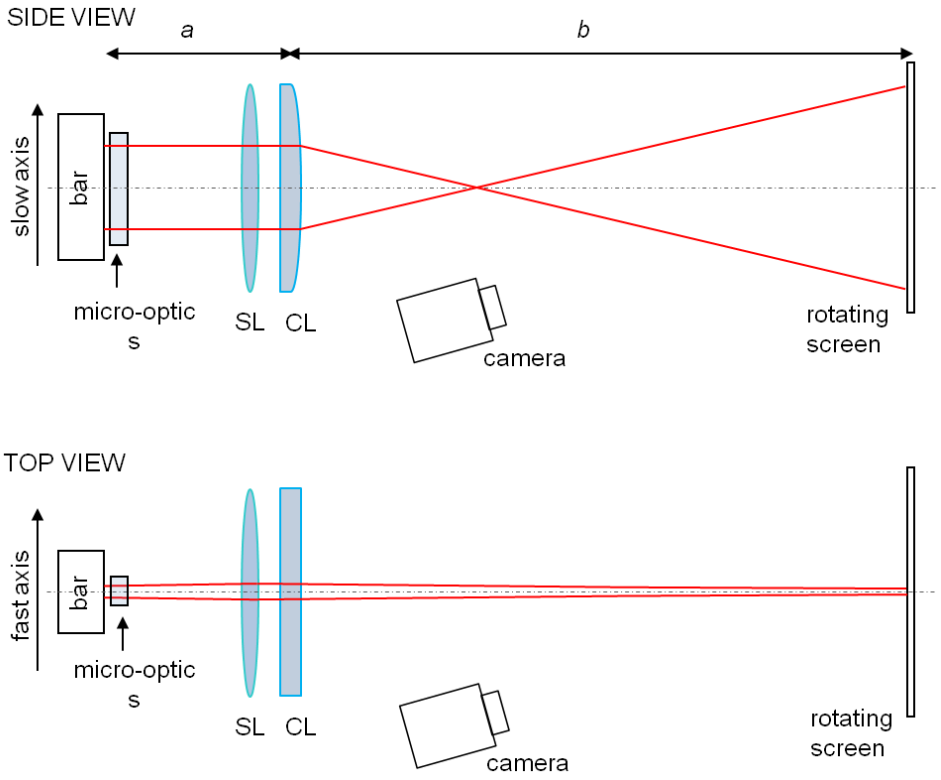


Fig.4.4. Experiments setup for emitter resolved far field measurement (SL - 1m spherical lens, CL – 200 mm cylindrical lens).

The emitter resolved far field pattern view was particularly useful for the alignment of fast axis lenses and corrective optics (see Chapter 6). It was also a convenient way to visualize the principle of operation of the wavelength stepping refractive beam deflector introduced in Chapter 8.

#### *4.2.1.3 Beam selection in densely packed laser diode arrays*

Some of the experiments performed in this project required information on the pointing accuracy across a bar to be evaluated. The pointing direction in the slow and fast axes

are measured for each emitter based on the far field patterns generated for individual emitters selected from the bar. To obtain this, a beam selector is introduced into the setup shown in Fig. 4.2. The selector consists of two prisms forming a slit with adjustable width and mounted on a translation stage (see Fig. 4.5). The beams from different emitters are selected by manually scanning the slit across the bar. The remaining beams pass through the AR-coated legs of the prisms and are totally internally reflected at the hypotenuse and sent to the beam dumps. For each selected beam, a 1m focal length produces a far field pattern on the scattering disc placed at the focal distance of the lens. The pattern was then recorded using a Spiricon CCD camera. The centroid position for each beam was calculated using the Spiricon software to determine the pointing variation across the bar.

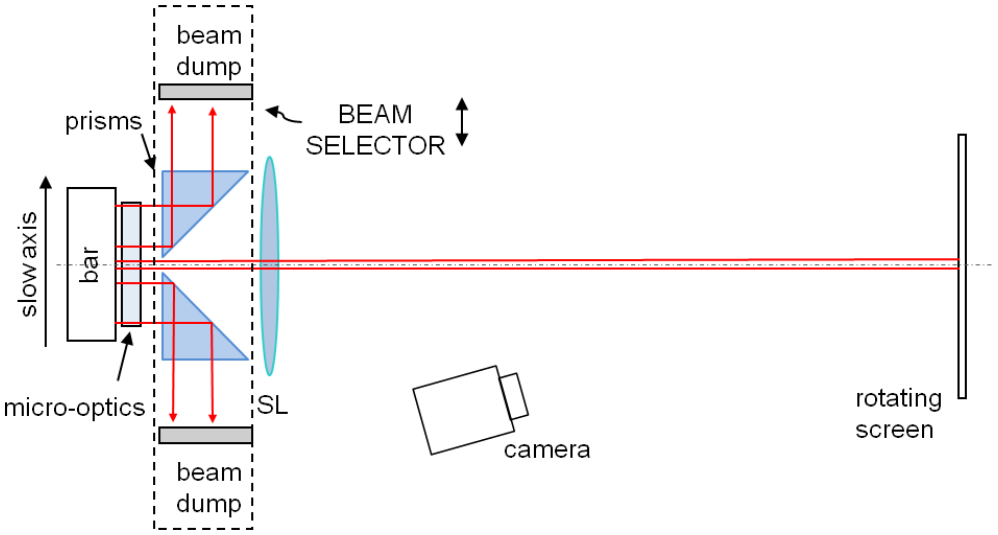


Fig.4.5. Experimental setup for pointing error measurement for individual emitters.

Such a procedure was used to evaluate the pointing accuracy across the bar with dual axis corrective optics in Chapter 6. It also provided the information for necessary to allow an understanding of some of the results on phase-locking shown in Chapter 9.

### 4.2.2 Spectral analysis of LDAs

The spectral analysis of the diode laser bars is performed in a two-fold manner simultaneously by using a single channel high resolution spectrometer to view an individual emitter in a bar and the imaging spectrometer to produce and view the spatially-resolved spectra of all of the emitters at the same time. The two techniques provide different sets of information and together provide the basis for a comprehensive analysis.

### 4.2.2.1 High resolution spectra for single emitters in a bar

The high resolution spectra are used to investigate the longitudinal mode structure and spectral linewidths of single emitters and fine wavelength variation across a bar obtained by an automated scan in the slow axis direction. They are also used to provide a calibration for the imaging spectrometer used in the measurement branch shown in Fig. 4.1 (c).

The spectra from the individual emitters are obtained in a configuration shown in Fig. 4.6 using a modified 0.5 m SPEX spectrograph. A fibre adaptor at the entrance slit is used to hold a multimode fibre that couples light into the spectrograph. The readout for the wavelength is performed with a line camera based on a linear CCD sensor array (LC1, Thorlabs) mounted at the exit slit. Prior to the experiments, an accurate calibration of the spectrometer was performed for the range 964-989 nm using two emission lines of Argon provided with a HG-1 Mercury Argon calibration lamp (Ocean Optics). This confirmed 17 pixels per nanometer of resolution and 60 pm FWHM of spectral resolution. The opposite end of the fibre is attached to a black screen with a pinhole that is mounted in a translation stage. A set of spherical lenses produces a magnified (10x) near field image of the bar at the screen. In this way, the scanning fibre end can provide a read-out of the spectrum of the individual emitters.

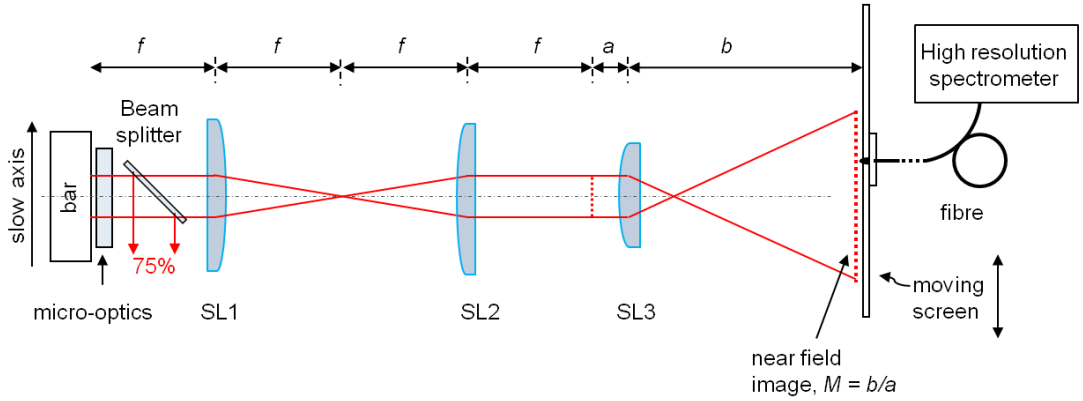


Fig. 4.6. Experimental setup with single channel high resolution spectrometer (SL1, SL2 – spherical lenses with focal length f = f1 = f2 = 250 mm, SL3 – spherical lens with focal length f3 = 75 mm).

The high resolution spectrum for a selected single emitter within a bar carries information about the longitudinal mode structure, spectral width and accurate wavelength of the laser beam. Spectral measurements taken at different laser operating conditions can also be used to characterise the thermal tuning behaviour of the laser. Moreover, an automated scan across the bar reveals even the fine variations between the emitters. Such an accurate spectral analysis was particularly useful in investigations on wavelength variation within a VHG-locked spectrum of a laser bar (see Chapter 7).

#### *4.2.2.2 Emitter resolved spectrum of a full bar*

For the purpose of experiments on wavelength locking of laser arrays, it was highly desirable to be able to view the spectra for all individual emitters in a bar simultaneously. In this way, an instant real-time evaluation rather than the slower scanning method described above can be provided. The commonly-used approach of viewing the composite spectrum of the beam from a full bar brings insufficient information for such experiments [104]. In a full bar spectrum, partial/incomplete locking of the bar is indicated by a side-spectrum appearing at the wavelength of the natural radiation. The emitters that remained unlocked cannot be identified, so it is difficult to explain why the full locking could not be obtained. The combination of the emitter resolved spectrum with the simultaneous viewing of the spatial properties of the beams as performed in this project helps to establish the link between the locking efficiency and the beam parameters such as divergence, pointing direction and detuning of the natural spectrum from the Bragg wavelength of the VHG used. As shown in Chapter 7, this approach allowed the efficiency of VHG locking to be quantified and the causes of its reduction to be better understood.

The emitter resolved spectra of laser bars are obtained using a novel imaging spectrometer set-up based on the symmetric Czerny-Turner configuration implemented with a modified 0.3 m Bentham M300 illustrated in Fig. 4.7. A telescope composed of two spherical lenses creates a near field image of the bar at the input slit of the monochromator, and the width of the input slit could be adjusted for maximum spectral resolution. In the vertical direction, the optical configuration of the monochromator creates an image of the input slit at the position of the exit slit. In the horizontal direction, a diffraction grating with a groove density of 1800 lines/mm translates the wavelength of each beam into an angle that is than transformed into a position on the image formed at the plane of the exit slit. A CCD camera records the image created atthe position of the exit slit of the monochromator. The original slit with limited width range was removed to ensure that the dispersed spectral image over the full range of observed wavelengths could be recorded by the CCD camera. Based on a comparison with the high resolution spectra obtained with the SPEX spectrometer introduced in the previous section, the spectral resolution of the imaging spectrometer is estimated to be about 0.3 nm. The camera definition is as high as 30 pixels per nanometer. Although the resolution is 5-fold lower than that obtained in the configuration shown in Fig. 4.6, the imaging spectrometer provides the great advantage of a live view of the spectrum of all emitters simultaneously. The acquisition of the spectral images is performed with

BeamStar software (Ophir Photonics Group). A quick extraction of the parameters of interest can be obtained by post-processing of the data with Matlab-based software.

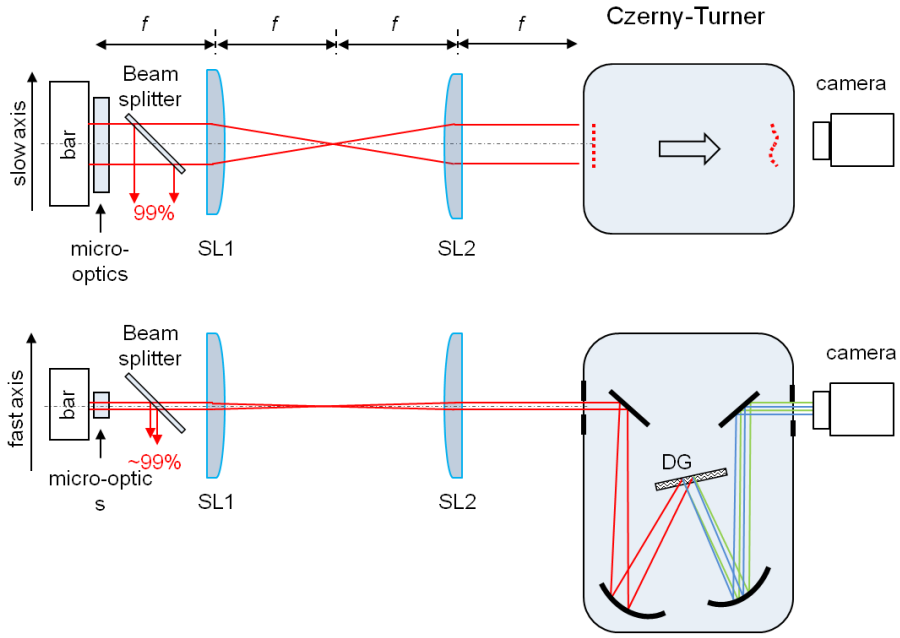


Fig.4.7. Imaging spectrometer based on Czerny-Turner monochromator (SL1, SL2 – spherical lenses with focal length f1 = f2 = f = 250 mm, DG – diffraction grating 1800 lines/mm).

In this work, the spectral images of bars were mainly used to perform a fast evaluation of the VHG-locking efficiency. The images were numerically processed to quantify the power content within the bandwidth of the VHG (see Chapter 7). It was also a convenient way of presenting results on wavelength stepping of a laser diode bar, as introduced in Chapter 8. In the experiments on phase-locking with VHGs as described in Chapter 9, the live-view of emitter resolved spectrum was a very useful indicator for the alignment of the VHG.

Beyond the locking experiments, the spectral images of unlocked bars are also very informative in terms of the properties of free running lasers. The non-uniform wavelength distribution across the bars provides evidence for external feedback from a FAC lens, as manifested by spectral splitting into bands (see Chapter 6). The images can also enable the visualization of the impact of a temperature gradient, packaging induced stress, inhomogeneities in wafer fabrication or epitaxy, that were previously widely studied with micro-photoluminenscence measurement technique [191-194]. As opposed to scanning methods, the imaging spectrometer approach allows the viewing all emitters at the same time, thus revealing any mode chopping and splitting into multiple bands that may occur non-uniformly across a bar while the operating conditions are changing. Although, none of the listed affects were specifically

quantified in this thesis, this is a very interesting way of viewing such behaviour and would be worth extending in future work.

## 4.3 Wavefront sensing

The beam quality of high-power diode laser arrays can be significantly improved by beam shaping methods, such as the introduction of corrective refractive optics [98], refractive beam shapers [195] or diffractive optical elements [196, 197]. However, such sophisticated methods for beam shaping require accurate information about the shape of the wavefront of the initial laser beam.

Many different techniques for wavefront characterisation were developed over time. Some of them, such as the Hartmann wavefront sensor [198] and Shack-Hartmann wavefront sensor [199, 200], are based on geometrical approaches which involve sampling of the beam by precisely located apertures and defining the local wavefront tilt based on the position of the sampled beams at a detection plane. Alternatively, interferometric wavefront sensors such as shearing interferometers [201-203] or the Twyman-Green interferometer [204] can be used, which involve extracting the wavefront from an interferogram. However, a wavefront sensor designed for high-power laser diode arrays (HPLDAs) is required to handle both coherent and incoherent beams at high power levels. It is also required to offer a large dynamic range to cover large variations in the phase front and good accuracy to resolve the errors leading to a reduction of brightness of HPDLAs. None of the commercially available sensors can answer such stringent requirements. Thus, to address this problem, a PhD project was undertaken by Monjardin [17] in 2002 aimed at developing a unique wavefront sensing device designed specially to work with HPLDAs. As a result of his work, a versatile wavefront sensor based on the Hartman principle with an accuracy of 19 μrad and angular range of ±48 mrad was developed. Monjardin and co-workers overcame the power handling issues and the need to speed-up the wavefront measurement so that it became possible to accurately characterise even large diode laser stacks in an automated process. The device scans a plane at a given distance from the laser facet and for each scanned point provides information about the local intensity and wavefront slope for the laser beam. Numerical integration allows reconstruction of the local wavefront data into the Optical Path Difference (OPD) across the beam. The reconstructed wavefront data contains accurate information about collimation errors, pointing errors, lens aberrations etc. The device is now a commercialized fully automated platform that provides accurate data on the wavefront shape and intensity distribution of laser diode arrays.

Thanks to collaboration with PowerPhotonic Ltd, the author had access to the wavefront sensing device to investigate in detail the properties of the laser bars. Some of the results presented later in Chapter 6 will prove that the accuracy of the wavefront measurement significantly surpass that obtainable from the conventional imaging techniques discussed in section 4.2.1

Originally, the tool was mainly used to characterise the beam in the fast axis direction to provide correction data for fast axis errors. However, at some points of the project, the wavefront sensor was also used as a general tool for accurate beam characterisation in both the fast and slow axis directions.

## 4.4 Custom laser-written refractive optics

The technique for laser writing of free-form refractive optics was developed by former members of the *Laser and Photonics Application Group*, prior to this research. Preliminary work on $CO_2$-laser ablation of silica was carried out by Markillie [15]. Subsequently, Nowak extended this work to the laser fabrication of optical components and also developed an efficient technique for laser smoothing of a refractive surface in silica glass [205]. As a result of his work, a laser machining system capable of producing an arbitrary shape, low scatter (below 1%) refractive surfaces with surface depth modulation of 10-30 μm with depth accuracy of about 200 nm [206] was developed.

Since the first report on the successful fabrication of such micro-optics was published [15], the process has been significantly improved, including for example a high performance control system for the laser.

### 4.4.1 Unique method for fast axis correction

Based on this technology, a method for the correction of beams from high-power diode lasers has been developed. The optical path difference (OPD) across the laser beams measured with the wavefront sensing device [17] at a small distance from the laser facet (typically less than 1 mm) before the adjacent beams begin to overlap can be compensated by laser-written corrective optics. A typical surface depth modulation for such a structure is about 10 μm. Such a refractive component can be applied to either bars or stacks, providing efficient correction of diode bar ‘smile’, FAC lens attachment errors and its imperfections. It has a potential of brightness improvement by a factor of up to x10 [98]. For example, this technique has been used in a 1.8kW 20-bar diode laser system [207]. Corrective optics have also been used for fast axis correction for a 10-

element tapered emitter bar with a 100 μm pitch, which was used in the experiments on diffraction-coupling presented in Ref. [188]. Since these early demonstrations, the use of custom designed/fabricated micro-optics for beam enhancement has been provided as a commercial product and used in multiple high-power laser diode systems.

In this work, the laser-written optics technique is exploited in a number of brightness enhancement systems i) by improving the performance of previously-developed techniques, ii) by extending existing brightness improvement techniques, and by the development of novel techniques which produce brightness enhancement of laser diode arrays. In particular, the use of refractive optics for fast axis correction has been demonstrated to produce brightness enhancement for 49-element single-mode emitter bars and 19-element broad-area emitter bars with a demonstrated capability to enhance the performance of beam combining and wavelength locking techniques.

### 4.4.2 Flexible design for refractive optics

The flexibility of the laser-written optics technique allowed it to be extended towards multi-functionality, producing multiple optical functions in the same micro-optic element. Within the framework of a collaboration with PowerPhotonic Ltd, a set of multi-functional laser-written optics based on designs prepared by the author were manufactured and supplied for use in this project. The free-form optics design was used to combine the fast axis correction with an array of slow axis collimating lenses as well as an array of beam deflectors. The dual-axis refractive optics capable of providing fast axis correction and slow axis collimation is introduced in Chapter 6. The laser-written reflectors were used in experiments on the wavelength stepping of a laser diode bar presented in Chapter 8. The variety of multi-function custom refractive optics mentioned above produced by the laser direct write technique provide a very significant improvement of the results obtained during the project and allowed us to extend the range of possible experiments that could be undertaken.

## 4.5 Summary

The techniques employed for laser beam measurement that have been discussed in this chapter were used to provide reliable spatial and spectral information on laser diode array devices and their output beams. The biggest challenges for beam characterisation were imposed by power handling and the closeness of the array-packing of the emitters in the bars. These issues were overcome in the multi-functional laser diagnostics configuration developed for the purpose of this project, which allowed the spatial beam

properties and spectral behaviour to be emitter-resolved and observed simultaneously. In many experiments discussed in the thesis, such a parallel approach was the only way to obtain a comprehensive set of results. The optical setups for spatial beam characterisation were used to evaluate the performance of the dual-axis refractive optics technique discussed in Chapter 6. The dedicated spectral analysis system combined with simultaneous recording of spatial beam properties was a key method to evaluate the performance of the wavelength locking of ultra-collimated laser diode arrays in a external cavity configuration with VHG.

The second group of methods introduced in this chapter consisted of using a set of unique tools facilitated by PowerPhotonic Ltd. The wavefront sensing device was widely used for accurate beam characterisation to provide a set of data needed for fast axis error correction. The laser-written optics technique not only provided the corrective optics to enhance the beam quality of the laser used in the project, but also allowed additional beam formatting customized for the needs of the experiments.

The capacity to perform a set of original experiments, which are at the core of this thesis was strongly dependent on both the diagnostics methods developed by the author and also the optics ‘tools’ facilitated by PowerPhotonic Ltd.

# Chapter 5.
# Optical inter-leaving for a stack of single-mode emitter bars

## 5.1 Introduction

The work presented in this chapter was carried out in collaboration with the ORC, University of Southampton, BAE Systems and PowerPhotonic Ltd, as a part of the UK TSB Consortium Project 'LAMPS'. The aim of the project was to format a beam from a high-power diode laser stack so that it could be coupled with square-core fibres produced by collaborators at the University of Southampton. The part of the project realised at Heriot-Watt University aimed to provide a design for and the optical testing of a beam shaping system for a commercial high brightness diode laser stack (Nuvonyx Inc.) consisting of 7 single-mode emitter bars. Prof. Howard J. Baker prepared the optical design for the beam combining components. Dr Roy McBride and his colleagues in PowerPhotonic Ltd performed a wavefront scan for the stack and provided the laser-written optics for the fast axis correction. The author was responsible for the assembly and optical testing of the beam shaping system for the high-power diode laser stack. The work was performed in the early stage of the author's PhD study.

The beam combining method used in this project consisted of optical inter-leaving a fraction of the length of each bar into the space between the unformatted parts of the bars. As opposed to the approach previously proposed in [97], the aperture filling for a laser stack is performed here by splitting the beams in the slow axis direction and optically inter-leaving them in the stacking direction, leading to the equalisation of the beam parameter product (BPP) for the stack. A similar approach was presented in [94], where the beams of a 10-bar stack were interleaved by a set of rectangular cubes and two stripe mirrors resulting in a 3-fold beam quality improvement. The method used in this project employed a stripe mirror and a comb mirror to inter-leave the beams for a stack. The fast axis correction, applied to each bar prior to the combining, improves the beam quality of the beams and offers the prospect of better brightness. The technique has the potential to provide a 2- or 3-fold beam quality improvement, depending on the arrangement of the inter-leaving scheme.

This chapter presents the basic concept of inter-leaving and the results obtained with a 2:1 beam inter-leaver applied to the 7-bar Nuvonyx diode laser stack. Section 5.2 introduces the initial properties of the stack and defines the goal for the following work.

Section 5.3 presents the concept of beam formatting and the design of the beam interleaver. The mounting procedure and optical testing are described in Section 5.5. The brightness enhancement obtained with this technique is discussed in Section 5.6.

## 5.2 Initial beam properties of the 7-bar single-mode emitter stack

The diode laser stack used in this project is comprised of 7 bars that produce 30 W of power each, providing about 210 W output power at 975 nm for the full stack. The bar spacing is 2.03 mm and each bar contains 49 single-mode emitters spaced by 200 μm. The stack included a factory-mounted fast axis collimating lens with 0.91 mm EFL and refractive index of 1.823 at 808 nm and array slow axis collimators with approximately 1 mm focal length. Fig. 5.1 shows a picture of the diode stack and the arrangement of the collimating optics. Prior to the experiments on beam shaping, a laser-written corrective optics was provided by PowerPhotonic Ltd to perform corrections for smile and collimation errors for each bar in the stack, using the technique discussed in Chapter 4.

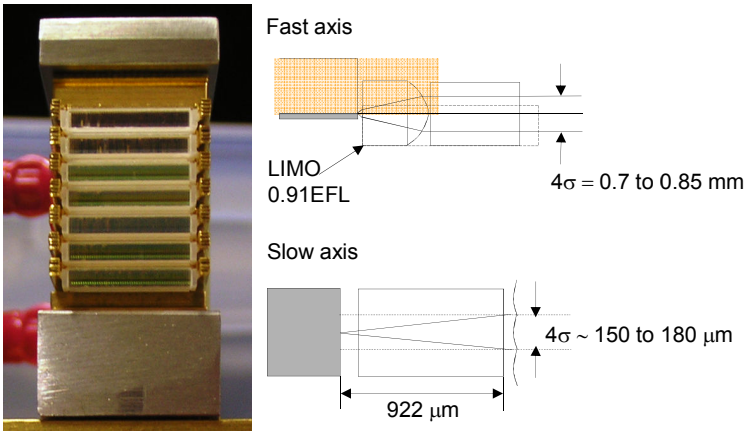


Fig. 5.1. Picture of the 7-bar Nuvonyx diode laser stack and the drawings of the collimation optics pre-mounted on the stack.

Due the architecture of the stack, the geometry of each individual emitter and the collimating optics used, the beam parameter product for the output beam is highly asymmetric. Fig. 5.2 shows the near field and the far field images of the stack, captured in an experiment discussed later in Section 5.5.

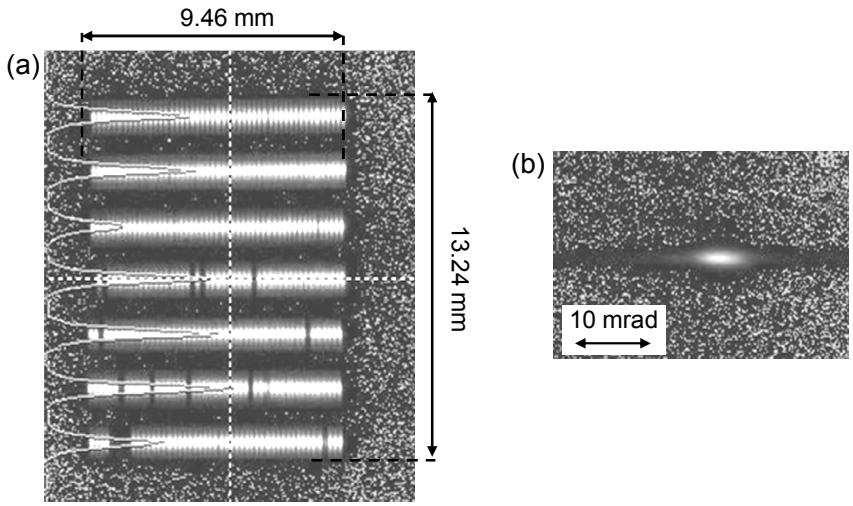


Fig. 5.2. Near field image (a) and far field pattern (b) of the 7-bar Nuvonyx diode laser stack before beam formatting.

The far field divergence angles based on the full-width at 5-95% for the fast and slow axis directions of the stack are 5.1 mrad and 35.7 mrad, respectively. As a result of the correction performed by the laser-written optics, the far field pattern of the stack is nearly the same as the far field of individual emitters, since the smile-induced pointing errors were eliminated. The slow axis tails in the far field pattern are evidence of beam truncation by the slow axis collimating optics. The closely-packed 49-emitter bars are difficult to collimate in the slow axis. As shown in Chapter 6, the single-mode beams begin to overlap at distance of about 700 μm of reduced optical distance from the laser front facet. For the 1 mm focal length of the slow axis lenses used, the effect of spilling onto the adjacent lenses and truncation by the edges of the lenses can be considerably larger (see later in Section 6.6). Based on the recorded far field pattern, the power sent to the tails was estimated to be about 10%, contributing to the power loss in the beam combining system.

The dimensions of the emitting area are 13.24 mm and 9.46 mm for the fast- and slow axis directions, respectively. Following the definition provided by Eq. (2.13) in Chapter 2, the initial beam parameter product for the stack is equal to:

$$\mathrm{BPP_{fast}} = \mathrm{w_{fast}} \cdot \Theta_{\mathrm{fast}} = 6.62\ \mathrm{mm} \cdot 2.55\ \mathrm{mrad} = 16.88\ \mathrm{mm.mrad}$$

$$\mathrm{BPP_{slow}} = \mathrm{w_{slow}} \cdot \Theta_{\mathrm{slow}} = 4.73\ \mathrm{mm} \cdot 17.85\ \mathrm{mrad} = 85.43\ \mathrm{mm.mrad}$$

where $w$ is the size of the emitting area and $\Theta$ is the far field divergence angle of the output beam, both defined as half-width at 5-95% of power containment. Thus, the beam parameter product in the slow axis direction is 5-fold larger than the beam parameter product in the stacking direction. A beam with such a high asymmetry cannot

be focused into a small spot or coupled into a fibre. Thus, the goal of this work is to perform BPP equalisation by decreasing the size of the emitting area in the slow axis direction with only a slight increase of the fast axis dimension, with the far field divergence along both axes conserved. This outcome is obtained by reformatting of the near field of the beam, while preserving the far field pointing direction for all beams.

## 5.3 A concept of aperture filling by optical inter-leaving

The concept for beam formatting used in this project is illustrated in Fig. 5.3. The beams are split in the slow axis direction and then inter-leaved in the stacking direction. Using this approach, the slow axis beam parameter product is reduced, leading towards the desired beam symmetrisation with the dead spaces between the bars being filled up. A similar approach was earlier realized for an array of $CO_2$ lasers in Ref. [208]. The method can be considered as a modified version of the Hanna-Clarkson technique [91] discussed in Chapter 3.

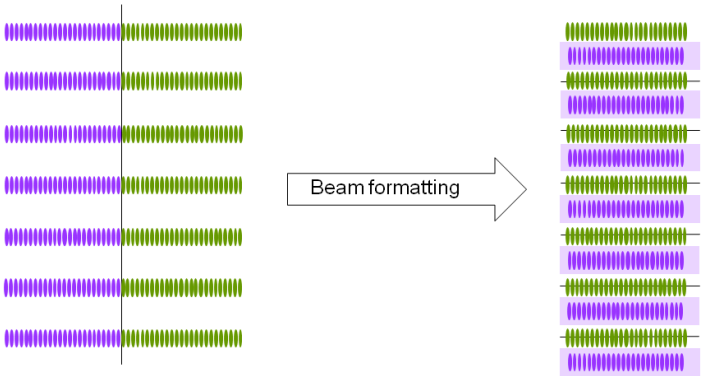


Fig. 5.3. Concept of beam shaping by 2:1 optical-interleaving.

The concept illustrated in Fig. 5.3 was realised with a set of mirrors that slice the beam along the stacking dimension and redirect the selected part of the beam into the space between the unchanged parts of the beams. The beam shaping system consisted of two parallel plates separated by distance $d$ and aligned with angle $\beta$ to the optical axis as shown in Fig. 5.4. Plate 1 is a comb mirror designed in such a way that its HR-coated fingers fit in between the beams. Plate 2 is an HR-coated silica glass element that deflects the selected parts of beam towards the fingers of the plate. In fact, it chops the incident beam in half in the slow axis direction and then deflects half of the beams to the fingers on the plate 1. The angle of deflection is then compensated by Plate 1, which is appropriately tilted about the fast- and slow axes. Thus, the propagation direction of the deflected beams is parallel to the original optical axis. By this operation, the beam dimension in the slow axis is reduced by half and the far field pattern of full stack is conserved.

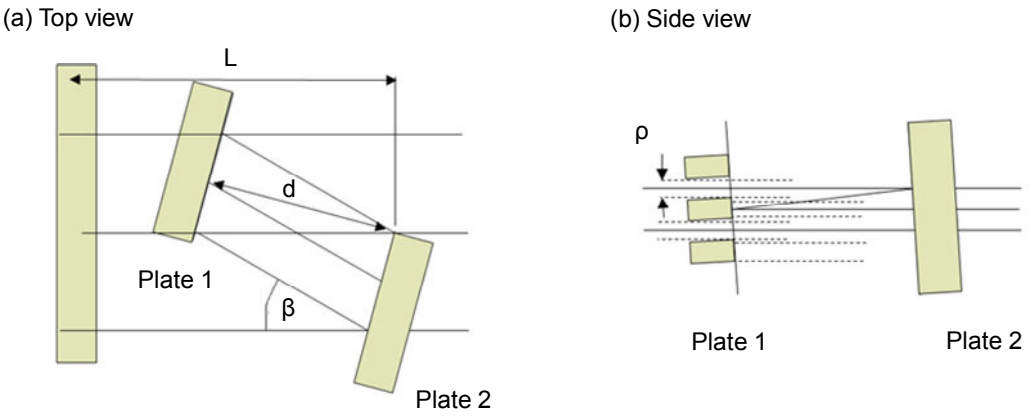


Fig. 5.4. The scheme of the 2:1 beam inter-leaver.

As the free apertures of half of the stack are filled by the beams of the other half of the stack, the filling factor in the stacking direction is increased and the beam dimension in the slow axis direction is decreased. In this way, the geometrical mean of the overall beam parameter product (see Eq. 2.10) for the stack is improved nearly by a factor of $\sqrt{2}$.

### 5.3.1 Design for 2:1 beam inter-leaver

The size of the clear aperture between the comb mirror, marked as $\rho$ in Fig. 5.4(b), is particularly critical for the performance of the technique. It is very important to ensure that the beam spacing at the plane of Plate 1 is significantly bigger than the full beam width. For the fixed bar spacing of the stack, the parameters $L$, $d$ and $\beta$ must be chosen appropriately, so that no beam truncation on the beam shaping optics could occur. To minimize the losses in such a system, the design of optical components, their position and alignment tolerances require careful consideration.

For the 2.03 mm bar-to-bar spacing and in a range 0.7-0.85 mm fast axis beam size, a minimum gap of 1.18 mm between the adjacent beams should be allowed. To minimize the risk of clipping of the beams, the width of the 'fingers' was designed to be 1.05 mm. In the stacking direction, the pointing accuracy of the beams and the alignment tolerance of the mirrors needs to be such as to ensure that the positions of the beams at Plate 1 are aligned with a tolerance of ±150 μm.

Thanks to the accurate correction of the fast axis errors performed for each bar in the stack by the corrective optics designed and manufactured by PowerPhotonic Ltd, all beams occupy the minimum space in the fast axis direction and remain separated at the vertical mirror edge.

The use of the 900 μm focal length lenses for fast axis collimation resulted in the Rayleigh range being approximately 0.3 m. Thus, the additional distance of 19 mm

travelled by the redirected beams (see Fig. 5.5) has negligible effect on the fast axis propagation.

It is worth noting that, if shorter focal length FAC lenses were used, e.g. the 600 μm focal length lenses used in all experiments described later in this thesis, a smaller beam dimension in the fast axis direction (~400 μm) could be obtained and the Rayleigh range would be larger than 100 mm. It can be then estimated that if the shorter focal length FAC lenses were to be used, the beam shaper could be designed to overlap 2 beams within the gap between the bars resulting in a 3-fold improvement of the slow axis beam parameter product for the stack.

A schematic diagram of the 2:1 beam inter-leaver designed for the 7-bar diode stack is presented in Fig. 5.5.

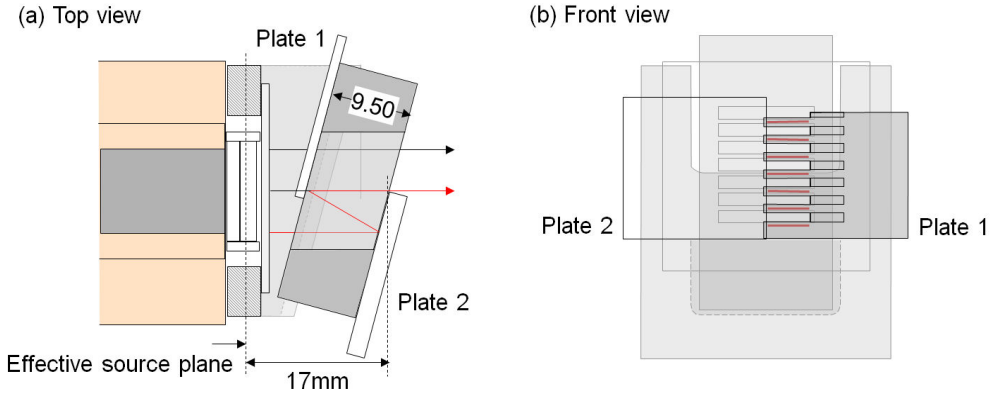


Fig. 5.5. Design of the 2:1 beam inter-leaver (a) top view at the cross-section at the centre of the beam, (b) front view.

Both mirrors illustrated in Fig. 5.5 were fabricated in silica glass. Plate 1 was AR-coated on both sides and then HR-coated on the front side. The slots 7 mm long and 1.05 mm wide were cut with diamond wheel by Mr. Neil Ross at Heriot-Watt University. Plate 2 was HR-coated.

## 5.4 Mounting and optical testing of the 2:1 beam inter-leaver

During alignment of the beam inter-leaver, the near and far field images were recorded simultaneously. The near field image carried the information about the number of emitters reflected by Plate 2 (mirror) and the relative positions of the beams in the near field. In this way, the course alignment of the inter-leaver could be obtained. For more accurate alignment, the relative pointing of the beams was recorded. Fig. 5.6 presents the diagnostic setup used for the alignment and mounting of the beam shaping optics.

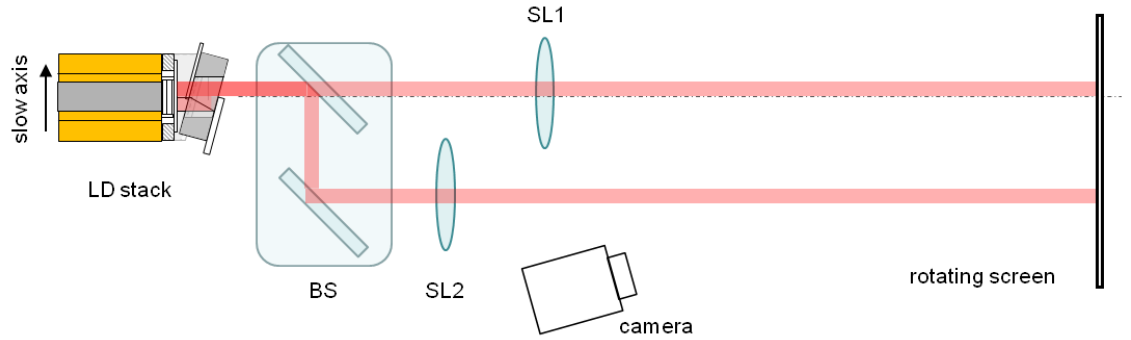


Fig.5.6. Diagnostic setup for alignment and mounting of the 2:1 beam inter-leaver, SL1 – 400 mm focal spherical lens, SL1 – 1 m focal length spherical lens, BS - 50:50 beam splitter.

A 50:50 beam splitter is used to allow the far field pattern and the near field image to be observed simultaneously. A 400 mm focal length spherical lens creates a near field image of the plane of Plate 1 at the viewing screen. A 1 m focal length spherical lens produces a far field pattern of the stack at the same viewing screen. Some examples of both images taken during the alignment process are presented in Fig. 5.7. The set of pictures shows that the near field image can remain unchanged, while the pointing error is introduced to the deflected half of the bar. This results in a double peak in the far field pattern for the full stack.

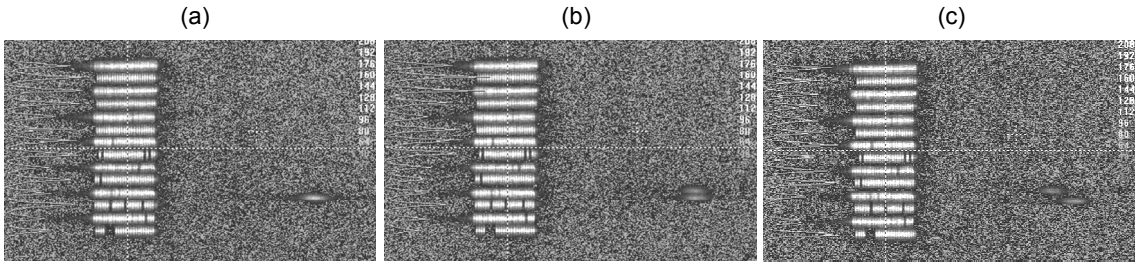


Fig. 5.7. Alignment of the 2:1 beam inter-leaver for: (a) optimal position, (b) pointing upwards and (c) pointing upwards and right.

The final images after optimum alignment are presented in Fig. 5.8 (b). For comparison, the same images taken for the stack before shaping are shown in Fig. 5.8 (a). Clearly the tails produced by the slow axis collimation optics significantly affect the beam quality of the stack.

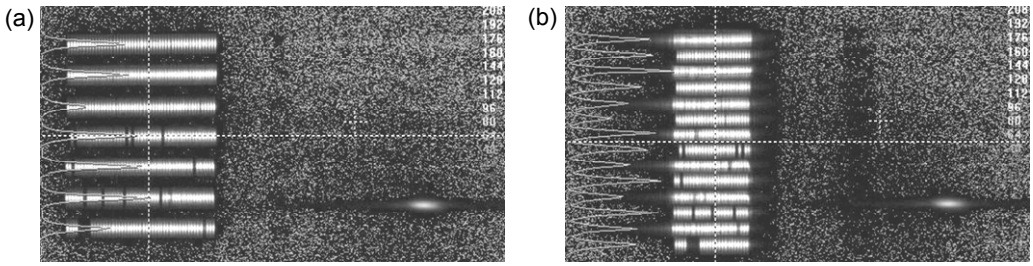


Fig. 5.8. Near field image (left) and far field (right) of the stack without (a) and with (b) beam inter-leaver.

A set of specially designed support structures was used to enable easy assembly of the beam shaping optics into their designed positions. Once the mirrors were optimally aligned in front of the stack, they were attached to the support structure using a UV-cured adhesive. Fig. 5.9 shows the stack with the attached beam formatting optics in place.

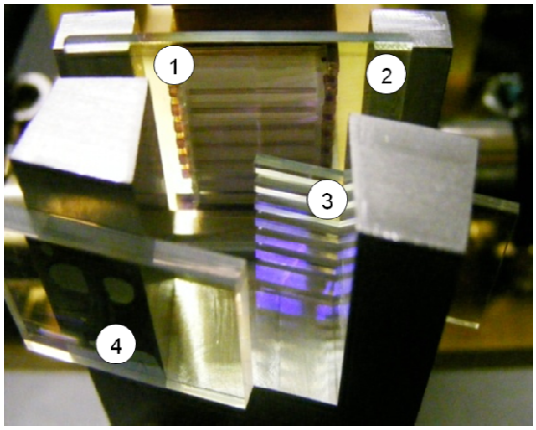


Fig. 5.9. Picture of the laser diode stack with assembled beam shaping optics: 1 - collimation lens arrays, 2 - corrective optics, 3 – comb mirror (plate 1), 4 - mirror (plate 2).

## 5.5 Brightness improvement of the spatially combined single-mode emitter stack

The overall performance of the technique can be evaluated by determining the improvement that is achieved in the measured values of the beam parameter product and the power loss of the beam formatting method. The output power of the stack with the inter-leaver was measured to be 190 W. Compared to the initial power measured of 209 W, this corresponds to about 9% loss due to beam formatting. The loss is attributed to the scatter at the edges of the slow axis collimation lenses and at the edges of the comb mirror. The evidence of both effects can be seen in the beam profile presented in Fig. 5.10, as well as in the knife-edge curves plotted later in Fig. 5.11.

The final beam parameter product was calculated based on the near field image and the far field pattern of the beam-shaped stack taken with a camera looking more closely at each image separately (see Fig. 5.10).

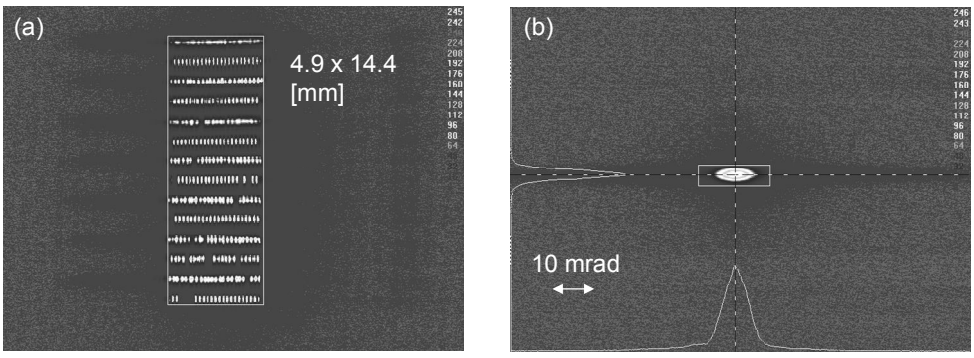


Fig. 5.10. Near field image (a) and far field (b) of the stack with the beam inter-leaver.

The emission beam with dimensions of 9.46 × 13.24 mm and full width at 5-95% divergence angles of 5.1 × 35.7 mrad were transformed into a distribution with dimensions of 4.9 × 14.4 mm with the same far field divergences. Thus, the slow axis beam parameter product was reduced by nearly factor of 2, while the fast axis beam parameter remained close to its initial value, increasing by only factor of 1.08. In this way, an improvement in the beam quality was obtained and the power density effectively enhanced.

Fig. 5.11 presents the knife-edge curves calculated based on the far field pattern of the output beam recorded with a CCD camera. While the fast axis beam profile is nearly diffraction limited, the slow axis curve reveals that a significant fraction of the power is contained in the tails.

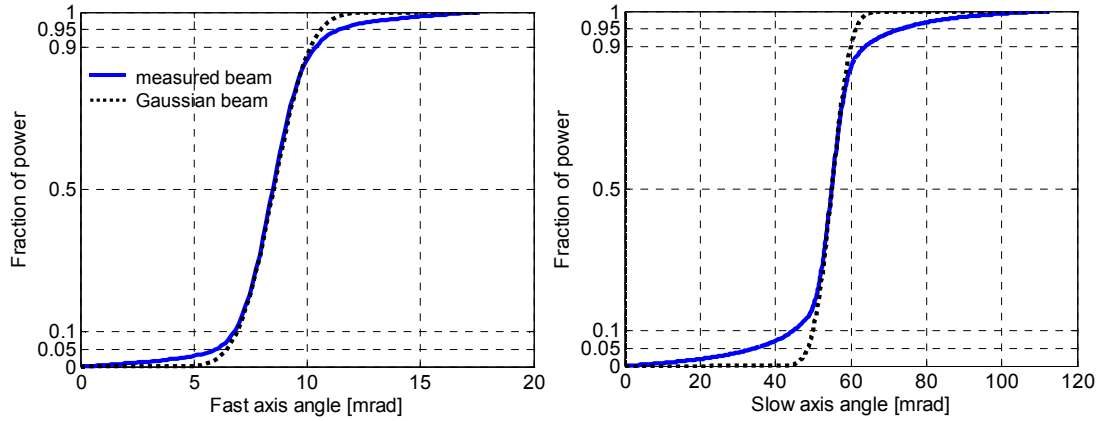


Fig.5.11. Knife-edge plots for fast- and slow axis direction.

The truncation of the beam by the slow axis collimation optics sends a significant amount of light to the tails, which results in a larger BPP in the slow axis direction. This indicates that an improvement in the slow axis collimation is necessary in order to avoid brightness degradation. This issue is addressed in Chapter 6, where custom focal length slow axis collimation is used to minimize the power loss caused by beam overlap at the lenses.

In the fast axis direction, despite the smile correction applied to each bar in the stack, a small fraction of the diode power is nevertheless transferred to the tails in the far field pattern. This can be attributed to the fact that the fast axis errors were corrected at a relatively large distance from the FAC lens, as the corrective optics had to be placed after the slow axis collimation lenses. Over a propagation distance, the phase errors of the beams develop into amplitude errors, which are impossible to compensate. Thus, the preferred approach is for the correction to be performed in a plane just after the FAC lens, allowing the near field wavefront errors to be compensated before they affect the

intensity distribution of the propagating beams [17]. In the work presented in Chapter 6, this issue is overcome by integrating the fast axis correction with the slow axis collimation into a single optical component. This allows the beams to be corrected effectively into nearly ideal Gaussian profiles.

Table 5.1 presents the beam parameter products calculated for the measured far field divergence defined as the angle containing 90% (5-95% knife-edge). For comparison, the results are also presented for 80% (10-90% knife-edge) of the power.

Table 5.1. Beam parameter product for the diode stack with beam formatting optics.

| **Power loss** | **Fast axis divergence, full-width [mrad]** | **Slow axis divergence, full-width [mrad]** | **$BPP_{fast}$ [mm mrad]** | **$BPP_{slow}$ [mm mrad]** | **$BPP_{slow}/BPP_{fast}$** |
|---|---|---|---|---|---|
| 10% | 5.1 | 35.7 | 18.36 | 43.73 | 2.38 |
| 20% | 3.45 | 17.4 | 12.42 | 21.32 | 1.72 |

The efficiency of the fibre coupling is strongly affected by the existence of the tails in the slow axis direction, so this is an issue. Allowing 20% of the power to be lost in both directions would lead to a total loss of 58%, including the 9% lost on beam shaping. In such an approach, a beam with a 12.21 × 21.32 mm.mrad beam parameter product could be used in a fibre coupling system.

If the tails in the slow axis are cut off leading to 20% loss and if 10% loss in the fast axis direction is allowed, the beam parameter product for the output beam will be 18.36 × 21.32 mm.mrad, which corresponds to a BPP ratio of 1.16:1. In combination with the power loss due to beam formatting, this gives a 65.5% overall power content in the output beam. Following Eq. 2.12, the RMS beam parameter product for the output beam is:

$$\mathrm{BPP_{RMS}} = \sqrt{\mathrm{BPP_{fast}^2} + \mathrm{BPP_{slow}^2}} = 28.13\ \mathrm{mm.mrad}$$

This means the beam can be coupled into a circular fibre with a 250 μm core diameter and 0.22 NA.

From this stage, further work on the project was performed at Southampton University. Shaif-ul Alam *et al.* [209] reported on using the diode laser stack to pump a fibre laser for a picosecond fibre MOPA system. The beam was coupled into a 25/340 μm ytterbium doped fibre.

## 5.6 Summary

The beam formatting method presented in this chapter has proven its capacity to improve the beam parameter product ratio of diode laser stacks. By reducing the beam parameter product in the slow axis direction, it provides a source that can be used for pumping a fibre laser. The results show a nearly 2-fold beam parameter product reduction in the slow axis direction with the prospect of further improvements in the future. The technique is fairly straightforward and can be applied to various types of diode laser stacks. It is clear that the performance of the technique depends strongly on the initial beam quality of the bar. To achieve low loss inter-leaving, the correction of the fast axis pointing errors is critically important.

Further improvement in the performance of the technique in terms of efficiency and output beam quality could be obtained by addressing the issue with the slow axis collimation of densely-packed single-mode emitter bars and by allowing the fast axis correction to be performed at a closer distance to the fast axis collimating lens. Fast axis correction is more difficult to perform when SAC and FAC lenses are factory mounted. This chapter shows that a small pitch single-mode emitter bar can be efficiently combined only if the challenge of providing effective optics is addressed. The experience gained in this project motivated the work on custom slow axis collimation optics combined with fast axis correction, as presented in the next chapter.

# Chapter 6.
# Laser-written optics for fast axis correction and slow axis collimation

## 6.1 Introduction

The highly divergent emission of a typical diode laser in the fast axis direction requires beam collimation to be applied in most diode laser systems. Although slow axis collimation is not necessary for many applications, it is an important approach to improve the beam parameter product of a bar by aperture filling. In combined diode laser systems, it can often reduce power loss and enhance the performance of beam combining methods. For both axes, the collimation optics must be appropriately chosen and accurately aligned to conserve power and beam quality as much as possible.

In the fast axis direction, the collimation of high numerical aperture beams is usually performed with plano-aspheric lenses made from high refractive index glass and optimized specifically for laser diode emission. The main determinants of the fast axis beam quality are lens quality, lens alignment and smile error of the bar.

The challenge of efficient slow axis collimation arises mainly from the close-packing of emitters in a bar. High performance of slow axis collimation can only be obtained if the optimal aperture filling at the plane of the lenses is obtained. In order to obtain the minimum possible beam parameter product for a bar, the underfilling of the lens aperture should be avoided. The consequences of overfilling can be even more severe. As shown in Chapter 5, beam truncation by the edges of the lenses can lead to significant power loss and beam quality degradation. To avoid these issues, the focal length for slow axis lenses must be accurately chosen to ensure that the beams are collimated before they begin to overlap with adjacent beams. To prevent underfilling and minimize loss due to scatter and aberration at the edges of the lenses, the active region of the lenses must be maximized. It is particularly important in the case of a small pitch laser bar, where beam truncation on collimation optics can lead to significant power loss in beam combined systems.

Good collimation in both the fast- and slow axis directions can enhance the performance of brightness improvement techniques, such as line narrowing [69, 70, 210], spectral beam combining [13, 135, 141] or phase-locking [158, 159, 188]. It does

this by increasing the amount of the light that can be efficiently coupled back to the emitters in external cavity configurations, reducing power loss and preventing beam quality degradation for the output beam. Ideally, effective compensation of the fast axis errors and precise slow axis collimation need to be obtained at minimum penalty on power loss and system complexity.

The objective of this project was to provide a laser system where the smile and collimation optics no longer constrain the performance of beam combining methods. In order to achieve this goal, the laser-written refractive optics technique introduced in Chapter 4 was extended to provide a single optical component that combines fast axis correction with slow axis collimation [211]. The approach of using laser-written optics addresses the particularly demanding issue of slow axis collimation of small pitch laser bars, where accurate and efficient collimation is difficult and the use of an expensive custom focal length lens array would normally be necessary to optimize the fill-factor and avoid drastic power loss in the optical system. This technique can be applied in external cavity laser diode arrays, where smile-induced pointing errors prevent efficient and uniform feedback along a bar [104, 210]. The results for enhanced VHG-locking of laser bars with dual axis corrective optics are presented in Chapter 7.

In this chapter, a detailed analysis of the performance of the fast axis correction combined with slow axis collimation is investigated for two types of laser diode bars. The first type is a 200 μm pitch array of 49 single-mode emitters [44], emitting 30W at 975 nm. The second bar is a standard off-the-shelf 500 μm pitch 19-emitter broad-area emitter bar, producing 60W at about 972 nm.

The work described in this chapter was performed in collaboration with PowerPhotonic Ltd. The author was responsible for design and optical testing of the corrective and collimating optics. The corrective optics were designed based on wavefront measurements performed by the author using the wavefront sensing device (see Section 4.3) facilitated by PowerPhotonic Ltd. The optical designs for the refractive surfaces for the fast axis correction were prepared following the algorithm described in [17].

Section 6.2 introduces the concept of the laser-written dual-axis refractive optics technique. The lasers used in the experiments are introduced in Section 6.3. Sections 6.4 and 6.5 discuss the challenges of beam quality restoration in the fast- and slow axis directions, respectively, and present the performance of the dual-axis component. For clarity, the design and optical performance of dual-axis optics in the fast- and the slow-axis directions are discussed separately. Section 6.6 summarises the results on beam

quality enhancement by using the dual-axis refractive optics for the high brightness laser bars.

## 6.2 Dual-axis laser-written refractive optics technique

In this project, the technique for producing laser-written refractive surfaces in silica glass [16, 98] is extended towards dual functionality by combining the corrective surface with a slow axis lens array [211]. Such a dual-axis component can be placed after the fast axis collimation lens as shown in Fig. 6.1.

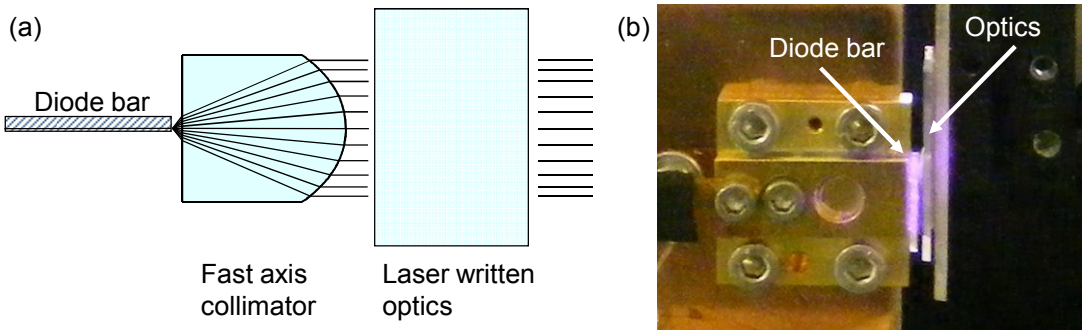


Fig. 6.1. Simplified drawing (a) and a picture of a CS-mounted laser bar mounted with the laser-written optics.

The flexibility of the technique allows the correction of errors produced by arbitrary smile deformation and lens aberrations, as well as producing a slow axis lens array with custom pitch and focal length. For the purpose of the experiments conducted in this project, a set of refractive optics components including a fast axis correction plate, slow axis collimation lens arrays, and a single component combining both fast axis correction and slow axis collimation were designed and manufactured. Lens arrays with a 200 μm pitch and 700 μm, 850 μm and 900 μm focal lengths and a 500 μm pitch lens array with 2.2 mm focal length were designed, produced and optically tested. The silica plates were custom-fabricated by PowerPhotonic Ltd, based on the designs provided by the author.

## 6.3 Laser diode bars used in the experiments

The bars used in this work were provided by Bookham/Oclaro. Three different types of sources were used, including two types of single-mode emitter bars and a standard broad-area emitter bar. The main difference between the types of single-mode emitter bars lies in reflectivities of the front facets of the lasers. All bars were passively cooled and mounted on CS-mounts. A summary of the basic parameters of the bars is shown in Table 6.1.

Table 6.1. Basic parameters of the diode bars used in the experiments on dual-axis refractive optics

| Laser | No. of emitters | Pitch [μm] | Emitter width | Total power [W] | Smile* [μm] | $f_{FAC}$ [μm] | $f_{SAC}$ [μm] |
|---|---|---|---|---|---|---|---|
| BSM1 | 49 | 200 | ~6 μm | 30 | 3.8 | 590 (LIMO) | 700 |
| BSM2 | 49 | 200 | ~6 μm | 30 | 3.8 | 600 (Ingeneric) | 900 |
| BSM3 | 49 | 200 | ~6 μm | 30 | 1.5 | 600 (Ingeneric) | 850 |
| BBA | 19 | 500 | ~100 μm | 60 | 0.7 | 600 (Ingeneric) | 2200 |

* peak-to-valley smile value

Bar BSM1 contains 49 emitters spaced by 200 μm. The emitters with approximately 6 μm wide ridges produce a single spatial mode in both directions, similar to the sources described in [44]. The overall output power is 30W at 40A of drive current. The threshold current for the bar is 1.6A. The emission wavelength is 976 nm. The smile of the bar was measured to be 3.8 μm (peak-to-valley).

In Table 6.1, BSM2 corresponds to the same laser as BSM1, but with different collimating optics attached, as explained later in this section.

Bar BSM3 is a separate laser, which has a similar geometry to bars BSM1/BSM2. However, for this laser, the reflectivity of the front facet was reduced to approximately $10^{-4}$ [212] to allow better performance in the experiments on wavelength locking and phase-locking in external cavity configurations (see Chapters 7 and 9). It is worth noting that despite the very low front facet reflectivity, bar BSM3 still operates as a laser with a 2 A threshold current and more than 30 W of output power at 40A of drive current. The L-I characteristics for the two types of single-mode emitter bars are shown in Fig. 6.2. High efficiency lasing of bar BSM3 indicates extremely high gain in the active region of the ridge emitters.

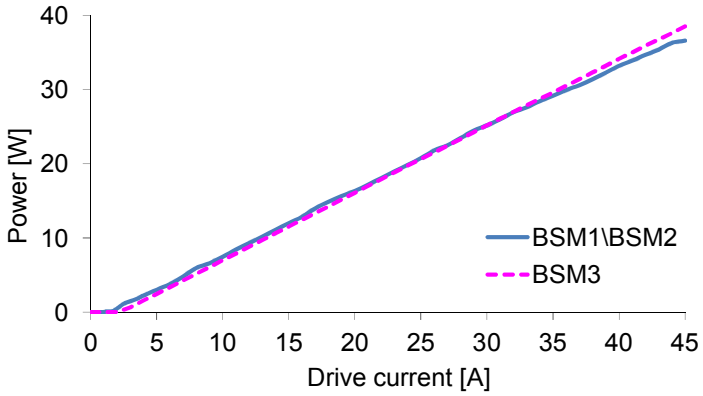


Fig. 6.2. Output power as a function of operating current.

The third type of laser bar used in this work, was a standard 19-broad-area emitter bar (BBA) with 60 W of output power at 980 nm. The 100 μm wide emitters are spaced by 500 μm. The smile of the bar was measured to be as low as 0. 7 μm (peak-to-valley).

The technique presented in this chapter was applied to all the bars, but only bar BSM2 is described in detail to provide a full case study. The single-mode emitter bars are of main interest in this study, as they are an example of brightness enhanced sources. The work on the broad-area emitter bar was conducted in order to prove that the technique is applicable for standard, commonly used types of sources.

### 6.3.1 Fast axis collimation optics

The lasers used in this project were individually lensed with one of the two types of FAC lenses: FAC-08-600 with a focal length of 600 μm and a refractive index of 1.776 at 808 nm (from Ingeneric GmbH) and FAC590-D with a focal length of 590 μm and a refractive index of 1.823 at 808nm (from LIMO).

When choosing the FAC lens and the method of mounting, compatibility with the slow axis collimation optics must be considered. Strictly speaking, the size of the lens and the mounting structure must not restrict the optimal positioning of the slow axis lenses. Slow axis collimation must be performed at a distance where the adjacent beams are still separated, so that light scatter to adjacent lenses can be avoided. As discussed in Section 6.6, this issue is particularly critical for small pitch single-mode emitter laser bars, for which the beams begin to overlap as close as 700 μm from the laser facet.

The Ingeneric lenses were factory-attached to a standard 1 mm thick mounting tab (see Fig. 6.3 (a)). In this case, access to the lens is restricted by the 0.2 mm of mounting tab sticking out at the front of the lens. This determines the minimum focal length of the slow axis collimation optics to 800 μm.

In the case of the LIMO lenses, their standard mounting tabs with a thickness of 1.5 mm would restrict the minimum focal length of the slow axis lenses to ~1.15 mm resulting in significant light beam overlap at the plane of the lenses. In order to allow the slow axis collimation to be placed closer to the laser, the LIMO lens used in this project was attached in-house to a 0.8 mm mounting tab, as shown in Fig. 6.3 (b).

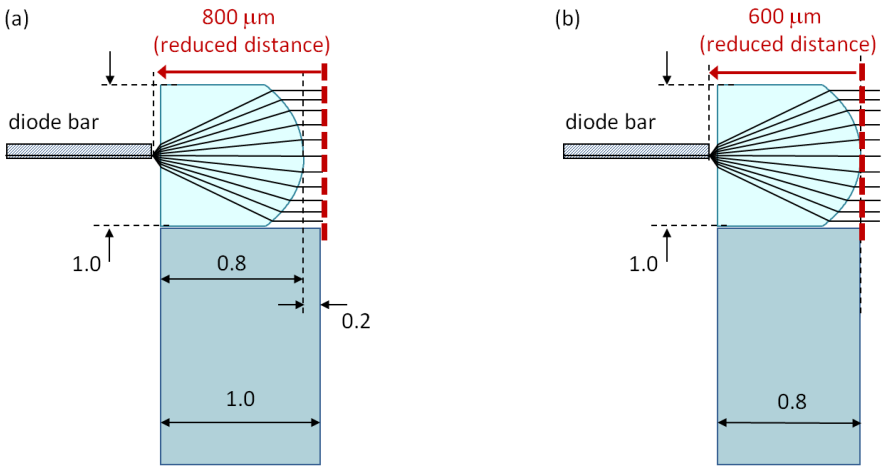


Fig.6.3. Fast axis lenses on mounting tabs: (a) Ingeneric lens mounted on a 1 mm thick tab, (b) LIMO lens mounted on a 0.8 mm thick tab.

The next section describes the alignment process and discusses the fast axis errors induced by lens misalignment and the 'smile' error of a bar.

## 6.4 Beam quality degradation of fast axis collimated laser bars

### 6.4.1 Fast axis collimation lens alignment errors

The performance of the fast axis collimation is highly sensitive to the alignment of the micro-lens. The sensitivity for all degrees of freedom is inversely proportional to the focal length of the lens used. Considering that the position and angular adjustment of the lens can significantly affect the beam quality of a bar, the collimation process requires all 6 degrees of freedom (see Fig. 6.4) of the micro-lens to be accurately controlled. In this work, the fast axis collimating lens was attached to a holder mounted on a 6-axis manipulation stage. In the lensing process, the optimum alignment of the lens was determined based on the emitter resolved far field pattern of the bar obtained in the setup presented in Fig. 4.4. The recorded pattern provides assessment of lens position errors that stem from the different degrees of freedom (see Fig. 6.5 and 6.6).

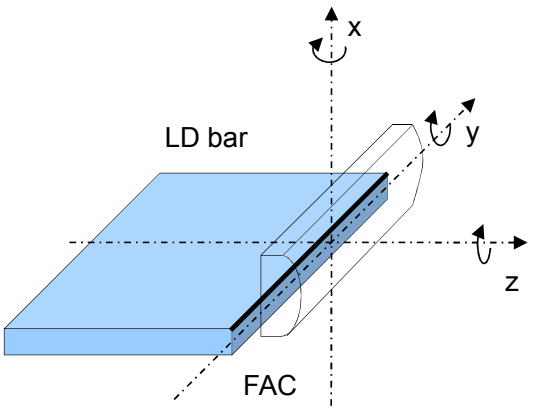


Fig. 6.4. Degrees of freedom of a fast axis collimating lens.

When the fast axis collimation lens is placed in front of a bar, a coarse adjustment is required to make the emitter resolved far field pattern appear in the field of view of the camera. The correct pointing direction for the bar was obtained using a He-Ne laser beam as a guide. To achieve the desired pointing direction, the position of the lens in the x-direction is adjusted accordingly. The effect of the alignment errors for each degree of freedom can be observed by fine manipulation of the lens. Figures 6.5 and 6.6 show some examples of the emitter resolved far field pattern for a 49 single-mode emitter bar revealing typical lens alignment errors.

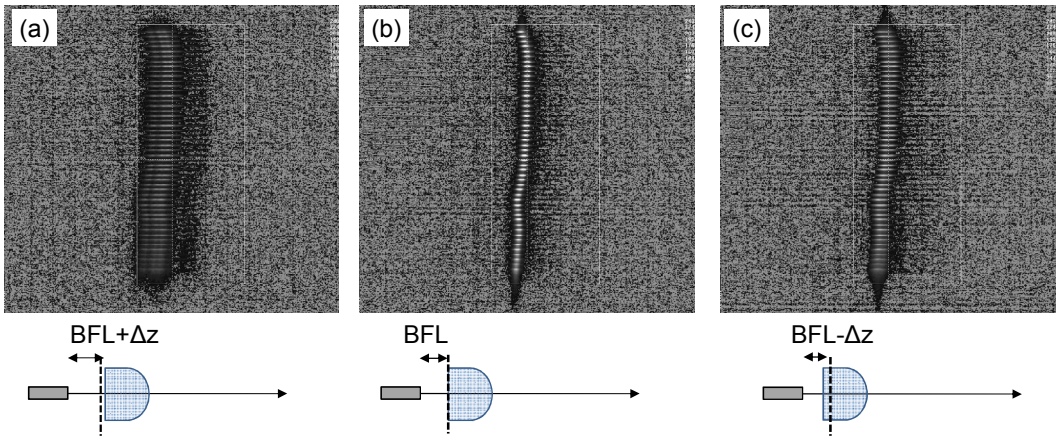


Fig.6.5. The effect of defocus of the fast axis collimating lens.

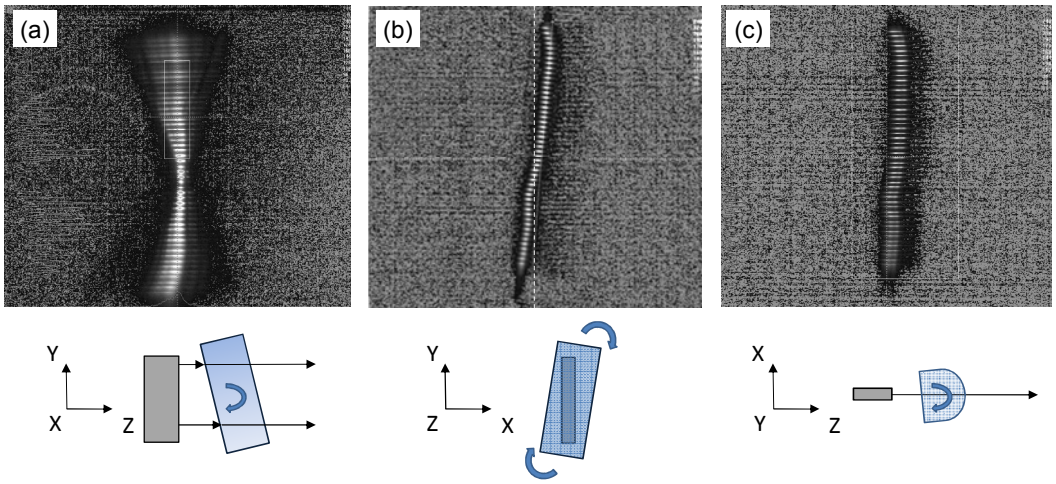


Fig.6.6. The effect of moving the lens beyond (left) and before the back focal point of the lens.

In particular, Fig. 6.5 illustrates the defocusing error caused by axial displacement of the lens in the z-direction. Defocus can be also induced by tilt about the x-axis, as shown in Fig. 6.6 (a). In this case, the top and bottom parts of the bar go out of focus and the emitter resolved far field image of the bar forms a bow tie shape. Based on the observations in the experiment on errors illustrated in Fig. 6.5 and 6.6, an adjustment tolerance of less than 1 μm for the axial displacement and about 100 μrad for the tilt

about the x-axis is needed to avoid a noticeable increase in the divergence. Clearly, these two degrees of freedom are the most critical for the fast axis lens alignment.

Other, less sensitive alignment errors are presented in Fig. 6.6 (b) and (c). The tilt about the z-axis produces a linear change in the pointing direction across the bar. The change in the pointing direction for individual emitters is caused by variations in the position of the beams relative to the centre of the lens, leading to different deflection angles for the individual emitters. A similar effect occurs when the lens is axially displaced in the x-direction. In this case, however, all the beams encounter the same deflection error resulting in a pointing error for the full bar. It is worth noting that the effect of a positioning error in the x-direction may counteract with the roll error (tilt about y-axis). The effect of the roll error manifests itself as a pointing error and beam distortion caused by asymmetric aberrations on one side of the lens, as illustrated in Fig. 6.6 (c). The roll error can to a certain extend be compensated by the x-position error of the lens. In the setup used for lensing (see Fig. 4.4), these two effects appeared to be indistinguishable, preventing perfect alignment of the lens. The collimated beams can preserve their pointing direction, but have poorer beam quality at off-axis incidence at the lens due to aberrations and truncation by the edge of the lens. The beam distortion caused by the roll error is difficult to observe in the imaging system used for lensing, but the asymmetric beam profile and truncation by the edge of the lens become evident from the results of accurate wavefront measurement, as discussed in Section 6.4. Although it is difficult to eliminate the roll error completely, with careful lensing procedures the impact of this error can be negligible.

In summary, the alignment of a FAC lens needs to be performed within tight tolerances in all six degrees of freedom. The defocus error, however, is particularly difficult to avoid due to the short depth of focus of typical FAC lenses. Therefore, the z-position of the lens and rotation about x-axis must be accurately controlled in applications where the far field divergence of the beams is critical or a well defined spot size at a given plane is required.

In systems, which spatially [94, 96, 97] or spectrally [135, 139, 141] combine multiple laser diode arrays, pointing errors of individual emitters and bar-to-bar pointing variation are often detrimental to their performance. Pointing errors can cause a number of issues in large beam combined systems, including beam truncation by the optical components, widening and inhomogeneity of the combined beam. In external cavity configurations, these can also lead to loss in feedback from wavelength locking components. In FAC-lensed bars, pointing angle of the beams can be strongly affected

by displacement of the lens in x-direction, rotation about z-axis or smile-induced deformation of the bar. For bars with lens misalignment or significant smile error, it is often required to apply an additional compensation for pointing errors to maximize their performance in beam combining systems.

### 6.4.2 Mounting of the micro-lens

As the fast axis lens alignment accuracy is very critical, the process of mounting of the micro-lens must be also well controlled to ensure minimum positioning errors. An appropriate adhesive must be chosen and a careful lensing procedure must be performed. The adhesive must have low shrinkage and movement during curing as well as during the long term operation of the laser. In this work, an optical UV-cured adhesive Norland NOA68 was used to attach the fast axis collimation lenses to the mounts of the laser bars.

Fig. 6.7 illustrates three different stages of the lensing procedure. The lens, attached to a 6-axis manipulator arm by a weak 'dicing tape', is first pre-aligned and subsequently removed to the side in order to provide clear access for the adhesive to be dispensed onto the surface of the laser mount (see Fig. 6.7 (a)). Once the adhesive is applied, the lens is moved back into its optimal position in front of the laser. The adhesive is then cured with a UV light source so that the manipulator arm can be gently removed, leaving the lens in the fixed position. Between the different stages of the lensing procedure, the laser output beam is monitored at low current levels to ensure that any movement or shrinkage of the adhesive does not introduce lens misalignment errors.

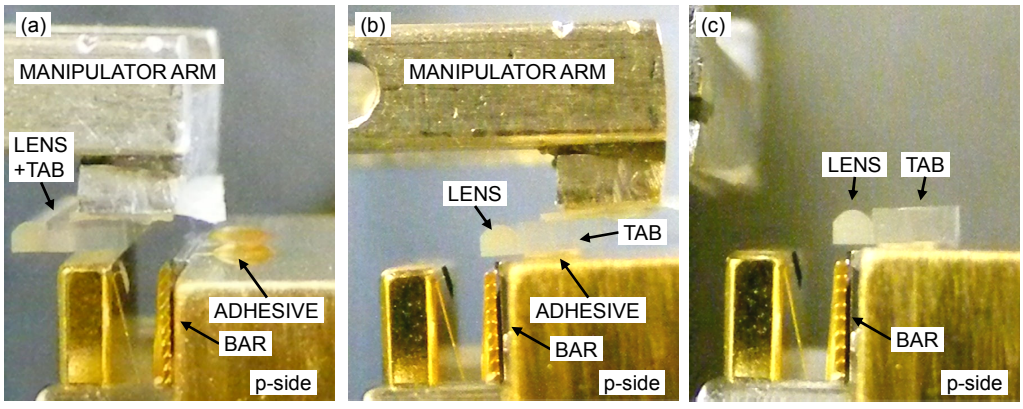


Fig. 6.7. Mounting of micro-lens (a) applying adhesive (pre-aligned lens held on the manipulator arm), (b) disengaging from the lens tab (adhesive UV-cured), (c) lens attached to the mount of the bar.

*Lensing with the LIMO lens (bar BSM1)*

Bar BSM1 was lensed in-house with the 590 μm focal length LIMO FAC lens, which was attached to a custom 0.8 mm thick mounting tab to facilitate the positioning of the slow axis collimation optics just after the FAC lens, as mentioned in Section 6.3. The mounting tab was attached to the lens with a slight angle due to misalignment error during assembly. As a consequence, the distance between the tab and the laser mount was larger than the actual back-focal length of the lens and came to approximately 250-300 μm. During the UV curing, 1.5% of linear shrinkage resulted in a few micrometers of axial displacement of the lens. The defocusing error induced by the shrinkage significantly increased the far field divergence of the beams. As shown in Fig. 6.8, illustrating the emitter resolved far field patterns of the bar before and after curing, the displacement and a slight rotation of the lens caused by shrinkage of the adhesive resulted in significant beam quality degradation.

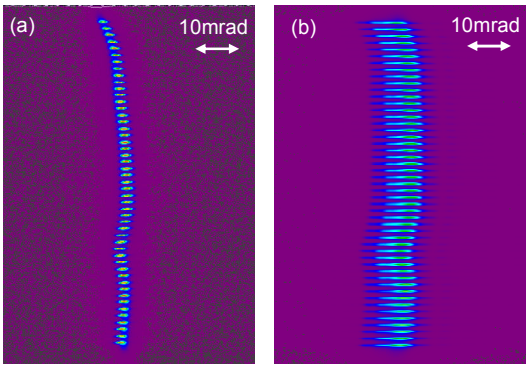


Fig 6.8. Emitter resolved far field pattern of the bar BSM1 with (a) optimally aligned FAC lens, before curing, and (b) the lens displaced after curing.

*Lensing with the Ingeneric lens (bar BSM2)*

The same bar was later re-lensed with the 600 μm focal length Ingeneric lens mounted on the factory-attached mounting tab. The bar was then designated as bar BSM2 from then on. This time, the thin layer of adhesive allowed the shrinkage to have negligible effect on lens alignment. In the lensing performed in an active mode operating near the lasing threshold, the thermal expansion of the laser mount was minimized and the quality of the collimation could be monitored throughout the process. Using this approach. the optimum beam quality was preserved. The beam profile looked like the one shown in Fig. 6.8 (a).

### 6.4.3 Smile error

The smile that is evident in the emitter resolved fast axis far field of the bar BSM2 shown in Fig. 6.8 (a) produced a 6 mrad pointing that corresponds to 3.8 μm of peak-to-valley smile. The non-uniform pointing across the bar results in the widening of the overall far field pattern of the bar, as illustrated later in Fig. 6.12 (b).

## 6.5 Beam quality enhancement in the fast axis direction

### 6.5.1 Compensation of fast axis errors

In this section, the fast axis errors of the single-mode emitter bar (BSM2) lensed with a 600 μm focal length FAC lens are analysed and the performance of the correction with laser-written optics is discussed.

An accurate determination of the fast axis errors was obtained by wavefront sensing measurements performed by the author using the device introduced in Section 4.3. The laser beam was scanned at the plane in close proximity to the collimating lens (~100 μm) with a 5 μm step along the fast axis and a 200 μm step in the slow axis. The measurement provided precise information on the wavefront shape and intensity distribution for each emitter in the bar.

Figure 6.9 (a) presents the intensity distribution in the fast axis for all 49 emitters in the bar. The beam profile reveals some collimation errors that could not be recorded in the lensing procedure performed with the optical imagining configuration described in Section 4.2. In particular, the evident asymmetry and rapid cut-off of one of the edges of the beams caused by the roll error of the collimating lens was not detected during lensing. As a result of the roll error, a fraction of the beam is truncated at the edge of the lens. As the beam continues to propagate, the roll error induces beam distortion appearing as a ‘leaning’ towards one side.

Fig. 6.9 (b) shows the wavefront slope data measured across the bar. For an ideal collimated beam, the slope across the bar would be represented by a horizontal line at zero level corresponding to a pointing direction parallel to the z-axis. Non-zero values of the slope indicate off-axis pointing. The recorded variation of the slope along the 49 emitters corresponds to the 6 mrad angular spread in pointing direction across the bar. The ripples in the wavefront are attributed to the lens imperfections. Lenses with low surface flatness and processing marks can produce wavefront distortions that cause deterioration in the quality of beam of the beams. The λ/4 (peak-to-valley) surface quality claimed by the manufacturers may be sufficient to produce noticeable distortion.

In particular, the cuttings marks left by the rough grinding wheel are not sufficiently smoothed away and lead to diffraction that produces side lobes in the far field. The steep slopes at the edges of the beam are related to the strong deflection by the edges of the lens.

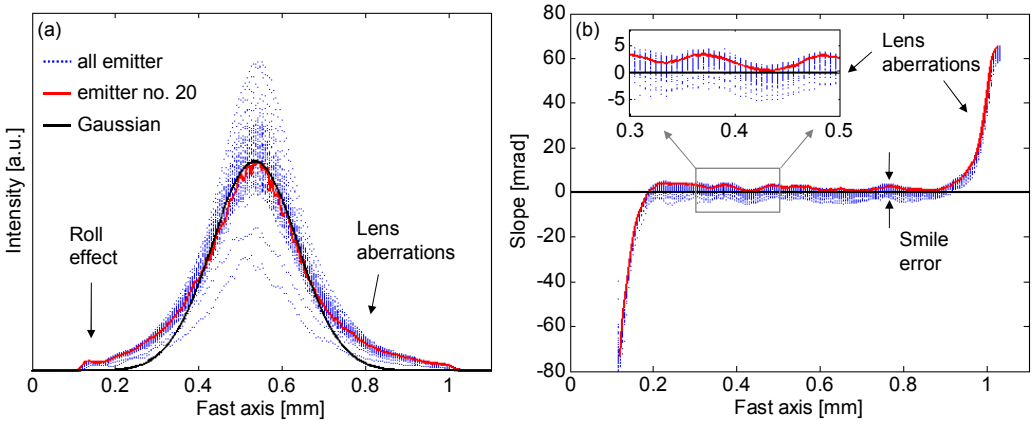


Fig. 6.9. Intensity distribution and slope of the wavefront measured with the wavefront sensor for the 49 single-mode emitters in the bar.

The measured wavefront data was used to design an appropriate corrective surface to compensate the smile error and lens aberrations following the algorithm presented in [17]. Based on the discrete values of the slope, the shape of the wavefront in the fast axis direction $WS_{i,j}$ can be reconstructed using a simple trapezoidal numerical integration method:

$$\mathrm{WS_{i+1,j}} = \mathrm{WS_{i,j}} + \left(\mathrm{step} \cdot \frac{\mathrm{SL_{i,j}} + \mathrm{SL_{i+1,j}}}{2}\right). \tag{6.2}$$

The wavefront deformation for each emitter can be corrected by a refractive surface with local slope values determined by:

$$\mathrm{SL_{i,j}} = \frac{-\mathrm{WS_{i,j}}}{\mathrm{n}-1}, \tag{6.3}$$

where $n$ is the refractive index of silica glass equal to 1.45 and $WS_{i,j}$ are the local wavefront heights. Fig. 6.10 illustrates the wavefront shape for three different emitters in the bar and the shape of the corresponding corrective surfaces.

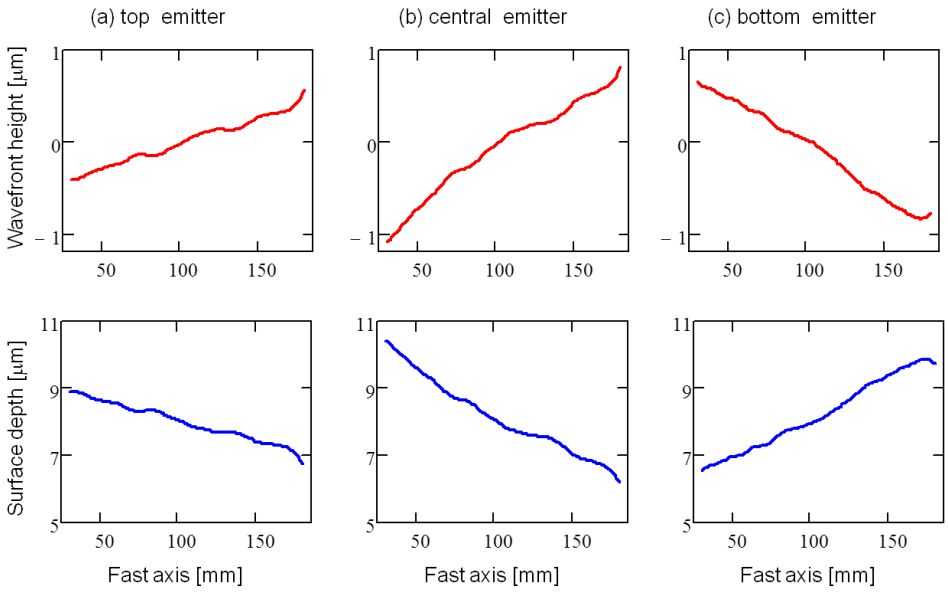


Fig. 6.10. Measured wavefront of a single emitter (top) and a shape of the corresponding corrective surface (bottom).

The corrective surface profiles defined for individual emitters spaced by 200 µm are interpolated in the slow axis direction into the 10 µm step array required for the laser machining process. In this way, a map for the full corrective surface written in silica glass for the bar can be obtained. The map designed for bar BSM2 is presented in Fig. 6.11. Based on this design, the optics was custom-produced by PowerPhotonic Ltd. The low scatter, accurate surface was AR-coated by Helia Photonics Ltd. Applying such a refractive surface eliminates the optical path difference across the beam and results in a significant improvement in the beam quality of the beams.

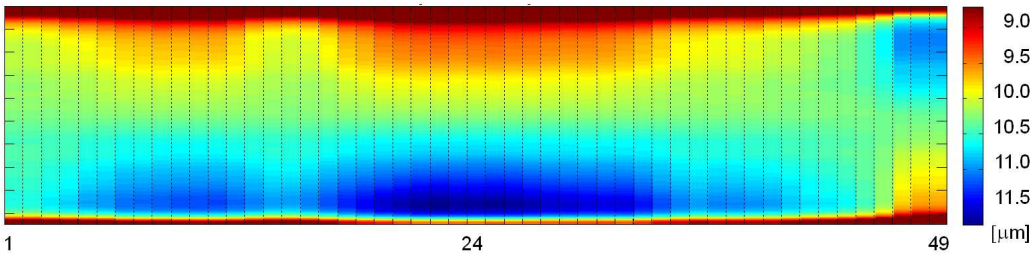


Fig. 6.11. Surface depth map for the corrective optics.

The optical testing of the corrective optics was performed using the optical imaging systems introduced in Section 4.2.1. For illustrative purposes, the emitter resolved far field pattern and a far field pattern of the full bar before correction are presented in Fig. 6.12. Fig. 6.13 shows the same images taken for the bar with the corrective optics placed after the fast axis collimation lens. The pointing error of the bar is successfully compensated and the overall far field divergence of the bar is clearly reduced.

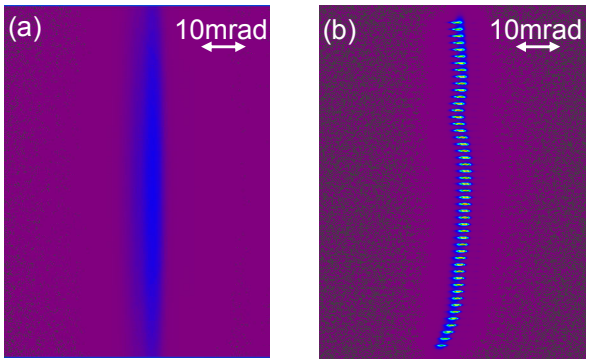


Fig. 6.12. (a) Far field pattern and (b) emitter-resolved far field pattern for bar BSM2 before correction.

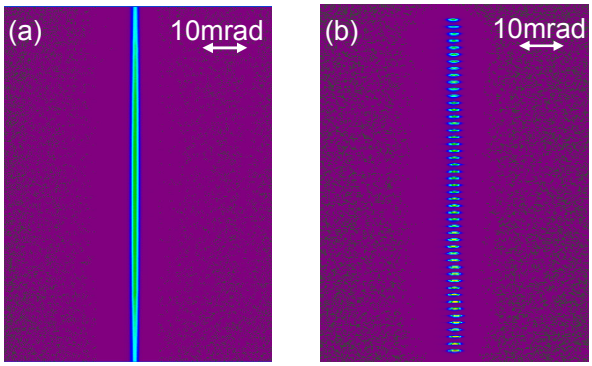


Fig. 6.13. (a) Far field pattern and (b) emitter-resolved far field pattern for bar BSM2 after correction.

The knife-edge curves calculated based from the far field pattern data for the full bar (see Section 4.2.1) are presented in Fig. 6.14, illustrating the beam quality improvement when the fast axis correction is applied. Clearly, the power in the tails is transferred into the main beam, narrowing the beam. The far field divergence is reduced from 3.7 mrad to 2.47 mrad (5-95%). This corresponds to a beam propagation factor value of $M^2$~1.3, assuming a beam width of 600 μm leaving the FAC.

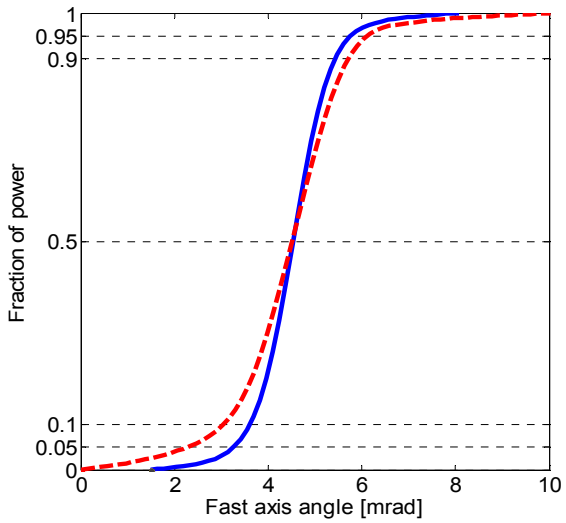


Fig. 6.14. Power in the bucket curves for uncorrected and corrected BSM2 calculated in fast axis direction. Published in [211].

The same correction method was applied to the rest of the bars. Fig. 6.15 presents the emitter resolved fast axis far field patterns of bars BSM1, BSM2, BSM3 and BBA before and after the correction was applied.

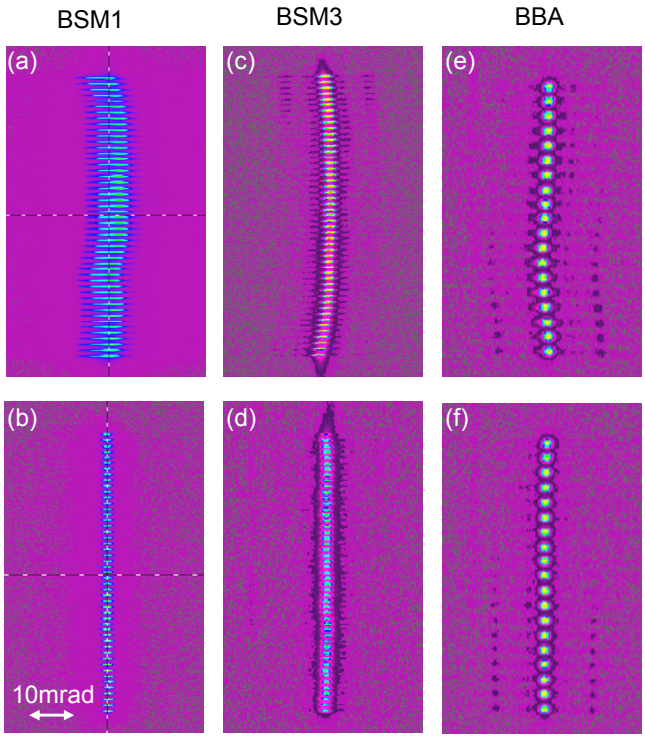


Fig. 6.15. Emitter resolved far field patterns of the bars used in the experiments before (top) and after (bottom) fast axis correction.

In all the cases, the beam quality of the laser arrays was noticeably improved. The results of correction for BSM1 prove that even severe lensing errors can be fully corrected to a uniform pointing beam set with nearly diffraction limited fast axis divergence. The image for the uncorrected broad-area emitter bar (Fig. 6.15 (e)) reveals significant side lobes produced by the aberrations of the fast axis collimating lens. In this case, the fast axis correction was performed at 2.6 mm of physical distance from the laser facet, so the distortion could only be minimized.

### 6.5.2 Pointing accuracy across a corrected bar

To evaluate the performance of the fast axis correction, the pointing variation across the bar was measured with the setup discussed earlier in Section 4.2.1. Fig. 6.16 presents the measured pointing direction of each emitter beam for the uncorrected and corrected bar. The smile-affected beams exhibit a non-uniform pointing distribution matching the emitter resolved far field pattern shown in Fig. 6.12 (b). In the corrected bar, all of the emitters point in the same direction within an RMS error of 3% of the far field divergence of the bar, independent of drive current.

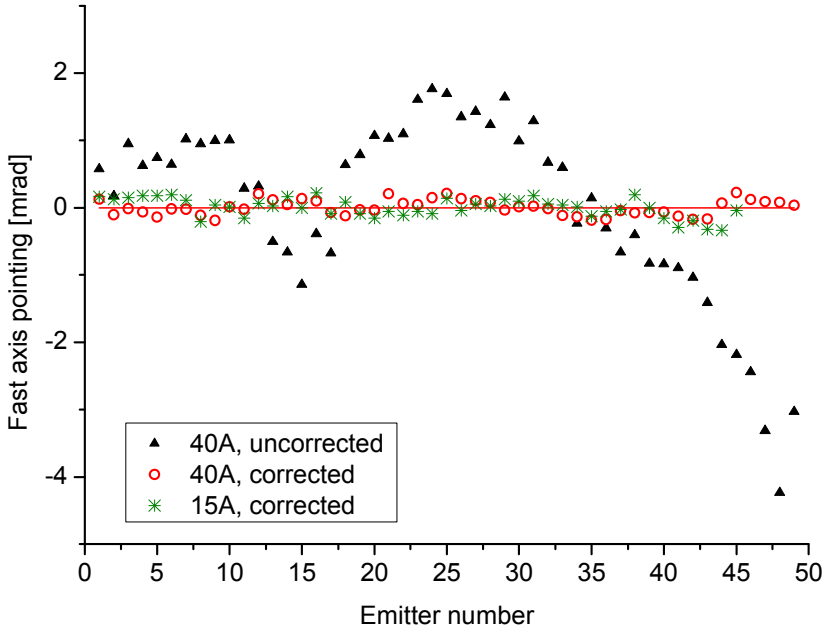


Fig. 6.16. Fast axis pointing direction of individual emitters in the uncorrected and corrected bar.

The fast axis correction efficiently improved the beam quality of the laser bar. A nearly-diffraction-limited beam and consistent pointing across the bar were obtained. It is worth noting that the high performance of the correction was obtained despite the addition of slow axis lenses in the longitudinal direction of the component.

## 6.6 Slow axis collimation with a laser cut lens array

### 6.6.1 Slow axis collimation issues

The single-mode emitter bars used in this project exhibit very interesting, but equally demanding properties in the slow axis direction. The narrow stripe ridge waveguides ensure better beam quality with $M^2$ as small as 1.1. On the other hand, narrow beams exhibit a divergence of 11.2º (full width $1/e^2$), which is considerably higher than the 7-8º (full width $1/e^2$) for a typical broad-area emitter. Additionally, the small emitter spacing of 200 μm imposes stringent requirements on the collimating optics.

To proceed with addressing the collimation issue for the single-mode emitter bars, it was necessary to collect divergence data and investigate the impact of the change of temperature on the chip for the passively cooled single-mode emitter bars. An investigation of the thermal performance of such a bar, with emphasis on its far field divergence is described in the following section.

Once the divergence data for the bars is collected, the focal length of the slow axis lens array must be chosen appropriately to ensure the maximum beam parameter product improvement and to avoid beam overlapping at the plane of the lenses. It will

be shown in Section 6.6.1.2, that it is particularly important to address these two issues for densely packed single-mode beams.

### *6.6.1.1 Slow axis divergence of passively cooled diode laser bars*

For broad-area emitters, an increase in drive current leads to beam quality degradation in the slow axis direction resulting in an increase in slow axis divergence. This is caused by thermally induced non-linear effects in the active area of the lasers. The single-mode ridge emitters with a slow axis dimension of about 6 µm and good optical confinement are expected to provide a lower sensitivity to the change of operating condition. In order to investigate the behaviour of passively cooled single-mode emitter bars, the slow axis far field divergence was measured at different drive current levels.

Fig. 6.17 shows the slow axis far field divergence of the single-mode emitter bar as a function of the drive current compared with the typical behaviour of a broad-area emitter bar.

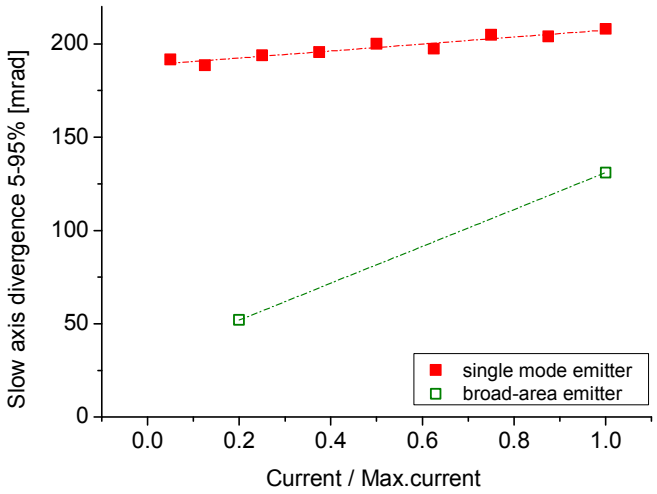


Fig. 6.17. Slow axis divergence vs. drive current measured for an array of 49 single-mode emitters and typical BA bar.

The divergence angle of the single-mode emitter bar increases by approximately 10% throughout the drive current range, reaching 207 mrad (5-95%) at the maximum drive current of 40 A. For the broad-area emitters, the divergence at maximum drive current is of the order of 250% of the divergence close to the threshold. In contrast to broad-area emitters, the slow axis far field divergence of the single-mode emitter bar is locked to the size of the waveguide rather than being dependent on thermal effects in its active area.

### 6.6.1.2 *Slow axis collimation of a closely packed laser diode array*

The slow axis divergence of broad-area emitters can be improved by a factor of two, while the nearly-diffraction limited beam from the narrow-stripe ridge emitters can be effectively collimated if appropriate optics is applied. Efficient slow axis collimation with a standard SAC lens can only be achieved when the fill factor of the bar, defined as emitter size divided by emitter spacing, is less than 0.5. In more demanding cases, using two cylindrical lenses in series in the so called telescope lens arrays may be required [79]. For effective collimation, the focal length of the collimating optics must be significantly larger than the size of the emitter to ensure that the condition $z >> Z_{Rayleigh}$ is satisfied. Optics placed in the near field will not collimate the beam and additionally, may increase the divergence angle. For the single-mode emitters used in this project, the Rayleigh range is very short (<30 μm). Thus, the far field condition will be always satisfied at any distance beyond the fast axis collimating lens.

To avoid power loss caused by light spilling over onto the adjacent element, the collimation must be performed before the adjacent beams begin to overlap. Fig. 6.18 shows a scheme of slow axis collimation of a laser bar with the fast axis lens attached. Fig. 6.18 (a) illustrates a correct approach in which a slow axis lens array is placed close enough to collimate the beams before they begin to overlap. Fig. 6.18 (b) shows a case in which the beams begin to overlap before they reach the slow axis collimating lenses.

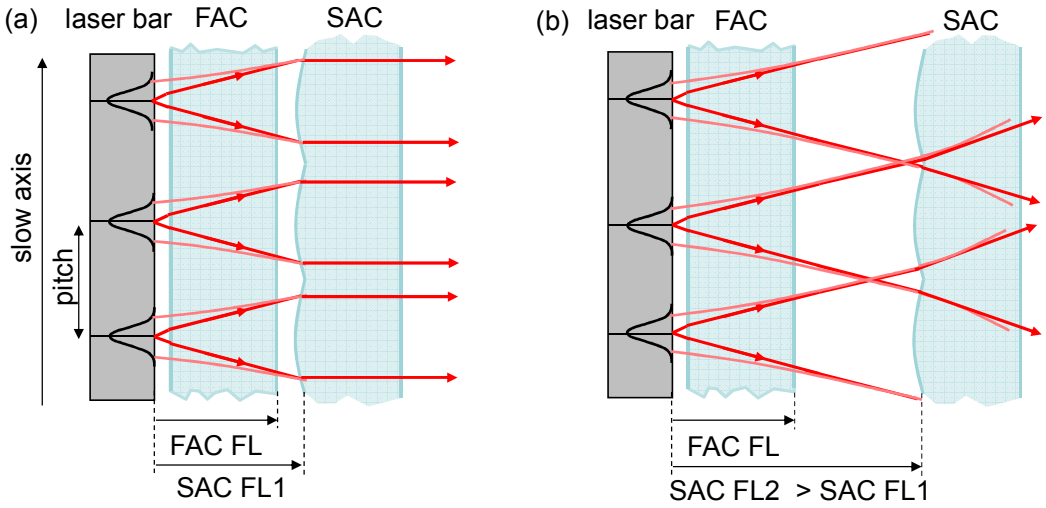


Fig. 6.18. Slow axis collimation scheme for (a) correctly attached slow axis collimating lens array and (b) for the SAC lens array placed after the overlapping distance of the laser beams.

The fraction of the light that spills over to the adjacent lenses is scattered at the edges of the lenses and contributes to the side lobes in the far field. In a beam combining system, the scattered light is most likely to be cut off, leading to undesired power loss, as seen in [141]. The minimum applicable focal length of a slow axis lens is

defined by the effective focal length (EFL) of the fast axis collimator. Additionally, under typical conditions the attachment of the optics may require further spacing from 100 μm up to 700 μm (see Section 6.4.1.2).

For typical cases of 400 or 500 μm pitch bars, there is a range of collimation optics that allows the fraction of power sent through the lens joints to be minimised by choosing a sufficiently small FAC lens and matching the focal length of the SAC lens array to reach the non-overlapping distance. For a given divergence angle, the smaller the pitch, the shorter is the distance at which the beams begin to overlap. This makes it more difficult to achieve efficient slow axis collimation. Fig. 6.19 illustrates how the acceptable focal length of the slow axis collimating lenses differs between commercially available sources, including typical broad-area emitter bars with 19 and 25 elements with a slow axis divergence of 7-8º (full width at $1/e^2$) and an array of 49 single-mode emitters with slow axis divergence above 12º (full width at $1/e^2$). The estimated power contained within the aperture of a slow axis collimating lens is plotted as a function of the distance between the lenses and the laser facet for typical diode laser bars. The intensity distribution at the plane of the lens was calculated based on Gaussian beam propagation. The apertures of the lenses were assumed to be equal to the emitter spacing, neglecting the fact that the value of the useful aperture for a typical micro-lens is in the range 90-95%. Depending on the size of the emitters and the $M^2$ value in the slow axis direction, each case presented in Fig. 6.19 must be considered separately.

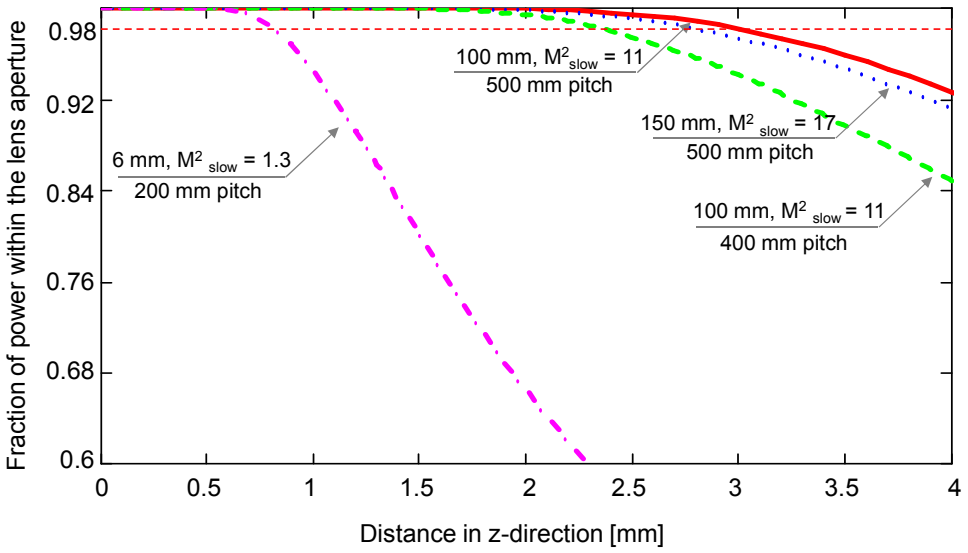


Fig. 6.19. Estimated power contained in the aperture of a slow axis collimating lens as a function of distance.

For typical broad-area emitter bars, the distance at which 100% of power is contained within the lens aperture is extended up to 2 mm. This defines the maximum

distance at which the lens can be placed without beam truncation. The range of typical focal lengths for fast axis collimation is 600-2500 μm and an appropriate range of SAC lens arrays with 400 or 500 μm pitch are also commercially available. Thus, the range of standard micro-optics sufficiently matches the requirements for the effective slow axis collimation of typical broad-area bars. However, the choice for focal length for slow axis collimators for the 200 μm pitch single-mode emitter bar is limited. As shown in Fig. 6.19, despite their good beam quality in the slow axis, the beams of the 6 μm aperture emitters already begin to overlap at a distance of 700 μm. The predicted overlap distance was confirmed experimentally by intensity scans performed at several distances from the laser facet using the wavefront sensing device introduced in Section 4.3, here adapted as a scanning beam profiler. The limited non-overlapping distance is due to the small spacing between the emitters and their high divergence angle, which was measured to be 207 mrad (5-95%) at 40 A (see previous section).

For the bar with a FAC lens attached in-house to the 0.8 mm mounting tab (see Section 6.3), an array of 700 μm focal length lenses was designed and tested. For the bars lensed with the FAC lens on a standard 1 mm thick tab, SAC arrays with 850 μm and 900 μm focal lengths were used. The impact of beam overlap and truncation by the aperture of the lenses for these cases is further investigated in the section on the optical performance of laser-written collimation lens arrays (Section 6.5.3).

### 6.6.2 Laser-written lens arrays

The F-numbers for 200 μm aperture lenses with 700 μm and 900 μm focal lengths were 3.5 and 4.5, respectively. Micro-lenses with such low F numbers are difficult to produce with conventional manufacturing techniques and the commonly used photolithography technique can be expensive when a low F number lens with custom array pitch is needed. In this work, the arrays of such lenses were produced by the laser cutting and polishing process introduced in Chapter 2.

The slow axis collimators were designed as arrays of combined plano-convex cylindrical lenses with a parabolic profile with a radius of curvature equal to:

$$R = f \cdot (n_0 - 1), \tag{6.4}$$

where $f$ is the effective focal length of the lens and $n_0$ is refractive index of silica glass which is equal to 1.451. The shape of the lens will be then described by:

$$G(x) = \frac{x^2}{-2 \cdot R}. \tag{6.5}$$

The design of the small 200 µm pitch micro-lens arrays requires careful consideration when it is to be produced with a laser cutting technique. In particular, the deep edges of the lenses are difficult to reproduce in the cutting process, where the size of the beam of approximately 30 µm is comparable with the size of the feature itself. As shown in Fig. 6.20, for a given lens aperture, the shorter the focal length of the lens, the larger sag is required and the steeper the edges of the lenses are.

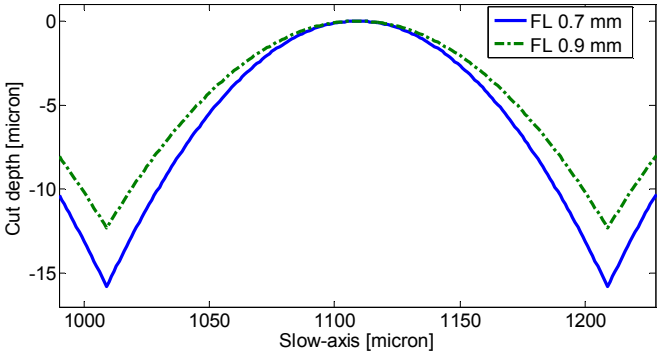


Fig. 6.20. Designed profile of a single slow axis collimating lens in a lens array.

A lens with a 700 µm focal length requires a depth modulation of about 16 µm and imposes high requirements on the laser cutting process. Figures 6.21 and 6.22 show typical shape deformations of laser cut cylindrical lenses for the two cases.

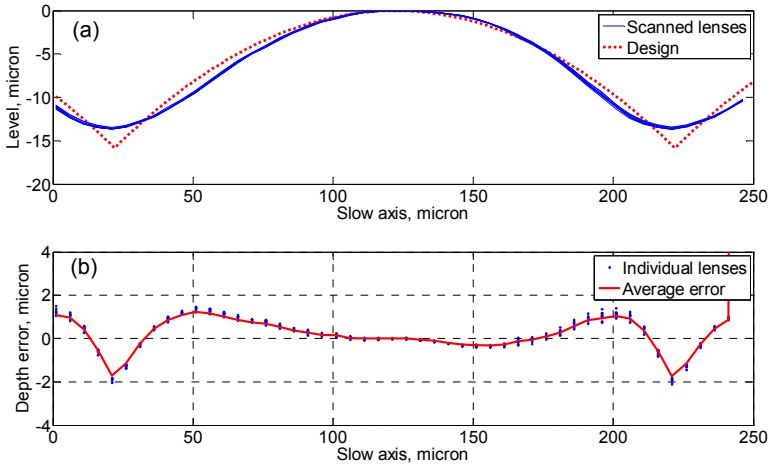


Fig. 6.21. Cross-section of individual lenses in the lens array (focal length 700 µm) scanned with a high accuracy profilometer (SCANTRON) (a) and the depth error across the lenses (b).

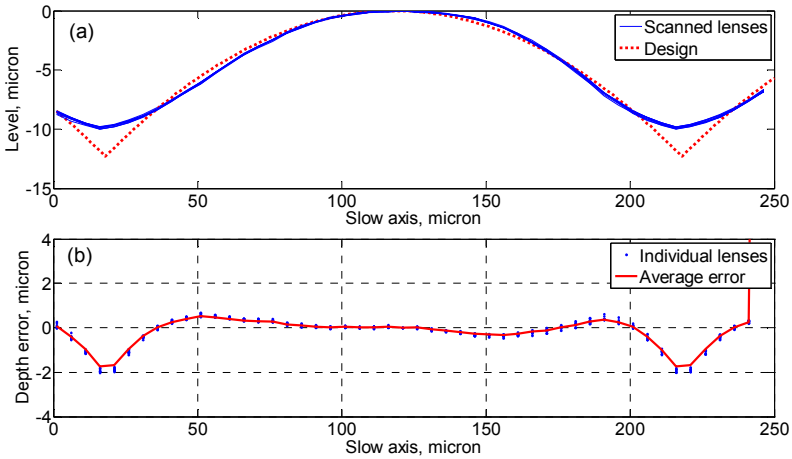


Fig. 6.22. Cross-section of individual lenses in the lens array (focal length 900 μm) scanned with a high accuracy profilometer (SCANTRON) (a) and the depth error across the lenses (b).

The laser smoothing process that was employed reduced the local surface roughness to less than 10 nm, as measured with an AFM. Thus, the scattering by the laser-written optics is negligible, and the shape accuracy is most critical for the performance. It is evident that the laser cutting/smoothing technique produces rounding of the desired sharp structures at the joint. For the small 200 μm pitch micro-lens array, it is particularly important to avoid light scattering` at the joints and to minimize the dead-spaces between the lenses. Moreover, the ascending slopes (defined with respect to the cutting direction, as marked in Fig. 6.21 and Fig. 6.22) exhibit a slight undercut, while the descending slope suffers from some excess of the material. This results in an asymmetric shape of the lens, which can lead to beam deformation.

The work on the improvement in the shape in the lenses was performed in collaboration with Dr Josef J. Wendland from PowerPhotonic Ltd. The cross-section of the lens array with a corrected shape is presented in Fig. 6.23. The deviation between an actual optical surface and its designed surface is plotted in Fig. 6.23 (a). The red line corresponds to the depth error distribution averaged over the full lens array (55 lenses). For the 900 μm focal length lens, the size of the dead spaces was reduced resulting in an active lens width of about 170 μm for each lens with a maximum phase error of about λ/4 (peak-to-valley).

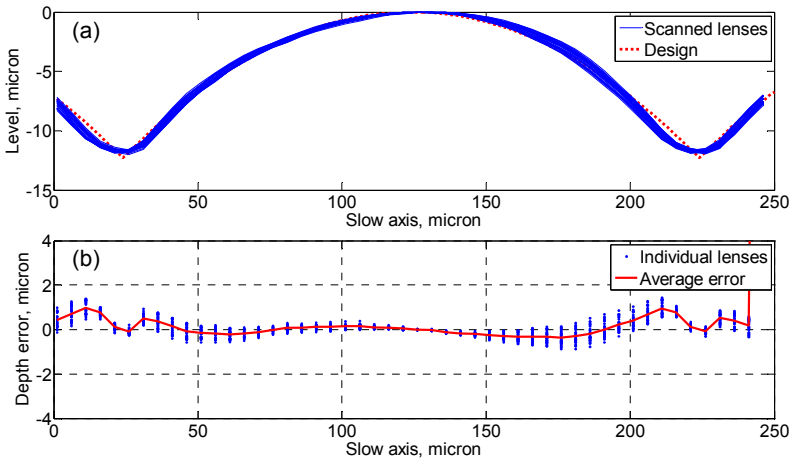


Fig. 6.23. Cross-section of the lens array (focal length 900 μm) scanned with a high accuracy profilometer (SCANTRON) (a) and the depth error across a single lens (b).

Although the corrected shape of the lenses is noticeably improved, further enhancement can still be achieved. For a better correction method, the depth error distribution should be obtained based on exactly the same type of structure so that it would account for the depth of the cut surfaces.

The accuracy of the focal length obtained for the lenses is well controlled. The focal length calculated based on profiles of the 50 lenses varies by less than 2% of the designed value.

## 6.7 Optical testing of laser-written SAC lens array

The laser-cut lens arrays were optically tested with the bars described in Section 6.3. For each case the intensity distribution in the far field was recorded with the setup presented in Fig. 4.2. The laser-written lens array was placed in front of the laser and aligned to the optimal position with a set of adjusters. Fig. 6.24 shows the far field patterns of the bars with the refractive optics that combines the fast axis correction with a slow axis collimating lens array. The far field patterns in Fig. 6.24 (a) and 6.24 (c) correspond to single-mode emitter bars collimated with a 200 μm pitch SAC array with focal lengths of 700 μm, 850 μm and 900 μm, respectively. The pattern in Fig. 6.24 (d) is produced by the broad-area emitter bar with a 500 μm pitch SAC array with a 2.2 mm focal length. As mentioned in the previous section, the slight beam truncation on the edges of the lenses produces asymmetric tails in the far field. For the single-mode bars, the effect appears to be stronger for the lens with the longer focal length. The beams in the 49 single-mode emitter bar begin to overlap at a reduced distance from the laser facet of about 700 μm. This results in the beam truncation by the edges of the lenses

when the 900 μm focal length collimation optics is used. In each case, however, the amount of power contained in the tails was estimated to be less than 10%.

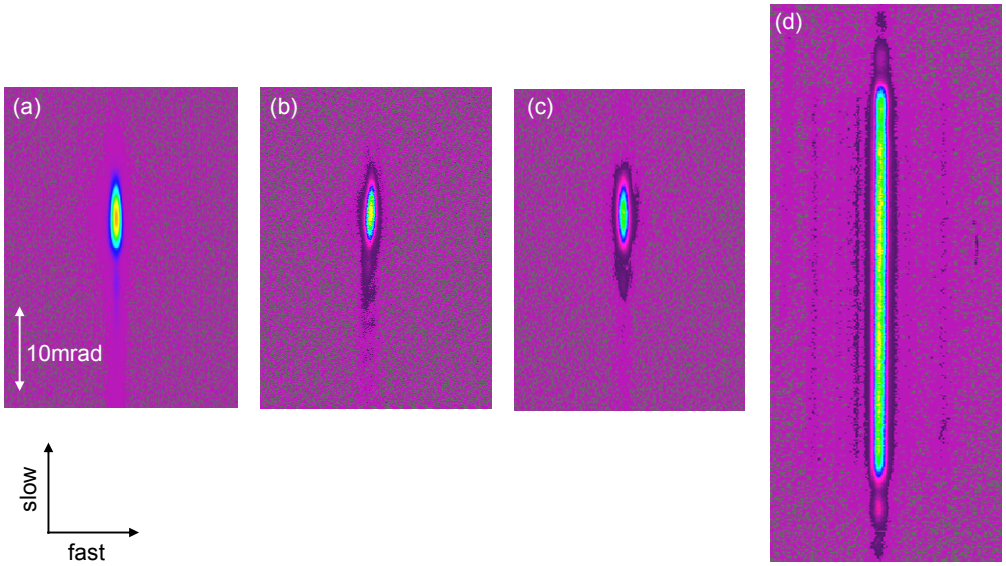


Fig. 6.24. Far field patterns of the bars with laser-written optics for fast axis correction and slow axis collimation: (a) bar BSM1 with 700 μm FL SAC array, (b) bar BSM2 with 900 μm FL SAC, (c) bar BSM3 with 850 μm and (d) bar BBA with 2200 μm FL SAC.

To illustrate the impact of beam truncation for lens arrays placed at different distances from the laser, Fig. 6.25 presents the power in the bucket curves measured for the full bar with 700 μm and 900 μm focal length lenses.

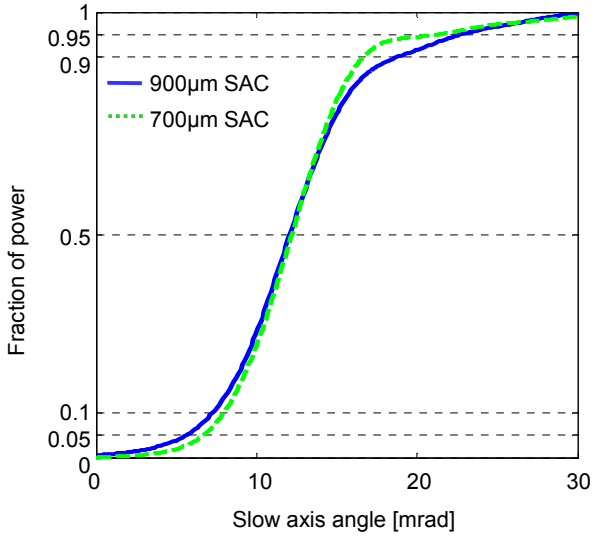


Fig.6.25. Slow axis knife-edge graph comparing slow axis collimation for a bar lensed with 700 μm (BSM1) and 900 μm (BSM2) focal length lenses.

Clearly, for the longer focal length, a larger fraction of the power is transferred into the tails in the far field. However, even for this case, a satisfactory slow axis far field divergence of about 17 mrad was obtained (full width at 5-95%).

### 6.7.1 Pointing accuracy in the slow axis direction

Following a procedure similar to the one used for the evaluation of the fast axis correction, the pointing accuracy in the slow axis direction was investigated for the laser-written slow axis collimation lens arrays. The single-lateral mode emitter bar is a very suitable source for detailed analysis of the accuracy of the slow axis collimation. Good beam quality in the slow axis direction allows the detection of very small changes in the pointing directions of the individual emitters.

#### *6.7.1.1 Effect of pitch mismatch between a bar and the slow axis collimation lens array*

The slow axis pointing direction for each emitter in bar BSM2 was recorded in the setup shown in Fig. 4.5. This allowed the pointing direction of each emitter in the bar to be measured individually. Figure 6.26 plots the slow axis pointing angle as a function of emitter number. Emitters are numbered from the bottom of the bar. A positive pointing angle means pointing downwards.

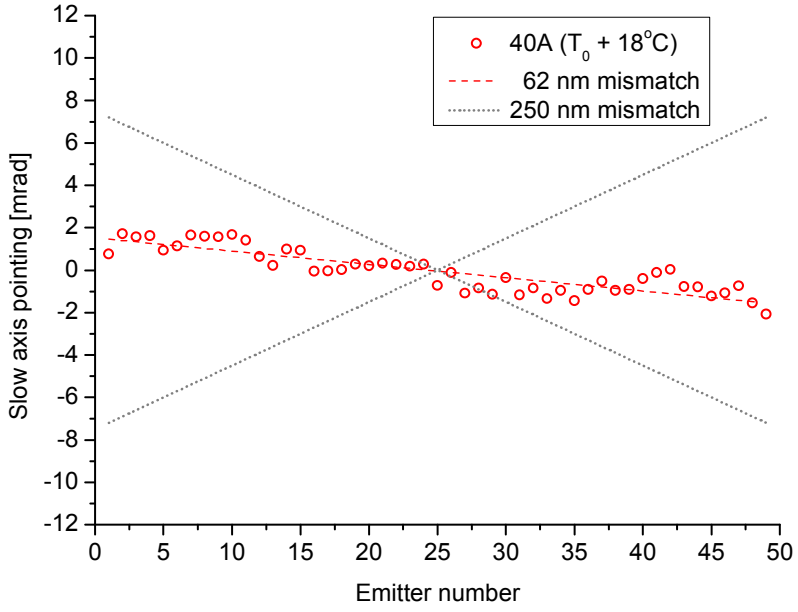


Fig.6.26. Measured slow axis pointing error (red) and estimated pointing error corresponding to the pitch mismatch of 250 nm (blue) between the laser bar and the 200 µm pitch 900 µm lens array (BSM2). The slow axis divergence recorded during the experiment was 21.4 mrad (5-95%).

The measurement revealed a small slow axis pointing angle variation along the bar, following a sloping trend line. The observed variation can be explained by a slight pitch mismatch between the laser bar and the lens array. The explanatory drawing in Fig. 6.27 illustrates what happens when the pitch of the lens array is bigger than the pitch of the laser bar. While the middle emitter in the bar is co-aligned with the midpoint of the corresponding lens, the bottom emitters are located above the lens

centre and the top emitters are placed below the lens centre. As a consequence, for the vertically mounted bar, the upper emitters point upward and the lower emitters point downward as if the overall laser beam was slightly diverging.

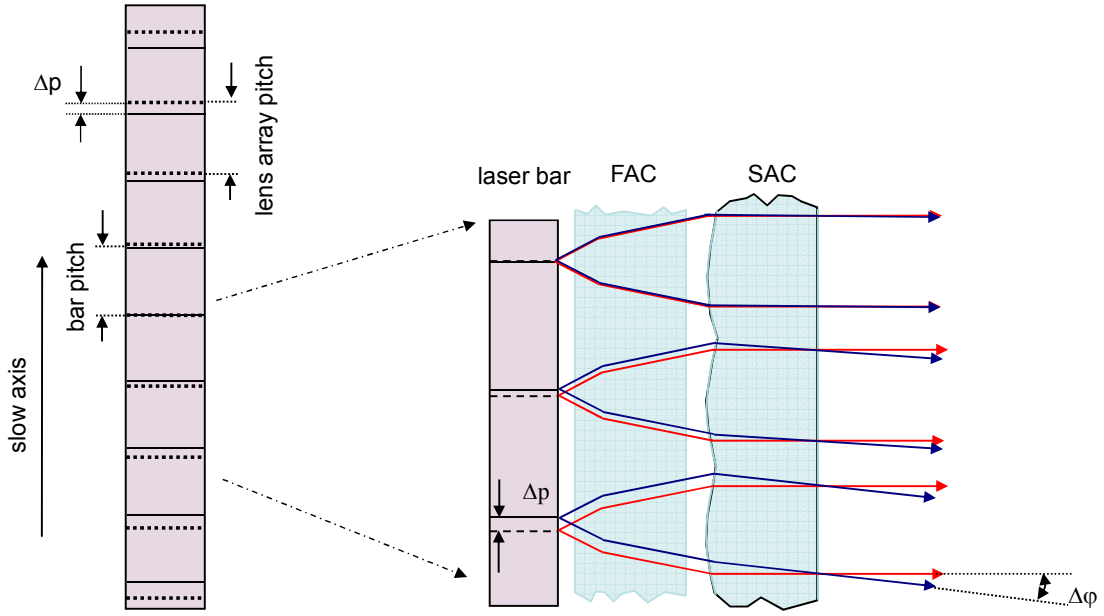


Fig.6.27. Explanatory drawing for pointing error caused by a slight pitch mismatch between the lens array and the laser bar. Picture adapted from [213].

The small change of pointing direction $\Delta\varphi$ is determined by the relative displacement between the centres of the emitters and the midpoints of the corresponding lenses. The pointing error for individual beams along the bar can be estimated based on:

$$\Delta\varphi \cong \frac{\Delta p}{f}, \tag{6.6}$$

where $\Delta p$ is the displacement of the laser beam with respect to the midpoint of the lens, and $f$ is the focal length of the slow axis collimating lenses. The pointing errors measured for the bar with the 900 µm focal length laser-written SAC lens array shown in Fig. 6.26 ranges from -2 mrad to 2 mrad for the end emitters. Following the relationship in Eq. 6.6, the displacement of the end emitters is calculated to be 1.8 µm. This corresponds to a 60 nm pitch mismatch, which is only 0.03% of the pitch. For comparison, the shaded area in Fig. 6.26 represents the range of pointing error predicted for the case of ±0.25 µm of pitch difference between the bar and a 200 µm pitch lens array that is typically offered by the providers of slow axis lens arrays. This level of pitch mismatch can produce an angular spread as large as 14 mrad. This shows that the mismatch effects that could be detected are considerably smaller than the accuracy offered by commercial providers.

The observed pitch mismatch could arise from encoder calibration errors in the X-Y tables used for the laser cutting of the optics or from mask magnification calibration errors in the chip processing. The chip bonding stress which tends to compress GaAs relative to the copper base can also contribute to the final emitter spacing. At this stage, it is difficult to offer an unambiguous explanation for what causes the mismatch. However, a better understanding of how it affects the performance of slow axis collimation can be gained by investigation of the change of the pointing direction at different operation conditions presented in the next section.

### *6.7.1.2 Effect of thermal expansion on the slow axis collimation*

The expansion of the laser bar can contribute to the relative position of the midpoints of the lenses and the individual emitters. The expansion of the silica glass is negligible. At 40 A drive current, the pitch of the lens array was found to be slightly larger than the emitter spacing (see previous section). Intuitively, a lower drive current (or temperature of the coolant) will produce less thermal expansion of the bar and consequently increase the pitch difference between the bar and the lens array. To obtain confirmation of this hypothesis, the pointing error at different operating conditions was measured. The high resolution spectrometer (0.5 m SPEX) introduced earlier in Section 4.2.2 was used to estimate the change of the chip temperature, based on the thermal wavelength tuning effect. A comparison of two cases with 15 A and 40 A values of drive current is illustrated in Fig. 6.28. The temperature change corresponding to the change of current was $\Delta T = 18$ºC.

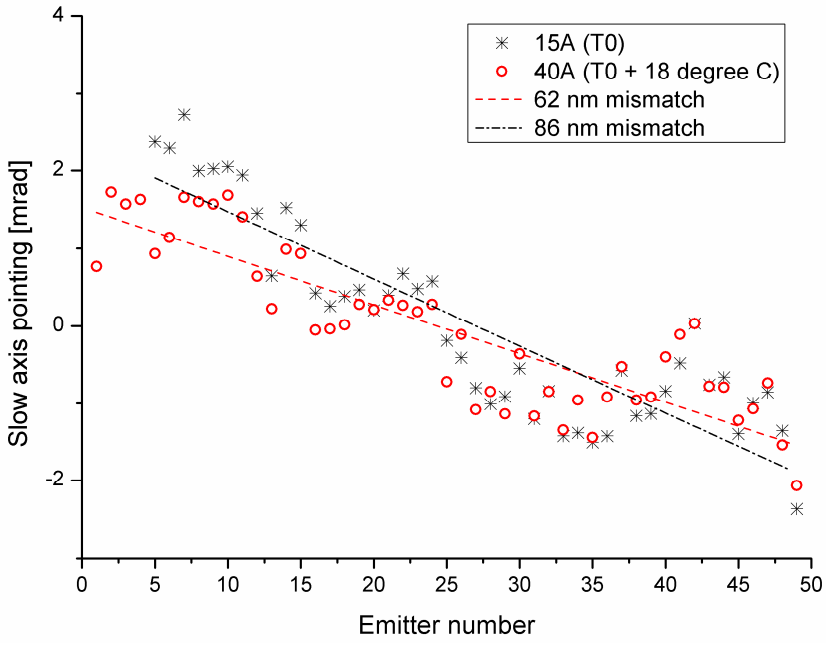


Fig.6.28. Slow axis pointing error measured at $T_0$ (black) and $T_0 + \Delta T$ (red). The slow axis divergence recorded during the experiment was 21.4 mrad (5-95%). Adapted from [213].

As expected, a decrease in the temperature consolidated the effect of pitch mismatch. The relative pointing error of the emitters increased with a decrease of the drive current. The corresponding change of the pitch mismatch was 24 nm which is equivalent to an 0.012% change in the emitter spacing. A change of the temperature of 18ºC is expected to increase the emitter spacing by 0.0103% for the thermal expansion coefficient of GaAs of $5.73 \cdot 10^{-6}$ $K^{-1}$. This agrees with the detected change in relative alignment between the bar and the lens array. It should be noted that the bar is mounted on a copper sub-mount, which is then attached to a copper passive heat exchanger, so the linear thermal expansion is likely to be slightly higher than for free GaAs.

The pointing errors along the bar caused by temperature dependent pitch mismatch are still within 10 % of the far field divergence. When the pitch mismatch effect is subtracted, the RMS pointing error along the bar remains low at a value of 6 % of the far field divergence. This is considered to be a very satisfactory result obtained with the laser-written optics technique. For further improvement, the fixed pitch error can be corrected by the use of a weak positive cylindrical lens, or in the future by a small modification of the design for the custom lens array.

## 6.8 Summary

In the work presented in this chapter, the flexibility of the laser machining technique that provides arbitrarily shaped refractive surfaces with low scattering loss was used to provide a single optical component that combines a corrective surface for the wavefront errors with compensation in the fast axis and an accurate slow axis collimation. To the knowledge of the author, this is the first time when laser-written optics has been used to provide ultra-collimation in both axes for full size laser diode bars.

This flexible laser writing technique is an attractive alternative to conventional optical manufacturing techniques, such etching, replication, molding or grinding. Unlike any of these techniques, it is capable of cost effective production of custom focal length, small pitch lens arrays with simultaneous correction of the fast axis errors. The customisation of the focal length lens array allows the slow axis fill factor to be optimised and the power loss due to collimation to be minimised. The technique proves to be particularly useful for small pitch bars, which impose stringent requirements on the collimating optics. It has addressed collimation cases for which the commercial solutions were not easily available at the time when the work was performed. The technique is very beneficial for single-mode bars and could also be applied to tapered

emitter bars [55, 214, 215] or SCOWLS [58, 216], where nearly-diffraction-limited optics would be very attractive for brightness scaling experiments.

In this chapter, the use of dual-axis refractive optics was demonstrated for 49-single-mode emitter bars with a 200 μm pitch and for a standard 19-broad-area emitter bar. Optical testing with a single-mode emitter bar revealed good pointing accuracy in both directions. The process of smile compensation is clearly unaffected by the addition of the slow axis collimation functionality to the refractive optics showing that the two processes are unambiguously additive. A low value of the fast axis RMS pointing error (3% of the far field full-angle divergence) has been achieved. Accurate slow axis collimation turns out to be optically demanding due to the thermal expansion and bonding-induced deformation of the laser chip. A temperature-dependent pitch mismatch between the laser chip and the slow axis collimation silica lens was observed to produce a linear variation of the pointing angle. At full operating current, the mismatch pitch of about 0.03% of the 200 μm pitch is still much smaller than the tolerances offered by commercial microoptics providers and the overall pointing angle variation was less than 10% of the beam divergence. The RMS pointing angle varies within 6% of the far field divergence angle when the pitch mismatch effect is subtracted. As a result of this work, an array of highly parallel beams was obtained with 5-95% full-width far field divergence angles of 2.47 mrad and 17 mrad in fast and slow axis directions, respectively.

Good control of the spatial properties of laser diode arrays is crucial for further development of brightness improvement techniques including spatial multiplexing, external cavity feedback methods, and high resolution wavelength combining. The results presented in this chapter show that laser-written optics provides an effective solution for difficult collimation cases, such as that encountered in Chapter 5, where the dual axis optics could significantly improve the performance of the beam formatting. In the following chapter, it is also shown that accurate dual-axis collimation enhances the performance of wavelength locking in an external cavity configuration with a volume holographic grating.

# Chapter 7.
# Enhanced wavelength locking of ultra-collimated diode laser bars using Volume Holographic Gratings

## 7.1 Introduction

Volume holographic gratings (VHGs) offer attractive solutions for wavelength control and spectral beam combining of diode lasers. They surpass conventional diffraction gratings with their low thermal expansion, high spectral selectivity, low absorption and high customizability (see Chapter 3). However, as with dispersive gratings, the performance of VHGs can strongly depend on the spatial properties of incident laser beams. In particular, in a VHG-based external cavity diode laser array (ECDLA) configuration, the smile-induced fast axis pointing errors of a bar are translated to a non-uniform distribution of the optical feedback along the bar. It will be shown in this chapter that sufficiently large pointing errors can significantly limit the amount of feedback received by an emitter and obstruct wavelength locking [210]. Due to the reduced feedback, full locking of all emitters in a bar can be limited to a narrow range of temperatures [67]. When uniform feedback across the laser bar is obtained, full locking can be achieved even with a low reflectivity VHG, bringing the potential for loss reduction in the system. Thus, the reduction of the smile effect is necessary to enhance the performance of VHG-locking for laser bars.

In this work, the laser-written dual-axis optics technique, introduced in Chapter 6, is used to provide excellent spatial properties of a laser diode bar, so that it is possible to operate feedback from volume holographic gratings under ideal illumination conditions. As opposed to previously reported techniques used for smile compensation, such as a tilted cylindrical lens [69] or a compound external cavity as in [217], the technique used here does not reduce the compactness and flexibility of the optical system.

The results presented in this chapter will also demonstrate that the use of slow axis collimation (SAC) significantly increases the level of feedback in an external cavity configuration. The issue of beam truncation by the collimation optics, particularly for small pitch SAC-arrays, will be also addressed, as it leads to reduced feedback and increased power loss in external cavity configurations.

The advantage of smile-correction and ultra-collimation for wavelength locking is demonstrated for high brightness single-mode emitter bars as well as for standard broad-area bars. The laser bars used in this chapter are a 49 single-mode emitter bar (BSM2), a 49-single-mode emitter bar with low reflectivity on the front facet (BSM3) and a 19 broad-area emitter bar (BBA).

During one of the parallel experiments bar BSM2 died due to excessive feedback from a 40% reflectivity grating. Thus, some of the measurements for this bar could not be completed.

The VHG used in this chapter has 15% reflectivity and 200 pm bandwidth. The grating was provided by Ondax Inc. The performance of VHG-locking for the two types of bars was analysed for different collimation conditions. In both cases, full locking over the range of temperatures available in the experiment could be maintained independently of the distance between the laser bar and the VHG, when dual-axis corrective optics were used for fast axis correction and slow axis collimation.

This chapter is organised as follows. Section 7.2 raises the issue of feedback reduction in an external cavity configuration. For a better understanding of mechanisms of feedback loss, both the effective reflectivity of a VHG and the impact of pointing errors and beam truncation are discussed. Section 7.3 presents a comprehensive spectral analysis approach used in the experiments on VHG-locking. The spectral properties of free running bars are examined to provide a base for further investigations on wavelength locking. Finally, Section 7.4 presents the results on VHG-locking of the two types of bars and discusses the improvement of the performance of the ECDLAs with dual-axis refractive optics.

## 7.2 Effective feedback in an external cavity laser diode array with a VHG

The effective feedback is defined here as the fraction of light that is efficiently coupled back to the fundamental mode of the laser waveguide. In an external cavity configuration with a reflective volume holographic grating (see Fig. 7.1), the feedback is determined by the effective reflectivity of the VHG used and the losses and distortion induced by the optics in the cavity, which prevent the reflected light from being fully coupled to the fundamental mode of the laser.

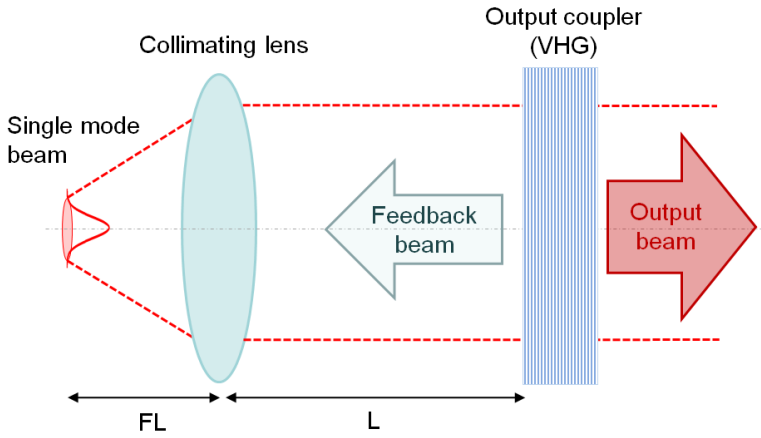


Fig. 7.1. Scheme of an external cavity configuration.

### 7.2.1 Reflectivity of the VHG

The amount of light diffracted by a VHG strongly depends on the angular and spectral properties of the beam, as discussed in Chapter 3. Fig. 7.2 shows the spectral and angular selectivity graphs for the VHG used in this chapter, which were calculated in the same manner as discussed in Section 3.4.2.

The grating has a 200 pm FWHM bandwidth and 15% maximum diffraction efficiency at normal incidence. The FWHM angular selectivity is approximately 2.4 degrees.

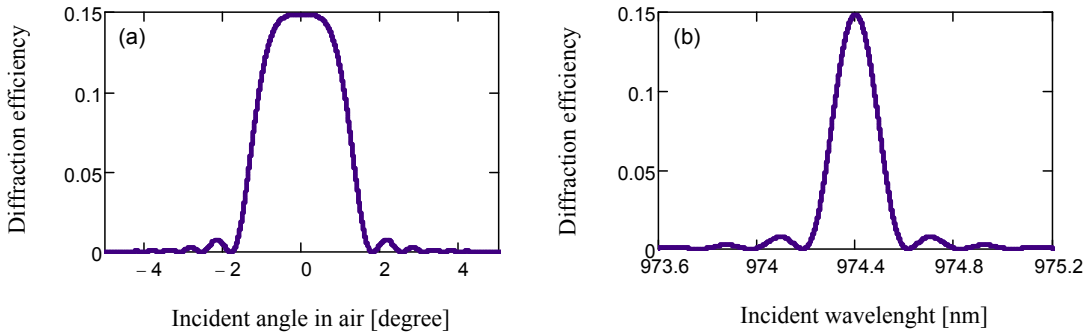


Fig. 7.2. (a) Angular selectivity and (b) spectral selectivity graphs for the VHG used in the experiments.

The shape of the selectivity graphs determines what fraction of a polychromatic diverging beam is reflected from the VHG. This has been widely studied in the literature [117, 218] and discussed in Section 3.4. The remaining question is how much of the grating reflection can be fed back to the emitters. In order to address this question, the feedback factor associated with losses in the external cavity is estimated in the following section.

### 7.2.2 Feedback factor associated with losses on the collimating optics

In order to determine the reduction of feedback due to losses in the collimation optics, the propagation of a single-mode beam in an external cavity configuration was investigated. In a real case, the amount of light that is fed back to the emitters depends on the geometry of the cavity, the quality of the beams as well as lens aberrations and defocus. In this work, only a simplified model of beam propagation was used to estimate the level of feedback in an external cavity. The first approximation assumes the paraxial propagation of a Gaussian beam in an ABCD optical system. The model accounts for smile induced pointing error and beam truncation by the apertures of the collimating lenses. For simplicity, $M^2$ was assumed to be equal to 1. Lenses are assumed to be thin and aberration-free, and aligned at the focal length from the facet of the laser.

A single transverse mode beam is presented as a fundamental mode Gaussian beam and can described by a complex radius of curvature $\tilde{q}$ related to the spot size *ω(z)* and radius of curvature *R(z)* by [219]:

$$\frac{1}{\tilde{q}} = \frac{1}{R(z)} - j \cdot \frac{\lambda}{\pi \cdot \omega^2(z)}, \tag{7.1}$$

where $\lambda$ is the wavelength of the beam. The propagation law for this parameter can be written as:

$$\tilde{q}(z) = \frac{A \cdot \tilde{q}_0 + B}{C \cdot \tilde{q}_0 + D}, \tag{7.2}$$

where the A,B,C and D are elements of the ABCD matrix of the optical system, and $\tilde{q}_0$ is the initial value of the complex radius of curvature defined as:

$$\tilde{q}_0 = j\frac{\pi \cdot \omega_0^2}{\lambda} = j \cdot Z_R, \tag{7.3}$$

where $Z_R$ is the Rayleigh range of the beam and $\omega_0$ is the radius of the beam waist radius (at z = 0). Based on the new value of complex radius of curvature, the new beam spot size and radius of curvature of the beam can be obtained from:

$$\omega'(z) = \sqrt{\frac{-\lambda}{\pi \cdot \mathrm{Im}\left(\frac{1}{\tilde{q}(z)}\right)}}, \tag{7.4}$$

and

$$R'(z) = Re\left(\frac{1}{\tilde{q}(z)}\right). \tag{7.5}$$

The system under consideration contains a collimating lens with focal length f ($f_{FAC}$ = 590 μm in the fast axis direction and $f_{SAC}$ = 900 μm in the slow axis direction) and an output coupler, as shown in Fig. 7.1. A ray transfer matrix for the round trip back to the collimating lens is given by:

$$\mathrm{M_{ext}} = \begin{pmatrix} \mathrm{A} & \mathrm{B} \\ \mathrm{C} & \mathrm{D} \end{pmatrix} = \begin{pmatrix} 1 & 2\cdot\mathrm{L} \\ 0 & 1 \end{pmatrix} \cdot \begin{pmatrix} 1 & 0 \\ \frac{-1}{\mathrm{f}} & 1 \end{pmatrix} \cdot \begin{pmatrix} 1 & \mathrm{f} \\ 0 & 1 \end{pmatrix} = \begin{pmatrix} \frac{\mathrm{f}-2\cdot\mathrm{L}}{\mathrm{f}} & \mathrm{f} \\ \frac{-1}{\mathrm{f}} & 0 \end{pmatrix}, \tag{7.6}$$

where $L$ is the external cavity length and $f$ is the focal length of the collimating lens.

Using the propagation law described by equation 7.2, the amplitude of the Gaussian beam at the plane of a collimating lens can be calculated. The amplitude of the initial beam can be written as:

$$\tilde{\mathrm{u}}_0(\mathrm{x}_0) = \sqrt{\frac{1}{\omega_0}\sqrt{\frac{2}{\pi}}}\exp\left[\frac{-(\mathrm{x}_0-\mathrm{x}_\mathrm{s})^2}{{\omega_0}^2}\right], \tag{7.7}$$

where $x_s$ is the smile-induced offset of the initial beam. The amplitude profile is normalised to unit power. The effect of smile on the position and pointing of a beam propagating in the ABCD system is calculated using the ray transfer matrix:

$$\begin{pmatrix} x_{sf} \\ \Theta \end{pmatrix} = M_{ext} \cdot \begin{pmatrix} x_s \\ 0 \end{pmatrix}, \tag{7.8}$$

where $x_s$ is the offset of the initial beam and $x_{sf}$ and Θ are the offset and pointing error of the feedback beam at the plane of the collimating lens, respectively. The new position of the centre of the beam is given by:

$$\mathrm{x_{sf}} = \left[\mathrm{M_{ext}} \cdot \begin{pmatrix} \mathrm{x_s} \\ 0 \end{pmatrix}\right]_0, \tag{7.9}$$

and the new angle of incidence is then given by:

$$\Theta = \left[M_{ext} \cdot \begin{pmatrix} x_s \\ 0 \end{pmatrix}\right]_1. \tag{7.10}$$

Thus, the complex amplitude at the plane of the collimating lens can be written as:

$$\tilde{u}_1(x_1) = \sqrt{\frac{\sqrt{2}}{\sqrt{\pi}\omega'(z)}} \cdot \exp\left[\frac{-(x_1 - x_s)^2}{(\omega'(z))^2} - \frac{i\pi(x_1 - x_s)^2 R'(z)}{\lambda} - \frac{2i\pi(x_1 - x_s)\Theta(z)}{\lambda}\right], \quad (7.11)$$

where $\sqrt{\frac{\sqrt{2}}{\sqrt{\pi}\omega\prime(z)}}$ is the amplitude normalisation factor, $exp\left(\frac{-(x_1-x_s(z))^2}{(\omega\prime(z))^2}\right)$ is the offset of the Gaussian beam amplitude induced by the smile, $exp\left(\frac{-2i\pi(x_1-x_s)\Theta(z)}{\lambda}\right)$ is the phase factor related to the pointing angle and $exp\left(\frac{-i\pi(x_1-x_s)^2 R\prime(z)}{\lambda}\right)$ is the phase factor for the new beam curvature. Thus, equation 7.11 provides a description of the return feedback beam at the plane of the collimating lens. Now, for a given lens aperture, the complex amplitude of the beam at the plane of the emitter can be obtained by calculating the diffraction integral back to the facet. A generalized one-dimensional Huygens' integral for a given ABCD optical system was presented in [220] as:

$$\tilde{u}_2(x_2) = \sqrt{\frac{i}{B\lambda}} \int_{-\infty}^{\infty} \tilde{u}_1(x_1) \exp\left[\frac{-i\pi}{B\lambda}(Ax_1^2 - 2x_1x_2 + Dx_2^2)\right] dx_1. \quad (7.12)$$

For this system the input wave $\tilde{u}_1(x_1)$ is the complex amplitude of the beam at the plane of the lens. The ABCD matrix for the simple system of a focusing lens with focal length f and the input beam at the plane of the lens is given by:

$$M_{focus} = \begin{pmatrix} A & B \\ C & D \end{pmatrix} = \begin{pmatrix} 0 & f \\ \frac{-1}{f} & 1 \end{pmatrix}. \quad (7.13)$$

Thus the diffraction integral will simplify to:

$$\tilde{u}_2(x_2) = \sqrt{\frac{i}{f\lambda}} \int_{-a/2}^{a/2} \tilde{u}_1(x_1) \exp\left[\frac{-i\pi}{f\lambda}(-2x_1x_2 + x_2^2)\right] dx_1, \quad (7.14)$$

where *f* and *a* are the focal length and the aperture of the lens, respectively. In this way, complex paraxial ray optics provides information about the profile of the feedback beam back at the plane of the collimating lens, so that the effect of beam offset and truncation (visualised in Fig. 7.3 and 7.7) can be estimated.

Knowing the complex amplitude of the feedback beam at the facet of the emitter $\tilde{u}_2(x_2)$, the feedback to the fundamental mode of the laser can be calculated using the amplitude overlap integral:

$$I = \int \tilde{u}_0(x_0)\,\overline{\tilde{u}_2(x_0)}\,dx_0. \quad (7.15)$$

The square of the absolute value of the overlap integral quantifies the mode matching between the initial beam and the feedback beam reaching the facet of the laser:

$$\eta = |I|^2. \tag{7.16}$$

η gives information on what fraction of the light diffracted by the VHG is effectively coupled back to the fundamental mode of the laser waveguide. When the full beam is effectively fed back into the fundamental mode of the emitter, η = 1.

The above approach was used to predict the impact of smile error and beam truncation by the collimating optics and the amount of feedback that can be obtained in an external cavity configuration. The following sections present the results of calculations of the feedback factors for the fast- and slow axes, separately.

### *7.2.2.1 Loss of feedback in fast axis direction*

In the fast axis direction, the amount of feedback received by an emitter in a bar can be affected by the smile deformation, which leads to a displacement of the feedback beam relative to the position of the emitter, as shown in Fig. 7.3. At a certain level of pointing error and for a given length of the external cavity, the displaced feedback beam can also be asymmetrically truncated by one of the edges of the FAC lens.

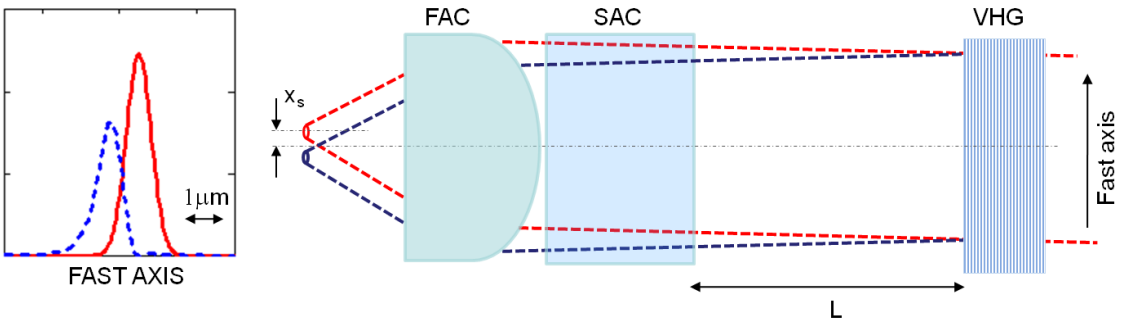


Fig. 7.3. Scheme of an external cavity configuration in the fast axis dimension, $x_s$ is the smile offset for a given emitter. The change in profile of the return beam is exaggerated for illustrative purpose.

Fig. 7.4 plots the beam profiles at the plane of the FAC lens for the initial beam and feedback beams one after round trip in 20 mm and 50 mm long external cavities. For these calculations, the active aperture of the FAC lens was assumed to be equal to 0.95 mm.

As seen in Fig. 7.4 (a), a 1 micron smile offset in the 50 mm long cavity leads to a noticeable beam truncation by the edge of the lens.

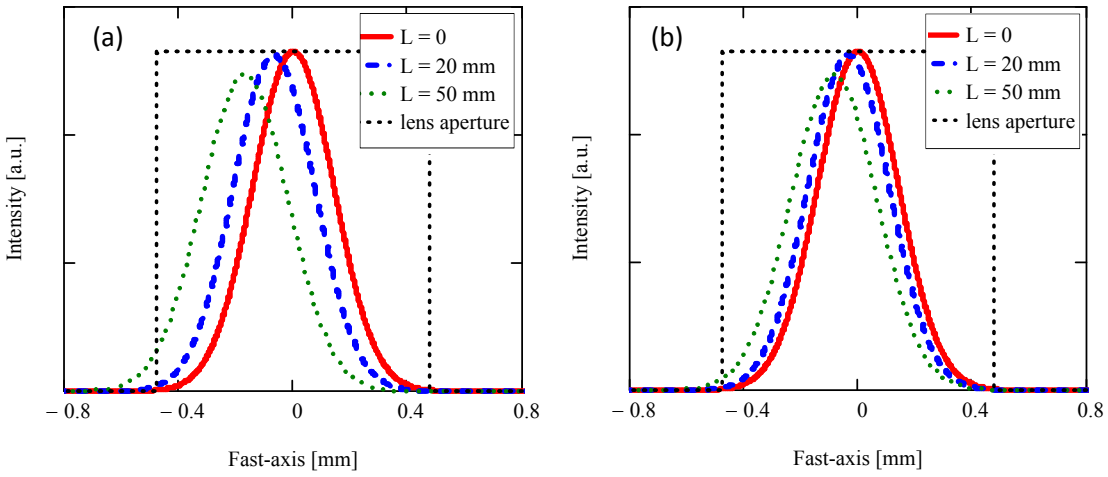


Fig. 7.4. Fast axis beam profile at the FAC lens before (red line) and after round trip in the 20 mm (blue dashed) and 50 mm (green dotted) long external cavity for (a) 1 µm, (b) 0.5 µm smile offset.

The profile of the feedback beams at the facet is calculated using the diffraction integral given by equation 7.14 and illustrated in Fig. 7.5. Clearly, the angle and the position error of the feedback beam entering the FAC lens lead to significant displacement of the beam re-imaged at the facet. For the case with 1 micron smile, this results in severe feedback loss, caused by the very small overlap between the initial beam and the feedback beam, as shown in Fig. 7.5 (a). Fig. 7.5 (b) shows the results of the same calculations conducted for a 0.5 micron of smile offset. As shown in Fig. 7.6, the overlap between the beams for this case corresponds to about 10% efficient coupling.

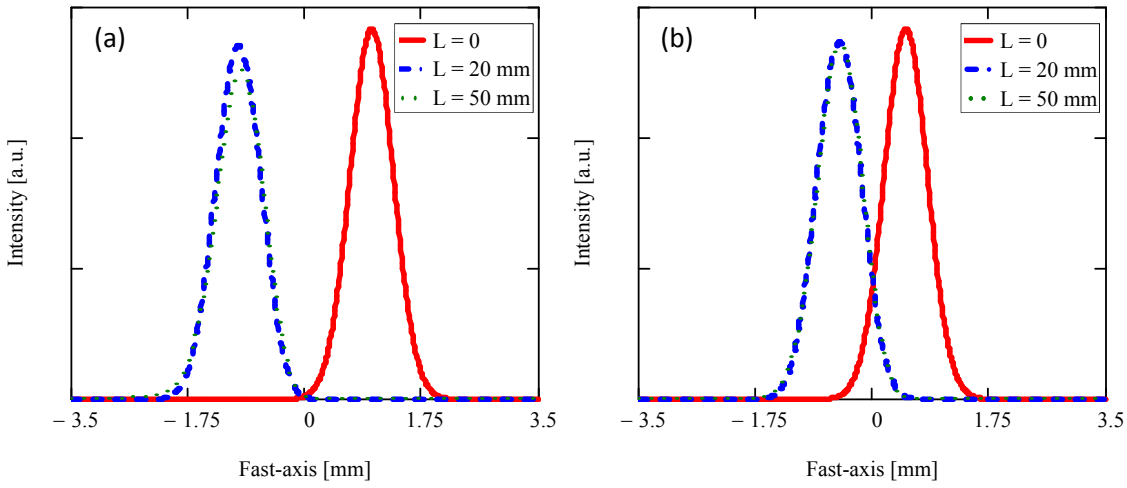


Fig. 7.5. Fast axis beam profile at the laser facet: initial beam (red line) and feedback beam after round trip in the 20 mm (blue dashed) and 50 mm (green dotted) long external cavity for (a) 1 µm, (b) 0.5 µm smile offset.

By simulating the propagation of the beams with different smile errors in a simple external cavity configuration, Fig. 7.6 shows the effective feedback in the fast axis direction as a function of the cavity round-trip length.

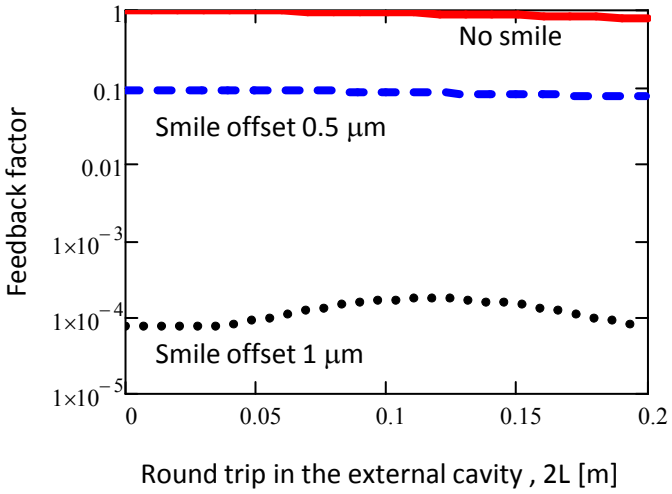


Fig. 7.6. Effective feedback as a function of propagation distance in the fast axis direction ($Z_R$ = 256 mm).

As evident in Fig. 7.6, the feedback factor in the fast axis direction does not change with the length, of the cavity but strongly drops with the size of the smile. In fact, it is the angular error of the feedback beam and the displacement of the emitter that obstruct the imaging of the feedback beam back onto the aperture of the emitter. As the Rayleigh range of the beam in fast axis direction is long ($Z_R$ = 256 mm), the impact of the divergence of the beam propagating in the external cavity is relatively unimportant.

### *7.2.2.2 Loss of feedback in slow axis direction*

In the slow axis direction, there are two issues that can potentially limit the efficiency of the feedback. Firstly, the closely packed emitters require a small aperture lens array that can lead to significant beam truncation, as shown in Fig. 7.7. It is particularly critical for the single-mode emitter bar with 200 µm pitch, where the beams start to overlap as close as 700 µm away from the laser facet (see Chapter 6).

Secondly, as was reported in Chapter 6, even a very small pitch mismatch between the laser array and the lens array can produce an offset between the end emitters and the centres of the lenses of about 1.8 µm. In this section, the feedback factor related to the beam truncation by the small aperture lenses and the possible impact of the recorded pitch mismatch of the SAC lens array are investigated.

For the calculations presented in this section, an active aperture of the SAC lenses of 170 µm was used, which agrees with the results presented in [211] and in Chapter 6.

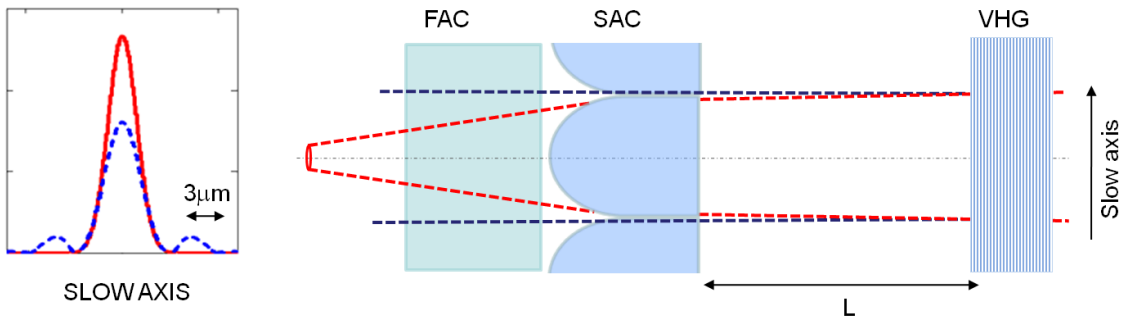


Fig. 7.7. Scheme of an external cavity configuration in the slow axis direction. The change in profile of the return beam is exaggerated for illustrative purpose.

Similar to the calculations for the fast axis direction, the beam profile for the feedback beam at the plane of the slow axis collimating lens is obtained based on the complex paraxial approximation for the Gaussian beam. The profile of the initial beam and the feedback beams at the plane of the SAC lens for different cavity lengths are plotted in Fig. 7.8.

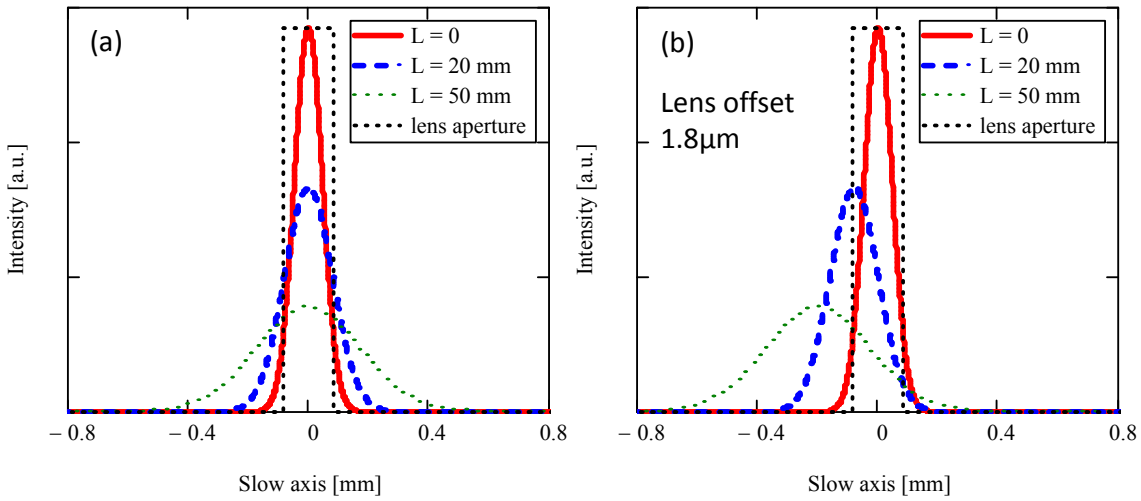


Fig. 7.8. Beam profile at the SAC lens before (red line) and after round trip in the 20 mm (blue dashed) and 50 mm (green dotted) long external cavity for (a) lens centred with the emitter, (b) 1.8 µm offset between the emitter and the lens.

Clearly, after the round trip in the cavity the remaining divergence in the slow axis direction produces beam widths that extend significantly beyond the apertures of the lenses. For the case with 1.8 µm offset between the emitter and the centre of the lens, the diverged beam is additionally displaced. The truncation of the beam produces diffraction ripples in the far field, resulting in a decrease of the power coupled back into the emitter. As shown in Fig. 7.9 (b), the amount of truncated power increases as the cavity length increases.

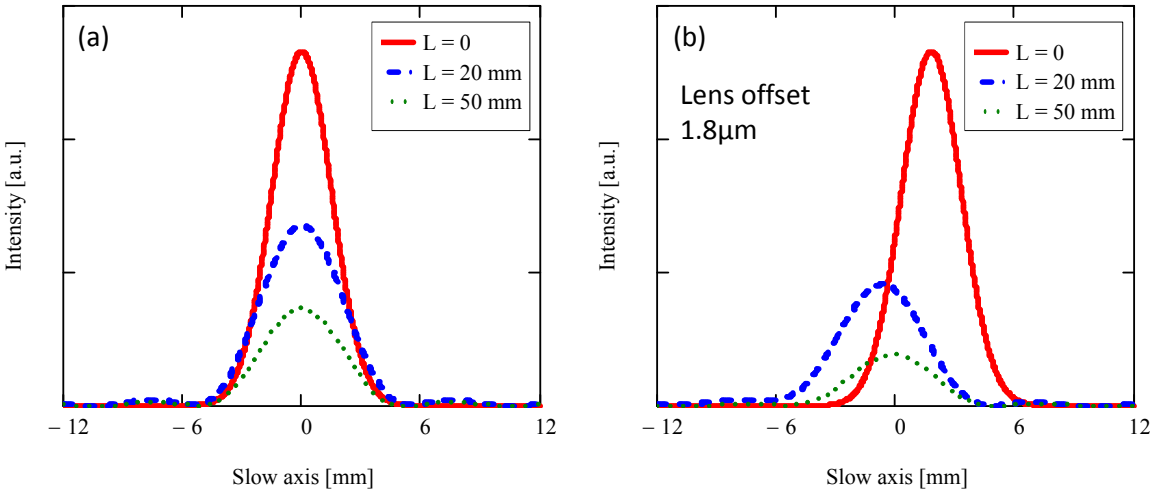


Fig. 7.9. Slow axis beam profile at the facet: initial beam (red line) and feedback beam after round trip in the 20 mm (blue dashed) and 50 mm (green dotted) long external cavity for (a) lens co-aligned with the emitter, (b) 1.8 µm offset between the emitter and the lens.

The effects of beam truncation and beam displacement are quantified by the overlap integral of the calculated beam profiles. Fig. 7.10 presents the slow axis feedback factor as a function of cavity length.

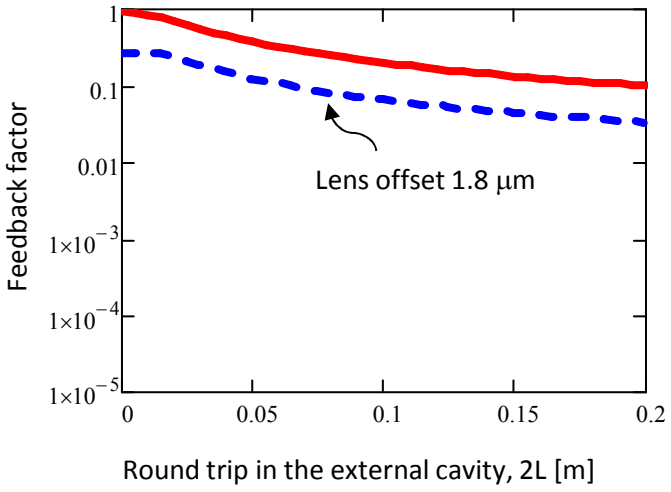


Fig. 7.10. Effective feedback as a function of propagation distance in the slow axis direction ($Z_R$ = 28 mm).

The short Rayleigh range of the beam (28 mm) combined with small active aperture of the lenses (approximately 170 µm [211]) leads to beam truncation, which is strongly dependent on the length of the cavity. Thus, the feedback factor decreases with the length of the round trip in the external cavity. The drop of feedback caused by the offset between the beam and the lens (here caused by the pitch mismatch) is less significant than the impact of equivalent smile-induced offset in the fast axis direction. This is due to two factors. Firstly, the longer focal length of the SAC lens produces a

smaller angular error for the same offset. Secondly, the wider aperture of the emitter in the slow axis direction can accept greater displacement of the feedback beams re-imaged by the SAC lens.

In a VHG-locking configuration (Fig. 7.1), the amount of feedback received by each emitter is determined by a product of the feedback factors in the fast and slow directions and the diffraction efficiency of the VHG used. The above calculations showed that only a fraction of the light reflected from the VHG is efficiently coupled back into the emitters. The remaining light is scattered by the edges of lenses or absorbed by the spaces between the emitters.

In the slow axis direction, beam spread and truncation by the edges of the lenses are the main factors limiting the amount of feedback. These effects strongly depend on the round-trip length of the cavity. It will be shown later in this chapter, good slow axis collimation is necessary to maintain good feedback in a VHG-based external cavity configuration.

In the fast axis direction, the main issue is the displacement of the feedback beam re-imaged by the FAC lens back at the plane of the laser facet caused by the smile-induced offset between the emitters and the lens. The calculations suggest that, due to the short focal length of the FAC lens and small aperture of the emitters, the angular errors produced by a 1μm smile offset may reduce the feedback by a factor of $10^{-4}$. However, while the paraxial approximation is good for describing the propagation of the single-mode beams in the slow axis dimension, the paraxial approximation may be no longer be accurate for the high divergence angle in the fast axis. Moreover, the model assumed perfect lenses. In a real laser system, imperfect and slightly misaligned lenses will produce larger or scattered images at the laser facet. For some cases, this may result in a higher feedback than predicted by the model. The beam spread due to aberrations, which was neglected in this model, may allow a low level of feedback to be obtained. As shown later in Section 7.4.2, even the weak side lobes produced by an imperfect fast axis lens can partially lock some emitters in a bar when the natural wavelength of the laser is close to the Bragg wavelength of the VHG.

In practice, the actual impact of the smile error is expected to be less critical than predicted by the calculations. The results presented later in this chapter show that full locking of the bar can still be obtained with a smile offset by as much as 1.9 μm when the detuning range and distances between the laser and the VHG are sufficiently small.

It is difficult to determine the minimum feedback level required for the full locking of a laser emitter. The exact value for the front facet reflectivity of the lasers

used in the experiments was not specified by the provider. However, as shown later in Section 7.3.1, feedback from the AR-coated facet of a FAC lens (which is estimated to be less than $10^{-4}$) can influence the spectrum of the laser. Thus, the feedback provided by a VHG must be comparable to this value. In the case of wavelength locking with a VHG, the effectiveness of the feedback will also strongly depend on the difference between the natural wavelength of the laser and the Bragg wavelength of the grating. The larger the difference, the greater the feedback that is needed to wavelength-lock the laser [219].

For robust locking of all emitters in a bar, a sufficient level of feedback must be provided uniformly along the bar. It is desirable to ensure high feedback efficiency for all emitters simultaneously, so that a low reflectivity VHG can be used for the full locking of laser bars. Alternatively, the feedback loss caused by high divergence or pointing errors could be compensated by using VHGs with a higher diffraction efficiency, but this would lead to an increase of the power loss of the system.

## 7.3 Spectral properties of free running laser bars

Prior to the experiments on VHG-locking of diode laser bars, the spectral properties of free running lasers were investigated using the optical system introduced earlier in Section 4.2.2. The wavelength distribution across the bars as well as high resolution spectra of single emitters were studied. The main focus of this work was the impact of residual reflection from the fast axis collimating lens. Tuning with temperature and current are also investigated.

The bars used in this section are the 49 single-mode emitter bar (BSM2) and the 19 broad-area emitter bar (BBA). Both lasers, as introduced in Chapter 6, are passively cooled on a CS-mount and lensed with 600 μm FL fast axis collimating lenses.

### 7.3.1 Non-uniform wavelength distribution across FAC-lensed bars

The emitter resolved spectra of the bars were observed over a full range of drive currents and cooler temperatures, using the experimental setup shown in Fig. 4.7. The high resolution spectra of single emitters were recorded in the configuration shown in Fig. 4.6.

Figures 7.11 and 7.12 show spectra recorded for the two bars and reveal evidence of a multi-peak wavelength distribution, which is characteristic for operation with external feedback [221, 222]. This is believed to be caused by the back reflection from the FAC lens. Knowing that the residual reflection from the FAC lens is less than 1%,

the maximum feedback provided by the lens can be estimated to be less than $10^{-4}$, accounting for the divergence of the reflected beam and the size of the emitter aperture (calculated for a single-mode emitter in similar manner as in Section 7.2.2).

Fig. 7.11 (a) shows that in the case of the single-mode emitter bar, the multi-peak spectra of the emitters are more evident at high drive currents and vary across the bar. This can be caused by a combination of factors. The intrinsic properties of the bar, such as packaging induced stress, inhomogeneities in wafer fabrication and temperature gradient across the bar may also significantly contribute to the spectral behaviour of the laser. Additionally, a slight misalignment of the FAC lens may result in non-uniform feedback across the bar. A better understanding of these effects requires further investigation, including spectral analysis of the laser without the FAC lens and alignment of the FAC lens with simultaneous monitoring of the spectrum. This could be realized as a part of future work.

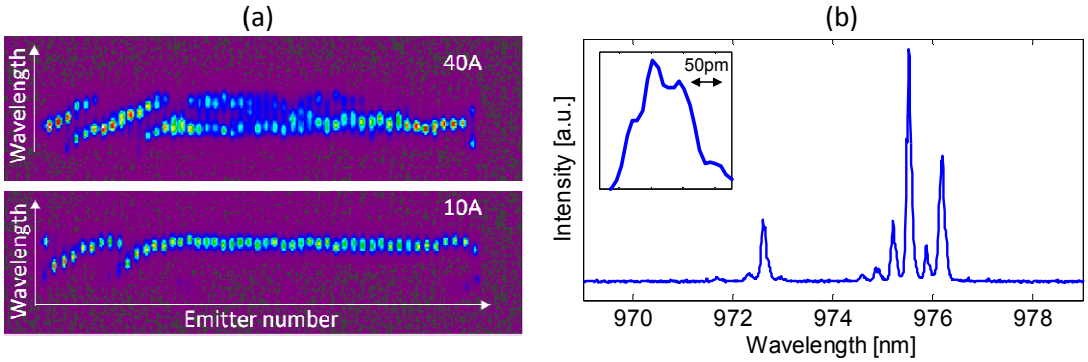


Fig. 7.11. Bar BSM2: (a) Imaging spectrometer view of free running spectrum at 10A and 40A total current. (b) High resolution spectrum of a single-mode emitter at 40A of drive current and 19°C of temperature on the CS mount, inset: zoom-in to one of the peaks.

A high resolution spectrum recorded for an emitter selected from the single-mode emitter bar allows a more accurate description of spectral behaviour to be obtained. As shown the inset of Fig. 7.11 (b), the ~40 pm longitudinal mode spacing corresponding to 3.5 mm internal cavity length could be nearly resolved. The approximately 3 nm spacing between the two spectral bands in Fig. 7.11 (b) is a consequence of external feedback provided by the reflection from the back face of the fast axis collimating lens, which forms a 150 μm etalon with the front facet of the laser. Significant fringe visibility indicates that the level of feedback from the back facet of the FAC lens is comparable to the laser facet coating reflectivity. Finally, the 309 pm spacing between the fine peaks is a consequence of the reflection from the front facet of the FAC lens that forms a 1.54 mm etalon composed of reduced distance between the exit face of the FAC lens and the optical thickness of the lens that are nominally equal to 150 μm and

1.42 mm, respectively, for the Ingeneric lenses with refractive index of 1.776 and EFL of 600 μm.

Similar observations were performed for the broad-area bar. However, as shown in Fig. 7.12 (a), this time the spectrum of the laser was modulated by the feedback from the FAC lens over the full range of driving currents. Note that the tilt of the spectral image is a result of the alignment error in the imaging system and should be neglected.

It has been observed that with the current increase, the wavelength of each emitter jumps by the amount equal to the mode separation of the external cavity formed by the back face of the FAC lens. The effect of mode jumping for a selected single emitter is visualized in Fig. 7.13 (b). A similar effect for a single laser diode was studied in [221].

The wavelength shift from the emitter to emitter corresponds to half of the mode spacing of the facet to FAC etalon. This indicated that the etalon length varies by λ\4 from emitter to emitter as discussed in [223]. To produce such a difference across the bar, the FAC lens must have been be tilted by about 0.5 mrad as an error in lens attachment.

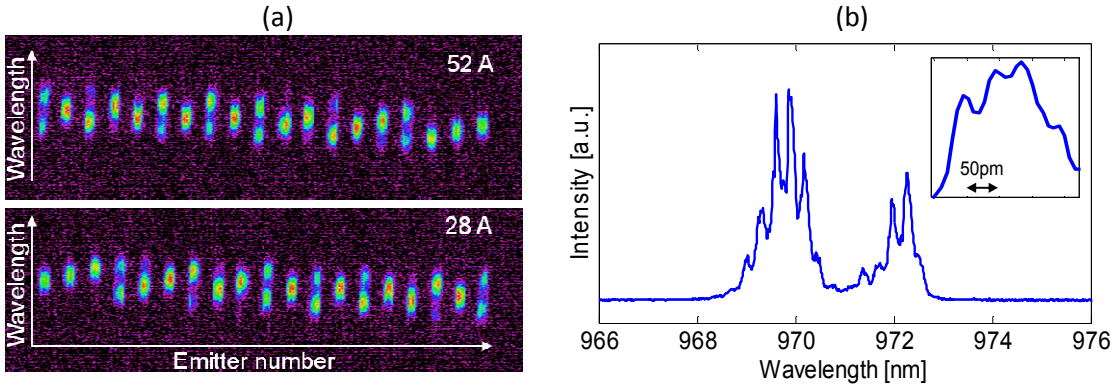


Fig. 7.12. (a) Emitter resolved spectra of the unlocked bar BBA bar recorded at 52A (top) and 28A (bottom) of drive current. (b) High resolution spectrum of a single broad-area emitter measured at 50A and 20˚C of temperature on the CS mount, inset: zoom-in to one of the peaks.

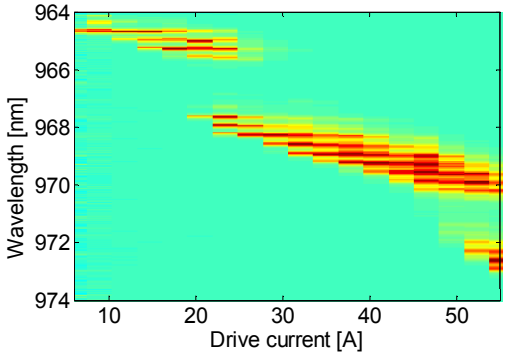


Fig. 7.13. Montage of spectra for a single broad-area emitter in the emitter bar recorded at different levels of drive current.

Similarly to the previous case, the high resolution spectrum of a selected broad-area emitter shown in Fig.7.12 (b) provides clear evidence of external feedback provided by both faces of the FAC lens. The coarse spacing of about 2.6 nm is produced by the approximately 180 μm etalon effect caused by reflection from the back facet of the FAC lens. The 300 pm spaced peaks are due to the etalon formed by the front facet of the laser and front face of the lens, which are spaced by 1.57 mm of reduced distance. Compared to the single-mode emitter spectrum analysed above, the estimated cavities formed by the FAC lens are slightly longer. This is most likely due to different alignment of the lens. The contrast of the spectrum is also lower, which suggests that the ratio between the feedback from the lens and the reflectivity of the laser front facet is lower.

The cavity length of the broad-area emitters is 3.5 mm and the longitudinal modes spaced by 40 pm are nearly resolved in the inset of Fig. 7.12 (b).

### 7.3.2 Wavelength tuning with temperature

The effect of thermal tuning for the two bars was analysed based on a high resolution spectra recorded for a single emitter selected from the bar for different coolant temperatures.

Fig. 7.14 plots the peak wavelength as a function of the temperature of the CS mount for the single-mode emitter bar BSM2. The two solid lines correspond to the peak wavelengths of the two spectral bands, as shown earlier in Fig.7.11. Both bands tune with a slope nearly equal to the nominal 0.3nm/K.

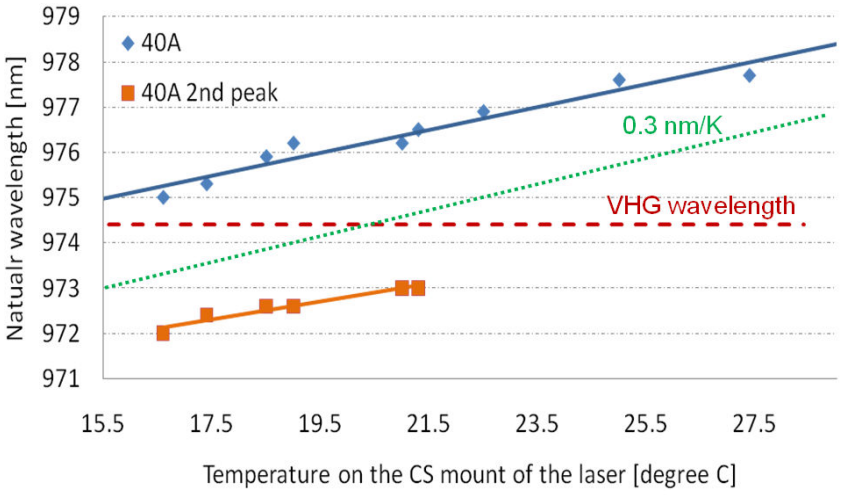


Fig. 7.14. Spectrum of a single emitter vs. temperature at 40A of drive current.

The dashed red line indicates the Bragg wavelength of the VHG used in the experiments on wavelength locking, as introduced in Section 7.2.1. The maximum

detuning of the natural wavelength of the laser and Bragg Wavelength of the VHG determines the required locking range. According to this measurement, at 40 A of drive current, the maximum difference between the natural wavelength and the VHG wavelength is about 4 nm. This indicates that to obtain locking over the full range of temperatures available in the experiments, a locking range of ± 4 nm will be required.

Results on the thermal tuning of the broad-area emitters are presented in Fig. 7.15, where the peak wavelength for a selected broad-area emitter is plotted as a function of the temperature of the CS mount.

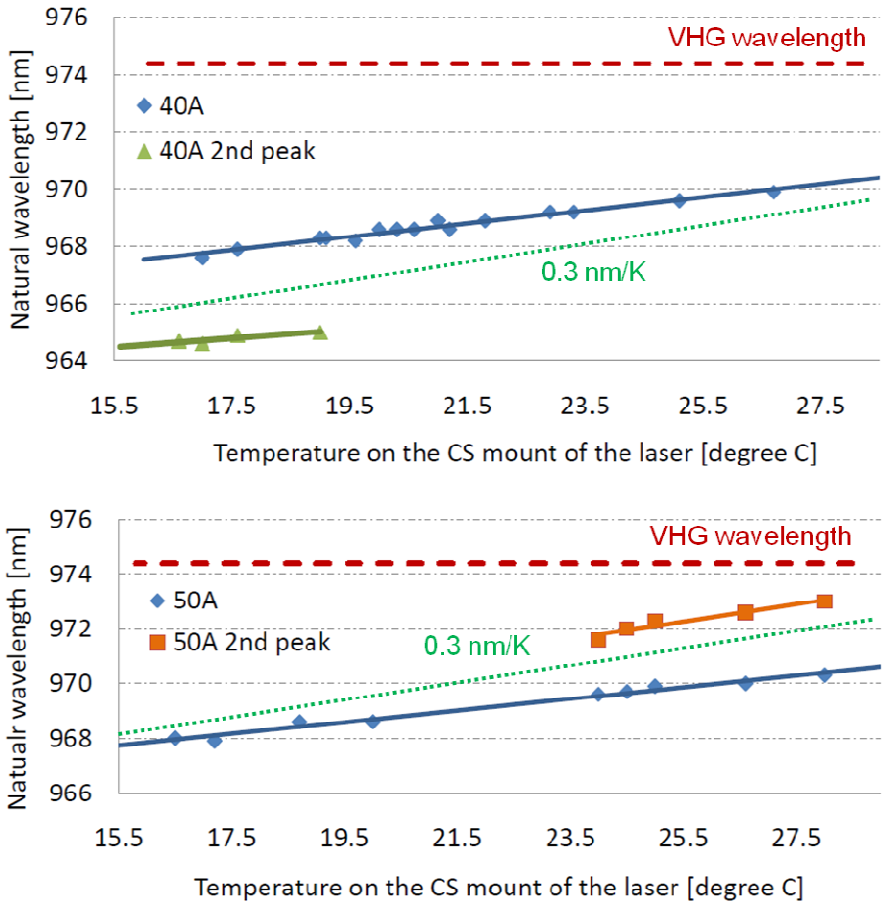


Fig. 7.15. Peak wavelength of a single emitter as a function of temperature (top) at 40A drive current, (bottom) at 50 A of drive current.

The 'natural' temperature dependence is skewed by back reflection from the FAC. Thus, similar to the results for the singlemode emitter bar, two separate tuning plots are presented, one for each of the observed spectral bands. The Bragg wavelength of the VHG used later in the experiments on wavelength locking is marked with a red line. As shown in Fig. 7.15 (top), the emitter operating at 40A and 16ºC requires over 9 nm of locking range to be fully locked to the VHG wavelength. In such conditions, robust wavelength locking over a large range of temperatures can only be achieved when sufficiently high feedback is delivered, as shown later in Section 7.5.3.

## 7.4 Sensitivity of the optical feedback to misalignment

In this section, the sensitivity of optical feedback to misalignment is investigated based on the measurement of the angular acceptance for VHG-locking for single emitters selected from the bars. The angular acceptance is determined by rotating the VHG, which simulates a pointing error of the laser beam. The VHG used in this experiment has 200 pm FWHM bandwidth at 974.4 nm, diffraction efficiency of 15% and angular acceptance of 2.4˚, as introduced in Section 7.2.1.

Fig. 7.16 illustrates the experimental procedure for the measurement of the angular acceptance in the fast (a) and slow (b) axis directions. In this experiment, full bars were operated, but only the spectrum of a selected single emitter was recorded as a function of the tilt angle. The grating was mounted on a 6-axis manipulator and placed at a 6 mm distance from the SAC exit surface. The bars were de-smiled and collimated in both axes with dual axis corrective optics (see Chapter 6).

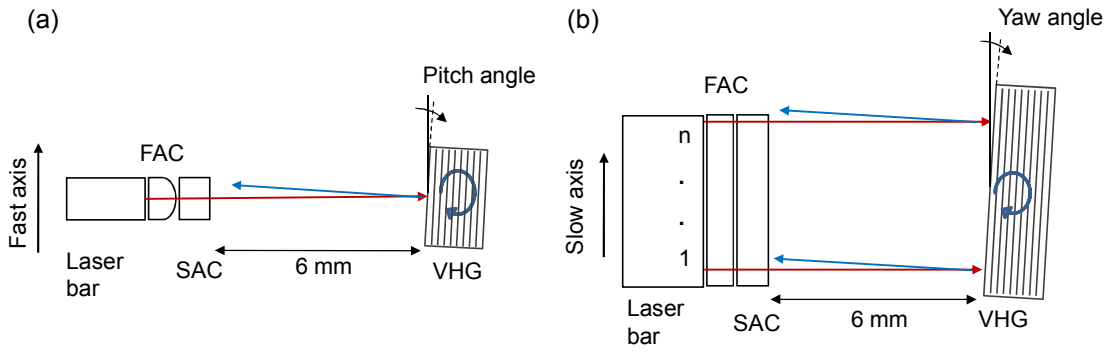


Fig. 7.16. Experimental setup for determination of angular sensitivity of VHG locking in (a) fast and (b) slow axis direction.

Initially, the VHG was aligned for normal incidence. This was achieved by observing the emitter resolved spectra of full bars simultaneously with a high resolution spectrum from a selected emitter. At normal incidence, all emitters in the bar were fully locked to the nominal wavelength of the VHG. Once the initial alignment was achieved, a fine rotation of the VHG was used to introduce an angular error in the feedback beam to simulate misalignment errors in the cavity and pointing errors of the laser beams. In such a configuration, the rotation of the VHG by an angle of $\delta\theta = \delta x/EFL$ is equivalent to the smile-induced displacement of the emitter with regard to the centre of the collimating lens of $\delta x$, where EFL is the effective focal length of the lens. Thus, in the fast axis direction, the smile effect resulting in a 1 micron displacement of the emitter can be simulated by a 1.6 mrad tilt of the VHG. In the slow axis direction, a small offset between the emitters and the centres of the collimating lenses can be caused by e.g. pitch mismatch between the SAC array and the laser array (see Chapter 6). A pointing

error caused by a 1.8 μm offset between the emitter and the SAC lens can be simulated by a VHG tilt of 2.1 mrad.

The following sections present a study of the angular acceptance for locking, which was performed for single emitters selected from both the 49 single-mode emitter bar with low reflectivity on the front facet (BSM3) and the 19-broad-area emitter bar (BBA).

Angular acceptance is defined here as the maximum angle between the laser beam and the normal to the facet of the VHG, for which the laser remains fully locked. The sensitivity to misalignment can depend on the detuning from the Bragg wavelength as the larger the difference between the locked wavelength and the free running wavelength, the more feedback is needed for locking. To address this, the measurements were performed for different operational conditions.

### 7.4.1 Angular acceptance of VHG-locking for a single-mode emitter

Fig. 7.17 shows montages of the spectra for a single emitter selected from bar BSM3 recorded at different values of fast axis angle rotation of the VHG (pitch angle in Fig. 7.16). The measurements were taken for two different operating conditions: (a) at 15A and 20˚C on the CS mount; and (b) at 14A and 17˚C on the CS mount. The two cases correspond to 3.3 nm and 3.8 nm of detuning from the Bragg wavelength of the VHG, respectively.

The narrow spectral line at 974.4 nm represents the locked portion of the spectrum with a linewidth of 200 pm FWHM. The emission spread over shorter wavelengths corresponds to the emission of the free running laser and indicates that the laser either locks only partially or goes fully out of lock under these conditions. For both sets of conditions presented in Fig. 7.17, the emitter was locked over a range of approximately ±7 mrad. It is worth mentioning that when a similar test was done for bar BSM2 with higher reflectivity on the front facet, locking was only maintained over a range of ±2 mrad. Locking of BSM3, exhibited less sensitivity to alignment due to the fact that it has reduced reflectivity of the front facet.

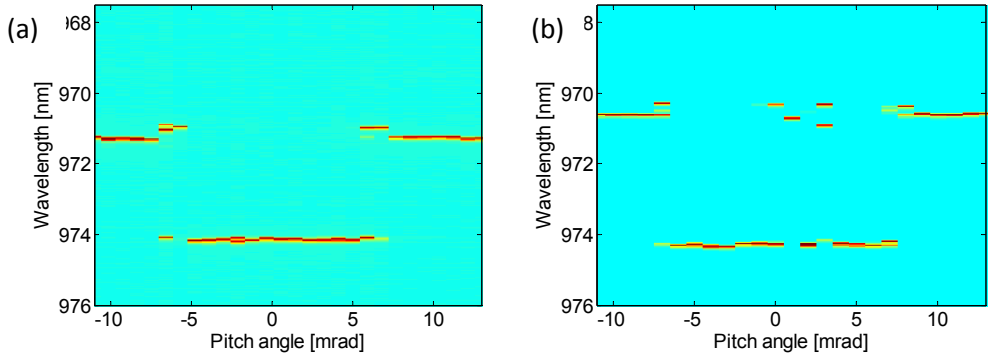


Fig. 7.17. Montage of spectra of a single emitter selected from bar BSM3 as a function of fast axis tilt of VHG. The laser was operated at (a) 15A / 20˚C and (b) 14A / 17˚C.

The alignment sensitivity in the slow axis direction was also investigated. The spectra plotted versus yaw angle of the VHG (see Fig. 7.16 (b)) are presented in Fig. 7.18.

In this experiment, the tilt of the VHG was observed to cause the investigated emitter to be injected by the light from the adjacent emitters. As the Bragg condition of the VHG is tuned by change of incident angle, the emitter receives feedback at a slightly different wavelength to that at normal incidence. The locked spectra follow the theoretical curve (blue line) defining angular tuning of the VHG used.

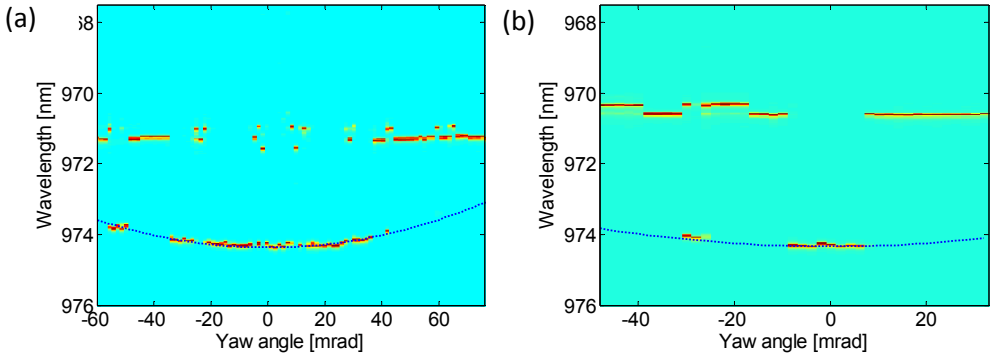


Fig. 7.18. Montage of spectra of a single emitter selected from bar BSM3 as a function of slow axis tilt of VHG. The laser was operated at (a) 15A / 20˚C and (b) 14A / 17˚C.

### 7.4.2 Angular acceptance of VHG-locking of a broad-area emitter

Fig. 7.19 shows the sequence of high resolution spectra recorded at different VHG tilt angles measured for a single broad-area emitter selected from the bar operated at (a) 50 A and (b) 40 A. The two sets of conditions correspond to 5.4 nm and 6 nm of detuning from the Bragg wavelength, respectively. This time, a slight difference in angular acceptance was observed, caused by the difference in detuning for the two cases. An angular acceptance of 0.8 mrad was measured for a 50A drive current and 0.6 mrad was measured for 40A drive current.

The results indicate that smile errors greater than 0.7 µm peak-to-valley and 1.0 µm peak-to-valley for the two cases are sufficient to prevent full locking of the broad-area emitter.

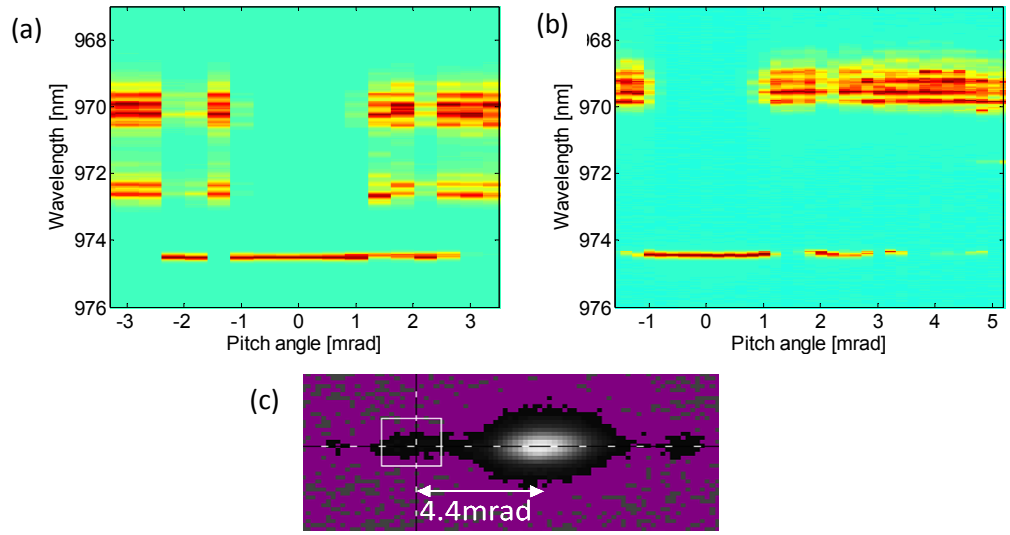


Fig. 7.19. Montage of spectra of a single emitter selected from bar BAI as a function of fast axis tilt of VHG. The laser was operated at (a) 50A / 27˚C and (b) 40A / 25.5˚C. (c) Far field pattern of the emitter.

Fig. 7.19 (a) also illustrates an effect of partial locking of the emitters by the feedback received from the side lobes of the beam. The two angular bands in which the emitter locks partially correspond to the locations of the side lobes visible Fig. 7.19 (c). Apparently, the side lobes of the beam provide enough feedback to partially lock the emitter at angles beyond the window of angular acceptance. The power contained in the side lobes was estimated to be approximately 2% of the power in the main lobe.

Although the angular acceptance in the slow axis direction is not as critical as in the fast axis direction, the limits to the range of angles for which the emitter remains fully locked could also be determined. As shown in Fig. 7.20, the 6 nm of required locking range allows ±12 mrad of maximum deviation from normal incidence. When the natural wavelength is tuned to 5.4 nm away from the locking wavelength, the angular acceptance increases to ±16 mrad. Evidently, the large aperture of the emitter in the slow axis direction ensures a better acceptance for offset and angular errors of feedback beams than in the fast axis direction. However, as shown in the next section, the emitters will still suffer from a significant reduction in feedback when the slow axis of the laser is uncollimated, as in Fig. 7.25.

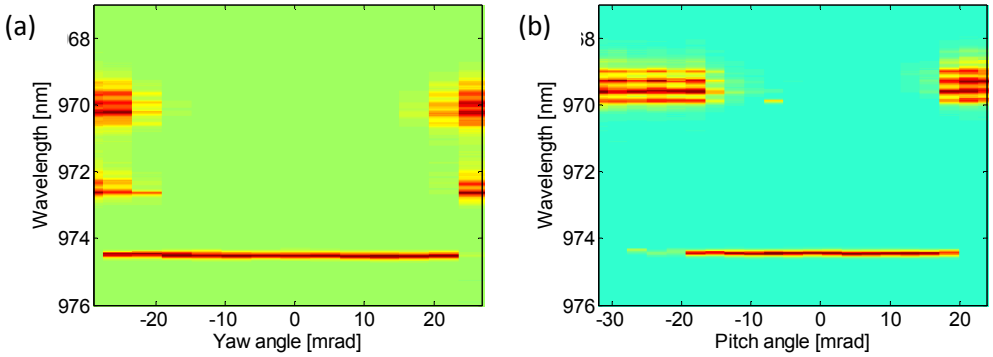


Fig. 7.20. Montage of spectra of a single emitter selected from bar BBA as a function of slow axis tilt of VHG. The laser was operated at (a) 50A / 27˚C and (b) 40A / 25.5˚C.

## 7.5 Wavelength locking of full size laser bars

This section presents results on the wavelength locking of full size laser bars. It addresses the main objective of the work, which was to evaluate the impact of the spatial properties of the beams on the wavelength locking of full diode laser bars and to obtain the maximum possible locking efficiency.

The bars used in the following experiments include the single-mode emitter bar BSM2 and the broad area emitter bar BBA. Some results on the single-mode emitter bar with a low reflectivity the front facet (BSM3) are introduced in Section 7.5.2 for the purpose of comparison.

Section 7.5.1 introduces the method for quantifying the quality of locking for a bar used in this work. Using these criteria, the angular acceptance of the wavelength locking for full bars is investigated in Section 7.5.2. The performance of VHG-locking for different collimation cases for the laser bars is discussed in Sections 7.5.3 and 7.5.4.

### 7.5.1 Criteria and tolerances for full locking of a laser bar

Emitter resolved spectral images of the bar were used to provide a quick determination of the efficiency of the VHG-locking. The locking efficiency was defined as the fraction of the power contained within the bandwidth of the VHG. This was calculated based on the image recorded at the output slit of the imaging spectrometer (see Fig. 4.7). Some examples of spectral images are shown in Fig. 7.21.

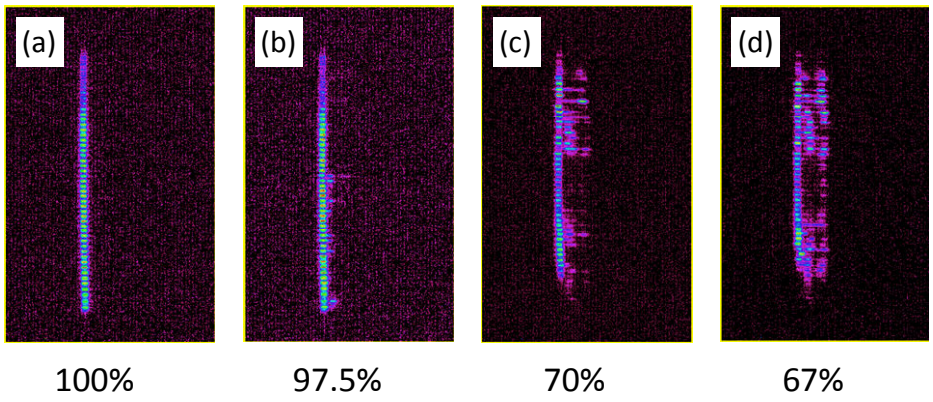


Fig. 7.21. Emitter resolved spectra of the 49-emitter bar VHG-locked with (a) 100% locking efficiency, (b) 97.5% locking efficiency, (c) 70% locking efficiency, and (d) 67% locking efficiency.

As illustrated in Fig. 7.21 (a), 100% efficiency means that all emitters in the bar are fully locked to the bandwidth of the VHG. A drop of efficiency indicates that some of the emitters went out of lock either partially (by producing light at the VHG wavelength as well as at their natural wavelength) or fully (by emitting only at their natural spectral line). It is worth noting that for the examples shown in Fig. 7.21, the free running spectrum is partly overlapping with the spectral band of the VHG, so the locking efficiency will not be calculated to be zero. In this case, it is important to know the natural wavelength of the laser for the given current and temperature to interpret the calculated values correctly.

### 7.5.2 Angular acceptance for locking of full laser bar

The above criteria were applied to the evaluation of the angular acceptance for 100%-efficient VHG-locking for full size bars. The maximum accepted angle is defined as the angle at which at least one of the emitters in the bar goes fully, or partially out of lock. This angular acceptance is determined for different levels of required locking range, which is defined here as the maximum difference between the Bragg wavelength of VHG at normal incidence and the most outlying natural wavelength along the bar.

The bars were equipped with both a fast axis collimating lens and a dual-axis optics performing fast axis correction and slow axis collimation (see Chapter 6). The experiment is performed using the setup presented in Fig. 7.16. However, this time the low resolution emitter resolved spectra of the full bars are recorded with the imaging spectrometer (see Fig. 4.7). Similarly to the experiment conducted for single emitters (Section 7.4.1), the fast- and slow axis pointing errors are again simulated by tilting the VHG.

For the single-mode emitter bar (BSM2), the measurement was performed at three different currents to impose natural lasing at different wavelengths. In this way, the angular acceptance of the locking was evaluated for different levels of detuning from the Bragg wavelength.

As shown in Fig. 7.22, the angular acceptance in the fast axis direction varies from 3.2 mrad for 2 nm of detuning to 2.2 mrad for 4.5 nm of detuning. In the slow axis direction, the acceptance drops more rapidly with the increase in wavelength detuning. For the range from 2 nm to 4.5 nm of detuning, the maximum accepted angle varies from 15.6 mrad to 4 mrad. Such a strong dependence indicates a drastic feedback drop caused by angular misalignment in the slow axis.

The results confirm that the larger detuning from the wavelength of VHG, the more feedback is needed to pull the emission wavelength to the locking wavelength. The pointing error simulated by tilting of the VHG leads to a drop in the amount of reflected light that is fed back into the apertures of the emitters. The more feedback that is needed for full locking, the less the angular tilt that can be accepted.

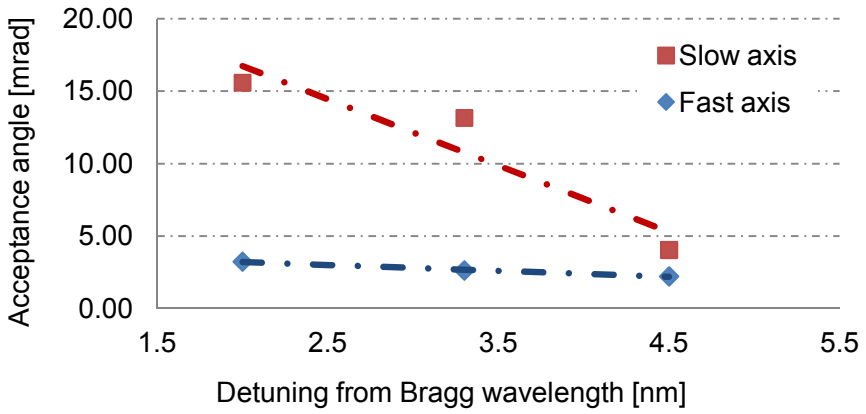


Fig. 7.22. Angular acceptance for VHG locking vs. detuning from the Bragg wavelength. The laser-VHG distance was 12 mm.

The angular acceptance for the full bar was also determined for different distances between the laser and the VHG, as shown in Fig. 7.23. As expected based on the analysis in Section 7.2.2, an increase in distance significantly reduces angular acceptance the in slow axis direction. Due to the fact that the distance decreases the feedback in the slow axis, the angular acceptance in the fast axis is also reduced.

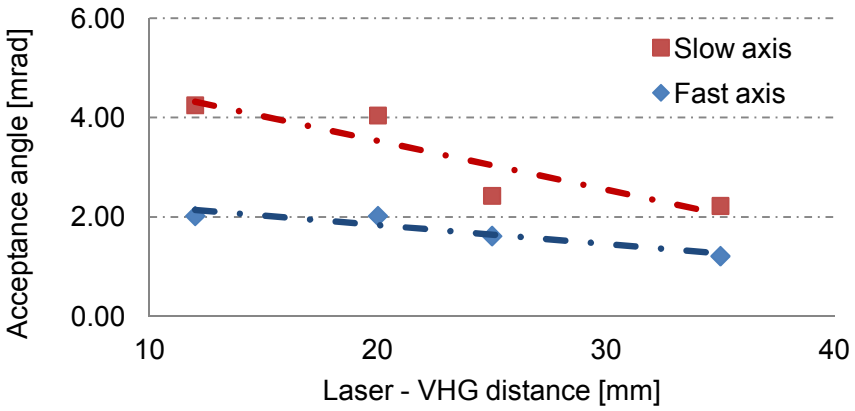


Fig. 7.23. Angular acceptance for VHG locking vs. distance laser-VHG. The detuning from the Bragg wavelength was 4.5 nm.

Similar experiments were performed with bar BSM3, which has a lower reflectivity front facet than BSM2. When the operating conditions were set to produce detuning of 4.1 nm, acceptance angles of 5.4 mrad in the slow axis direction and 3 mrad in the fast axis directions were obtained when the VHG was placed at 25 mm away from the laser. Compared with the data for BSM2 in Fig. 7.23, the reduced reflectivity of the front axis resulted in a better angular acceptance of the VHG of the BSM3.

The alignment sensitivity for the VHG-locking of a broad-area emitter bar was also investigated. The broad-area emitters were observed to remain locked for up to several milliradians of the slow axis rotation of the VHG. For this case, the fast axis misalignment sensitivity was the main concern. Thus only the impact of fast axis error, typically produced by smile in diode bars, was investigated. When the bar was operated at 5.4 nm away from the VHG wavelength, it remained fully locked over the range of 1.57 mrad corresponding to 0.91 μm of smile error. The tuning ranges of 6 nm and 6.2 nm required the angular error to be less than 1.14 and 0.94 mrad, (corresponding to 0.68 μm and 0.56 μm smile), respectively. The results show that for a smile greater than 1 μm peak-to-valley, the locking range for the full locking of all emitters in the bar can be limited. In practice, the wavelength of the bar and the wavelength of the VHG will have to be matched closely enough (less than 5 nm) to allow 100%-efficient locking of the bar.

### 7.5.3 Extended locking range for laser bars with dual-axis corrective optics

Thermal stability is one of the most important parameters of a wavelength locked laser. The temperature range in which all emitters in a laser diode bar are fully locked depends on the level and uniformity of the feedback along the bar. When the feedback is limited

by either high divergence or the pointing errors of individual emitters, the range of efficient locking is narrowed.

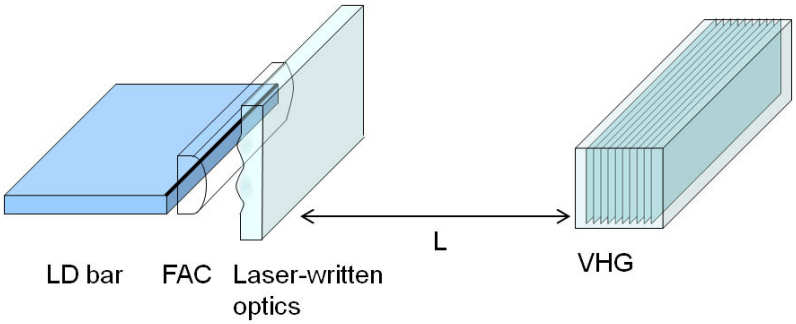


Fig.7.24. Experimental setup for measurement of locking range in an external cavity laser array with the VHG.

To determine the dependence of the locking range on the spatial properties of the beams, the locking efficiency was measured as a function of heat sink temperature for bars with FAC lens only, with the addition of a fast axis corrective surface, and with the combined FAC correction with SAC lens array. The two bars used in these experiments were BSM2 and BBA. For both laser bars, a set of laser-written optics was placed in front of the laser, allowing each of them to be aligned into its optimal position when required. In this way, the VHG-locking could be investigated for the laser with different collimation conditions. The 15% diffraction efficiency VHG was placed in front of the laser as shown in Fig. 7.24. For each collimation case, the VHG was aligned to its optimal position to ensure that as many emitter as possible were locked. After the alignment, the temperature of the coolant was changed to induce a change of temperature of the laser running at a constant current.

The results of such measurements performed for the 49 single-mode emitter bar are plotted in Fig. 7.25. Each data point corresponds to the locking efficiency estimated based on the low resolution spectrum recorded by the imaging spectrometer system for the given conditions, as explained earlier in Section 7.5.1. The drive current was 40 A and at 17.5 ˚C the detuning of the natural wavelength of the laser from the Bragg wavelength of the VHG reached its minimum. The VHG was placed at a distance of 3 mm away from the laser.

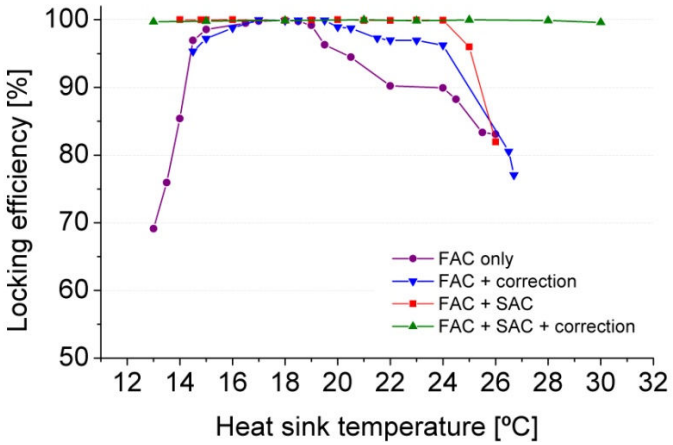


Fig. 7.25. Efficiency of locking with a VHG with DE =15% as a function of heat sink temperature

Clearly, lack of slow axis collimation significantly narrows the temperature range of efficiency locking. The slow axis divergence of the bar is about 7 degrees (FWHM), while the angular selectivity of the VHG used is about 2 degrees. Consequently, only a small fraction of light can be coupled back into the laser aperture along the slow axis direction. This effect is particularly strong for narrow stripe single-mode emitters.

For the bar without slow axis collimation, adding the fast axis correction improves the efficiency of the VHG locking. This is because the feedback level, which is already low due to high divergence of the beam, becomes even lower when the pointing error displaces the feedback beams imaged onto the laser facet.

Fig. 7.25 shows that the fast axis correction combined with the slow axis collimation provides nearly 100% efficiency for the full range of temperatures allowed by the available hardware. The recorded temperature range of 17˚C corresponds to about 5 nm of locking range.

A similar experiment was conducted with the 19-broad-area emitter bar measured at 40A with the VHG-laser placed at a distance of 6 mm. The results are shown in Fig. 7.26. At 15.5˚C, the most outlying natural wavelength of the bar was about 965 nm, which is 9.4 nm away from the Bragg wavelength of the VHG used. When the laser beams were collimated in the fast axis only, a maximum obtained detuning of 4.2 nm was obtained. When the SAC lens array was added, the uncorrected fast axis errors limited the locking range to +/- 4.5nm.

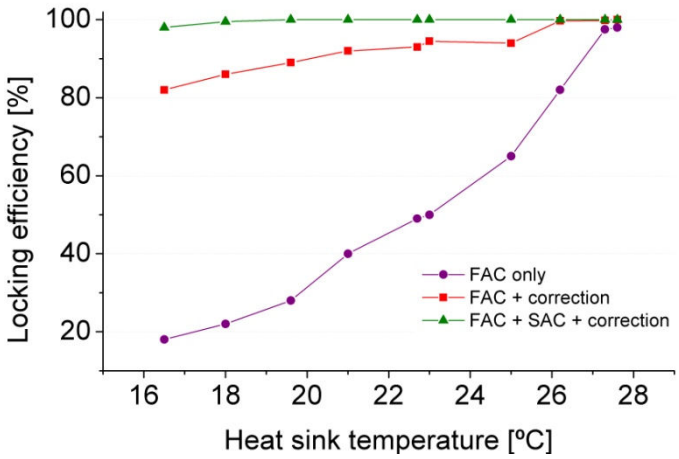


Fig.7.26. Locking efficiency as a function of temperature on the CS mount for the broad-area bar.

### 7.5.4 Distant locking of laser bars with dual-axis corrective optics

The divergence and pointing errors of the beams both will create a stronger feedback reduction as the distance between the VHG and the laser bar increases. This behaviour was investigated by observing the drop of efficiency while moving the VHG away from the laser bar, as pictured in Fig. 7.27.

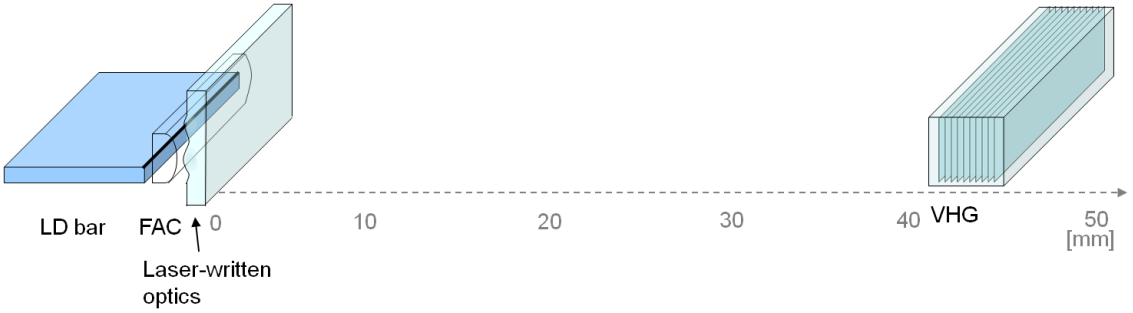


Fig. 7.27. Experimental configuration for wavelength locking with a distant VHG.

Fig. 7.28 plots the locking efficiency as a function of VHG-laser distance, estimated the same way as described in the previous section. The measurements were performed at 18.5˚C of heat sink temperature and 40A of drive current. These conditions correspond to a natural lasing wavelength of 976 nm. The required feedback needs to be strong enough to pull the laser emission by 0.6 nm.

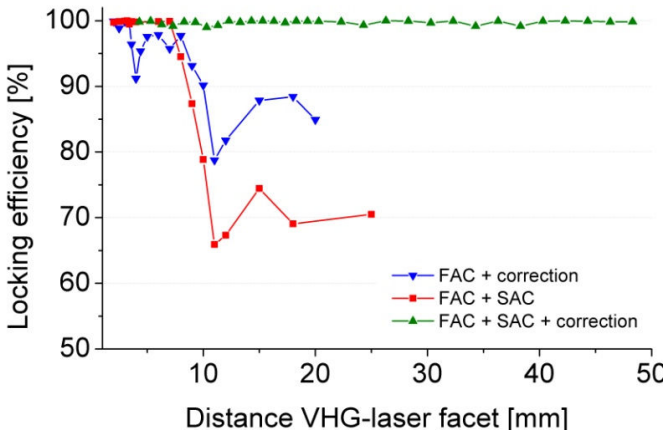


Fig.7.28. Locking efficiency as a function of laser-VHG distance for the bar BSM2. Driving current was 40A, temperature on the CS mount was 18.5˚C.

The fast axis error correction combined with slow axis collimation allowed uniform, 100%-efficiency locking at VHG-laser distances up to 48 mm. As shown in Chapter 8, full locking in a 110 mm folded cavity configuration was obtained. By contrast, locking in the case of the uncorrected bar with fast- and slow axis collimating optics can only be obtain at distances up to 10 mm. For the corrected bar without the SAC lens in place, the first emitters appeared to go out of lock at distances as small as 5 mm. As predicted in the calculations in Section 7.2.2, the feedback factor drops rapidly with laser-VHG distance in the absence of slow axis collimating lenses.

Similar investigations performed for the 19-emitter broad-area bar showed a slightly weaker dependence on the slow axis collimation. As shown in Fig. 7.29, the broad-area emitter bar with dual-axis corrective optics locked with 100% efficiency up to the distance limited by experimental arrangement.

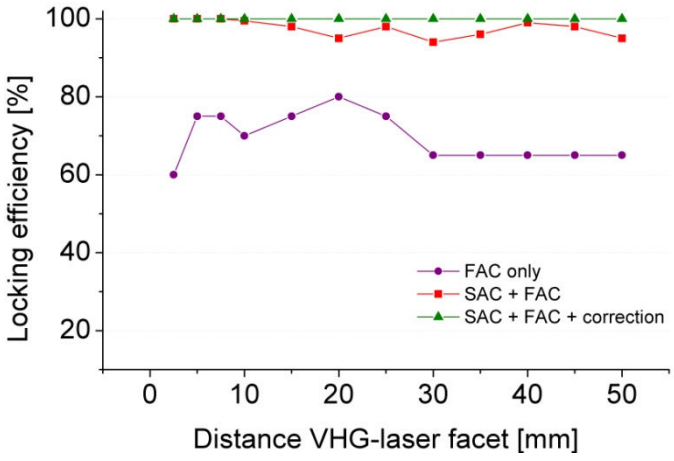


Fig.7.29. Locking efficiency as a function of laser-VHG distance for the bar BBA. Driving current was 40A and temperature on the CS mount was 26˚C.

## 7.6 Summary

The experiments presented in this chapter revealed that the effectiveness of wavelength locking of single-mode emitter bars strongly depends on beam quality and co-alignment in both axes. Although the accuracy of beam pointing was less critical for the broad-area emitter bar, the 9 nm locking range and distant locking could only be achieved for the bar with slow axis collimation and fast axis correction. In both cases, the locking efficiency was improved by the dual-axis correction technique, which enabled feedback to be high and uniform along the bar. It has been shown that wavefront compensation can redirect the feedback beam, so that it returns to the laser facet with matching mode field radius - thereby increasing the feedback power coupled into the waveguide mode. The results provide a quantitative guide to the accuracy of the wavefront compensation required for the efficient locking of diode laser bars. It can be concluded that, if the smile is corrected to produce less than 0.8 mrad (that is 0.5 μm smile with 600 μm FL lens), all emitters will be fully locked over a wide range of temperatures and distances. Thus, for applications where a large locking range is necessary, the smile does not need to be fully corrected but minimized. This is an important result for applications where compensators with a fixed pattern smile correction could be provided.

The extended locking range of ±4 nm for the single-mode emitter bar and ±9 nm for the broad-area bar obtained in this project offer significant advantages for various approaches employing the VHG-locking technique. In a practical wavelength locked system containing multiple laser bars, the deviation of the locked wavelength from the bar's natural wavelength for each bar-VHG pair can be imposed by the thermal drift, drive current range and bar-to-bar wavelength variation (normally provide with ±5 nm tolerance). To develop a system that is insensitive to these factors, efficient feedback control must be performed. Moreover, as is shown in the next chapter, a large locking range enables experiments on wavelength selection by angular tuning in a folded cavity configuration.

Optimization of the spatial properties of the beams allows a lower reflectivity VHG or one with more wavelength selectivity to be used for efficient locking. It is important to choose between the level of beam quality improvement and the reflectivity of the VHG to obtain low loss and highly reliable wavelength locking. Using low-scatter laser-written optics to optimize spatial properties of the laser beams has a clear advantage over employing a high reflectivity VHG in a system with non-uniform feedback.

# Chapter 8.
# Wavelength selection and stepping methods for laser diode arrays

## 8.1 Introduction

The work presented in this chapter addresses the challenge of effective wavelength selection for diode laser arrays. The target applications for the techniques developed in this project can be classified into three groups according to their different requirements.

For the first group of applications, including laser pumping and sensing, all the elements in a laser array must be locked to a common, well-specified wavelength. To achieve this, a centre wavelength of a spectrally locked laser is fixed by the nominal wavelength of a spectrally selective coupler. In some cases, accurate wavelength selection obtained with an off-the-shelf wavelength locking output coupler can improve the cost-effectiveness of a system.

The second group of applications covers the laser sources for spectroscopy used for gas sensing [224, 225] or blood tests [226]. For these applications, a full laser array must be locked to a wavelength that can be tuned over a large spectral range. Inexpensive wavelength-tuned diode lasers offer a very attractive solution for many of these applications.

The last group of applications include spectral beam combining systems [13] and multi-wavelength sources [227, 228]. These require the individual elements in a laser array to be locked to different, well-specified wavelengths. Spectral beam combining, in particular, requires narrow bandwidth sources at uniformly spaced wavelength intervals. Generally, whether a laser array is to be fixed to a well defined wavelength, to multiple wavelengths, or tuned over a large spectral range, efficient techniques for wavelength selection are highly desirable.

Wavelength tuning of diode laser arrays has been demonstrated with different techniques. Most commonly, an angular tuning of diffraction grating in a Littrow or Littman cavity configuration is utilized [70, 107-109]. More recently, VHG-based techniques have begun to dominate over the conventional approaches for wavelength locking. These are now of great interest to those working in the field, as they provide efficient techniques for realising VHG-based tunable diode laser arrays. As discussed in

Chapter 3, VHGs can be tuned thermally or angularly. Due to the very limited locking range that can be achieved by thermal tuning of a VHG, the angular tuning approach is used in this work to provide a widely tunable, efficiently locked laser diode bar.

The results on VHG-locking of laser arrays presented in the previous chapter show that dual-axis collimation and fast axis correction allow the uniform locking of all emitters in a laser bar to be maintained over large distances between the VHG and the laser. This creates perfect conditions for experiments on wide-range wavelength selection by the angular tuning of a VHG in a folded cavity configuration. The details of the technique and the results are discussed in Section 8.3.

Part of this work aimed to develop an innovative technique for the wavelength stepping of laser arrays. Based on the same principle presented in Section 8.3, a folded cavity is established individually for each element of the array by using an array of micro deflectors. In this way, the wavelength across the bar can be varied with uniformly spaced, narrow wavelength intervals providing an excellent source for dense spectral combining. To obtain this, the laser-written optics technique, used earlier to provide dual-axis corrective optics (see Chapter 6), was extended even further here to achieve triple functionality by adding an array of deflectors into the dual-axis optics. The concept of wavelength stepping for a laser array is introduced in Section 8.4. Section 8.5 presents results obtained with the first experimental realisation of the wavelength stepped laser array (WSLA) demonstrated with the single-mode emitter bar.

## 8.2 Angular tuning of a VHG

This section introduces the basic principle of angular tuning of a VHG and presents examples of tuning curves measured for some of the VHGs used in this thesis.

The wavelength of a beam diffracted by a VHG for a given angle of incidence is determined by the Bragg condition:

$$\lambda = \lambda_0 \cdot \cos(\theta), \tag{8.1}$$

where θ is an angle of incidence and $\lambda_0$ is the diffraction wavelength at normal incidence. Thus, the Bragg wavelength of the VHG can be tuned by the change of the angle of the incident beam.

The angular tuning of VHGs was investigated for three different gratings with 200 pm bandwidth. The gratings were characterised by different reflectivity of 15%, 25% and 40%. The gratings were provided by Ondax Inc. The tuning curves were obtained by recording the transmission spectra of a broadband source as a function of the angle

of rotation for the VHG. The experimental setup is presented in Fig. 8.1. A 2 mW beam from a superluminescent diode emitting at 960 - 990 nm was collimated to produce a 0.8 mm beam size at the VHG. A part of the beam was diffracted by the VHG and the remaining beam was transmitted through the grating and launched with an input fibre into a high resolution spectrometer. The VHG was mounted on a rotation stage and incrementally rotated to change the angle with respect to the incident beam. For each angle, a ~200 pm wide dip in the transmitted spectrum was recorded at the wavelength satisfying the Bragg condition in Eq. 8.1. Fig. 8.2 shows examples of the transmitted spectra with dips at 972.5 nm and 973.5 nm, corresponding to the rotation of the VHG by 6.2˚ and 5˚, respectively. In this way, the tuning effect could be illustrated by plotting the transmission spectrum as a function of the angle rotation.

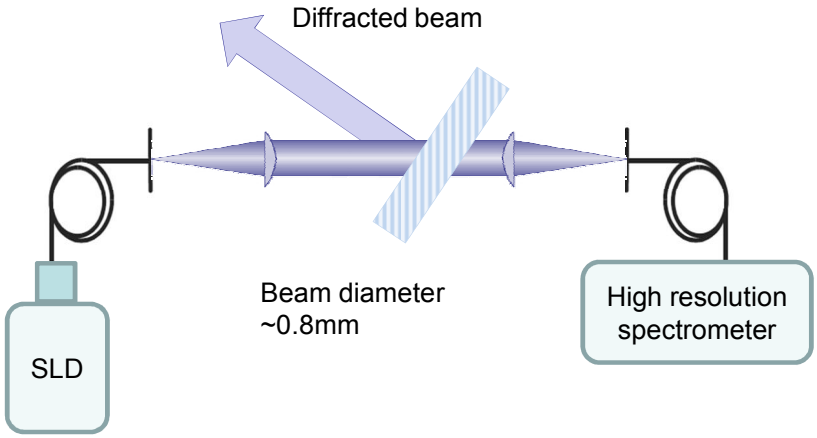


Fig.8.1 Experimental setup for measurement of angular tuning curve of VHGs.

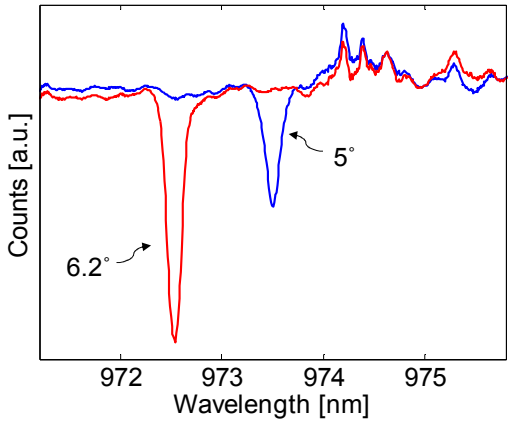


Fig.8.2. Spectra transmitted through the VHG recorded for two different angle of rotation.

Fig. 8.3 shows the results of a spectral transmission measurement performed with a 40% diffraction efficiency and 200 pm bandwidth VHG. The VHG was rotated with 0.22˚ steps from -5˚ to 8˚ from normal to the optical axis. The wavelength of the diffracted beam varied accordingly over the range from 975.2 down to 971 nm. The

recorded angular tuning curve delineated by the blue regions follows the theoretical cos(θ) dependence marked with a red dashed line.

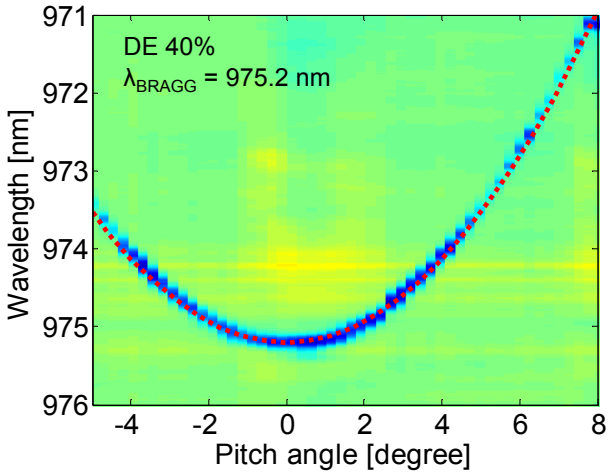


Fig. 8.3. Montage of individual spectra measured at different rotation angles, with the theoretical *cos(θ)* curve superimposed (red dotted line).

It has been observed that at the end of the recorded tuning range the dip in the transmission spectra (as in Fig. 8.2) got shallower indicating that the fraction of diffracted light was reduced. This effect can be explained by the drop of effective reflectivity of the VHG at large angles of incidence for finite size beams [112, 229].

Similar measurements were performed for two other VHGs with reflectivities of 15% and 25%, which were later used in the experiments on wavelength tuning in an external cavity configuration. The measured data confirmed that their angular tuning curves for the two gratings follow the Bragg condition with Bragg wavelengths at normal incidence of 974.4 nm and 976 nm, respectively. The tuning curves for the gratings are illustrated in Fig. 8.4. The data obtained for the gratings provided a calibration curve for the design of the wavelength stepping beam deflector discussed later in Section 8.4.

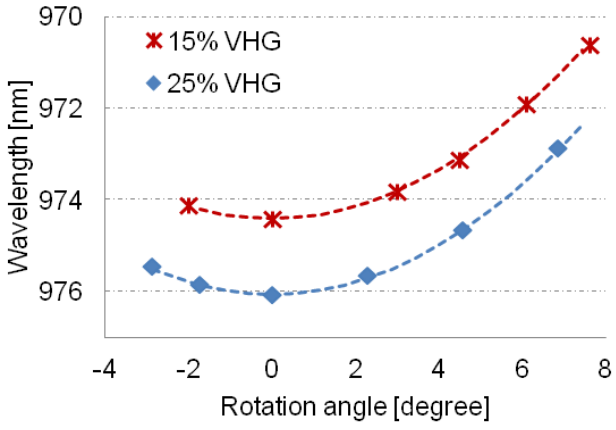


Fig.8.4. Measured tuning curves for two different VHGs.

## 8.3 Wavelength selection in a folded cavity configuration

This section reports on wavelength selection for a full size diode laser array performed in a folded cavity configuration that employs an angularly tuned VHG. The angular tuning of VHG-locked diode lasers reported previously by Moser *et al.,* was based on the 'cat's eye' configuration (see Chapter 3) with a FAC-lens and provided a limited range of angular tuning of 1 nm for a single VHG-locked diode laser [121] and about 0.6 nm range tuning for a 19-broad-area emitter bar [125]. Here, the limitations of this technique are overcome by placing the folding mirror beside the collimating optics, so that the angular range for the feedback beam is not constrained by the aperture of the lens. A similar approach was earlier applied in configurations with fibre lasers [129] and optical parametric oscillators [127]. The results presented in Chapter 7 show that the robust wavelength locking achieved due to good beam quality of the laser array with dual-axis corrective optics now enables such an approach to be applied to a full size laser array. In particular, high pointing accuracy and good collimation in both directions allows for a sufficient level of feedback to be maintained for all emitters over a wide range of detuning from the natural wavelength of the laser. Efficient 'distant locking' allows the optimal arrangement of the external cavity to be obtained without loss in locking efficiency. The next section discusses the folded cavity configuration and the results obtained with a single-mode emitter bar.

### 8.3.1 Folded cavity architecture

The external cavity configuration used for wavelength selection for a full size diode laser bar is shown in Fig. 8.5. The cavity consisted of the laser bar with dual-axis collimation optics, the 15%-reflective VHG and a HR-coated silica plate acting as folding mirror. The laser used in this experiment was the single-mode emitter bar BSM3. As described earlier in Chapter 6, the spatial properties of the beams were determined by the dual-axis collimation and correction provided by the laser-written optics resulting in high pointing accuracy across the bar and good dual-axis collimation.

The VHG was mounted on a 3-axis rotation stage and placed at a distance L from the exit surface of the slow axis collimating lens. The rotation of the VHG redirects the off-axis diffracted beam towards the folding mirror placed beside the collimation optics of the bar. The change of angle between the VHG and the incident beam leads to tuning of the diffraction wavelength, as shown in the previous section. The diffracted beam (oblique to the incident beam) is reflected from the folding mirror, diffracted a second time and sent through the collimation optics which focuses it on the exit aperture of an

emitter. In this way, the diffracted beam is counter-propagating with the initial laser beam. To ensure feedback in the folded cavity, the angle of rotation of the folding mirror is adjusted for each orientation of the VHG.

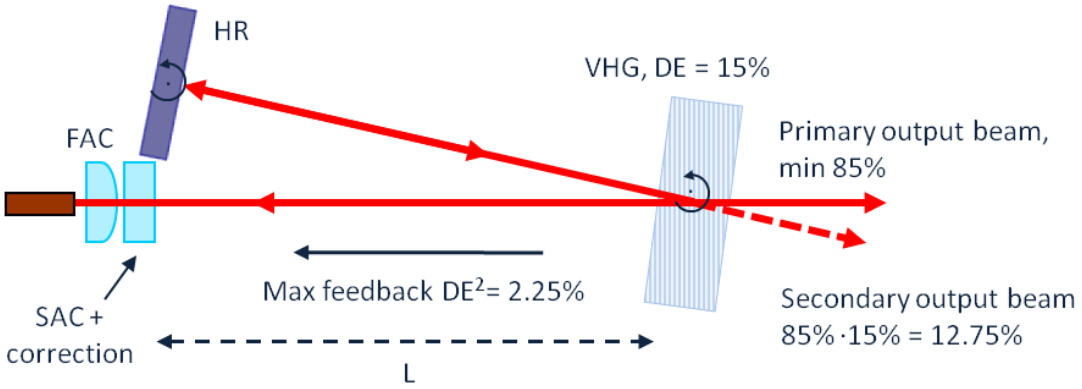


Fig. 8.5. Scheme of the experimental setup for wavelength selection in a folded cavity with a VHG.

The range of available wavelengths is determined by the maximum acceptable detuning from the natural wavelength of the laser and the range of achievable angles of incidence. The detuning range is related to the amount of feedback provided and the tuning capability of the laser. In such a configuration, the feedback beams are diffracted by the VHG twice before they are sent back to the emitters. In this double diffraction arrangement, the maximum diffraction efficiency scales as $DE^2$, where DE is the nominal diffraction efficiency of the VHG. This leads to a decrease of the available feedback. Thus, it is very important to provide the maximum possible feedback by ensuring good beam co-alignment and collimation.

The range of angles of incidence for which the beams reflected from the VHG can be efficiently fed back into the emitters is determined by the spatial properties of the beams and the geometry of the folded cavity. The minimum angular detuning from the wavelength at normal incidence is determined by the gap between the folding mirror and collimating optics, but is minimized when the VHG is at a large distance from the laser. Here, the VHG was placed 35 mm from the laser. Sufficiently high feedback with the distant VHG could be obtained due to the excellent spatial properties of the beams, as discussed in Chapter 7.

### 8.3.2 Experimental results on wavelength selection

Fig. 8.6 shows the experimental results on the wavelength selection obtained with the single-mode emitter bar. The wavelength of the locked bar was measured as a function of the angle of rotation of the VHG. The grating was angularly tuned over a 12 degree range, producing wavelength selection over an 8.5 nm band. The maximum detuning

range achievable in this configuration was measured to be approximately 4 nm. The experiment was repeated at two different temperatures on the CS mount.

When the laser was set to operate at 14.4˚C, the natural lasing wavelength was matched with the centre of the tuning range, thereby maximizing the range of wavelengths that could be obtained. Fig. 8.6 (b) shows the spectral images recorded at points A and B marked in Fig. 8.6 (a) with circles. They confirm that the wavelength of the bar can be tuned over a range of 8 nm with all emitters remaining nearly-100% locked.

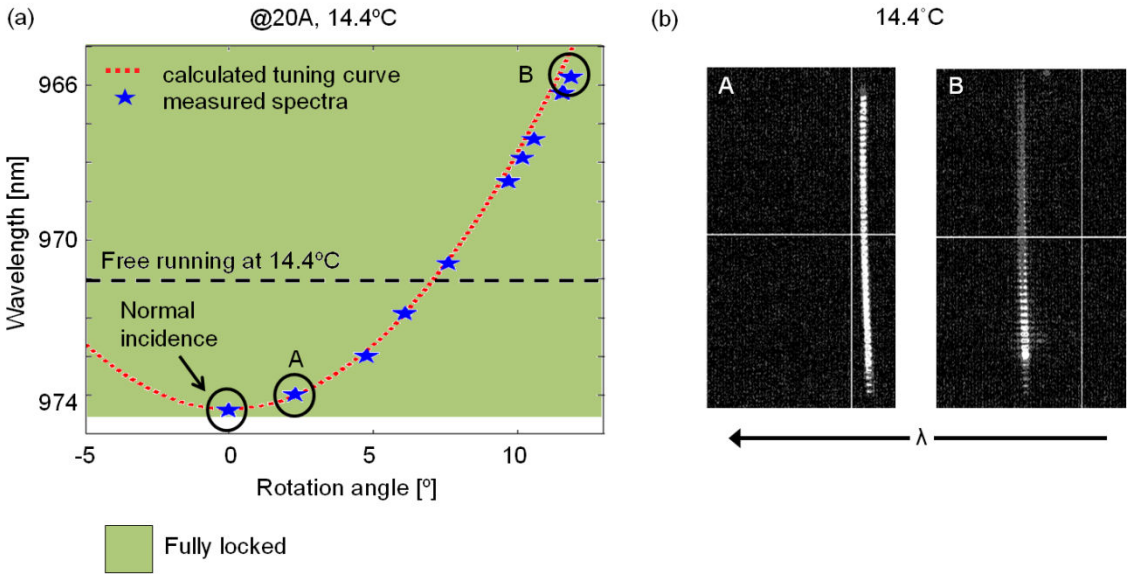


Fig. 8.6. (a) Wavelength measured as a function of angle of rotation of the VHG in the folded cavity configuration. (b) Imaging spectrometer view of the angularly tuned spectra at chosen points A and B in graph (a).

Fig. 8.7 (a) shows the results of similar measurements made with the laser temperature set to 23.3˚C, where its free running wavelength was about 973 nm. The measurement point D corresponds to 7.2 nm detuning from the Bragg wavelength of the VHG. The emitter resolved spectrum of the bar recorded at point D shown in Fig. 8.7 (b) illustrates the partial locking that is obtained beyond the full locking range obtained in this configuration. These results indicated that it is important to match the operating conditions for the laser with the Bragg wavelength of the VHG to obtain maximum range of wavelengths with a given laser-VHG pair. Alternatively, an appropriate VHG could be selected to match the wavelength of the laser at its nominal operation conditions.

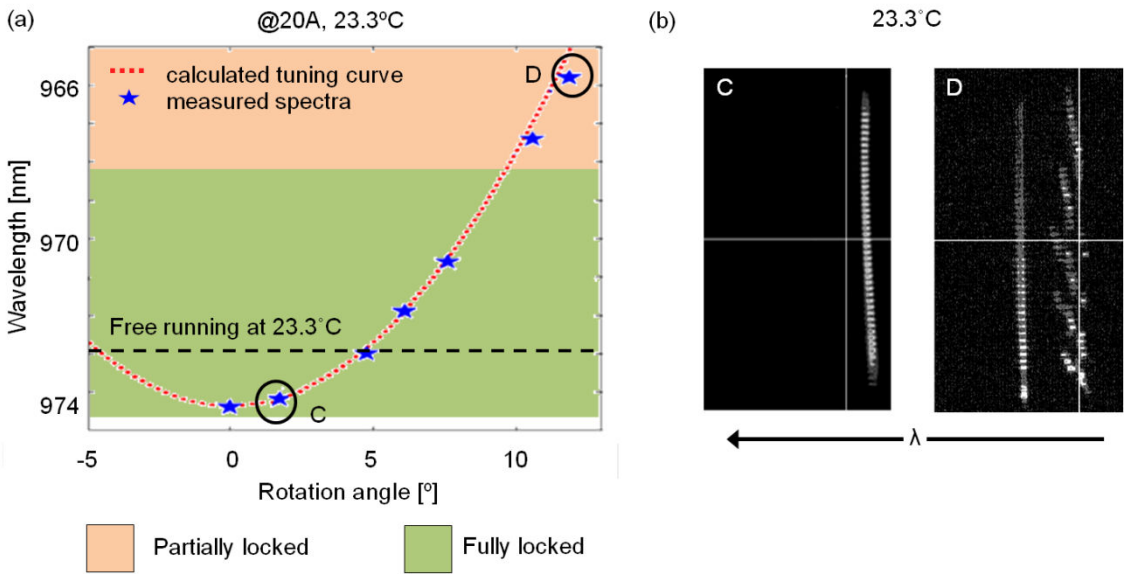


Fig. 8.7. (a) Wavelength measured with high resolution spectrometer as a function of angle of rotation of the VHG in the folded cavity configuration. (b) Imaging spectrometer view of the angularly tuned spectra at chosen points in graph shown in Fig. 8.7.

It is also worth noting that the ±4 nm of maximum acceptable detuning from free running wavelength of the laser obtained in the folded cavity is smaller than the over 5 nm of locking range reported in Section 7.5.3 for locking at normal incidence onto the VHG. This may be explained by the reduced feedback in the folded cavity configuration due to the double diffraction arrangement and the drop of effective reflectivity of the VHG at larger angles of incidence, as mentioned earlier in Section 8.2.

The results presented in this section demonstrate robust locking of the single-mode emitter bar into a wavelength selectable from an 8.5 nm spectral range using a single VHG. The power loss in the folded cavity configuration is mainly determined by the reflectivity of the VHG and was measured to be less than 15% in the case investigated in this work. Based on the results on VHG-locking of broad-area emitters presented in Chapter 7, it can be assumed that the tunability range would be even larger if the technique was applied for a standard broad-area bar. Future work could include repeating the experiment for a standard broad-emitter bar.

## 8.4 Wavelength stepping for VHG-locked bar

The aim of this part of the work was to vary wavelength across a laser array using a standard uniform VHG. The approach presented in this chapter has the potential to replace the use of expensive chirped VHGs for multi-wavelength sources for spectral beam combining.

### 8.4.1 Concept of wavelength stepping by a deflector array

Here, the concept of wavelength selection in a folded cavity is extended by forming a slightly different folded cavity for each element (or group of elements) in the laser array using an array of beam deflectors. Each of the folded cavities has an angular arrangement satisfying a different Bragg condition so that it provides feedback at a different wavelength. In this work, the deflector array is combined with the dual-axis corrective optics introduced in Chapter 6, into a single optical component. However, for simplicity the concept of wavelength stepping is illustrated for a simple case, where the function of the deflectors is delivered by separate components. The principle of this approach is presented in Fig. 8.8.

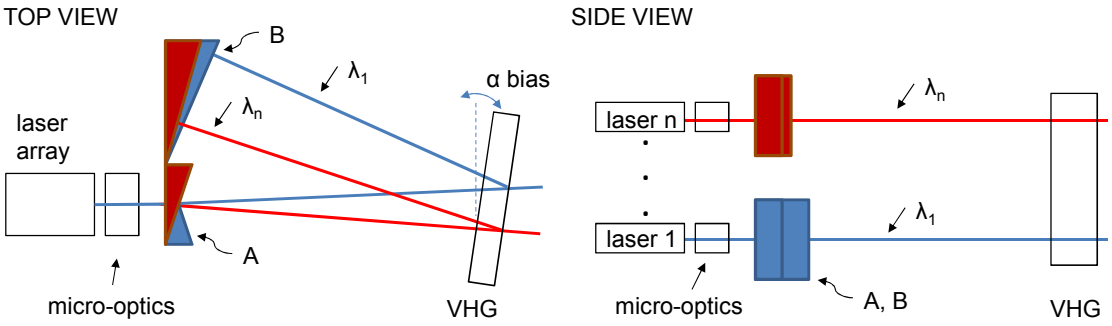


Fig. 8.8. Concept for wavelength stepping in a laser array; A,B - beam deflecting/reflecting prisms.

The individual cavities are formed by paired prisms as marked with A and B in Fig. 8.8. Prism A refracts a beam to be incident upon a VHG at an angle corresponding to an appointed Bragg wavelength. The VHG tilted by $\alpha_{BIAS}$ reflects a portion of the beam towards the HR-coated prism B, which acts as a folding mirror. The prism B sends the feedback beam back into the VHG along the same trajectory. The spectrally filtered feedback beam is then diffracted back towards the collimating optics of the laser and coupled back into the apertures of the emitter. Such a cavity is formed for each element in the array (or group of elements) individually with paired prisms A and B conforming to a different Bragg condition.

The range of wavelengths and corresponding angles is chosen based on angular tuning curve of the VHG. For a reflective VHG the tuning curve is symmetric with respect to normal incidence. The VHG is tilted by a bias angle ($\alpha_{BIAS}$) and the angles of individual beams ($\theta_i$) are varied around that value, as illustrated in Fig. 8.9. This produces feedback at the appointed wavelength ($\lambda_i$).

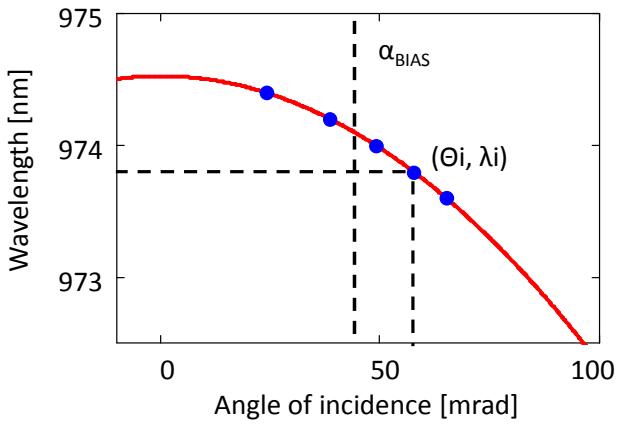


Fig. 8.9. Principle of selecting wavelengths/angles for individual elements in a laser array.

The concept of wavelength stepping for a diode laser bar can be realized in different ways, depending on the geometrical limits for a given set of parameters, including wavelength step and number of emitters. Fig. 8.10 illustrates the two basic variants for the arrangement of the deflector arrays.

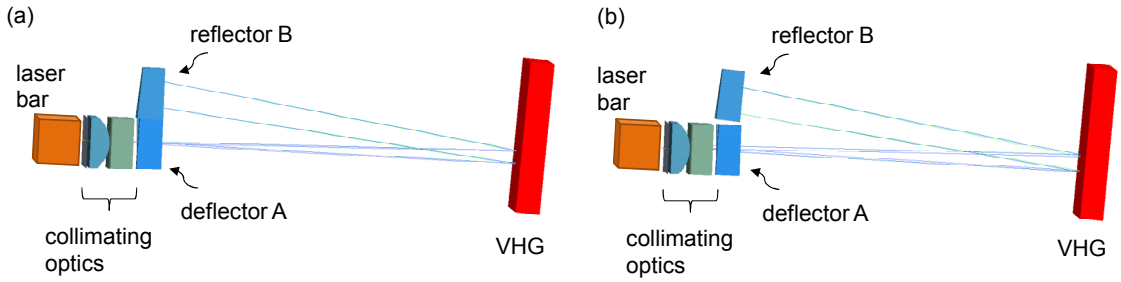


Fig. 8.10. Wavelength stepping configurations: (a) deflector A and reflector B combined into a single component, (b) separate deflector A and reflector B.

In the first variant shown in Fig. 8.10 (a), an array of laser-written deflectors is integrated so that deflector A and reflector B (see Fig. 8.8) are integrated into a monolithic component. The advantage of such an approach is high compactness. However, the structure of the deflector B needs to compensate for the bias tilt of the VHG and requires a large cutting depth.

To avoid this problem the plates B can be separate from plates A and tilted to compensate for the bias of the VHG, as illustrated in Fig. 8.10 (b). In such an arrangement, both deflectors are easy to cut with the laser technique discussed earlier. The downside of the approach is separate alignment is required for both components.

In this work, the deflectors A are combined with fast axis correction and slow axis collimation into a single optical component and the function of deflectors B is delivered by a rotating (i.e. tilting) mirror, as explained later in this chapter.

### 8.4.2 Design considerations of a deflector for wavelength stepping

The design of a λ-stepped laser diode array needs to account for the properties of the laser array and the capabilities of the laser-written optics technique used for manufacturing of the deflectors.

The essential parameters of the design are the range of wavelengths and the corresponding angles of incidence on the VHG. The smaller the angular range, the easier it is to produce the beam deflectors with high accuracy, as the required cutting depth is smaller. Moreover, for a large angular spread of the beams, the positional spread of the beams at plate B is also correspondingly large. Consequently, the manufacturability of the wavelength stepped laser array depends on the wavelength spread. Thus, for a given size of wavelength interval (determined by the linewidth of a locked laser, if spectral overlap is to be avoided), the difficulty increases with the number of emitters to be spectrally stepped. Therefore, for the first prototype of a WSLA, performed for a 49-emitter bar, only 5 and 7 wavelength steps were used to minimize the cost and lead time for the first demonstration (see later in Section 8.5).

It is also worth noting the tilt of the VHG determines the position on the tuning curve and thus the dependence between the angular and spectral spread of the beams. It is desirable to choose the fragment of the tuning curve were the maximum wavelength range can be obtained for a given angular spread. However, it is also necessary to account for the drop in diffraction efficiency at large angles of incidence on the VHG, as discussed in Section 5.3.5 and in [112, 229]. Finally, the angle of the VHG needs to be large enough to ensure that the diffracted beams do not hit the collimation optics of the λ-stepped bar.

Similarly to all above parameters of the design, the length of the cavity interacts with the limits for the rest of the parameters. The longer cavity, the larger beam spread at the VHG and plate B. Also, as discussed in Chapter 7, the larger the distance between the VHG and the laser, the smaller the fraction of the diffracted light that is fed back into the emitters. The lower limit for the cavity length is the minimum distance for which the diffracted beam avoids the collimating optics in the first half of the round trip for a reasonably small angle of incidence on the VHG. The same limit was encountered in the experiment with the folded cavity described in Section 8.3, where the cavity had to be long enough to allow a small detuning to be obtained without beam truncation on the collimation optics.

## 8.5 Optical testing of a λ-stepped single-mode emitter bar

For the first experimental realisation of a λ-stepped laser array, the deflectors in plate A were designed to be combined with a dual-axis corrective optics (see Chapter 6) and optically tested with the 49 single-mode emitter bar (BSM3), introduced in Chapter 6.

In the experimental evaluation of the technique for λ-stepping, two simplifications were introduced to the approach illustrated in Fig. 8.10 (b). Firstly, the wavelength was stepped for groups of emitters in the bar to keep the angular spread of beams small. Secondly, the role of plate B was realized with a rotating mirror made of an HR-coated silica glass. In the configuration shown in Fig. 8.11, a folded cavity for one of the angles produced by the array of deflectors A was formed at a time. Using the simplified approach aimed to provide a proof of concept in a quick and inexpensive manner.

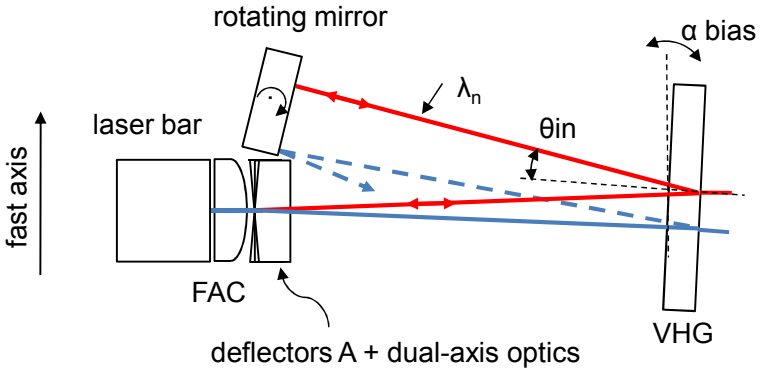


Fig.8.11. Experimental setup for the first demonstration on wavelength stepping for laser diode array.

The array of deflectors A was designed to deflect subgroups of emitters in the bar by a slightly different angle. In this way, each group of emitters was deflected and then is diffracted into a slightly different angle and wavelength towards the rotating mirror. The rotation of the mirror enables the locking of the emitters in the bar group-by-group. For a fixed position of the VHG, each of the groups is locked to a different wavelength once the angle of the rotating mirrors is appropriately aligned.

For this experimental demonstration, two different arrays of deflectors were designed and manufactured: a 5-section and 7-section array of deflectors, both incorporating deflection, slow axis collimation and fast axis correction. Based on the design provided by the author, the laser-written plates were manufactured by PowerPhotonic Ltd. The results of the optical testing of the components are discussed in the following sections.

### 8.5.1 5-section beam deflector combined with a dual-axis corrective optics

Fig. 8.12 shows a surface map for a 5-section beam deflector combined with an SAC array and fast axis correction. Each section was designed to deflect a group of 10 emitters into a common angle in the fast axis direction, which was different for each group.

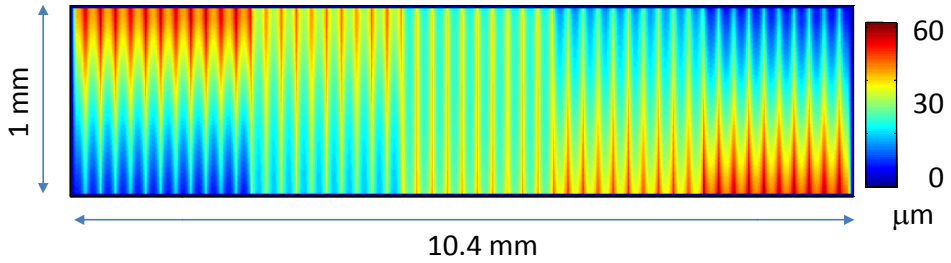


Fig. 8.12. Design of a 5-section beam deflector combined with dual-axis corrective optics.

Fig. 8.13 shows a far field pattern and emitter resolved far field pattern for the full bar with a 5-section beam deflector combined with dual-axis corrective optics. In the fast axis direction, the expected pointing difference between the groups of emitters was recorded. In the slow axis direction, noticeable tails in the far field patterns and unintended change in the slow axis pointing were revealed. The peak-to-valley slow axis pointing error was measured to be 7.9 mrad. The deflectors combined with fast axis correction and slow axis collimation required a large cutting depth. At the time when the plates where manufactured, the deep structures could not be cut with sufficient accuracy. As a consequence, the SAC lenses were highly distorted (very asymmetric, leaning) resulting in pointing error in the slow axis.

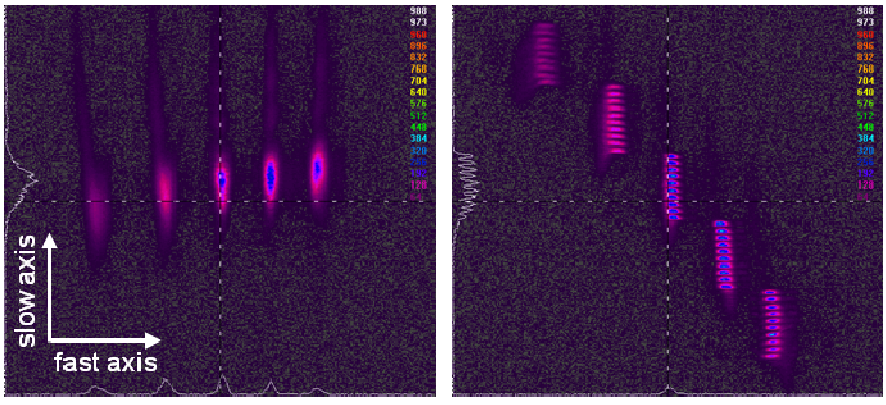


Fig. 8.13. Far field pattern of full bar (a) and emitter resolved fast axis far field image (b) for the bar with the 5-section beam deflector.

The results show that combining a deflector with SAC and fast axis correction makes the laser cutting of the structure challenging and requires further improvement. Since these experiments were conducted, PowerPhotonic Ltd has significantly improved

their process for optics manufacturing and currently similar optics can be produced with much better accuracy.

Despite the reduced performance of the slow axis lenses, the experimental concept of λ-stepped laser array was demonstrated. The 25% reflectivity VHG, introduced in Section 8.2, was placed in front of the laser with the deflector arrays and aligned to form an external cavity with the group of emitters pointing on-axis (group 3). In this way, all of the emitters in the group were fully locked to a narrow line at 976.05 nm. Subsequently, the VHG was tilted by approximately 79 mrad ($\alpha_{BIAS}$) to send the beams towards the mirror placed beside the fast axis collimating lens, as illustrated in Fig. 8.11. From then on, the angle of the VHG remained fixed, and the folding mirror was rotated to form a cavity for each group of emitters ensuring the diffracted beams are sent back to the emitters. Fig. 8.14 shows the emitter resolved spectra of the bar (measured with the setup shown in Chapter 4, Fig. 4.7) for different alignments of the folding mirror.

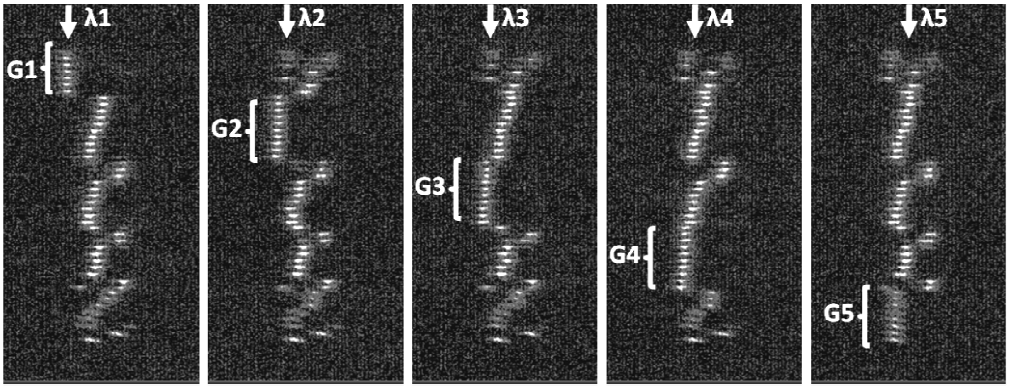


Fig. 8.14. Emitter resolved spectra of the bar with the λ-stepping deflector for one out of 5 groups locked at once. The laser bar operated at 10A of drive current and 23˚C on the CS mount.

The laser operation conditions were chosen to tune the natural wavelength of the laser to proximity of the VHG wavelength. It was observed during this experiment, that the locking range was much smaller than that achieved in Section 8.3. This is due to the fact that the VHG is tilted by a relatively large angle, which reduces the effective reflectivity of the VHG. Additionally, the slow axis beam distortion may also affect the feedback efficiency.

The peak wavelength for each locked group was measured with a high resolution, spectrometer using the setup shown in Fig. 4.6. The actual average pointing angle for each of the groups was measured using the configuration for beam selection shown in Fig. 4.5. Using this set of data, the wavelength measured for each group and the

theoretical wavelength calculated for the measured pointing angle of the beams (see Eq. 8.1) was plotted in Fig. 8.15.

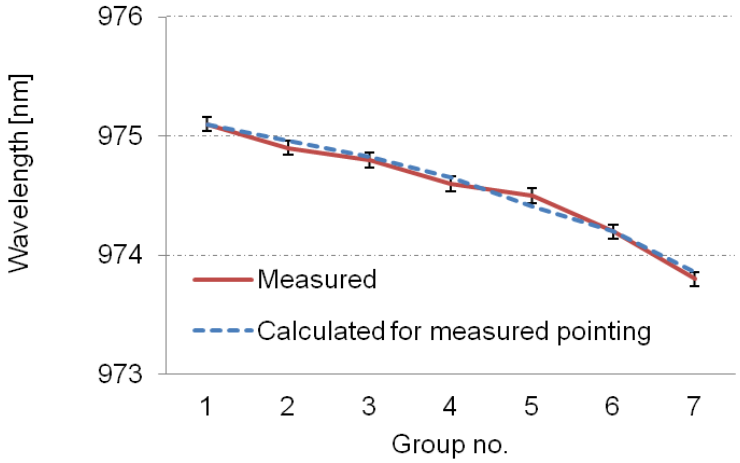


Fig. 8.15. The peak wavelength measured for the 5 groups of 10 emitters compared with the theoretical wavelength calculated for the measured pointing direction.

The wavelength spread within the bar was 0.9 nm. It is worth noting, that both the slow and fast axis pointing directions contribute to the tuning of the Bragg wavelength of the VHG. The folding mirror has to compensate for angles in both directions to ensure maximum feedback. The error bars in the plot correspond to the uncertainty of the wavelength measurement associated with the 60 pm resolution of the SPEX spectrometer (see Section 4.2.2).

The determination of error for the measurement of average pointing for groups of emitters is difficult. As seen in Fig. 8.13 (a), the far field patterns have a very irregular shape and the measurement of the centroid may provide slightly ambiguous results. Even with limited accuracy, however, the results clearly show the behaviour of the emitters that are locked by the angularly tuned VHG. For better results, the issue of slow axis beam degradation must be resolved, but the first results are very encouraging.

### 8.5.2 7-section beam deflector combined with a dual-axis corrective optics

Fig. 8.16 shows the cutting map for the wavelength-stepping beam deflector with 7 sections. This time, the emitters are divided into 7-emitter subgroups.

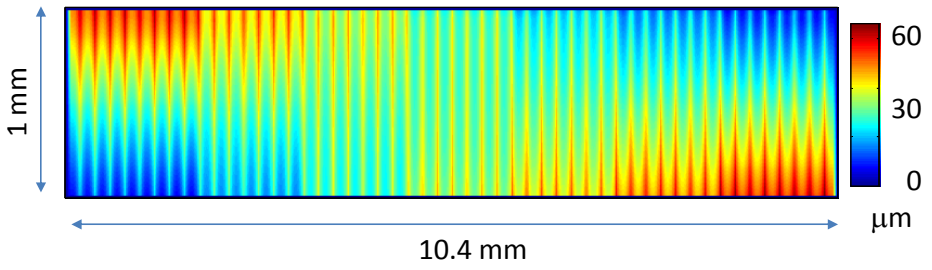


Fig 8.16. Design of a 7-section beam deflector combined with dual-axis corrective optics.

The component was optically tested with the single-mode emitter bar, following the same procedure described in the previous section. The far field patterns are presented in Fig. 8.17. Similarly to the previous case, lens distortion affected the pointing angle and beam profile in the slow axis direction. A slow axis pointing variation of 6.6 mrad (peak-to-valley) was recorded.

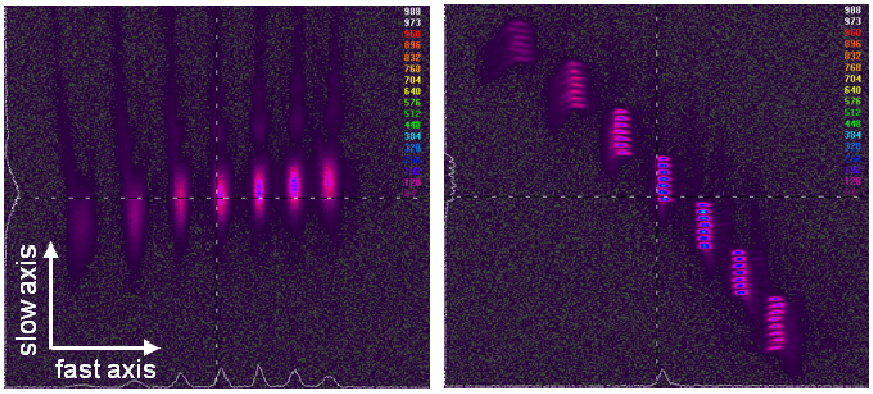


Fig. 8.17. Far field pattern of full bar (a) and emitter resolved fast axis far field image (b) for the bar with the 7-sections beam deflector.

For the VHG tilted by a bias angle of 82 mrad, the rotation of the folding mirror was used to lock the subsequent groups of emitters into different wavelengths. The wavelength measured for each group with the high resolution SPEX spectrometer along with the wavelength calculated for the measured average pointing of each group is plotted in Fig. 8.18. For this case, a wavelength range of 1.3 nm across the bar was obtained. Similarly to the results for 5-section beam deflector, good agreement with the expected wavelengths was achieved.

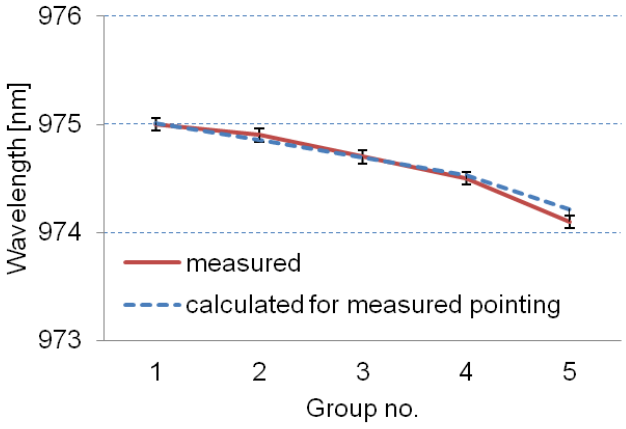


Fig.8.18. The peak wavelength measured for the 7 groups of 7 emitters compared with the theoretical wavelength calculated for the measured pointing direction.

## 8.6 Summary

The results on wavelength selection in the folded cavity show that efficient, low loss locking can be achieved to any wavelength over a range of 8.5 nm. This is, to the knowledge of the author, the best result obtained with a full size laser diode array. Such performance gives an advantage for systems where the flexibility of choosing the right wavelength is desirable without expensive customisation of the wavelength locking components.

The results obtained with the folded cavity encouraged further extension of the technique towards wavelength stepping for laser diode arrays. The experiments with the first prototypes of wavelength stepped arrays confirmed the feasibility of the approach and exposed areas that require further improvement. In the next generations of the wavelength stepped laser arrays, the bias angle of the VHG must be reduced so the drastic drop off in efficiency can be avoided. The shape errors can be easily improved in the next iteration of the design and manufacturing process. Once this issue is resolved, such a triple-function component can provide wavelength stepped laser array with dual-axis collimation with no additional penalty for the power loss.

Alternatively, better performance of the wavelength-stepping beam deflector can also be obtained by reducing the errors in the surface shape. This can be done either by fabricating it as a monolithic element using a more accurate process or by assembling it from discrete wedge elements, and applying it to an ultra-collimated laser array. In this way, the errors in surface shape can be easily eliminated.

In the future, multi-wavelength laser arrays locked with standard VHGs should provide excellent sources for spectral beam combining methods employing transmitting VHGs [143, 230] or diffraction gratings [13, 65].

# Chapter 9.
# Phase-locking of single-mode emitter bar

## 9.1 Introduction

Over the last few decades a number of different attempts at the phase-locking of laser diode arrays have been reported, including active methods employing complex algorithms for electronic control of the phases of individual elements [166] and passive methods based on self-organising external cavities [158, 159, 182] or phase gratings [231, 232]. However, the mutual coherence of all elements in large, high-power arrays has not so far been achieved.

As discussed in Section 3.6, the quarter-Talbot cavity is a particularly promising approach for fully passive phase-locking of laser diode arrays, ensuring maximum discrimination between the in-phase and out-of-phase modes [170]. Recent developments in phase-locking in Talbot cavities provided encouraging results with coherent output at multi-Watt power levels. In Ref. [159], a 10-element array of tapered emitters coherently combined in a VHG-based quarter-Talbot cavity provided 1.2 W of highly coherent output beam. Huang *et al.* [157] reported on a quarter-Talbot cavity formed for a 10-emitter array of individually addressed single-mode SCOWL emitters (introduced in Section 2.4.4), where an output of over 7 W was achieved for a low fill factor collimation case and 2 W was obtained for the same bar with a micro-lens array producing a high fill factor. There were also reports of phase-locking experiments performed with full size broad-area emitter bars. In Ref. [158], off-axis feedback from a half-Talbot cavity was used to coherently lock an array of 47 broad-area emitters and resulted in a high visibility interference pattern in the far field recorded for the full bar at 12.8 W of output power. However, the reported width of the interference peaks was 15 times wider than expected for the 47 coherently combined emitters, indicating that locking into independent sub-groups within the bar had been observed.

Despite the noticeable progress, the phase locking of large, high fill factor arrays obtained in a simple configuration that enables robust locking at high drive current remains an unattained challenge for research on the phase-locking of diode lasers. The main inhibiting factors for the phase-locking of large arrays are often attributed to spectral detuning and spatial non-uniformities [180, 233].

The objective of the work presented in this chapter was to explore the behaviour of a high fill factor 49 single-mode emitter bar in a quarter-Talbot cavity configuration. Here, the dual-axis laser-written optics introduced in Chapter 6 is used to ensure uniform feedback across the bar by providing high accuracy collimation. The quarter-Talbot cavity is formed with a VHG acting as an output coupler. In such a configuration, the spectra of all emitters in the bar are efficiently locked into a narrow bandwidth, so that the performance of the phase-locking is not affected by the wavelength spread across the bar and thermal tuning. As shown in Chapter 7, wavelength locking for the ultra-collimated bar can be obtained over a wide range of spectral detuning and maintained at large distances between the laser and the VHG. This is particularly important for the experiments, where good feedback across the bar must be maintained for the VHG placed at the relatively large quarter-Talbot distance of 20.5 mm for the bar used.

This chapter is organised as follows. Section 9.2 introduces the experimental configuration of the quarter-Talbot cavity formed for a 49 single-mode emitter bar. Section 9.3 presents results on phase-locking obtained for the full aperture 49-emitter bar. Section 9.4 describes the experiments and observations performed on the locking of subgroups of emitters selected from the bar. Sections 9.5 and 9.6 present the results of locking experiments at higher drive currents and the locking of a larger number of emitters, respectively. A summary of the chapter is presented in Section 9.5.

## 9.2 Quarter-Talbot cavity configuration

The laser used in this work was the 49 single-mode emitter bar, labelled earlier in Chapter 6 as BSM3. The 6 μm wide emitters are spaced by 200 μm. The internal cavity length of the emitters is 3.6 mm, which leads a 40 pm longitudinal mode spacing. For the purpose of these experiments, the front facet of the bar was AR-coated. However, due to the high gain in the active region, the residual reflectivity ($\sim 10^{-4}$) is sufficient to maintain lasing for the free running bar, as mentioned in Section 6.3.

The bar was fitted with a 600 μm FAC lens and dual-axis corrective optics, providing smile correction and a 900 μm SAC lens array. The correction reduced the fast axis pointing angle variation across the bar to less than 100 μrad. In the slow axis direction, an angular spread of about ±2 mrad (approximately 10% of the far field divergence) was produced as the result of a slight pitch mismatch between the lens array and the laser bar. The pitch mismatch issue was discussed in more detail in Section 6.7.

For the 0.9 mm focal length of the slow axis collimating optics, the beam size at the lenses was approximately 170 μm. As far as phase-locking is concerned, the high fill factor of the laser array is desirable, since it leads to a smaller number of interference peaks being obtained in the far field. On the other hand, the low divergence of the emitters allows for less interaction between the beams and may reduce the strength of coherent locking.

The Talbot distance for the bar is $2p^2/\lambda \approx 82$ mm, where $p$ is the emitter spacing. The quarter-Talbot cavity was formed with a reflecting VHG acting as an output coupler. The VHG placed at 20.5 mm from the front surface of the SAC lens array, as illustrated in the Fig. 9.1. In this way, the Talbot imaging which is a consequence of the Fresnel diffraction of the beam propagating in a uniform medium (in this case in air), occurs for the periodic light distribution at the plane of the lens array. After one round trip propagation between the lens array and the VHG, a self-image is produced back at the lenses, which is then focused at the laser facet.

The VHG used in these experiments has a nominal reflectivity of 25% at 976 nm with a spectral FWHM bandwidth of 200 pm and angular selectivity of approximately 42 mrad (FWHM). The experimental setup is entirely passive. No active thermal control was applied to the VHG.

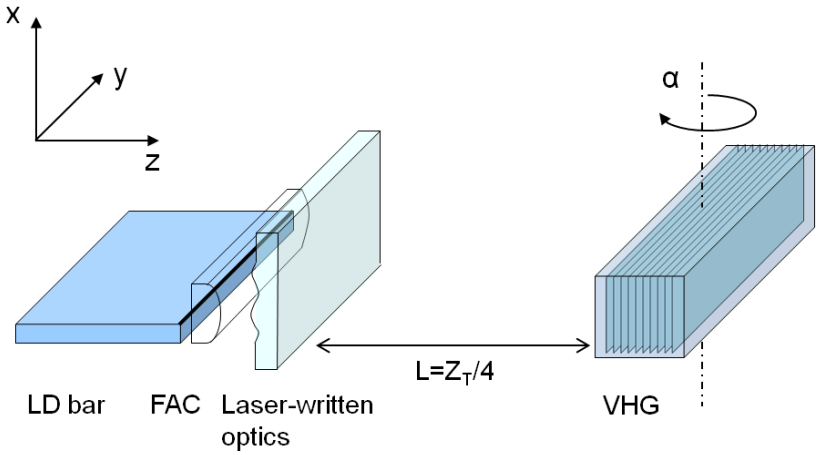


Fig. 9.1. Experimental configuration of the quarter-Talbot cavity.

## 9.3 Locking of the full 49 single-mode emitter bar

In this section, the behaviour of the full 49 single-mode emitter bar in the external cavity configuration introduced is studied in Fig. 9.1. The far field patterns presented in Fig. 9.2 were recorded in a measurement setup similar to that shown in Fig. 4.2, where a 1 m spherical lens (now placed behind the VHG) is used to produce a far field pattern at a rotating screen. The far field pattern was then recorded with a CCD camera.

Fig. 9.2 (a) presents the far field pattern for the free running bar recorded at 10A of drive current and 23.5˚C. At this current level, the bar produces 7 W of output power. A nearly Gaussian beam with asymmetrical tails is produced by the slightly distorted 900 μm focal length slow axis lenses, as discussed in Chapter 6.

For the same operating conditions, the VHG was placed at the quarter-Talbot distance from the front surface of the SAC lens array, as shown in the Fig. 9.1.It was aligned for normal incidence, so that out-of-phase mode distribution shown in Fig. 9.2 (b) was observed in the far field. The pattern exhibits two main peaks spaced by $\lambda/d$ = 4.88 mrad, providing evidence of out-of-phase mode operation. The power of 5.3 W measured for the locked bar was about 25 % lower than the power obtained for the free running bar at the same current level.

Fig. 9.2 (c) shows the far field distribution recorded for the VHG tilted by $\alpha \approx$ 2.44 mrad (= $\lambda/2d$). As expected (see Section 3.6), the far field distribution forms a pattern characteristic for in-phase mode operation.

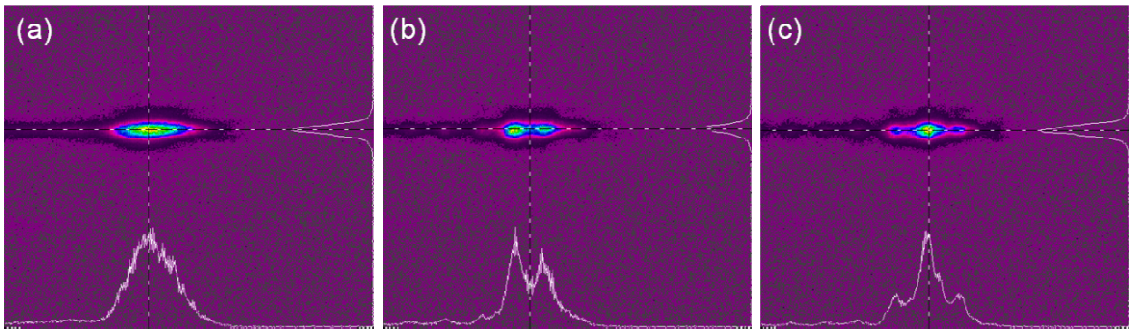


Fig. 9.2. Far field patters measured at 10 A for (a) unlocked bar, (b) bar locked in quarter-Talbot cavity at normal incidence at the VHG, (c) bar locked in quarter-Talbot cavity with the VHG tilted by 2.44 mrad.

In both cases, the intensity distribution is still significantly different from theoretical predictions. The far field patterns exhibit low visibility of about 36% which indicates the appearance of incoherent components in the output beam. The full-width half-maximum width was measured to be about 2.8 mrad, which is 28 times the diffraction limit for the 49 coherent sources.

The results thus show low effectiveness of the coherent locking. There are many potential reasons for coherence degradation. In the experiments with linear arrays of waveguide $CO_2$ lasers presented in [233], it was shown that in large array phase-locking, subgroups of emitters tend to lock into separate, mutually incoherent supermodes. As a consequence, the coherence of the overall output beam is reduced. The break-up into subgroups of locked emitters within a large array may be attributed to geometrical imperfections, which produce non-uniformity in the longitudinal mode structure as well as the spatial properties of individual beams. It is thus difficult to

coherently combine a large number of emitters, due to the challenge of keeping them all uniform in both spectrum and propagation direction.

In order to investigate how different sections of the laser array contribute to the overall far field pattern, a specially constructed beam selector was placed outside the external cavity to view the far field pattern formed for only a selected group of emitters at a time. The experiment and performed observations are discussed in the following section.

### 9.3.1 Viewing subgroups of emitter in the locked bar

In the setup shown in Fig. 9.3, the full bar locked in the quarter-Talbot cavity is scanned by an adjustable beam selector formed by a pair of prisms (see Section 4.2.1.3) in order to investigate the effect of local phase-locking within the bar. The selector is placed after the VHG so that the self-imaging effect inside the cavity occurs for the full bar, while the far field pattern is observed for only a subgroup of selected emitters at any one time. In this experiment, the slit of the beam selector is adjusted to select seven emitters and send the beams from the rest of the emitters to beam dumps.

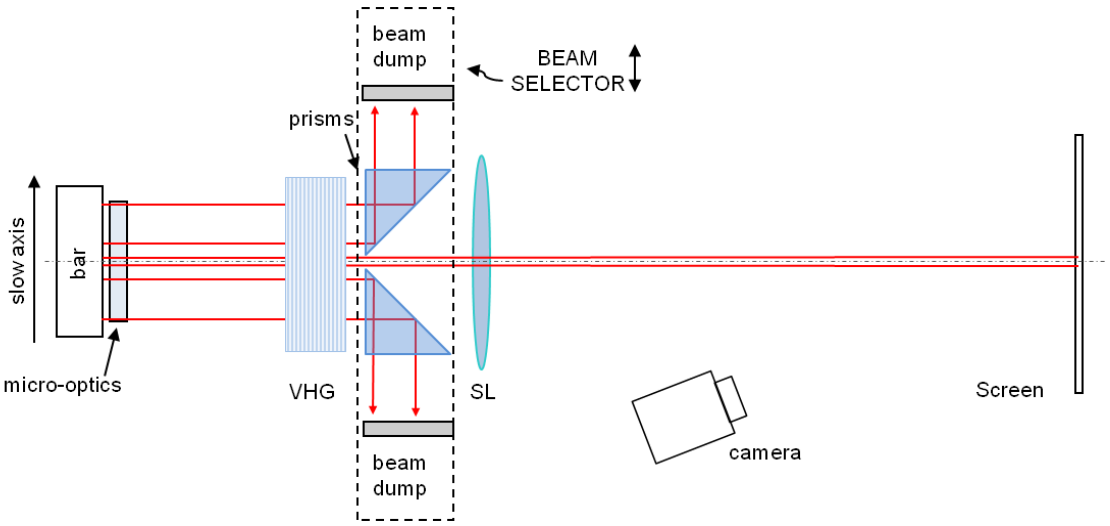


Fig. 9.3. Experimental setup for viewing of a group emitters at a time selected from the full bar locked in the quarter-Talbot external cavity.

Fig. 9.4 (a) shows the far field pattern recorded for the full bar in the external cavity aligned for the maximum fringe visibility in the in-phase mode distribution. The alignment of the cavity remained unchanged throughout the rest of the experiment. The out-of-cavity beam selector was then moved along the slow axis, allowing the far field patterns formed by different parts of the bar to be observed. Fig. 9.4 (b) illustrates several examples of the near field and the corresponding far field images recorded for different positions of the beam selector. The near field images are obtained with the

imaging spectrometer (see Section 4.2.2.2). In this way, they provide information on the number of included emitters as well as their wavelength, which is here clearly locked into the VHG bandwidth throughout the experiment. It is also worth noting that the beam selector is placed at the specific distance where the adjacent beams overlap. Therefore it is likely that some fraction of the power from the beams close to the edge of the selector can also be included in the far field distribution. However, as the purpose of this experiment was to provide only a qualitative observation, the magnitude of the light spilling over from the emitters beyond the observed group is not critical.

The observed patterns shown in Fig. 9.4 (b) indicate that phase-locking occurs locally within the bar. The regions with relatively good locking are interleaved with regions with no coherent behaviour. While the emitters at one end of the bar tend to lock into the out-of-phase supermode, the emitters at the opposite end tend to lock to the in-phase supermode. The overall far field pattern is a superposition of the locally locked and unlocked beams. As a consequence, the fringe visibility in the observed interference pattern is rather poor.

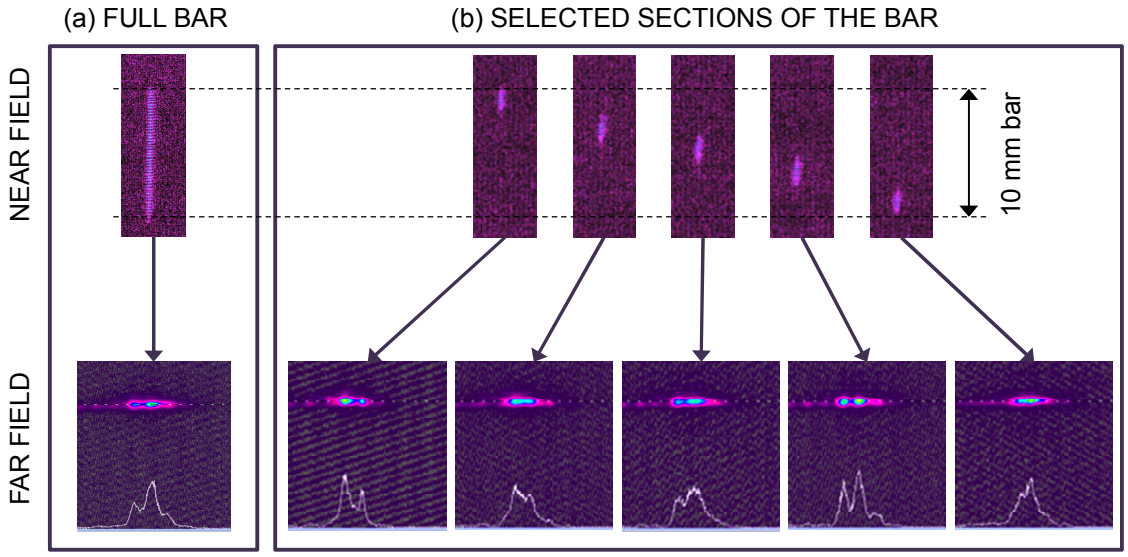


Fig. 9.4. (a) Near and far field images for the full bar. (b) Near and far field images recorded for different positions of the beam selector selecting seven emitters at a time.

## 9.4 Phase-locking of eight single-mode emitters

As shown in the previous section, some parts of the bar tend to lock into a coherent supermode more easily than others and considerable efficiency of coherent locking can be achieved within a sub-group of emitters at the local level. In this section, the independent phase-locking of subgroups of emitters selected from the bar was investigated in order to explore the local behaviour that contributes to the poor performance of locking of the full bar discussed in previous section.

### 9.4.1 In-cavity beam selector for locking of subgroups of emitters

For the experiments described here, the beam selector is placed inside the external cavity, so that the self-imaging effect occurs *only* for subgroups of emitters (see Fig. 9.5). The sharp cut-off is ensured by the edges of the prism and the compact size of the beam selector allowed it to be placed in the cavity very close to the collimating optics, so as to separate beams before they begin to overlap significantly. In this way, locking of different parts of the bar can be investigated independently. As previously noted, the validation of phase-locking for the subgroups of single-mode emitters is performed by recording the far field patterns.

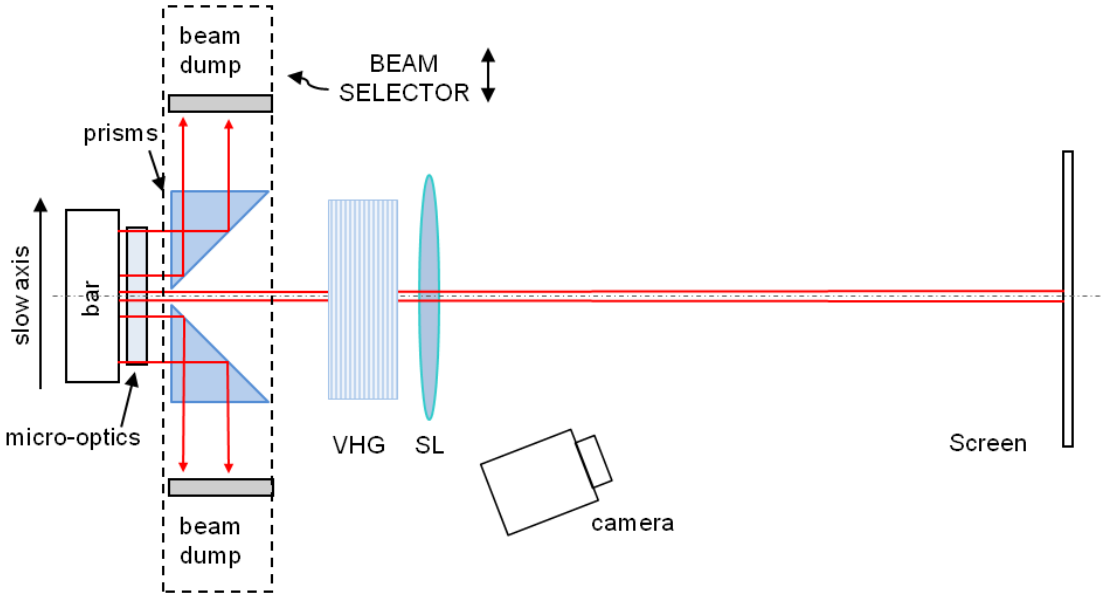


Fig. 9.5. Experimental setup for locking subgroups of emitters selected from the single-mode emitter bar.

### 9.4.2 Locking of subgroups of emitters in the cavity aligned for the full bar

In the experiment described in this section, the beam selector was adjusted to select eight emitters at a time and placed in a cavity that was initially aligned to obtain an in-phase mode distribution in the far field for the full bar (as in Fig. 9.2 (b)). The alignment of the cavity remained unchanged throughout the experiment described below.

Subsequently, the in-cavity beam selector was moved in 400 μm steps, which corresponds to shifting by two emitters at a time. For each position of the selector, the far field patterns were recorded with and without the VHG in the cavity. Removing the VHG was performed by translation in the fast axis direction and did not affect the angular alignment of the cavity. Based on the far field pattern recorded without the VHG, an average pointing for the group of eight emitters selected in each step was

obtained. The patterns observed with the VHG placed back in the cavity provided an indication of the type of supermode formed by each of the selected groups of emitters.

Fig. 9.6 plots the relative average pointing angle for the investigated groups of emitters as a function of the number of the centre emitter in the group and indicates the type of modal structure obtained. The results show that in the regions where average pointing angle is close to normal incidence, the emitters tend to lock to the out-of-phase mode. On the other hand, in the region where average pointing angle oscillates around 2.4 mrad ($\approx\lambda/2d$), the in-phase locking is preferred. This demonstrates that for fixed alignment of the VHG, the pointing angle variation across the bar is sufficient to produce different supermodes. In the sections of the bar with intermediate pointing directions and where the change in pointing from group to group is more rapid, no fringes or fringes with very poor visibility were observed. Clearly, the variation of pointing across the bar strongly affects the Talbot imaging effect inside the cavity and this needs to be corrected in order to achieve better performance of locking of the full aperture bar.

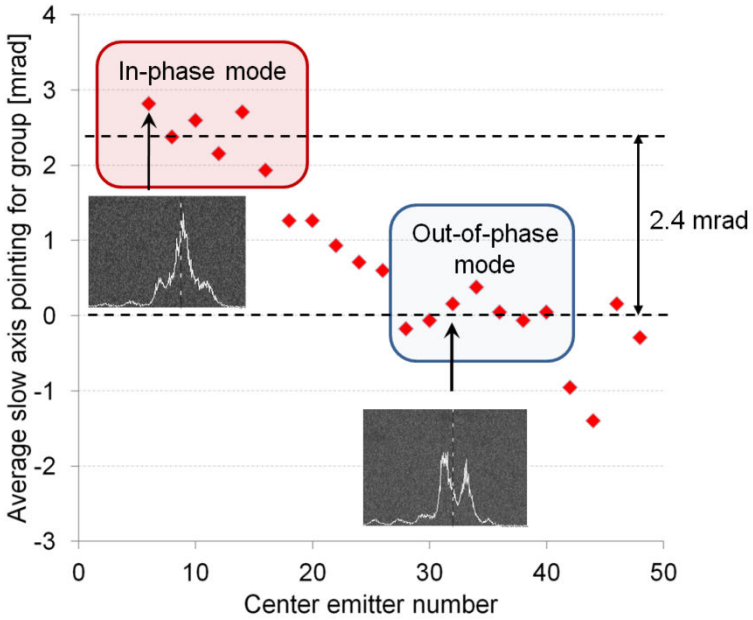


Fig. 9.6. Average pointing for groups of 8-emitters selected across the bar with examples of observed mode structures.

An example of the emitter-by-emitter pointing angle measurement for a bar lensed with a laser-written SAC-lens array was presented earlier in Fig. 6.25 in Chapter 6. The variation of approximately ±2 mrad can be corrected by a weak converging lens with a radius of curvature of about 2.5 m that would have to be designed for a particular current level (see Section 6.5.3.1). Such a lens can be produced with the laser writing technique. The random pointing variation may also be corrected, once it has been

accurately determined with the wavefront sensor device introduced earlier in this thesis. However, due to time constraints, phase-locking of the bar with corrected slow axis pointing could not be investigated before this thesis was submitted.

### 9.4.3 Cavity aligned for a subgroup of eight emitters

In the previous experiments, the cavity was aligned for maximum fringe visibility for the full bar. Now, the cavity alignment is optimized for a group of eight emitters selected from the region with relatively small pointing variation (see the group with centre emitter number 30 in Fig. 9.6).

Fig. 9.7 shows the far field patterns obtained for the external cavity formed for the 8 emitters and aligned for maximum fringe visibility of the (a) out-of-phase and (b) in-phase distributions. The measured profiles are close to the theoretical predictions shown in Fig. 9.7 (c) and (d), which were calculated as a diffraction integral of the near field distribution for an in-phase and out-of-phase mode distribution (as in Section 3.6.2.2).

The measured spacing between the fringes was 4.88 mrad, corresponding to the theoretical value of $\lambda/d$. Each of the two peaks in the measured out-of-phase distribution has a full-width half-maximum width of 1.4 mrad, which is 2.3 times the diffraction-limit for the eight emitters locked coherently. The width of the main peak in the in-phase distribution was measured to be 1.54 mrad, which corresponds to 2.5 times the diffraction-limit. The increased width of the interference peak suggests that, within the 8-emitter group, there are two independently locked subgroups of four emitters. Good coherence may be maintained within the groups (indicated by very high visibility of the patterns), but the two groups may be locked at different longitudinal modes, thereby remaining mutually incoherent.

The power obtained from the 8 coherently combined emitters at 10 A of drive current was about 1 W.

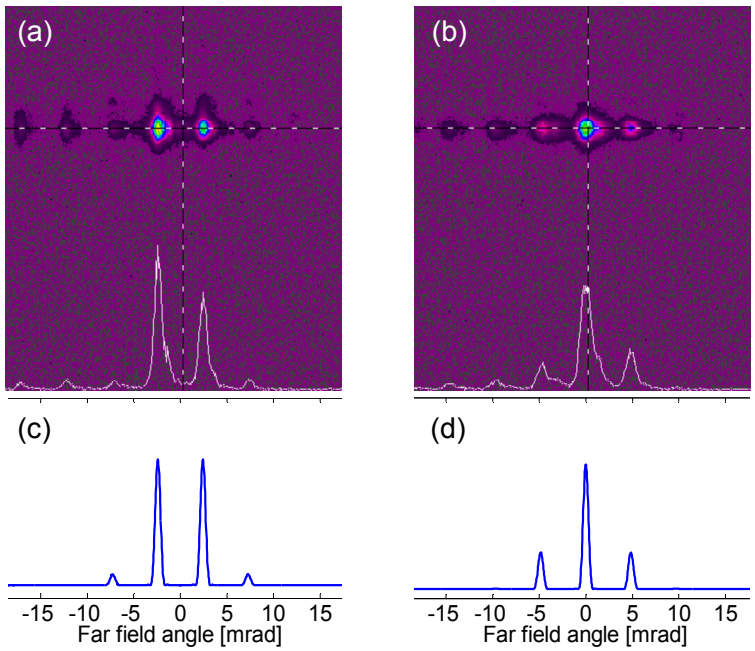


Fig. 9.7. In-phase (a) and out-of-phase (b) supermode distribution obtained for a group of 8 emitters at 10 A of drive current. Theoretical in-phase (c) and out-of-phase (d) mode profiles expected from the 8 coherently combined emitters.

### *9.4.3.1 Varying slow axis pointing angle for a fixed group locked emitters*

For the same group of 8 emitters, coherent locking was investigated as a function of the slow axis pointing (averaged over the eight emitters). The change of pointing direction was produced by a slight translation of the laser-written SAC lens array along the slow axis direction (see Fig. 9.1), which produces a change of relative position between the lenses and the corresponding emitters. The slow axis collimating optics was mounted on a manipulator and it could be carefully translated along the slow axis to provide a change of pointing direction for the appointed group of emitters without introducing any significant beam deformation.

The laser bar was operating at 10 A of drive current and with the temperature of the laser CS mount set at 23.6 ± 0.2˚C. In the configuration shown in Fig. 9.5, the VHG was aligned so as to obtain the interference pattern which exhibited the maximum visibility. From then on, the alignment of VHG and position of the beam selector remained unchanged and the far field pattern was observed for different pointing directions of the beams.

Fig. 9.8 plots the fringe visibility and indicates the mode type obtained for different average pointing angle of the group of eight emitters. The shift of the SAC-lens was not calibrated, but for each slightly changed position of the lens array the far field pattern was recorded for the unlocked emitters. The far field pattern was recorded

in a similar manner to the procedure in the previous experiment, to determine the resultant change in pointing.

The angular ranges for which the emitters lock into an out-of-phase and in-phase mode are spaced by approximately 2.2 mrad which is close to the expected $\lambda/2d$ = 2.45 mrad. Coherent locking occurs only in proximity of $\lambda/2d$, 0 and - $\lambda/2d$.

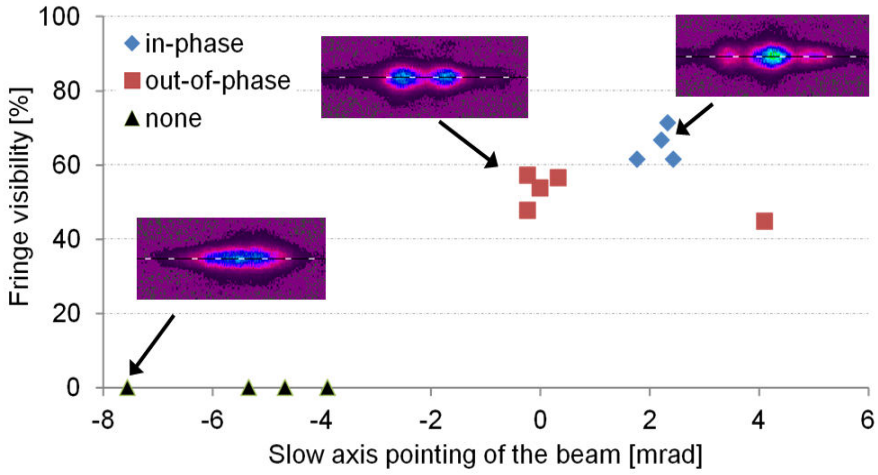


Fig. 9.8. Fringe visibility as a function of average pointing for the group of 8 emitters.

### *9.4.3.2 Acceptance angle for in-phase locking*

Before embarking on the correction of the slow axis pointing error in order to seek to achieve an improvement in the phase-locking performance, it is important to estimate the pointing accuracy that is actually required for the emitters to remain locked into the same mode. The following experiment consisted of a fine rotation of the VHG to determine the maximum angle for which the group of eight emitters remained locked into the in-phase mode. Fig. 9.9 plots the fringe visibility measured from the far field pattern for the 8-emitter group as a function of the angle of VHG. The acceptance angle for which the maximum visibility can be maintained was observed to be approximately 0.2 mrad. This means that in order to prevent the pointing variation from affecting the coherent locking, the pointing must be kept within the ± 0.1 mrad, which is less than 1% of the far field divergence.

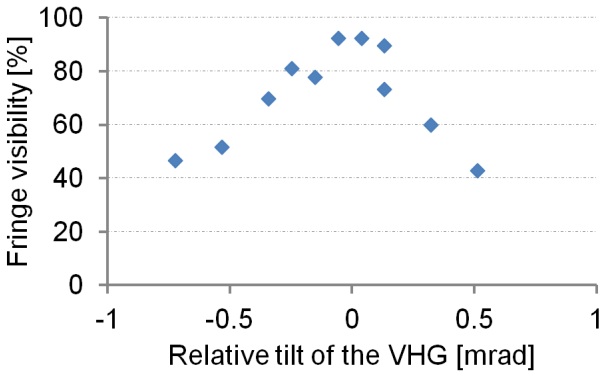


Fig. 9.9. Fringe visibility as a function of narrow tilt of the VHG measured relatively to the initial alignment for the maximum visibility in-phase distribution.

## 9.5 Locking at higher drive current

In this experiment, the far field pattern for a fixed group of 8 emitters was recorded at different current levels to explore the possibility of increasing the output power of the locked emitters. At each current level, the temperature of the CS mount was adjusted to maintain the same natural wavelength with lasing at 10A/23.6˚C taken as the reference value. In this way, the impact of the drop of locking efficiency due to large detuning from the Bragg wavelength was minimized. The average pointing for the eight emitters was also kept constant during the experiment.

Fig. 9.10 shows the series of far field patterns recorded at different drive current levels. As the current increases, the larger contribution from the incoherent emission of the laser is manifested by raised level of incoherent noise. The interference fringes are also broadened from 1.4 mrad at 10A up to 2.38 mrad at 18 A and 3.64 mrad at 30A. At 10A, 1W of output beam with visibility of 93% is obtained. At 18 A, 2 W of output power and visibility of 76% were recorded. At 30 A the power increased to about 3.5 W, but the visibility of the interference pattern dropped to 48%.

Coherence deterioration at high drive currents may be explained by mode competition between the intrinsic laser diode modes and the external cavity modes. As the reflection from the front facet is high enough to maintain lasing with no external feedback it would clearly need to be reduced significantly in order to obtain better phase-locking performance at higher current levels.

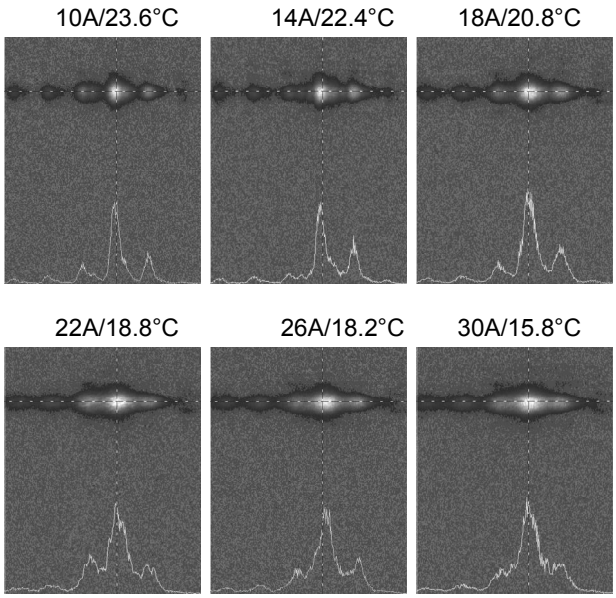


Fig. 9.10. Far field pattern of 8 emitters locked in the quarter-Talbot cavity recorded at different drive current levels.

## 9.6 Locking of larger groups of emitters

The desired increase in output power could in principle also be obtained by locking a larger number of emitters. In this experiment, the cavity was aligned to the maximum fringe visibility for a group of 11 emitters and subsequently the slit beam selector was gradually increased to include more emitters in the locked batch. Fig. 9.11 shows the far field patterns for different numbers of locked emitters. Clearly, the coherence of the combined beams strongly deteriorates when more emitters are added. The far field pattern visibility decreases with the increasing number of emitters from 75% for 11 emitters to 35% for 27 emitters.

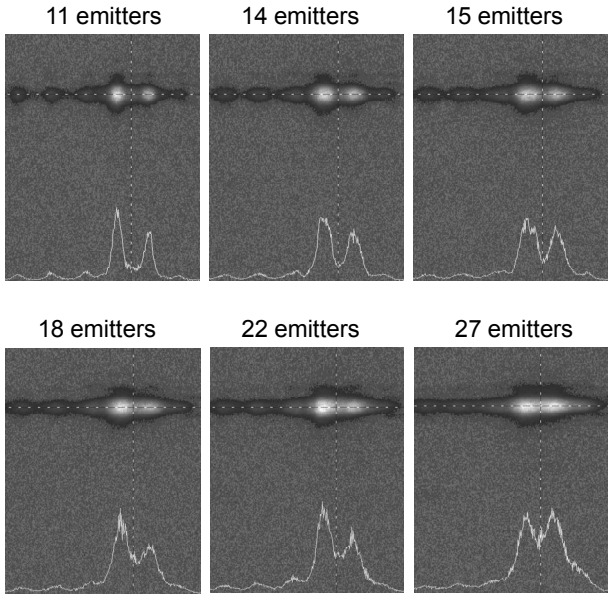


Fig. 9.11. Far field patterns recorded for different number of locked emitters.

Fig. 9.12 illustrates the decrease of fringe visibility obtained by adding more emitters by means of extending the slit of the beam selector. Fig. 9.12 (bottom) plots the pointing error for the emitters included in the locked batch. The degradation of coherence may be explained by the fact that the subsequent emitters added to the group contribute to the angular spread of the pointing angles.

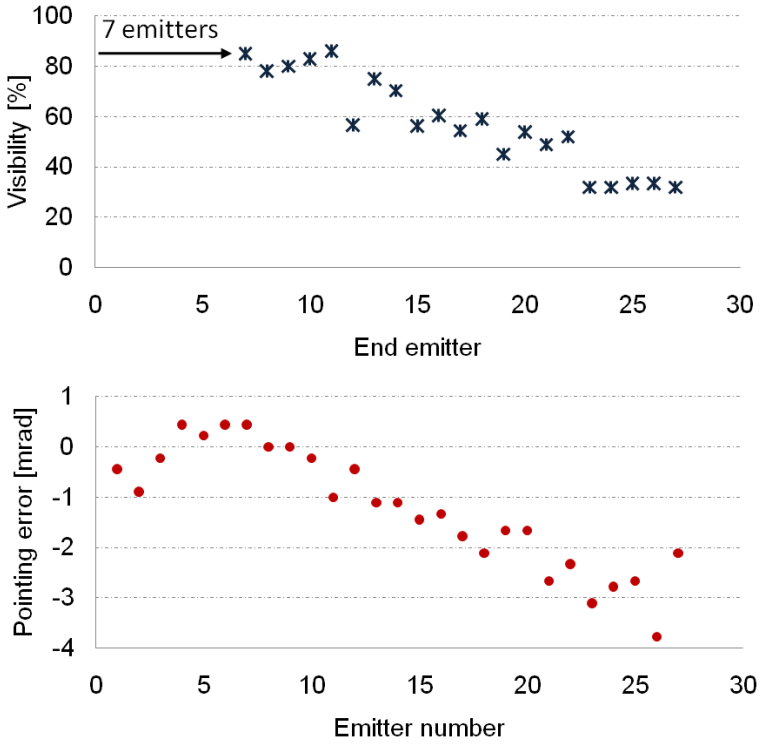


Fig. 9.12. (Top) Fringe visibility vs. number of emitters selected by the beam selector. (Bottom) Pointing of the emitters that are subsequently included in the locked batch of emitters.

## 9.7 Summary

In this chapter, coherent locking of a full 49 single-mode emitter bar as well as subgroups of emitters selected from the bar has been explored.

Experiments are described where the full aperture 49-emitter bar revealed that phase-locking occurred locally within the bar. The efficiency of coherent locking, as well as the type of supermode, were observed to vary strongly across the bar producing quite poor interference patterns in the far field.

The experiments on the locking of subgroups of emitters from the bar showed that the slow axis pointing variation across the bar strongly affects the phase-locking performance of the Talbot cavity. The angular spread of the beams caused by the pitch mismatch between the laser bar and the SAC lens array was sufficient to predispose different regions of the bar to lock to different supermodes for fixed alignment of the output coupler. The results indicate that improved performance of phase-locking for the

large single-mode emitter array may be obtained by ensuring that the slow axis pointing accuracy is maintained below 100 μrad.

For a group of eight emitters selected from the region of the bar with relatively uniform pointing angle, high visibility interference patterns at 1W of output power level were obtained. However, in this case, the fact that the output beam was nearly 2-times diffraction limited suggest that the 8-emitter group actually broke up into two subgroups that are mutually incoherent.

In summary, phase-locking at a high power level has not yet been achieved. However, the results shown in this chapter indicate that significant improvement can be achieved if the slow axis pointing uniformity is improved. Once this issue is resolved, future work will aim for locking larger groups of emitters and the investigation of locking with different fill factors of the array and higher reflectivity of the output coupler.

# Chapter 10.
# Conclusions and future outlook

This thesis reports on a series of improvements obtained in the area of beam combining of laser diode arrays. The techniques used in this work include spatial beam formatting, wavelength locking and phase-locking of laser diode arrays. Although most of the work was performed for single mode emitter arrays, the proposed approaches can be transferred to new types of sources such as mini-bars and low fill factor bars, which currently become increasingly popular in high brightness diode laser technology.

## 10.1 Spatial brightness improvement by dual-axis ultra-collimation

In Chapter 5, the spatial beam formatting technique was demonstrated, based on optical-interleaving of a beam in a stack of single-mode emitter bars with fast axis correction. This provided a nearly 2-fold reduction in the slow axis beam parameter product with the prospect of further improvements. The system built in this work was used by our collaborators at Southampton University to pump a picosecond fibre MOPA system with the results presented at Photonics West 2010 [209].

The results presented in Chapter 5 revealed a significant amount of power sent to the tails in the far field pattern of the single-mode emitter array as a result of severe beam truncation by the factory-mounted slow axis collimating optics. This highlighted the need for micro-optics optimized for high brightness laser diode arrays, which motivated the work presented in Chapter 6. Here, the multi-functional optical components are used to address the difficulty of the slow axis collimation of densely packed arrays and combine collimation with precise wavefront correction for laser diode arrays. Dual-axis laser-written optics were shown to provide high accuracy pointing of less than 3% (RMS) of the far field divergence in the fast axis direction and 10% (RMS) of far field divergence in the slow axis direction, obtained at no additional power loss penalty. In the slow axis direction, over 90% of the output power was contained in the main far field lobe. This shows a great improvement compared to the commercial solution used for the laser diode stack used in Chapter 5, where nearly 20% of power was sent to the far field tails, leading to significant power loss in the beam combining system.

The work in Chapter 6 was published in [211] and presented at Photonics West 2010 [213], as a response to the growing interest in brightness preserving optics for laser diode arrays.

Further work on the dual axis refractive optics, performed by PowerPhotonic Ltd, succeeded in resolving the issue of exact reproduction of the shape of the slow axis lenses. This product has been extended to include a larger range of available focal lengths and pitches of lens arrays for the commercial market.

Custom collimation combined with fast axis correction can significantly enhance the performance of many beam combining techniques. This approach can be applied to various types of laser diodes, including state-of-art high brightness sources. Currently, mini-bars with the length of 5-7 mm offer low smile and good beam parameter product in both directions, and therefore are very attractive for fibre coupling. However, the results presented in this thesis show that the high divergence of individual emitters and close packing of laser diode arrays are the main constrains for the performance of collimating optics. In the current mini-bars, the increased power per emitter often comes at the cost of higher far field divergence in the slow axis direction. This, in combination with small pitch of the bars, may increase the risk of beam truncation and power loss in collimation process. Thus, depending on application, one can consider low fill factor bars to be more attractive if the performance of micro-optics is critical. Low fill factor bars, offer higher power per emitter enabled by improved heat spreading. The large pitch allows the beams to be separated at the collimation optics, and thus minimize the power loss and beam quality degradation. Moreover, taking into account manufacturing, handling and packaging cost, the full size bars as well as full size micro-optics are still offering the most cost-efficient solution.

## 10.2 Enhanced wavelength locking and wavelength stepping of laser arrays

The use of the dual-axis corrective optics in a VHG-locking configuration provided an excellent improvement in the performance of the technique compared to the results seen in the literature until this point. The bars with ultra-collimated beams were wavelength locked over the full range of temperatures available in the experiments (>17˚C) and remained fully locked for the VHG placed at a distance of over 50 mm from the laser. This allowed a highly effective feedback to be delivered to all emitters in a bar. The results on the VHG-locking of laser arrays was presented at SPIE-DSS (2011), CLEO-QELS (2010) and CLEO Europe (2009) and are included in a journal publication which is in the final stage of preparation.

The enhanced wavelength locking with VHG opened up a new direction for work on VHG-based cavities. In a folded cavity configuration, wavelength selection over a range of 8 nm was performed for a full bar (Chapter 8). This presented a solution for achieving different wavelengths for multiple bars using a single VHG. The proposed technique can provide a relatively inexpensive source for the spectral combining of high-power laser diode arrays.

In Chapter 8, a similar approach, extended to wavelength stepping for a laser bar, is proposed to produce a source for dense spectral combining of laser bars. Laser-written arrays of deflectors are used to form independent folded cavities for different parts of a bar. This new approach is a competitive alternative to techniques discussed in Chapter 3, where the wavelength variation along a laser array is achieved by feedback from a diffraction grating (see Fig. 3.16) or by a chirped volume holographic grating (see Fig. 3.18). In the grating-based system illustrated in Fig. 3.16, the wavelength of the individual elements in the array is controlled by the feedback beams reflected from the remote output coupler. In such a configuration, locking into narrow bandwidths (<1nm) requires large cavity lengths of the order of several meters. This significantly reduces alignment tolerances and robustness of the system. The method for wavelength stepping by refractive optics proposed in this thesis allows the individual emitters in an array to be locked into extremely narrow bandwidths in a very compact arrangement. Such a spectrally stepped array can be treated like an independent module, which can be used in a spectral beam combining setup similar to the one in Fig. 3.16. Consequently, the diffraction grating becomes a passive, less critical component and the output coupler is not needed. This has the potential to improve the stability and the efficiency of spectral combining. Previously, it has been demonstrated in [139] that a robust spectral combining can be achieved for a laser diode array that is spectrally locked by a chirped VHG (see Fig. 3.18). The method proposed in this thesis is based on silica-based optical components that are easy to manufacture, and thus can be considered as a cost effective alternative to the chirped VHGs.

The first experiments on wavelength stepping of laser diode arrays provided encouraging results. The triple-function laser-written optics was designed and produced to incorporate fast axis correction, slow axis collimation and beam deflection in the fast axis direction. This allowed 5- and 7-sections of the bar to be locked into different wavelengths controlled by the pointing of the individual groups. Further development will include forming a wavelength stepped bar with a pair of matching optics for beam

deflection and folding in the external cavity. A related patent application was filed shortly before the thesis was submitted.

As discussed in Chapter 8, the angular range and the output spectrum of wavelength stepped laser arrays are inversely proportional to the number of combined elements. Thus, the laser arrays with small number of emitters are particularly attractive for this application. The technique has the potential to spectrally combine up to 10 emitters with the output spectrum of less than 5 nm. This could be realized with mini-bars or low fill factor bars, giving as advantage of high power per combined element. Therefore, the outlook of this work is to develop the approach into a full spectral beam combining system based on the new types of sources.

## 10.3 Phase-locking

A series of investigations on phase-locking of a full 49-emitter bar and for groups of emitters selected from the bar were presented in Chapter 9. This work revealed that the pointing variation in the slow axis direction is sufficient to predispose different fragments of the laser bar to lock to different supermodes, for the same alignment of the external cavity.

Encouraging results were obtained for a group of eight emitters, where high visibility interference patterns were achieved at 1W of output power level. These results are comparable with the state-of-the-art results in the current literature for a similar experiment on the passive phase-locking of laser diode array.

Further work in the future could involve additional correction to be applied to compensate for the slow axis pointing variation to improve the feasibility of effective phase-locking for the single-mode emitter bar. For this purpose, a weak lens combined with compensation for random pointing errors could be applied to obtain uniform pointing across the bar.

## 10.4 Beam characterisation and analysis techniques

Characterisation of high-power laser diodes is a growing concern in research and industry. One of the aims of this work was to develop measurement techniques providing the necessary degree of complexity to investigate the spatial and spectral properties of the beams: emitter resolved spectra, tuning, high resolution, pointing for each emitter etc. It was evident throughout the thesis, that many of the experiments could not have been performed without the multifunctional diagnostics system discussed in Chapter 4.

The value of the research was also significantly increased by employing the high accuracy beam characterisation technique based on the wavefront sensing device and the access to custom written optical components, available thanks to the close collaboration with PowerPhotonic Ltd. In this project, the flexibility of the laser-written technique was expanded towards new applications from ultra collimation, through beam shaping to wavelength stepping cavity configurations.

# REFERENCES


1. M. Kanskar, T. Earles, T. J. Goodnough, E. Stiers, D. Botez, and L. J. Mawst, *73% CW power conversion efficiency at 50 W from 970 nm diode laser bars,* Electronics Letters, **41**, 245-247, 2005.
2. A. Knigge, G. Erbert, J. Jonsson, W. Pittroff, R. Staske, B. Sumpf, M. Weyers, and G. Trankle, *Passively cooled 940 nm laser bars with 73% wall-plug efficiency at 70 W and 25 C,* Electronics Letters, **41**, 250-251, 2005.
3. G. Overton, S. G. Anderson, D. A. Belforte, and T. Hausken, *Laser marketplace 2010: how wide is the chasm?,* Laser Focus World, 32–49, 2010.
4. J. F. Seurin, C. L. Ghosh, V. Khalfin, A. Miglo, G. Xu, J. D. Wynn, P. Pradhan, and L. A. D'Asaro, *High-power high-efficiency 2D VCSEL arrays,* in *Vertical-Cavity Surface-Emitting Lasers XII,* Proc. of SPIE, San Jose, 2008.
5. J. F. Seurin, G. Xu, Q. Wang, B. Guo, R. Van Leeuwen, A. Miglo, P. Pradhan, J. D. Wynn, V. Khalfin, and C. Ghosh, *High-brightness pump sources using 2D VCSEL arrays,* in *Vertical-Cavity Surface-Emitting Lasers XIV,* Proc. of SPIE, San Francisco, 2010.
6. G. Chen and C. L. Tien, *Facet heating of quantum well lasers,* Journal of Applied Physics, **74**, 2167-2174, 1993.
7. M. Ziegler, J. W. Tomm, T. Elsaesser, C. Matthiesen, M. B. Sanayeh, and P. Brick, *Real-time thermal imaging of catastrophic optical damage in red-emitting high-power diode lasers,* Applied Physics Letters, **92**, 103514, 2008.
8. R. W. Lambert, T. Ayling, A. F. Hendry, J. M. Carson, D. A. Barrow, S. McHendry, C. J. Scott, A. McKee, and W. Meredith, *Facet-passivation processes for the improvement of Al-containing semiconductor laser diodes,* Journal of Lightwave Technology, **24**, 956, 2006.
9. P. Ressel, G. Erbert, U. Zeimer, K. Hausler, G. Beister, B. Sumpf, A. Klehr, and G. Trankle, *Novel passivation process for the mirror facets of Al-free active-region high-power semiconductor diode lasers,* Photonics Technology Letters, IEEE, **17**, 962-964, 2005.
10. P. Crump, H. Wenzel, G. Erbert, and G. Trankle, *Advances in spatial and spectral brightness in 800-1100 nm GaAs-based high power broad area lasers,* in *Technologies for Optical Countermeasures VI,* Proc. of SPIE, Berlin, 2009.
11. H. Wenzel, P. Crump, A. Pietrzak, X. Wang, G. Erbert, and G. Trankle, *Theoretical and experimental investigations of the limits to the maximum output power of laser diodes,* New Journal of Physics, **12**, 085007, 2010.
12. M. T. Knapczyk, J. H. Jacob, H. Eppich, A. K. Chin, K. D. Lang, J. T. Vignati, and R. H. Chin, *70% efficient near 1kW single 1-cm laser-diode bar at 20°C,* in *High-Power Diode Laser Technology and Applications IX,* Prof. of SPIE, San Francisco, 2011.
13. T. Y. Fan, *Laser beam combining for high-power, high-radiance sources,* IEEE, Journal of Selected Topics in Quantum Electronics, **11**, 567-577, 2005.

14. R. K. Huang, B. Chann, L. J. Missaggia, J. P. Donnelly, C. T. Harris, G. W. Turner, A. K. Goyal, T. Y. Fan, and A. Sanchez-Rubio, *High-brightness wavelength beam combined semiconductor laser diode arrays,* Photonics Technology Letters, **19**, 209-211, 2007.

15. G. A. J. Markillie, H. J. Baker, F. J. Villarreal, and D. R. Hall, *Effect of vaporization and melt ejection on laser machining of silica glass micro-optical components,* Applied Optics, **41**, 5660-5667, 2002.

16. K. M. Nowak, H. J. Baker, and D. R. Hall, *Pulsed-laser machining and polishing of silica micro-optical components using a CO~ 2 laser and an acousto-optic modulator [4941-15],* International Society for Optical Engineering; 1999, 2002.

17. J. F. Monjardin, *Wavefront characterisation and beam correction for high power diode laser arrays, PhD Thesis,* Heriot-Watt University, Edinburgh (2006).

18. R. N. Hall, G. E. Fenner, J. D. Kingsley, T. J. Soltys, and R. O. Carlson, *Coherent light emission from GaAs junctions,* Physical Review Letters, **9**, 366-368, 1962.

19. C. Fiebig, G. Blume, C. Kaspari, D. Feise, J. Fricke, M. Matalla, W. John, H. Wenzel, K. Paschke, and G. Erbert, *12W high-brightness single-frequency DBR tapered diode laser,* Electronics Letters, **44**, 1253-1255, 2008.

20. M. G. A. Bernard and G. Duraffourg, *Laser conditions in semiconductors,* Physica Status Solidi (b), **1**, 699-703, 1961.

21. H. F. Matare, *Light emitting devices,* Academic Press Inc, New York, 1976.

22. Z. I. Alferov, V. M. Andreev, D. Z. Garbuzov, Y. V. Zhilyaev, E. P. Morozov, E. L. Portnoi, and V. G. Trofim, *Investigation of the influence of the AlAs-GaAs heterostructure parameters on the laser threshold current and the realization of continuous emission at room temperature,* Sov. Phys. Semicond., **4**, 1573-1575, 1971.

23. H. Kroemer, *Heterostructure devices: A device physicist looks at interfaces,* Surface Science, **132**, 543-576, 1983.

24. T. Suhara, *Semiconductor heterostructure optical waveguides*, in *Semiconductor laser fundametals,* Marcel Dekker Inc., New York, 2004.

25. H. C. Casey, S. Somekh, and M. Ilegems, *Room-temperature operation of low-threshold separate-confinement heterostructure injection laser with distributed feedback,* Applied Physics Letters, **27**, 142-144, 1975.

26. K. Aiki, M. Nakamura, J. Umeda, A. Yariv, A. Katzir, and H. W. Yen, *GaAs-GaAlAs distributed-feedback diode lasers with separate optical and carrier confinement,* Applied Physics Letters, **27**, 145, 1975.

27. W. T. Tsang, *A graded-index waveguide separate-confinement laser with very low threshold and a narrow Gaussian beam,* Applied Physics Letters, **39**, 134-137, 1981.

28. C. Harder, P. Buchmann, and H. Meier, *High-power ridge-waveguide AlGaAs GRIN-SCH laser diode,* Electronics Letters, **22**, 1081-1082, 1986.

29. D. Sands, *Quantum well lasers*, in *Diode Lasers,* IOP Publishing Ltd, Bristol, 2005.

30. W. T. Tsang, C. Weisbuch, R. C. Miller, and R. Dingle, *Current injection GaAs-AlxGa1-xAs multi-quantum well heterostructure lasers prepared by molecular beam epitaxy,* Applied Physics Letters, **35**, 673-675, 1979.

31. J. J. Snyder, *Cylindrical micro-optics,* in *Miniature and Micro-Optics and Micromechanics,* Proc. of SPIE, San Diego, 1993.

32. A. R. Holdsworth and H. J. Baker, *Assessment of micro-lenses for diode bar collimation,* in *Laser Diode and LED Applications III,* Proc. of SPIE, San Jose, 1997.

33. T. Suhara, *Stimulated emission and optical gain in semiconductors*, in *Semiconductor laser fundametals,* Marcel Dekker Inc., New York, 2004.

34. D. G. Mehuys, *High-power semiconductor lasers*, in *Semiconductor Lasers II: Materials and Structures,* Academic Press, London, 1999.

35. W. C. Tang, H. J. Rosen, P. Vettiger, and D. J. Webb, *Evidence for current-density-induced heating of AlGaAs single-quantum-well laser facets,* Applied Physics Letters, **59**, 1005-1007, 1991.

36. D. Botez, *Design considerations and analytical approximations for high continuous-wave power, broad-waveguide diode lasers,* Applied Physics Letters, **74**, 3102, 1999.

37. L. Goldberg, D. Mehuys, M. R. Surette, and D. C. Hall, *High-power, near-diffraction-limited large-area traveling-wave semiconductor amplifiers,* IEEE, Journal of Quantum Electronics, **29**, 2028-2043, 1993.

38. D. G. Mehuys, *High-power semiconductor lasers*, in *Semiconductor Lasers II: Materials and Structures,* Academic Press, London, 1999.

39. D. Sands, *The double heterostructure laser*, in *Diode Lasers,* IOP Publishing Ltd, Bristol, 2005.

40. A. E. Siegman, *How to (maybe) measure laser beam quality,* in *Diode Pumped Solid State Lasers: Applications and Issues (DLAI),* Optical Society of America, 1998.

41. P. Loosen and A. Knitsch, *Incoherent Beam Superposition and Stacking*, in *High power diode lasers: Technology and Applications,* Springer New York, 2007.

42. B. Sumpf, M. Zorn, R. Staske, J. Fricke, P. Ressel, A. Ginolas, K. Paschke, G. Erbert, M. Weyers, and G. Trankle, *3-W broad area lasers and 12-W bars with conversion efficiencies up to 40% at 650 nm,* Selected Topics in Quantum Electronics, IEEE Journal of, **13**, 1188-1193, 2007.

43. H. Wenzel, F. Bugge, M. Dallmer, F. Dittmar, J. Fricke, K. H. Hasler, and G. Erbert, *Fundamental-lateral mode stabilized high-power ridge-waveguide lasers with a low beam divergence,* Photonics Technology Letters, IEEE, **20**, 214-216, 2008.

44. N. Lichtenstein, Y. Manz, P. Mauron, A. FiIy, and S. Arlt, *Single mode emitter array laser bars for high-brightness applications,* in *Semiconductor Laser Conference,* IEEE, 2004.

45. H. Wenzel, B. Sumpf, and G. Erbert, *High-brightness diode lasers,* Comptes Rendus Physique, **4**, 649-661, 2003.

46. E. S. Kintzer, J. N. Walpole, S. R. Chinn, C. A. Wang, and L. J. Missaggia, *High-power, strained-layer amplifiers and lasers with tapered gain regions,* Photonics Technology Letters, IEEE, **5**, 605-608, 1993.

47. S. D. DeMars, T. Oleskevich, A. Schoenfelder, and R. J. Lang, *400-mW single-mode fiber-coupled DFB laser at 980 nm,* IEEE, 1997.

48. K. Paschke, A. Bogatov, A. E. Drakin, R. Guther, A. A. Stratonnikov, H. Wenzel, G. Erbert, and G. Trankle, *Modeling and measurements of the radiative characteristics of high-power alfa-DFB lasers,* IEEE, Journal of Selected Topics in Quantum Electronics, **9**, 835-843, 2003.

49. S. O'Brien, R. Lang, R. Parke, J. Major, D. F. Welch, and D. Mehuys, *2.2-W continuous-wave diffraction-limited monolithically integrated master oscillator power amplifier at 854 nm,* Photonics Technology Letters, IEEE, **9**, 440-442, 1997.

50. R. Parke, D. F. Welch, A. Hardy, R. Lang, D. Mehuys, S. O'Brien, K. Dzurko, and D. Scifres, *2.0 W CW, diffraction-limited operation of a monolithically integrated master oscillator power amplifier,* Photonics Technology Letters, IEEE, **5**, 297-300, 1993.

51. G. Bendelli, K. Komori, S. Arai, and Y. Suematsu, *A new structure for high-power TW-SLA [Travelling wave semiconductor laser amplifier],* Photonics Technology Letters, IEEE, **3**, 42-44, 1991.

52. J. N. Walpole, E. S. Kintzer, S. R. Chinn, C. A. Wang, and L. J. Missaggia, *High-power strained-layer InGaAs/AlGaAs tapered traveling wave amplifier,* Applied Physics Letters, **61**, 740-742, 1992.

53. J. N. Walpole, *Semiconductor amplifiers and lasers with tapered gain regions,* Optical and Quantum Electronics, **28**, 623-645, 1996.

54. D. Mehuys, S. O'Brien, R. J. Lang, A. Hardy, and D. F. Welch, *5W, diffraction-limited, tapered-stripe unstable resonator semiconductor laser,* Electronics Letters, **30**, 1855-1856, 1994.

55. M. T. Kelemen, R. Kiefer, M. Mikulla, F. Rinner, J. Rogg, M. Walter, N. Wiedmann, and G. Weimann, *High-power high-brightness ridge-waveguide tapered diode lasers at 940 nm,* in *Test and Measurement Applications of Optoelectronic Devices,* Proc. of SPIE, San Jose, 2002.

56. D. Gloge and E. A. J. Marcatili, *Multimode theory of graded-core fibers,* Bell Syst. Tech. J, **52**, 1563-1578, 1973.

57. J. N. Walpole, J. P. Donnelly, P. J. Taylor, L. J. Missaggia, C. T. Harris, R. J. Bailey, A. Napoleone, S. H. Groves, S. R. Chinn, and R. Huang, *Slab-coupled 1.3-micron semiconductor laser with single-spatial large-diameter mode,* IEEE, Photonics Technology Letters, **14**, 756-758, 2002.

58. J. P. Donnelly, R. K. Huang, J. N. Walpole, L. J. Missaggia, C. T. Harris, J. J. Plant, R. J. Bailey, D. E. Mull, W. D. Goodhue, and G. W. Turner, *AlGaAs-InGaAs slab-coupled optical waveguide lasers,* Quantum Electronics, IEEE Journal of, **39**, 289-298, 2003.

59. R. Fehse, H. Konig, G. Gronninger, C. Lauer, U. Strauss, H. Kissel, M. Puschmann, and J. Biesenbach, *Low fill factor diode laser bars with high brilliance from 808 nm to 1020 nm for fibre coupling,* IEEE.

60. W. Pittroff, G. Erbert, B. Eppich, C. Fiebig, K. Vogel, and G. Traenkle, *Conductively Cooled 1 kW-QCW Diode Laser Stacks Enabling Simple Fiber Coupling,* Components and Packaging Technologies, IEEE Transactions on, **33**, 206-214,

61. Oclaro Inc., Available from: www.oclaro.com.

62. R. Feeler and E. Stephens, *High-density pulsed laser diode arrays for SSL pumping,* in *Laser Technology for Defense and Security VI,* Proc. of SPIE, Orlando.

63. A. Knitsch, A. Luft, T. Gross, D. Ristau, P. Loosen, and R. Poprawe, *Diode laser modules of highest brilliance for materials processing,* 2002.

64. V. Daneu, A. Sanchez, T. Y. Fan, H. K. Choi, G. W. Turner, and C. C. Cook, *Spectral beam combining of a broad-stripe diode laser array in an external cavity,* Optics Letters, **25**, 405-407, 2000.

65. T. H. Loftus, A. Liu, P. R. Hoffman, A. M. Thomas, M. Norsen, R. Royse, and E. Honea, *522 W average power, spectrally beam-combined fiber laser with near-diffraction-limited beam quality,* Optics Letters, **32**, 349-351, 2007.

66. B. L. Volodin, S. V. Dolgy, E. D. Melnik, E. Downs, J. Shaw, and V. S. Ban, *Wavelength stabilization and spectrum narrowing of high-power multimode laser diodes and arrays by use of volume Bragg gratings,* Optics Letters, **29**, 1891-1893, 2004.

67. G. J. Steckman, W. Liu, R. Platz, D. Schroeder, C. Moser, and F. Havermeyer, *Volume holographic grating wavelength stabilized laser diodes,* Selected Topics in Quantum Electronics, IEEE Journal of, **13**, 672-678, 2007.

68. L. B. Glebov, *Volume Bragg Gratings in PTR Glass--New Optical Elements for Laser Design,* Optical Society of America, 2008.

69. C. L. Talbot, M. E. J. Friese, D. Wang, I. Brereton, N. R. Heckenberg, and H. Rubinsztein-Dunlop, *Linewidth reduction in a large-smile laser diode array,* Applied Optics, **44**, 6264-6268, 2005.

70. E. Babcock, B. Chann, I. A. Nelson, and T. G. Walker, *Frequency-narrowed diode array bar,* Applied Optics, **44**, 3098-3104, 2005.

71. R. Tkach and A. R. Chraplyvy, *Regimes of feedback effects in 1.5-μm distributed feedback lasers,* Journal of Lightwave Technology, **4**, 1655-1661, 1986.

72. D. Mehuys, D. F. Welch, and L. Goldberg, *2.0 W CW, diffraction-limited tapered amplifier with diode injection,* Electronics Letters, **28**, 1944-1946, 1992.

73. G. Ferrari, M. O. Mewes, F. Schreck, and C. Salomon, *High-power multiple-frequency narrow-linewidth laser source based on a semiconductor tapered amplifier,* Optics Letters, **24**, 151-153, 1999.

74. R. Waarts, S. Sanders, R. Parke, D. Mehuys, R. Lang, S. O'Brien, K. Dzurko, D. Welch, and D. Scifres, *Frequency-doubled monolithic master oscillator power amplifier laser diode,* Photonics Technology Letters, IEEE, **5**, 1122-1125, 1993.

75. P. Loosen, J. Biesenbach, K. Du, C. R. Haas, R. Proprawe, and G. Treusch, *Design and industrial applications of high-power diode-lasers,* in *International Symposium on Gas Flow and Chemical Lasers and High-Power Laser Conference,* Edinburgh, 1997.

76. V. Sturm, H. G. Treusch, and P. Loosen, *Cylindrical microlenses for collimating high-power diode lasers,* in *Lasers in Material Processing,* Proc. of SPIE, Munich, 1997.

77. A. Pietrzak, P. Crump, H. Wenzel, G. Erbert, F. Bugge, and G. Trankle, *Combination of Low-Index Quantum Barrier and Super Large Optical Cavity Designs for Ultranarrow Vertical Far-Fields From High-Power Broad-Area Lasers,* Selected Topics in Quantum Electronics, IEEE Journal of, 1-8, 2011.

78. P. Crump, A. Pietrzak, F. Bugge, H. Wenzel, G. Erbert, and G. Trankle, *975 nm high power diode lasers with high efficiency and narrow vertical far field enabled by low index quantum barriers,* Applied Physics Letters, **96**, 131110, 2010.

79. D. Hauschild, *Optical emitter array with collimating optics unit*, Patent: US 6,384,981 B1, 2002.

80. LIMO Lissotschenko Mikrooptik GmbH, Available from: www.limo.de.

81. P. Schreiber, B. Hoefer, P. Dannberg, and U. D. Zeitner, *High-brightness fiber-coupling schemes for diode laser bars,* in *Laser Beam Shaping VI,* Proc. of SPIE, San Diego, 2005.

82. Y. Zheng and H. Kan, *Effective bandwidth reduction for a high-power laser-diode array by an external-cavity technique,* Optics Letters, **30**, 2424-2426, 2005.

83. S. Yamaguchi, T. Kobayashi, Y. Saito, and K. Chiba, *Collimation of emissions from a high-power multistripe laser-diode bar with multiprism array coupling and focusing to a small spot,* Optics Letters, **20**, 898-900, 1995.

84. P. Y. Wang, A. Gheen, and Z. Wang, *Beam shaping technology for laser diode arrays,* in *Laser Beam Shaping III,* Proc. of SPIE, Seattle, 2002.

85. T. Koenning, K. Alegria, Z. Wang, A. Segref, D. Stapleton, W. Fassbender, M. Flament, K. Rotter, A. Noeske, and J. Biesenbach, *Macro-channel cooled, high power, fiber coupled diode lasers exceeding 1.2 kW of output power,* in *High-Power Diode Laser Technology and Applications IX,* Proc. of SPIE, San, 2011.

86. G. Zheng, C. Du, C. Zhou, and C. Zheng, *Micrograting-array beam-shaping technique for asymmetrical laser beams,* Applied Optics, **44**, 3540-3544, 2005.

87. G. Zheng and S. Li, *High-power laser diode array beam-shaping by rhomboid prism arrays,* Journal of Optics A: Pure and Applied Optics, **10**, 075301, 2008.

88. B. Ehlers, K. Du, M. Baumann, H. G. Treusch, P. Loosen, and R. Poprawe, *Beam shaping and fibre coupling of high-power diode laser arrays,* 1997.

89. S. Heinemann and L. Leininger, *Fiber coupled diode lasers and beam-shaped high-power stacks,* in *Laser Resonators,* Proc. of SPIE, San Jose, 1998.

90. S. Bonora and P. Villoresi, *Diode laser bar beam shaping by optical path equalization,* Journal of Optics A: Pure and Applied Optics, **9**, 441, 2007.

91. W. A. Clarkson and D. C. Hanna, *Two-mirror beam-shaping technique for high-power diode bars,* Optics Letters, **21**, 375-377, 1996.

92. W. A. Clarkson, A. B. Neilson, and D. C. Hanna, *Beam shaper*, Patent: US Patent 5,825,551, 1998.

93. B. Jeffries and D. W. Coutts, *Asymmetric beam shaping of a diode-bar laser for multipass pumping of a thin-crystal laser,* JOSA B, **22**, 2121-2128, 2005.

94. X. Gao, H. Ohashi, H. Okamoto, M. Takasaka, and K. Shinoda, *Beam-shaping technique for improving the beam quality of a high-power laser-diode stack,* Optics Letters, **31**, 1654-1656, 2006.

95. H. J. Baker, N. Trela, D. R. Hall, R. McBride, and J. J. Wendland, *Beam Reformatting and Combining of High-Power Laser Diode Stacks,* Optical Society of America.

96. H. J. Baker, N. Trela, D. R. Hall, R. McBride, and J. J. Wendland, *Beam Reformatting and Combining of High-Power Laser Diode Stacks,* in *CLEO,* Optical Society of America, San Jose, CA, 2010.

97. H. J. Baker, J. F. Monjardin, P. Kneip, D. R. Hall, and R. McBride, *1.8 kW diode laser system for fibre-delivery using brightness-enhanced diode stacks and a novel final beam-shaper,* in *High-Power Diode Laser Technology and Applications VI,* Proc. of SPIE, 2008.

98. J. F. Monjardin, K. M. Nowak, H. J. Baker, and D. R. Hall, *Correction of beam errors in high power laser diode bars and stacks,* Optics Express, **14**, 8178-8183, 2006.

99. S. H. Ghasemi, M. R. Hantehzadeh, J. Sabbaghzadeh, D. Dorranian, M. Lafooti, V. Vatani, R. Rezaei-Nasirabad, A. Hemmati, A. A. Amidian, and S. A. Alavian, *Beam shaping design for coupling high power diode laser stack to fiber,* Applied Optics, **50**, 2927-2930, 2011.

100. F. Bachmann, *Industrial applications of high power diode lasers in materials processing,* Applied Surface Science, **208**, 125-136, 2003.

101. B. V. Zhdanov, T. Ehrenreich, and R. J. Knize, *Highly efficient optically pumped cesium vapor laser,* Optics Communications, **260**, 696-698, 2006.

102. A. B. Petersen and J. Gloyd, *Tunable, High Power, Narrow Band Emission from a Volume Grating-Controlled Diode Bar,* in *Advanced Solid-State Photonics (ASSP),* OSA, Nara, Japan, 2008.

103. T. G. Walker and W. Happer, *Spin-exchange optical pumping of noble-gas nuclei,* Reviews of Modern Physics, **69**, 629, 1997.

104. L. Meng, *High power 7-GHz bandwidth external-cavity diode laser array and its use in optically pumping singlet delta oxygen*. 2006, DTIC Document.

105. A. Gourevitch, G. Venus, V. Smirnov, D. A. Hostutler, and L. Glebov, *Continuous wave, 30 W laser-diode bar with 10 GHz linewidth for Rb laser pumping*. 2008, Optical Society of America. p. 702-704.

106. M. G. Littman and H. J. Metcalf, *Spectrally narrow pulsed dye laser without beam expander,* Applied Optics, **17**, 2224-2227, 1978.

107. B. Chann, I. Nelson, and T. G. Walker, *Frequency-narrowed external-cavity diode-laser-array bar,* Optics Letters, **25**, 1352-1354, 2000.

108. S. B. Bayram and T. E. Chupp, *Operation of a single mode external-cavity laser diode array near 780 nm,* Review of Scientific instruments, **73**, 4169, 2002.

109. B. L. Sands and S. B. Bayram, *Characteristics of a high-power broad-area laser operating in a passively stabilized external cavity,* Applied Optics, **46**, 3829-3835, 2007.

110. F. Wang, A. Hermerschmidt, and H. Joachim Eichler, *Narrow-bandwidth high-power output of a laser diode array with a simple external cavity,* Optics Communications, **218**, 135-139, 2003.

111. A. Jechow, V. Raab, and R. Menzel, *Tunable 6.8 W narrow bandwidth emission from a single-stripe continuous-wave broad-area laser diode in a simple external cavity,* Applied Optics, **47**, 1447-1450, 2008.

112. H. T. Hsieh, W. Liu, F. Havermeyer, C. Moser, and D. Psaltis, *Beam-width-dependent filtering properties of strong volume holographic gratings*. 2006, Optical Society of America. p. 3774-3780.

113. W. L. Bragg, *Cambridge Philos,* Soc, **17**, 43, 1912.

114. H. Kogelnik, *Coupled wave theory for thick hologram gratings,* The Bell System Technical Journal, Vol. 48, no. 9, November 1969, pp. 2909-2947, **48**, 2909-2947, 1969.

115. A. Gourevitch, G. Venus, V. Smirnov, D. A. Hostutler, and L. Glebov, *Continuous wave, 30 W laser-diode bar with 10 GHz linewidth for Rb laser pumping,* Optics Letters, **33**, 702-704, 2008.

116. I. V. Ciapurin, L. B. Glebov, and V. I. Smirnov, *Modeling of Gaussian beam diffraction on volume Bragg gratings in PTR glass,* 2005.

117. G. Lucas-Leclin, D. Paboeuf, P. Georges, J. Holm, P. Andersen, B. Sumpf, and G. Erbert, *Wavelength stabilization of extended-cavity tapered lasers with volume Bragg gratings,* Applied Physics B: Lasers and Optics, **91**, 493-498, 2008.

118. D. Vijayakumar, O. B. Jensen, and B. Thestrup, *980 nm high brightness external cavity broad area diode laser bar,* Optics Express, **17**, 5684-5690, 2009.

119. A. Gourevitch, G. Venus, V. Smirnov, and L. Glebov, *Efficient pumping of Rb vapor by high-power volume Bragg diode laser,* Optics Letters, **32**, 2611-2613, 2007.

120. G. Lucas-Leclin, D. Paboeuf, P. Georges, J. Holm, P. Andersen, B. Sumpf, and G. Erbert, *Wavelength stabilization of extended-cavity tapered lasers with volume Bragg gratings*. 2008, Springer. p. 493-498.

121. C. Moser, L. Ho, and F. Havermeyer, *Self-aligned non-dispersive external cavity tunable laser,* Optics Express, **16**, 16691-16696, 2008.

122. B. Jacobsson, J. E. Hellstrom, V. Pasiskevicius, and F. Laurell, *Widely tunable Yb: KYW laser with a volume Bragg grating,* Optics Express, **15**, 1003-1010, 2007.

123. F. Havermeyer, W. Liu, C. Moser, D. Psaltis, and G. J. Steckman, *Volume holographic grating-based continuously tunable optical filter,* Optical Engineering, **43**, 2017, 2004.

124. B. Fermigier, G. Lucas-Leclin, J. Dupont, F. Plumelle, and M. Houssin, *Self-aligned external-cavity semiconductor lasers for high resolution spectroscopy,* Optics Communications, **153**, 73-77, 1998.

125. C. Moser and F. Havermeyer, *Compact self-aligned external cavity lasers using volume gratings,* in *Laser Resonators and Beam Control XI,* Proc. of SPIE, 2009.

126. B. Jacobsson, C. Canalias, V. Pasiskevicius, and F. Laurell, *Narrowband and tunable ring optical parametric oscillator with a volume Bragg grating,* Optics Letters, **32**, 3278-3280, 2007.

127. B. Jacobsson, M. Tiihonen, V. Pasiskevicius, and F. Laurell, *Narrowband bulk Bragg grating optical parametric oscillator,* Optics Letters, **30**, 2281-2283, 2005.

128. J. W. Kim, P. Jelger, J. K. Sahu, F. Laurell, and W. A. Clarkson, *High-power and wavelength-tunable operation of an Er, Yb fiber laser using a volume Bragg grating,* Optics Letters, **33**, 1204-1206, 2008.

129. M. Hemmer, Y. Joly, L. Glebov, M. Bass, and M. Richardson, *Volume Bragg Grating assisted broadband tunability and spectral narrowing of Ti: Sapphire oscillators,* Optics Express, **17**, 8212-8219, 2009.

130. O. G. Andrusyak, *Dense spectral beam combining with volume Bragg gratings in photo-thermo-refractive glass, PhD Thesis,* University of Central Florida, (2009).

131. A. Knitsch, A. Luft, T. Gross, D. Ristau, P. Loosen, and R. Poprawe, *Diode laser modules of highest brilliance for materials processing,* in *Novel In-Plane Semiconductor Lasers,* Proc. of SPIE, San Jose, 2002.

132. K. Nosu, Ishio, H., Hashimoto, K. , *Multireflection optical multi/demultiplexer using interference filters,* Electron. Lett., **15**, 414–415, 1979.

133. G. Venus, L. Glebov, O. Andrusyak, I. Ciapurin, V. Rotar, and A. Sevian, *Dense Spectral Beam Combining with Volume Bragg Gratings in PTR Glass,* DTIC Document, 2006.

134. O. Andrusyak, V. Smirnov, G. Venus, V. Rotar, and L. Glebov, *Spectral combining and coherent coupling of lasers by volume Bragg gratings,* Selected Topics in Quantum Electronics, IEEE Journal of, **15**, 344-353, 2009.

135. B. Chann, R. K. Huang, L. J. Missaggia, C. T. Harris, Z. L. Liau, A. K. Goyal, J. P. Donnelly, T. Y. Fan, A. Sanchez-Rubio, and G. W. Turner, *Near-diffraction-limited diode laser arrays by wavelength beam combining,* Optics Letters, **30**, 2104-2106, 2005.

136. D. Vijayakumar, O. B. Jensen, J. Barrientos-Barria, D. Paboeuf, G. Lucas-Leclin, B. Thestrup, and P. M. Petersen, *Narrow line width operation of a 980 nm gain guided tapered diode laser bar,* Optics Express, **19**, 1131-1137, 2011.

137. F. Roser, S. Klingebiel, A. Liem, T. Schreiber, S. Hofer, J. Limpert, T. Peschel, R. Eberhardt, and A. Tunnermann, *Spectral beam combining of fiber lasers,* in *Fiber lasers III,* Proc. of SPIE, San Jose, 2006.

138. C. Wirth, O. Schmidt, I. Tsybin, T. Schreiber, T. Peschel, F. BrÃ¼ckner, T. Clausnitzer, J. Limpert, R. Eberhardt, and A. TÃ¼nnermann, *2 kW incoherent beam combining of four narrow-linewidth photonic crystal fiber amplifiers,* Optics Express, **17**, 1178-1183, 2009.

139. B. Chann, A. K. Goyal, T. Y. Fan, A. Sanchez-Rubio, B. L. Volodin, and V. S. Ban, *Efficient, high-brightness wavelength-beam-combined commercial off-the-shelf diode stacks achieved by use of a wavelength-chirped volume Bragg grating*. 2006, Optical Society of America. p. 1253-1255.

140. C. Hamilton, S. Tidwell, D. Meekhof, J. Seamans, N. Gitkind, and D. Lowenthal, *High power laser source with spectrally beam combined diode laser bars,* in *Proc. of SPIE,* 2004.

141. J. T. Gopinath, B. Chann, T. Y. Fan, and A. Sanchez-Rubio, *1450-nm high-brightness wavelength-beam combined diode laser array*. 2008, Optical Society of America. p. 9405-9410.

142. A. Sevian, O. Andrusyak, I. Ciapurin, V. Smirnov, G. Venus, and L. Glebov, *Efficient power scaling of laser radiation by spectral beam combining,* Optics Letters, **33**, 384-386, 2008.

143. X. Chu, S. Zhao, L. Shi, S. Zhan, J. Xu, and Z. Wu, *Expansion of the channel number in spectral beam combining of fiber lasers array based on cascaded gratings,* Optics Communications, **281**, 4099-4102, 2008.

144. L. Bartelt-Berger, U. Brauch, A. Giesen, H. Huegel, and H. Opower, *Power-scalable system of phase-locked single-mode diode lasers,* Applied Optics, **38**, 5752-5760, 1999.

145. J. R. Leger, M. L. Scott, and W. B. Veldkamp, *Coherent addition of AlGaAs lasers using microlenses and diffractive coupling,* Applied Physics Letters, **52**, 1771-1773, 1988.

146. J. R. Leger, *Lateral mode control of an AlGaAs laser array in a Talbot cavity,* Applied Physics Letters, **55**, 334-336, 1989.

147. W. Liang, A. Yariv, A. Kewitsch, and G. Rakuljic, *Coherent combining of the output of two semiconductor lasers using optical phase-lock loops*. 2007, Optical Society of America. p. 370-372.

148. T. M. Shay, V. Benham, J. T. Baker, B. Ward, A. D. Sanchez, M. A. Culpepper, D. Pilkington, J. Spring, D. J. Nelson, and C. A. Lu, *First experimental demonstration of self-synchronous phase locking of an optical array*. 2006, Optical Society of America. p. 12015-12021.

149. R. K. Huang, B. Chann, L. J. Missaggia, S. J. Augst, R. B. Swint, J. P. Donnelly, A. Sanchez-Rubio, and G. W. Turner, *High-Power Coherent Beam Combination of Semiconductor Laser Arrays,* in *High-Power Semiconductor Lasers (CMN), CLEO* Optical Society of America, San Jose, California, 2008.

150. D. Botez, *High-power monolithic phase-locked arrays of antiguided semiconductor diode lasers,* in *Optoelectronics, IEE Proceedings J* IET, 1992.

151. D. Botez, L. Mawst, P. Hayashida, G. Peterson, and T. J. Roth, *High-power, diffraction-limited-beam operation from phaseâ€ locked diodeâ€ laser arrays of closely spaced ˜leaky" waveguides (antiguides),* Applied Physics Letters, **53**, 464-466, 1988.

152. J. Banerji, A. R. Davies, and R. M. Jenkins, *Comparison of Talbot and 1-to- N-way phase-locked array resonators,* Applied Optics, **36**, 1604-1609, 1997.

153. J. Banerji, A. R. Davies, and R. M. Jenkins, *Phased array 1-to-N-way resonator with a convex mirror for phase conjugation,* Applied Optics, **44**, 3364-3369, 2005.

154. M. Lobel, P. M. Petersen, and P. M. Johansen, *Tunable single-mode operation of a high-power laser-diode array by use of an external cavity with a grating and a photorefractive phase-conjugate mirror,* JOSA B, **15**, 2000-2005, 1998.

155. J. S. Lawrence and D. M. Kane, *Broad-area diode lasers with plane-mirror and phase-conjugate feedback,* Journal of Lightwave Technology, **20**, 100, 2002.

156. F. X. D' Amato, E. T. Siebert, and C. Roychoudhuri, *Coherent operation of an array of diode lasers using a spatial filter in a Talbot cavity*. 1989, AIP. p. 816-818.

157. R. K. Huang, B. Chann, L. J. Missaggia, S. J. Augst, M. K. Connors, G. W. Turner, A. Sanchez-Rubio, J. P. Donnelly, J. L. Hostetler, and C. Miester, *Coherent combination of slab-coupled optical waveguide lasers,* in *Novel In-Plane Semiconductor Lasers VIII,* Proc. of SPIE, San Jose, 2009.

158. B. Liu, Y. Liu, and Y. Braiman, *Coherent beam combining of high power broad-area laser diode array with a closed-V-shape external Talbot cavity,* Optics Express, **18**, 7361-7368, 2010.

159. D. Pabœuf, G. Lucas-Leclin, P. Georges, N. Michel, M. Krakowski, J. Lim, S. Sujecki, and E. Larkins, *Narrow-line coherently combined tapered laser diodes in a Talbot external cavity with a volume Bragg grating,* Applied Physics Letters, **93**, 211102, 2008.

160. D. Pabœuf, D. Vijayakumar, O. B. Jensen, B. Thestrup, J. Lim, S. Sujecki, E. Larkins, G. Lucas-Leclin, and P. Georges, *Volume Bragg grating external cavities for the passive phase locking of high-brightness diode laser arrays: theoretical and experimental study,* J. Opt. Soc. Am. B, **28**, 1289-1299, 2011.

161. G. Lucas-Leclin, D. Paboeuuf, P. Georges, N. Michel, M. Calligaro, M. Krakowski, J. J. Lim, S. Sujecki, and E. Larkins, *External-cavity designs for phase-coupled laser diode arrays,* in *High Power Diode Lasers and Systems Conference,* IEEE, Coventry, 2010.

162. G. L. Abbas, S. Yang, V. W. S. Chan, and J. G. Fujimoto, *Injection behavior and modeling of 100 mW broad area diode lasers,* Quantum Electronics, IEEE Journal of, **24**, 609-617, 1988.

163. G. L. Abbas, S. Yang, V. W. S. Chan, and J. G. Fujimoto, *Injection behavior of high-power broad-area diode lasers,* Optics Letters, **12**, 605-607, 1987.

164. Y. Liu, H. K. Liu, and Y. Braiman, *Injection locking of individual broad-area lasers in an integrated high-power diode array,* Applied Physics Letters, **81**, 978, 2002.

165. L. J. Missaggia, S. M. Redmond, M. A. Brattain, M. K. Connors, K. J. Creedon, R. K. Huang, B. Chann, J. M. Caissie, A. Sanchez-Rubio, and G. W. Turner, *Advanced Packaging of High-Power Slab-Coupled Optical Waveguide Laser and Amplifier Arrays for Coherent Beam Combining,* in *CLEO Symposium on Laser Beam Combining III: Beam Combining and Locking of High-Power Diode Lasers* Optical Society of America, San Jose, 2010.

166. S. M. Redmond, K. J. Creedon, J. E. Kansky, S. J. Augst, L. J. Missaggia, M. K. Connors, R. K. Huang, B. Chann, T. Y. Fan, and G. W. Turner, *Active coherent beam combining of diode lasers,* Optics Letters, **36**, 999-1001, 2011.

167. H. F. Talbot, *Facts relating to optical science,* Philosophical Magazine Series 3, 1836.

168. J. R. Leger, *Microoptical components applied to incoherent and coherent laser arrays*, in *Diode Laser Arrays,* Cambridge University Press, Cambridge, 1994.

169. V. V. Antiukhov, A. F. Glova, O. R. Kachurin, F. V. Lebedev, V. V. Likhanskii, and A. P. P. m. Napartovich, V. D., *Effective phase locking of an array of lasers,* JETP Lett., **44**, 78-81, 1986.

170. D. Mehuys, W. Streifer, R. G. Waarts, and D. F. Welch, *Modal analysis of linear Talbot-cavity semiconductor lasers,* Optics Letters, **16**, 823-825, 1991.

171. J. R. Leger and G. J. Swanson, *Efficient array illuminator using binary-optics phase plates at fractional-Talbot planes,* Optics Letters, **15**, 288-290, 1990.

172. Q. Li, P. Zhao, and W. Guo, *Amplitude compensation of a diode laser array phase locked with a Talbot cavity,* Applied Physics Letters, **89**, 231120, 2006.

173. A. F. Glova, N. N. Elkin, A. Y. Lysikov, and A. P. Napartovich, *External Talbot cavity with in-phase mode selection,* Quantum Electronics, **26**, 614, 1996.

174. A. Yariv, *Quantum electronics* Wiley, 1989.

175. J. K. Butler, D. E. Ackley, and D. Botez, *Coupled-mode analysis of phase-locked injection laser arrays,* Applied Physics Letters, **44**, 293-295, 1984.

176. D. Botez, L. J. Mawst, G. L. Peterson, and T. J. Roth, *Phase-locked arrays of antiguides: model content and discrimination,* Quantum Electronics, IEEE Journal of, **26**, 482-495, 1990.

177. D. Lu, J. Chen, H. Yang, H. Chen, X. Lin, and S. Gao, *Theoretical analysis on phase-locking properties of a laser diode array facing an external cavity,* Optics & Laser Technology, **38**, 516-522, 2006.

178. R. M. Waarts, D. Nam, D. Welch, D. Streifer, W. Scifres, D. , *High-power, cw, diffraction limited, AlGaAs laser diode array in an external Talbot cavity* Applied Physics Letters, **58**, 2586, 1991.

179. V. V. Apollonov, S. I. Derzhavin, V. I. Kislov, A. A. Kazakov, Y. P. Koval, V. V. Kuz'minov, D. A. Mashkovskii, and A. M. Prokhorov, *Spatial phase locking of linear arrays of 4 and 12 wide-aperture semiconductor laser diodes in an external cavity,* Quantum Electronics, **28**, 257, 1998.

180. V. V. Apollonov, S. I. Derzhavin, V. I. Kislov, A. A. Kazakov, Y. P. Koval, V. V. Kuz'minov, D. A. Mashkovskii, and A. M. Prokhorov, *Phase locking of eight wide-aperture semiconductor laser diodes in one-dimensional and two-dimensional configurations in an external Talbot cavity,* Quantum Electronics, **28**, 344, 1998.

181. Q. Li, P. Zhao, W. Guo, and B. Liu, *The in-phase mode selection of a high-power diode laser array by a talbot cavity with an amplitude compensator,* Optics Communications, **270**, 323-326, 2007.

182. B. Liu, Y. Liu, and Y. Braiman, *Coherent addition of high power laser diode array with a V-shape external Talbot cavity,* Optics Express, **16**, 20935-20942, 2008.

183. C. J. Chang Hasnain, J. Berger, D. R. Scifres, W. Streifer, J. R. Whinnery, and A. Dienes, *High power with high efficiency in a narrow single lobed beam from a diode laser array in an external cavity,* Applied Physics Letters, **50**, 1465-1467, 1987.

184. L. Goldberg and J. F. Weller, *Narrow lobe emission of high power broad stripe laser in external resonator cavity,* Electronic Letters, **25**, 112-114, 1989.

185. V. Raab, D. Skoczowsky, and R. Menzel, *Tuning high-power laser diodes with as much as 0.38 W of power and $M^2$ = 1.2 over a range of 32 nm with 3-GHz bandwidth,* Optics Letters, **27**, 1995-1997, 2002.

186. X. Gao, Y. Zheng, H. Kan, and K. Shinoda, *Effective suppression of beam divergence for a high-power laser diode bar by an external-cavity technique,* Optics Letters, **29**, 361-363, 2004.

187. A. Jechow, V. Raab, R. Menzel, M. Cenkier, S. Stry, and J. Sacher, *1 W tunable near diffraction limited light from a broad area laser diode in an external cavity with a line width of 1.7 MHz,* Optics Communications, **277**, 161-165, 2007.

188. I. Hassiaoui, N. Michel, G. Bourdet, R. Mc Bride, M. Lecomte, O. Parillaud, M. Calligaro, M. Krakowski, and J. P. Huignard, *Very compact external cavity diffraction-coupled tapered laser diodes,* Applied Optics, **47**, 746-750, 2008.

189. C. Wirth, O. Schmidt, I. Tsybin, T. Schreiber, R. Eberhardt, J. Limpert, A. TÃ¼nnermann, K. Ludewigt, M. Gowin, and E. ten Have, *High average power spectral beam combining of four fiber amplifiers to 8.2 kW,* Optics Letters, **36**, 3118-3120,

190. T. Alahautala, E. Lassila, and R. Hernberg, *High power density beam from narrow diode-laser arrays in axial symmetry,* Applied Optics, **43**, 2760-2766, 2004.

191. J. W. Tomm, A. Gerhardt, R. Muller, V. Malyarchuk, Y. Sainte-Marie, P. Galtier, J. Nagle, and J. P. Landesman, *Spatially resolved spectroscopic strain measurements on high-power laser diode bars,* Journal of Applied Physics, **93**, 1354, 2003.

192. L. Pavesi and M. Guzzi, *Photoluminescence of AlxGa1-xAs alloys,* Journal of Applied Physics, **75**, 4779-4842, 1994.

193. E. Martin, J. P. Landesman, J. P. Hirtz, and A. Fily, *Microphotoluminescence mapping of packaging-induced stress distribution in high-power AlGaAs laser diodes,* Applied Physics Letters, **75**, 2521, 1999.

194. J. P. Landesman, *Micro-photoluminescence for the visualisation of defects, stress and temperature profiles in high-power III-V's devices* 1,* Materials Science and Engineering B, **91**, 55-61, 2002.

195. H. J. Baker, C. Ott, R. M. McBride, J. J. Wendland, and D. R. Hall, *Beam shapers for high power lasers, fabricated by laser micro-machining,* in *CLEO,* OSA, Baltimore, 2009.

196. R. de Saint Denis, N. Passilly, M. Laroche, T. Mohammed-Brahim, and K. Ait-Ameur, *Beam-shaping longitudinal range of a binary diffractive optical element,* Applied Optics, **45**, 8136-8141, 2006.

197. X. Tan, B. Y. Gu, G. Z. Yang, and B. Z. Dong, *Diffractive phase elements for beam shaping: a new design method,* Applied Optics, **34**, 1314-1320, 1995.

198. I. Ghozeil and D. Macalara, *Optical Shop Testing*. 1978, Wiley, New York. p. 361.

199. A. F. Brooks, P. J. Veitch, T. L. Kelly, and J. Munch, *Ultra-sensitive wavefront measurement using a Hartmann sensor,* Optics Express, **15**, 10370-10375, 2007.

200. D. R. Neal, J. Copland, and D. A. Neal, *Shack-Hartmann wavefront sensor precision and accuracy,* in *Advanced Characterization Techniques for Optical, Semiconductor, and Data Storage Components,* Proc. of SPIE, Seattle, 2002.

201. P. Hariharan, *Lateral and radial shearing interferometers: a comparison,* Applied Optics, **27**, 3594-3596, 1988.

202. J. C. Wyant, *Use of an ac heterodyne lateral shear interferometer with real-time wavefront correction systems,* Applied Optics, **14**, 2622-2626, 1975.

203. W. J. Bates, *A wavefront shearing interferometer,* Proceedings of the Physical Society, **59**, 940, 1947.

204. D. G. Kocher, *Twyman-Green interferometer to test large aperture optical systems,* Applied Optics, **11**, 1872-1874, 1972.

205. K. M. Nowak, H. J. Baker, and D. R. Hall, *Efficient laser polishing of silica micro-optic components,* Applied Optics, **45**, 162-171, 2006.

206. K. M. Nowak, *Rapid prototyping of micro-optics for brightness restoration of diode lasers, PhD Thesis,* Heriot-Watt University, Edinburgh (2003).

207. H. J. Baker, J. F. Monjardin, P. Kneip, D. R. Hall, and R. McBride, *1.8 kW diode laser system for fibre-delivery using brightness-enhanced diode stacks and a novel final beam-shaper*.

208. F. J. Villarreal, H. J. Baker, R. H. Abram, D. R. Jones, and D. R. Hall, *Beam reformatting of one-and two-dimensional arrays of CO2 waveguide lasers,* Quantum Electronics, IEEE Journal of, **35**, 267-272, 1999.

209. S. Alam, K. Chen, J. R. Hayes, D. Lin, A. Malinowski, H. J. Baker, N. Trela, R. McBride, and D. J. Richardson, *Over 55W of frequency doubled light at 530 nm pumped by an all-fiber diffraction limited picosecond fibre MOPA,* in *Photonics West,* Proc. of SPIE, Sa Francisco, 2010.

210. B. Köhler, T. Brand, M. Haag, and J. Biesenbach, *Wavelength stabilized high-power diode laser modules,* in *High-Power Diode Laser Technology and Applications VII,* Proc. of SPIE, San Jose, 2009.

211. N. Trela, H. J. Baker, and J. Wendland, *Dual-axis beam correction for an array of single-mode diode laser emitters using a laser-written custom phase-plate,* Optics Express, **17**, 23576-23581, 2009.

212. M. Krejci, Personal communication (2010).

213. N. Trela, H. J. Baker, J. J. Wendland, and D. R. Hall, *Demonstration of high pointing accuracy dual-axis collimation of 49 emitter diode bar using a laser-written custom phase-plate,* in *Proc. of SPIE,* 2010.

214. J. N. Walpole, H. K. Choi, L. G. Missaggia, Z. L. Liau, M. K. Connors, G. W. Turner, M. J. Manfra, and C. C. Cook, *High-power high-brightness GaInAsSb-AlGaAsSb tapered laser arrays with anamorphic collimating lenses emitting at 2.05 micron,* IEEE, Photonics Technology Letters, **11**, 1223-1225, 1999.

215. B. Sumpf, R. Hulsewede, G. Erbert, C. Dzionk, J. Fricke, A. Knauer, W. Pittroff, P. Ressel, J. Sebastian, and H. Wenzel, *High-brightness 735 nm tapered diode lasers,* Electronics Letters, **38**, 183-184, 2002.

216. R. K. Huang, L. J. Missaggia, J. P. Donnelly, C. T. Harris, and G. W. Turner, *High-brightness slab-coupled optical waveguide laser arrays,* Photonics Technology Letters, IEEE, **17**, 959-961, 2005.

217. B. Liu, Y. Liu, and Y. Braiman, *Linewidth reduction of a broad-area laser diode array in a compound external cavity,* Applied Optics, **48**, 365-370, 2009.

218. I. V. Ciapurin, L. B. Glebov, and V. I. Smirnov, *Modeling of Gaussian beam diffraction on volume Bragg gratings in PTR glass,* in *Practical Holography XIX: Materials and Applications,* Proc. of SPIE, San Jose, 2005.

219. A. E. Siegman, *Lasers,* University Science Books, 1986.

220. A. E. Siegman, *Complex paraxial wave optics*, in *Lasers,* University Science Books, 1986.

221. R. Lang and K. Kobayashi, *External optical feedback effects on semiconductor injection laser properties,* IEEE, Journal of Quantum Electronics, **16**, 347-355, 1980.

222. L. Goldberg, H. F. Taylor, A. Dandridge, J. F. Weller, and R. O. Miles, *Spectral characteristics of semiconductor lasers with optical feedback,* IEEE, Transactions onMicrowave Theory and Techniques, **30**, 401-410, 1982.

223. G. Acket, D. Lenstra, A. Den Boef, and B. Verbeek, *The influence of feedback intensity on longitudinal mode properties and optical noise in index-guided semiconductor lasers,* IEEE, Journal ofQuantum Electronics, **20**, 1163-1169, 1984.

224. D. Richter, A. Fried, B. P. Wert, J. G. Walega, and F. K. Tittel, *Development of a tunable mid-IR difference frequency laser source for highly sensitive airborne trace gas detection,* Applied Physics B: Lasers and Optics, **75**, 281-288, 2002.

225. Y. A. Bakhirkin, A. A. Kosterev, C. Roller, R. F. Curl, and F. K. Tittel, *Mid-infrared quantum cascade laser based off-axis integrated cavity output spectroscopy for biogenic nitric oxide detection,* Applied Optics, **43**, 2257-2266, 2004.

226. J. T. Olesberg, M. A. Arnold, C. Mermelstein, J. Schmitz, and J. Wagner, *Tunable laser diode system for noninvasive blood glucose measurements,* Applied spectroscopy, **59**, 1480-1484, 2005.

227. C. J. Chang-Hasnain, J. P. Harbison, C. E. Zah, M. W. Maeda, L. T. Florez, N. G. Stoffel, and T. P. Lee, *Multiple wavelength tunable surface-emitting laser arrays,* IEEE Journal of Quantum Electronics, **27**, 1368-1376, 1991.

228. W. Yuen, G. S. Li, and C. J. Chang-Hasnain, *Multiple-wavelength vertical-cavity surface-emitting laser arrays with a record wavelength span,* Photonics Technology Letters, IEEE, **8**, 4-6, 1996.

229. J. E. Hellstrom, B. Jacobsson, V. Pasiskevicius, and F. Laurell, *Finite beams in reflective volume Bragg gratings: theory and experiments,* IEEE, Journal of Quantum Electronics, **44**, 81-89, 2008.

230. Z. Sheng-bao, Z. Shang-hong, C. Xing-chun, W. Zhuo-liang, and S. Lei, *Spectral beam combining of fiber lasers based on a transmitting volume Bragg grating,* Optics & Laser Technology, **42**, 308-312, 2010.

231. G. Bloom, C. Larat, E. Lallier, G. Lehoucq, S. Bansropun, M. S. L. Lee-Bouhours, B. Loiseaux, M. Carras, X. Marcadet, and G. Lucas-Leclin, *Passive coherent beam combining of quantum-cascade lasers with a Dammann grating,* Optics Letters, **36**, 3810-3812, 2011.

232. D. Pabœuf, F. Emaury, S. de Rossi, R. Mercier, G. Lucas-Leclin, and P. Georges, *Coherent beam superposition of ten diode lasers with a Dammann grating,* Optics Letters, **35**, 1515-1517, 2010.

233. A. M. Hornby, H. J. Baker, A. D. Colley, and D. R. Hall, *Phase locking of linear arrays of CO2 waveguide lasers by the waveguide confined Talbot effect,* Applied Physics Letters, **63**, 2591-2593, 1993.